ON THE TURBULENCE-GENERATED SOUND AND CONTROL OF COMPRESSIBLE MIXING LAYERS

BY

RANDALL RAY KLEINMAN

DISSERTATION

Submitted in partial fulfillment of the requirements
for the degree of Doctor of Philosophy in Theoretical and Applied Mechanics
in the Graduate College of the
University of Illinois at Urbana-Champaign, 2010

Urbana, Illinois

Doctoral Committee:

Associate Professor Jonathan B. Freund, Chair
Assistant Professor Joanna M. Austin
Assistant Professor Daniel J. Bodony
Associate Professor Kenneth T. Christensen

Abstract

A mixing layer is a common model used to study the noise generation and mixing characteristics of the near-nozzle region of jets. This work presents three separate but related studies that investigate sound generation and active control for noise mitigation and mixing enhancement of such mixing layers. High-fidelity direct numerical simulations of temporal and spatial mixing layers are used for this in two and three dimensions.

The first study investigates the role of turbulence scales in generating the radiated far-field sound from temporally-developing, Mach 0.9 mixing layers. To do this, four mixing layers were simulated, starting from the same initial conditions but with Reynolds numbers that varied by a factor of twelve. Above a momentum thickness Reynolds number of 300, all the mixing layers radiate over 85 percent of the acoustic energy of the apparently asymptotically high-Reynolds-number value we are able to compute. Wavenumber spectra of turbulence energy and pressure show the expected Reynolds number dependence: the two highest Reynolds number simulations show evidence of an inertial range and Kolmogorov scaling at the highest wavenumbers. Far-field pressure spectra all decay much more rapidly with wavenumber than the corresponding near-field spectra and show significantly less sensitivity to Reynolds number. Low wavenumbers account for nearly all of the radiated acoustic energy. Implications of these results for jet noise large-eddy simulations are discussed.

The second study uses direct numerical simulations of Mach 1.3 mixing layers to characterize the physical mechanisms of flow actuation by localized arc-filament plasma actuators. A validated numerical model of the actuator is devised and placed, as in corresponding experiments, in a cavity in the nozzle near its exit. A rapid Joule heating caused by the plasma is thought to be the root mechanism of flow actuation based upon experimental observation. Simulations show that in the confined space of the cavity, the actuator creates a rapid flow expansion, which transfers

fluid mass upward and outward creating a synthetic-jet-like perturbation to the boundary layer. The actuation promotes vortex creation much closer to the nozzle than the baseline flow without actuation, increases the layer growth rate, and organizes the large flow structures. Placing the actuator in a cavity of half the original width increases the velocities responsible for the jet-like boundary layer perturbation and downstream mixing layer growth rate. An actuator model designed to produce the same pressure response without the rapid heating provides similar control authority.

The final study implements an automatic optimization procedure based on the adjoint of the perturbed and linearized flow equations. An algorithm is formulated to provide optimized control actuation for noise reduction and mixing enhancement objectives. The method is demonstrated to be successful on several model problems in two and three dimensions, in cases both with an explicitly represented "splitter" plate and cases where an appropriate inflow condition is imposed in its place. Cost functionals for noise reduction and mixing enhancement based on cross-stream velocity and pressure are formulated. Two-dimensional mixing layers with near-wall control are presented with velocity- and pressure-based spreading enhancement cost functionals. Both controls are able to maximize their respective cost functionals by over 50% and increase mixing layer thickness by 10-15% over the optimization time horizon. A three-dimensional, turbulent (spatially-developing) mixing layer is simulated and optimized with a noise reduction cost functional. The control successfully reduces the noise on a target plane below the mixing layer by 28% after 4 line search iterations of the optimization scheme.

To Karen, Madeline, Grace, and Jack.

Acknowledgments

While there are many people who are partially responsible for the level of education I have obtained, let me first thank my advisor, Jonathan Freund. Professor Freund offered me a research assistantship less than ten minutes after I first met him as a visiting prospective student. Ever since then, he has continuously guided me with fruitful discussion, technical knowledge, challenging questions, and enjoyable humor. I am especially appreciative of the high standards and expectations he has for me and my work. I consider myself blessed to have been advised by him these last few years.

Others to whom I am gratefully indebted to during my time at UIUC include: Renchi Raju, Dr. Hong Zhao, Dr. Mingjun Wei, Brian Taylor, John Fettig, Amir Ghalayan, Dr. Victor Topalian, David Lin, Dr. Arnab Samanta, and Jeonglae Kim. I would also like to thank the following professors for their contributions to my education: Profs. Robert Moser, Ken Christensen, Joanna Austin, Daniel Bodony, Mark Short, and Brian Thomas.

Next, I would like to thank my parents, Tommie and Joy, and Bethel University Physics Professors Brian Beecken and Keith Stein. My parents encouraged me from a very young age to do well in academics and work hard to the best of my abilities. The guidance and gentle nudging of Drs. Beecken and Stein are the main reason I decided to enter graduate studies.

I would like to acknowledge the Air Force Office of Scientific Research, the U.S. Department of Energy, and NASA for being major sources of financial support. Also, I would like to acknowledge the Department of Defense High Performance Computing and Modernization Program coupled with the Navy DoD Supercomputing Resource Center and the Maui High Performance Computing Center for providing computational resources for this work.

Last, I would like to thank my lovely and wonderful wife, Karen. There is no doubt in my mind that the work contained in this dissertation has only been possible because of her daily love, encouragement, and support. Since the tornado-warning-laden evening when we first arrived as newlyweds to our first apartment in Champaign, all of her activities have been in full support of me and my education. Karen, a description of the worth of your unconditional sacrifices over the past few years is unable to fit into so small a space.

Table of Contents

List of Tables . . . . . **xi**

List of Figures . . . . . **xii**

List of Symbols . . . . . **xvi**

Chapter 1 Introduction **1**

1.1 History and Motivation 1

1.2 Review of Past Work 4

1.3 Present Work 6

1.4 Overview of Accomplishments 8

Chapter 2 Simulation Techniques **12**

2.1 Governing Equations 12

2.2 Numerical Methods 14

2.2.1 Spatial Discretization 14

2.2.2 Spatial Discretization Near Walls 18

2.2.3 Mesh Considerations 19

2.2.4 Time Advancement 23

2.2.5 Boundary Conditions and Treatments 24

2.2.6 Solid Wall Boundaries 26

2.2.7 Numerical Stabilization 26

Chapter 3 The Sound from Mixing Layers Simulated with Different Ranges of Turbulence Scales . . . 28
3.1 Introduction . . . 28
3.1.1 A Model Turbulent Flow . . . 30
3.1.2 Temporal Mixing Layer Simulations . . . 30
3.2 Initial Conditions and Simulation Details . . . 31
3.3 Results . . . 33
3.3.1 Initial Flow . . . 33
3.3.2 Layer Growth . . . 36
3.3.3 Mean Flow and Reynolds Stresses . . . 39
3.3.4 Visualization . . . 45
3.3.5 Kinetic Energy Spectra . . . 46
3.3.6 Numerical Stabilization via Filtering . . . 53
3.3.7 Pressure Spectra . . . 54
3.3.8 Far-field Frequency Spectra . . . 58
3.3.9 Pressure Wave Attenuation . . . 62
3.3.10 Acoustic Power and Energy . . . 64
3.3.11 The Role of Vortex Pairing . . . 66
3.4 Discussion . . . 75
3.5 Conclusions . . . 76

Chapter 4 Numerical Modeling of Localized Arc-filament Plasma Actuators . . . 79
4.1 Introduction . . . 79
4.2 Experimental Characterization of LAFPA . . . 82
4.3 Numerical Plasma Heating Model . . . 83
4.4 Simulation Details . . . 85
4.4.1 Flow Domain and Parameters . . . 85
4.4.2 Numerical Methods . . . 87
4.4.3 Actuator Forcing Parameters . . . 88
4.5 Results and Discussion . . . 88
4.6 Actuator Model Validation . . . 89

4.6.1 Near-field Pressure . . . 90
4.6.2 Cavity Temperature . . . 90
4.7 Cavity Oscillation Dynamics – Baseline Simulation . . . 91
4.7.1 Background . . . 91
4.7.2 Cavity Pressure Spectrum – Baseline . . . 94
4.7.3 Rossiter Parameter Comparisons with Experiment . . . 99
4.7.4 Cavity Oscillation Frequency Evolution . . . 101
4.7.5 Conclusions . . . 103
4.8 Cavity Oscillation Dynamics – Actuated Simulation . . . 103
4.8.1 Observations . . . 103
4.8.2 Cavity Pressure Spectrum – Actuated . . . 109
4.8.3 Cavity Pressure Spectra for Varying Duty-cycle Forcing . . . 114
4.8.4 Conclusions . . . 116
4.9 Actuator Forcing Mechanisms . . . 117
4.9.1 Cavity Region Visualization – A Jetting Effect . . . 117
4.9.2 Vorticity Generation in the Near-nozzle Region . . . 122
4.9.3 Temperature and Cavity Effects . . . 131
4.9.4 Conclusions . . . 141
4.10 Frequency Spectra . . . 142
4.11 Conclusions . . . 147

Chapter 5 Adjoint-based Optimization of Compressible Mixing Layers . . . 151
5.1 Introduction . . . 151
5.2 Control Derivation and Implementation . . . 154
5.2.1 Governing Equations . . . 154
5.2.2 Cost Functionals . . . 156
5.2.3 Sensitivity to Control Perturbations . . . 158
5.2.4 Adjoint Problem Formulation . . . 160
5.2.5 Gradients of Cost Functionals . . . 161
5.2.6 Optimization Procedure . . . 164
5.3 Numerical Implementation . . . 164

5.4 Anti-Sound Internal Energy Source Results . . . 166
5.4.1 Control with No Price Term Considered . . . 166
5.4.2 Control with Finite Price Considered . . . 171
5.5 Near-wall Two-dimensional Internal Energy Control . . . 172
5.5.1 Simulation Parameters . . . 173
5.5.2 Optimization Results . . . 174
5.6 Three-dimensional Mixing Layer Control . . . 182
5.6.1 Flow and Simulation Parameters . . . 182
5.6.2 Simulation Methodology . . . 184
5.6.3 Flow and Adjoint Field Visualization . . . 185
5.6.4 Sound Control Results . . . 187
5.7 Conclusions . . . 188

Appendix A Decay of Non-planar Waves in Doubly-periodic Domains . . . 191

Appendix B The Adjoint of the Three-dimensional Compressible Navier-Stokes Equations . . . 194

Appendix C Adjoint Characteristic Boundary Conditions . . . 197
C.1 Derivation . . . 197
C.2 Implementation . . . 200
C.2.1 Adjoint Characteristic Variables . . . 200
C.2.2 Nonreflecting Boundary Conditions . . . 201
C.2.3 Solid Wall Boundary Conditions . . . 201

List of References . . . 203

Author Biography . . . 211

List of Tables

2.1 Coefficients for finite difference approximations to interior first and second derivatives. . . . 16

3.1 Mesh sizes and cross-stream stretching information. . . . 31

3.2 Reynolds numbers based on layer thickness for the temporal mixing layer simulations. . . . 35

3.3 Net acoustic energy $\mathcal{E}$ between labeled points in Fig. 3.23. . . . 66

3.4 Time intervals shown in Fig. 3.24 in far field and propagation-adjusted time intervals in Figs. 3.25 and 3.26. . . . 68

4.1 Mesh stretching constants for the actuator simulation domain 87

4.2 Rossiter modes and cavity oscillation frequencies for the baseline $L_c/D_c = 2$ simulation. . . . 98

4.3 Summary of cavity oscillation frequencies and parameters of all $L_c/D_c = 2$ simulations 117

List of Figures

1.1 Growth of airport noise restrictions since 1970 for ICAO-member airports. 3

2.1 Modified wavenumber curves of first derivative finite-difference schemes for the interior computational domain. 17

2.2 Derivatives of the cross-stream coordinate mapping function 21

2.3 Derivatives of the streamwise coordinate mapping functions 23

3.1 One-dimensional kinetic energy and pressure spectra of the initial conditions and the initial flow of ML3. 34

3.2 Streamwise and spanwise Taylor microscale evolution. 37

3.3 Momentum and vorticity thickness evolution. 38

3.4 Scaled mean velocity profiles of the ML2 and ML3 mixing layers. 40

3.5 Scaled Reynolds stress profiles for the ML1 mixing layer. 41

3.6 Scaled Reynolds stress profiles for the ML2 mixing layer. 42

3.7 Scaled Reynolds stress profiles for the ML3 mixing layer. 43

3.8 Scaled Reynolds stress profiles for the ML4 mixing layer. 44

3.9 Visualizations of pressure fluctuations and vorticity magnitude on the x-y plane. . . 47

3.10 Visualizations of dilatation of velocity and vorticity magnitude on the x-y plane. . . 48

3.11 Visualizations of vorticity magnitude on the $x - z$ plane. 49

3.12 One-dimensional kinetic energy spectra scaled by the initial momentum thickness. . 50

3.13 One-dimensional kinetic energy spectra scaled by the Taylor microscale. 51

3.14 One-dimensional kinetic energy spectra scaled by the Kolmogorov length scale. . . . 52

3.15 One-dimensional kinetic energy and pressure spectra of stabilized coarse mesh simulation compared to ML3. 54

3.16 One-dimensional streamwise pressure spectra of ML3 simulation at several cross-stream locations at propagation adjusted times. 55

3.17 One-dimensional pressure spectra in the near and far field scaled by the layer momentum thickness. . . . 57

3.18 One-dimensional pressure spectra in the near and far field scaled by the Taylor microscale. . . . 59

3.19 One-dimensional pressure spectra in the near and far field scaled by the Kolmogorov scale. . . . 60

3.20 $1/3$-octave frequency pressure spectra in the far field. . . . 61

3.21 Attenuation due to viscosity of far-field pressure spectra from pressure waves emanating from the mixing layers. . . . 63

3.22 Attenuation due to viscosity of frequency spectra from pressure waves emanating from the mixing layers. . . . 64

3.23 Acoustic power calculated in the far field. . . . 65

3.24 Net acoustic power of mixing layers labeling time intervals around peaks of $\mathcal{P}(t)$ for comparison with mixing layer pairing events. . . . 68

3.25 Space-time pressure evolution at $y = z = 0$ of the mixing layers. . . . 70

3.26 Space-time pressure evolution at $y = 0$ and $z = L_z/2$ of the ML1 and ML2 mixing layers. . . . 71

3.27 Pressure traces taken in far field at two spanwise and five streamwise locations where pairing events occurred in ML3. . . . 72

3.28 Number of black regions in Fig. 3.25 showing progression of pairing events. . . . 74

4.1 Drawing of the OSU nozzle showing actuator and cavity geometry. . . . 81

4.2 Schematic of the computational domain of the direct numerical simulations with the plasma actuator model . . . 86

4.3 Time series and frequency spectra of the time-varying portion of the actuator forcing function $w(t)$ . . . 89

4.4 Pressure and temperature comparisons with OSU jet experiments for actuator model validation. . . . 91

4.5 Cavity pressure spectra of the baseline $L_c/D_c = 2$ cavity. . . . 95

4.6 Sound pressure level in the $L_c/D_c = 2$ cavity of the baseline simulation with labels corresponding to the calculated peak frequencies in Table 4.2 . . . 98

4.7 Joint time-frequency analysis of the baseline cavity pressure spectrum . . . 102

4.8 Mean temperature and velocity profiles in the $L_c/D_c = 2$ cavity. . . . 104

4.9 Variation of actuator forcing amplitude coefficients . . . 108

4.10 Sound spectra in the $L_c/D_c = 2$ cavity of the actuated simulation . . . 110

4.11 Joint time-frequency analysis of the $L_c/D_c = 2$ cavity pressure transitioning from no actuation to 20 kHz, 10% duty cycle forcing . . . 112

4.12 Space-time pressure evolution at $y = 0$ in the baseline and actuated cavity simulations in the cavity region. . . . 113

4.13 Sound pressure level of the actuated $L_c/D_c = 2$ cavity at 5%, 10%, and 20% duty cycles. . . . 115

4.14 Time series visualization of velocity, dilatation, and temperature in the cavity region during actuator 'on' time of the $L_c/D_c = 2$ cavity. . . . 118

4.15 Time series visualization of the velocity vector field in the region of a narrow cavity ($L_c/D_c = 1$) during actuation. . . . 121

4.16 Mass flux out of the cavity for three duty cycles (5%, 10%, and 20%) and for the $L_c/D_c = 2$ and $L_c/D_c = 1$ configurations. . . . 122

4.17 Visualizations of the $L_c/D_c = 2$ cavity and near nozzle region 15.5 μs after the start of the actuation. . . . 125

4.18 Visualizations of the $L_c/D_c = 2$ cavity and near nozzle region 20 μs after the start of the actuation . . . 127

4.19 Visualizations of the $L_c/D_c = 2$ cavity and near nozzle region vorticity. . . . 128

4.20 Visualizations of the $L_c/D_c = 2$ cavity and near nozzle region 26 μs after the start of the actuation cycle. . . . 130

4.21 Space-time pressure evolution at $y = 0$ in the baseline and actuated cavity simulation with 10% duty cycle forcing downstream of the nozzle exit. . . . 132

4.22 Schematics of basic and reduced actuator models. . . . 134

4.23 Comparison of mixing layer momentum thickness for baseline and all cavity simulations. . . . 136

4.24 Comparison of ejected fluid temperature for all simulations with 10% duty cycle. . . . 137

4.25 Baroclinic torque in the near nozzle region 26 μs after the start of the actuation cycle for all simulations with 10% duty cycle. . . . 139

4.26 Cross-stream and streamwise velocity profiles above the nozzle wall and cavity just after fluid ejection. . . . 140

4.27 Visualization of the vorticity field of the alternative actuator source at several times after the actuation. . . . 142

4.28 Frequency spectra of mixing layer simulations with 10% duty cycle forcing. . . . 144

4.29 Comparison of pressure spectra for the baseline and $L_c/D_c = 2$ cavity with 10% duty cycle forcing. . . . 145

4.30 Streamwise variation of pressure amplitude at harmonics of f_{act} for various duty cycle forcing. . . . 147

5.1 Schematic of the adjoint-based procedure for determining sensitivity for a sound reduction control. . . . 152

5.2 Schematic showing the internal energy control test case for a sound reduction cost functional . . . 167

5.3 Evolution of pressure for the anti-sound control with no price term . . . 168

5.4 Instantaneous cost of baseline and optimized flow fields for the anti-sound control with $c_{\mathrm{p}} = 0$ . . . 170

5.5 Evolution of adjoint pressure for the anti-sound control with no price term . . . 170

5.6 Instantaneous cost of baseline and optimized flow fields for the anti-sound control with and without price term considered . . . 172

5.7 Two-dimensional mixing layer adjoint simulation domain . . . 173

5.8 Instantaneous cost of the two-dimensional mixing layer spreading enhancement optimizations . . . 175

5.9 RMS fluctuations of pressure and velocity in the two-dimensional mixing layer spreading enhancement optimizations . . . 177

5.10 Space-time pressure evolution of the baseline and controlled two-dimensional mixing layers . . . 178

5.11 Pressure frequency spectrum of the two-dimensional controlled and baseline mixing layers . . . 179

5.12 Normal and Reynolds stresses of two-dimensional spreading-enhancement controlled mixing layers . . . 181

5.13 Increase of momentum thickness for simulation with a spreading-enhancement cost functional . . . 182

5.14 Schematic of three-dimensional spatial mixing layer and target and control regions. 183

5.15 Inflow turbulence feeding schematic for three-dimensional spatial mixing layer simulation . . . 185

5.16 Three-dimensional mixing layer vorticity and dilatation visualization . . . 186

5.17 Visualization of adjoint pressure field of three-dimensional mixing layer . . . 186

5.18 Instantaneous cost functional for three-dimensional spatial mixing layer adjoint optimization. . . . 187

5.19 Comparison of the baseline and controlled dilatation field in the three dimensional mixing layer . . . 188

List of Symbols

Abbreviations

CFL	Courant, Friedrichs, and Lewy number, page 23
dB	Decibels, page 91
DC	Direct current, page 79
DNS	Direct Numerical Simulation, page 12
FFT	Fast Fourier Transform, page 16
Hz	Hertz (cycles per second), page 91
LAFPA	Localized Arc-filament Plasma Actuators, page 80
ML1-4	Temporal mixing layers, see §3.3.1, page 31
RF	Radio frequency, page 79
SPL	Sound Pressure Level, page 90
STFT	Short-time Fourier Transform, page 101

Greek Symbols

α	Phase-lag parameter/frequency ratio, page 93
α_q	Compact finite difference coefficients, see equation (2.12), page 14
α_{cl}	Viscous attenuation factor, page 62

Δt Numerical time step, page 23

ΔU Mean streamwise velocity difference, page 12

Δ Local mesh spacing, page 14

δ_ω Vorticity thickness, page 36

δ_ω^0 Initial vorticity thickness, page 36

δ_{99} Visual mixing layer thickness, page 27

δ_{f} Width of ML4 filtering region, see equation (2.43), page 27

δ_{ij} Kronecker delta, page 12

δ_{m} Momentum thickness, see equation (2.0), page 12

δ_{m}^0 Initial momentum thickness, page 12

$\dot{\omega}$ Terms in the vorticity evolution equation, see equation (4.25), page 123

ϵ Velocity potential perturbation magnitude, see equation (3.3), page 31

η Kolmogorov length scale, page 58

γ Ratio of specific heats, page 13

$\lambda_{\mathrm{x,z}}$ Streamwise and spanwise Taylor microscales, see equation (3.5), page 35

$\mathbf{\Lambda}_{\mathrm{x,y}}^{\dagger}$ Adjoint characteristic velocity matrices, page 198

μ Dynamic viscosity, page 14

ν Kinematic viscosity, page 87

ω Angular frequency, page 62

ω Vorticity, $\nabla \cdot \mathbf{v}$, page 122

ρu Streamwise momentum, page 12

ρv Cross-stream momentum, page 12

ρw Spanwise momentum, page 12

ρ Density, page 12

τ_{ij} Viscous stress tensor, page 12

ε Dissipation, page 49

φ Velocity Potential, see equation (3.2), page 31

$\varrho(y)$ Filter weighting function, page 27

$\xi(y)$ Buffer zone damping function, see equation (2.39), page 24

$\zeta(y)$ Filter strength function, see equation (2.40), page 25

Roman Symbols

t_{i}, t_{f} Actuator timing parameters, page 83

$\mathbf{A}^{\dagger}$ Adjoint coefficient matrices, page 194

$\mathbf{c}^{\dagger}_{\mathrm{x,y}}$ Adjoint characteristics vectors, page 200

$\mathbf{q}$ Vector of flow variables, $(\rho u,\, \rho v,\, \rho w,\, \rho,\, e)^T$, page 154

$\mathbf{q}^{\dagger}$ Vector of adjoint variables, $\left(\rho^{\dagger},\, u^{\dagger},\, v^{\dagger},\, w^{\dagger},\, p^{\dagger}\right)^T$, page 194

$\mathbf{q}_{\mathrm{bc}}$ Buffer zone base state vector, see equation (2.38), page 24

$\mathbf{q}_{\mathrm{filt}}$ Filtered flow variables in buffer zone, page 25

$\mathbf{S}^{\dagger}_{\mathrm{x,y}}$ Adjoint characteristic coefficient matrices, page 198

$\mathbf{v}$ Vector of flow velocities $[u\, v\, w\,]^T$, page 122

$\mathcal{C}$ Adjoint control region, page 166

$\mathcal{E}$ Acoustic Energy, page 66

$\mathcal{I}$ Instantaneous Cost Functional, page 169

$\mathcal{N}(\mathbf{q})$ Navier-Stokes Operator, see equation (5.0), page 154

$\mathcal{N}^\dagger(\mathbf{q})\mathbf{q}^\dagger$ Adjoint Operator, see equation (B.1), page 194

$\mathcal{P}(t)$ Net radiated acoustic power, page 64

$\mathcal{T}$ Adjoint target region, page 166

Ma Mach Number, page 14

Pr Prandtl Number, page 14

Re Reynolds Number, page 14

$\mathrm{Re_D}$ Reynolds number based on jet diameter, page 82

T_ϕ Control time horizon, page 156

a_q Compact finite difference coefficients, see equation (2.12), page 14

c Speed of sound, page 12

C_p Specific heat at constant pressure, page 14

C_v Specific heat at constant volume, page 12

D_c Cavity depth, page 82

D_j Jet diameter, page 82

e Total energy, page 12

e_i Internal energy, page 13

E_p One-dimensional pressure wavenumber spectrum, page 33

E_v One-dimensional kinetic energy wavenumber spectrum, page 33

f_act Actuator frequency, page 83

f_{a} Fundamental aeroacoustic loop frequency, page 95

f_{b} Modulating loop frequency, page 96

f_{c} Cavity resonance frequency, page 91

f_{n} Rossiter mode of n^{th} order, page 93

$g(s)$ Grid mapping function, see equation (2.26), page 19

g_0 Grid mapping parameter, see equation (2.29), page 20

k Wavenumber, page 15

k' Modified Wavenumber, see equation (2.12), page 15

k_{c} Ratio of convective to freestream velocity, page 93

k_{t} Thermal conductivity, page 14

$k_{\mathrm{x,z}}$ Streamwise and spanwise wavenumbers, page 31

L_{b} Width of computational buffer zone, page 24

L_{c} Cavity width, page 82

$L_{\mathrm{x,y,z}}$ Computational domain lengths in the x, y, and z directions, page 20

N_{p} Number of excitation modes, see equation (3.2), page 31

$N_{\mathrm{x,y,z}}$ Number of grid points in the x, y, and z directions, page 20

p Pressure, page 12

P_{act} Actuator power, page 83

p_{dc} Actuator duty cycle, page 83

r_0 Actuator model radius, page 83

S_{act} Actuator model internal energy source, page 83

S_{p} Frequency spectrum of pressure perturbations, page 58

T Temperature, page 12

t Time, page 12

$T(k\Delta)$ High-order filtering transfer function, page 26

t_0 Beginning time of simulation, page 33

T_{act} Actuator period, page 83

t_{r} Actuator rise time, page 83

U Mean streamwise velocity, page 12

u Streamwise velocity, page 12

u_i i^{th} Cartesian velocity component, page 12

V Velocity scale, page 12

v Cross-stream velocity, page 12

w Spanwise velocity, page 12

$w(t)$ Actuator time dependence function, page 83

x Streamwise Cartesian coordinate, page 12

x_i i^{th} mesh point, page 14

x_{act} Streamwise location of actuator model center, page 83

y Cross-stream Cartesian coordinate, page 12

y_{act} Cross-stream location of actuator model center, page 83

y_{b} Physical cross-stream boundary of simulation domain, page 24

y_{p} Location of physical domain boundary, page 24

z Spanwise Cartesian coordinate, page 12

K Acceleration parameter, page 87

Superscripts and Subscripts

$()'$ First derivative, page 14

$()'$ Perturbation from mean flow, see equation (3.5), page 32

$()''$ Second derivative, page 16

$()^*$ Dimensional quantity, page 12

$()^\dagger$ Adjoint quantity, page 194

$()_\infty$ Ambient, dimensional quantity, page 12

$()_i$ i^{th} component of vector quantity, page 12

$\hat{()}$ Fourier-transformed quantity, page 191

$\langle \cdot \rangle$ Inner product, see equation (5.19), page 160

$\overline{()}$ Averaged quantity, page 12

$\tilde{()}$ Favré (density-weighted) average quantity, page 12

Chapter 1

Introduction

1.1 History and Motivation

In the mid-1930's, two young aviation pioneers independently conceived of what would become the next generation of aircraft propulsion — a gas-powered turbine engine that would come be known as the turbojet. In the United Kingdom it was Frank Whittle, a 22 year-old Royal Air Force pilot and engineer, who began crafting a centrifugal-flow engine design in 1934. Some seven years later, the British government realized the promise of the technology and granted contracts for the development of three different military jet engines. Initially, the path to turbojet-powered flight was not altogether a smooth one. Citing performance issues and well-established piston engine development in America, the U.S. Navy voted in 1938 against pursing jet propulsion despite the promise of the British program.

Concurrent to Whittle's work, a German effort to produce viable jet engines was progressing even faster due to a more advanced design and generous private funding. Hans von Ohain, a graduate student in Physics at the University of Göttigen, began work on an axial-flow engine prototype in 1935. Using his own personal funding at first*, von Ohain enlisted the help of his automobile mechanic and master machinist Max Hahn to build the first prototype in the back of Hahn's garage. Von Ohain's advisor allowed him to run the initial tests in the courtyard of the University's academic building.[1] After partnering with aircraft industry giant Ernst Heinkel via his advisor's connections, von Ohain's design powered the first turbojet flight on August 27, 1939, just five days before the German invasion of Poland and the beginning of World War II. By the end

*Von Ohain used money from licensing patents derived from his doctoral work and from family contributions. Later headlines in the German press stated "Die Oma finanzierte den Ersten Jet" (Grandma Financed the First Jet Engine).[1]

of 1939, von Ohain and Heinkel's design was already several years ahead of allied development and the German government was financing four jet engine programs for the war effort.

History would show that despite its promise to bring considerable speed and maneuvuring advantages in aerial combat, aircraft powered by the new turbojet had relatively little impact on the outcome of World War II. The complex designs and hurried development delivered engines that, when compared to traditional piston engines, were relatively unreliable and difficult to repair once in service on the battlefield. Germany had begun mass production of the turbojet-powered Me-262 fighter plane by late 1944, but manufacturing was greatly hampered by the Allies' air superiority, which decimated industrial facilities and infrastructure. However, when allied scientists visited the German research facilities after the war, the evident sophistication of the German jet engine designs sparked a new determination to develop advanced jet-powered aircraft, especially in the United States.

Even with newly-acquired government and private industry backing, several major shortcomings inherent in all turbojets would have to be overcome before any type of jet engine would become the ubiquitous source of aircraft propulsion the reader is familiar with today. Turbojets had high fuel consumption, relatively low thrust, poor acceleration, and were notoriously loud (up to 114dB for sideline noise of the earliest turbojets[2]). These deficiencies had the capacity to halt the adoption of jet propulsion as the main power plant of post-War era aircraft.

Significant progress has been made in the last sixty years to increase the reliability, efficiency, and thrust capability of jet engines. These improvements have been the result of the development of advanced materials and manufacturing techniques, and better engineering design.[3] Technological innovations in the coming decades improved and corrected many of the early challenges presented by turbojets and led to the realization of supersonic military jets, aircraft-carrier-based jet fighters, long-range jet-powered military bombers, and of course commercial aircraft.

However, reduction of the noise generated by jets and jet-powered aircraft has proven to be an elusive problem. The extreme growth in the commercial aviation industry at the end of World War II due to the combination of surplus aircraft and aircraft manufacturing capability, job-seeking former military pilots, and stimulated global economies has pressed the noise issue for the com-

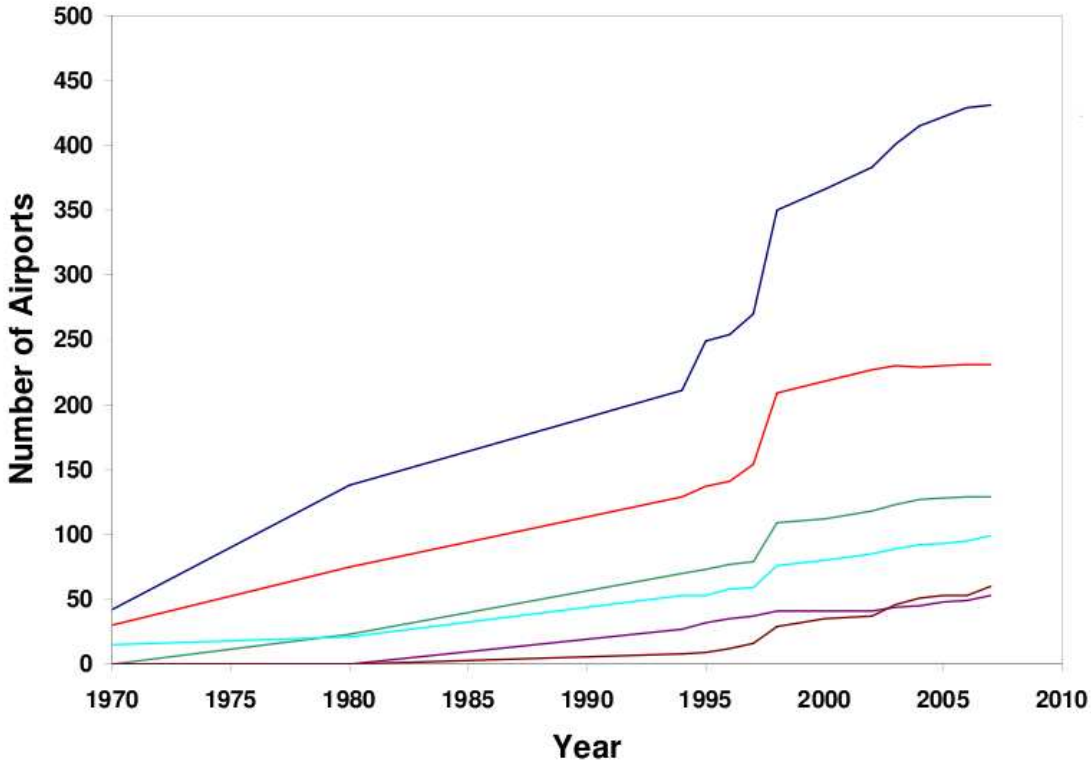

Figure 1.1: Growth of airport noise restrictions during the years 1970–2007 for ICAO-member airports as compiled in February 2008 as compiled by Boeing, Inc.[6] From top to bottom, the lines in the figure correspond to noise abatement programs, curfews, noise charges, noise level limits, operating quotas, and chapter 3-level aircraft restrictions.

mercial airline industry. In current times, it is estimated that over 30 million commercial flights carrying 1.8 billion passengers are flown every year throughout the world.[4,5] The sprawl of communities and demand for air travel has led to airports and residential properties being built right next to each other. As shown in Fig. 1.1, the number of airport noise regulations and related fines have steadily increased to help mitigate the issue with surrounding communities. Airlines and transportation bureaus lose significant revenue due to imposed curfews, restricted noise levels, operating quotas, and noise abatement programs for properties in the vicinity of airports.

For the military, the noise issue is not limited to the obvious need for stealth in combat scenarios. Noise from airbases in the United States has also been an important issue with many lawsuits being filed by surrounding communities. Several of these lawsuits have been successful and have

proven to be costly to the Department of Defense.

The need to reduce jet exhaust noise specifically is also important since it is dominant during landing and take-off and therefore has effects on humans and wildlife in the vicinity of airports. The excessive noise from jet engines was initially seen as somewhat of a nuisance and its environmental effects were all but ignored by governments. Research emerging in the 1970's linked noise pollution to negative ecological impacts as well as serious health effects in humans. Adverse effects in humans include hearing loss, tinnitus, hypertension, and other conditions.[4] Noise pollution has also been linked to the disruption of the feeding and nesting habits of wildlife (mostly birds) near airports.[5]

1.2 Review of Past Work

Concurrent with the work that emerged to improve the efficiency and safety of jet engines was research aimed at countering its adverse side effects, namely the mitigation of the noise produced by the turbulent exit flow. Beginning in the early 1950's, Lighthill[7] essentially birthed the field of aerodynamic sound generation (usually termed "aeroacoustics") by rearranging the exact compressible Navier-Stokes equations into a wave equation for the fluid density with a quadrupole-like source term. The jet flow is idealized as a distribution of acoustic sources in an ambient fluid at rest in the absence of any solid bodies. Recognized as the first successful mathematical attempt at a theoretical basis for noise modeling, it became known as an "acoustic analogy" since it technically was not a first-principles derivation of noise generation from a turbulent flow. Instead, the source in these equations was merely analogous to an externally applied source. Nevertheless, the theory allowed for the prediction of sound, but only when the complicated source term is known *a priori* through detailed measurements. These measurements are difficult to obtain experimentally and have only recently been obtained in full using direct numerical simulations,[8,9] a computationally expensive technique where no modeling is done and all scales of the flow are simulated. Naturally, the resolution requirements of this method restrict it from the ability to simulation many flows of engineering interest, including jet engines.

An additional complication in Lighthill's formulation results is its inability to separate the generation of sound from the flow-acoustic interactions involved. Physical mechanisms such as refraction and reflection due to the mean flow and turbulence are lumped into the source term; they are not included in the linear, homogeneous-medium, scalar wave equation operator. There have been notable reformulations by Lilley,[10,11] which follow the same strategy devised by Lighthill, that have incorporated propagation effects into the wave operator by moving terms from the source and removing terms which did not contribute to sound generation. However, the wave operator in Lilley's analogy supports homogeneous instability waves that grow unbounded in space. More recently, Goldstein[12] has derived a generalized acoustic analogy based on an arbitrary base flow which can be reduced to both the Lilley and Lighthill equations, but with better behaved instability modes. It should be noted that there have been several alternative jet noise theories proposed,[13–15] but none of which have been studied or used as extensively as the acoustic analogy approach.

Probably the most successful use of Lighthill's acoustic analogy was achieved by making simplifying approximations to the source term which resulted in a simple power law scaling.[7,16] The acoustic intensity was shown to be proportional to the eighth power of the jet exit velocity. This result provided engine designers a rule for reducing noise: higher bypass-ratio engines could have the same thrust with reduced exit velocity and could therefore be quieter. This knowledge was responsible for reducing jet noise levels by around 10dB until weight and thrust efficiency limits restricted larger engines and lower exit velocities.[17] However, further noise reductions are sought, for example, through NASA's Quiet Aircraft Technology project, whose current goal is to reduce perceived aircraft noise by 50 percent in 10 years and by 75 percent in 25 years, using 1997 levels as the baseline.[18]

Beyond the various forms of the acoustic analogy, a generalized theory of sound generation by aerodynamic flows has not emerged and one does not appear to be coming in the near future. Although a vast array of empirical jet noise data have been acquired in recent decades, a suitable predictive capability has yet to surface due to a fundamental lack of understanding of the physics involved in how turbulence generates noise. This has in turn hampered efforts to model the noise phenomenon and control it as necessary.

Therefore, the majority of design improvements over the past sixty years to enhance mixing and reduce jet noise have been due to costly trial-and-error experiments. Efforts have mostly centered on passive controls such as nozzle modifications. Tabs, chevrons, and other nozzle shape changes have been shown to increase mixing by generation of streamwise vorticity[19–22] and have reduced effective perceived noise by a few decibels with minimal thrust loss. But these devices are usually permanent fixtures, and they can only be optimized for a certain set of flow conditions. Thus, passive controls have the ability to create conditions which are less tolerable than uncontrolled cases. Acoustic analogies, while successful in motivating the high-bypass jet engine, offer little to no guidance for further noise reduction through geometry modification or active control strategies. With governmental regulations for noise reduction becoming more numerous and stricter in landing/takeoff zones, the future of mitigation relies on the following: an increased understanding of the subtle, complex noise sources inherent in a turbulent jet, and the use of active control technologies which have the ability to control turbulent flows with greater authority than their passive counterparts.

1.3 Present Work

The jet noise problem has created both a technological hurdle and a stimulating area of academic study. Advancing the understanding of noise generation due to a high-speed, near-nozzle, turbulent exit flow and subsequently controlling flows in this region to reduce jet exhaust noise are the motivating topics of this dissertation. One of the main topics of this work will concern the notion of scale as it pertains to noise generation and flow control for noise reduction. It wasn't until the 1970's that large-scale coherent structures were observed experimentally in free shear flows[23] and recognized to underlie the apparently random turbulence fluctuations even at high Reynolds numbers.. The structures form immediately downstream of the nozzle (in a jet) or splitter plate (in a mixing layer) and are qualitatively similar to the inviscid Kelvin-Helmholz instability. The large vortical eddies roll-up, pair, and merge downstream and entrain fluid from the streams above and below causing mixing and further entrainment[24] although this clear roll-up and pairing is not usually seen clearly at high Reynolds numbers. While there exists an extensive body of

research devoted to studying the dynamics and evolution of large scales in free shear flows especially at low Reynolds numbers (see Ho and Heurre[25] for a review), the contribution of radiated noise based on scale size has received far less attention. From a control perspective, the largest scales are expected to be more amenable to control because they are more persistent in time and space. The control can be more effective further from the actuation if it acts on the larger scales and thus scales are important for our study.

In this work we proceed to investigate aspects of both jet noise generation and active control through computational experiments and modeling of mixing layers, which are a reasonable and often used approximation to the initial shear layers of a jet. The near-nozzle region is the main focus since experimental evidence[26] has shown that the most annoying frequencies to the human ear originate in this flow region. Chapter 2 begins with a description of the simulation methodology used to compute the flows contained in this work. Chapter 3 proposes a simple numerical experiment which addresses one of the main questions in the development of current jet noise models: the issue of turbulence scale contribution to sound generation. By simulating turbulent mixing layers with different ranges of scales and comparing the characteristics of their sound fields, we aim to determine if a relation exists, and if so the nature of the relationship between the scales of a turbulent flow and their emission of sound. Implications of a scale relationship are important for the ability to control turbulent structures in jets, as well as for numerical simulations such as large-eddy simulation which incorporate turbulence modeling relative to flow scales.

We proceed in chapter 4 with a related computational investigation of active control of two-dimensional compressible mixing layers based on a companion experimental study. Recently, researchers at the Gas Dynamics and Turbulence Laboratory at The Ohio State University have developed actuators that have sufficient authority to impart strong perturbations to a high-speed, high-Reynolds-number laboratory jet over a wide range of frequencies and have achieved success in forcing the jet with various axisymmetric and azimuthal modes.[27] The technology shows considerable promise as a noise mitigation and mixing enhancement tool. The actuation is thought to be created by rapid Joule heating of the flow by generation of a localized arc-filament plasma in a small rectangular cavity near the jet's nozzle exit. A simple numerical model of the plasma is formulated and simulations under experimental conditions are performed to validate the model,

determine the mechanism of actuation, and probe the role of the cavity and forcing in the downstream evolution of the flow structures in the shear layer.

Lastly, we build upon a previously developed noise-reduction optimization framework[28,29] in Chapter 5. Using an adjoint-based approach, we formulate an automatic optimization procedure which circumvents flow complexities and may be used in future studies to derive control profiles to provide guidance on how to best utilize generalized actuators to reduce noise and enhance mixing. A derivation of the adjoint methodology is provided for noise reduction controls as well as controls to enhance layer spreading. Optimizations with solid boundaries are presented for an ambient two-dimensional flow field with an internal energy sound source and a two-dimensional mixing layer. Simulations of a three-dimensional, turbulent, free shear layer are also presented.

Each chapter provides its own introduction to the investigation, description of the methods used, report of results, and set of conclusions and future direction.

1.4 Overview of Accomplishments

In this section we briefly review the accomplishments of this work for each of the topics described in the previous section. The items are separated based on the chapter in which they are presented.

Chapter 2

- A parallelized, multi-platform, direct numerical simulation code to simulate the unsteady, compressible Navier-Stokes equations has been developed. The code is used to compute two- and three-dimensional spatially- and temporally-developing compressible mixing layers with or without isothermal solid walls in rectangular geometries. Agreement with the spreading rates and Reynolds stresses of experimental flows and other computations of mixing layers is demonstrated (in chapter 3).

- A formally 6^{th}-order dispersion-relation-preserving explicit finite difference scheme was derived and implemented for parallel simulations.

- A compact, pentadiagonal implicit filter designed to stabilized high-resolution simulations by removing the top 15% of wavenumbers was derived and implemented.

Chapter 3

- Four three-dimensional, temporally-developing, turbulent mixing layers with increasing Reynolds number are computed. Kinetic energy and pressure spectra in the near-field turbulent shear layer are computed and follow the appropriate wavenumber scalings when the range of scales is sufficient. Pressure wavenumber spectra in the hydrodynamic far field scaled by the momentum thickness, Taylor microscale, and Kolmogorov scale are compared with near field spectra. The sensitivity to Reynolds number is notably present in the near field, but far less pronounced in the far field. The two highest-Reynolds-number cases, which appear to have an inertial subrange, have far-field pressure spectra that collapse with the Taylor microscale suggesting the far-field sound is derived from near-field scales of this size.

- The acoustic power and energy computed in the far field show that the largest scales present in the shear layers make the most significant contribution to the sound field.

- The possibility of the noise in the sound field being due to the pairing of large scale structures is investigated. Visualization of the pairing events in the near field and corresponding pressure traces in the far field do not conclusively relate vortex pairing to sound generation.

Chapter 4

- A numerical model of a localized arc-filament plasma actuator is devised and implemented in a two-dimensional mixing layer simulation under experimental flow conditions and geometry.

- The actuator model is validated by available experimental data for downstream pressure level and generated temperatures in the cavity where the actuator is placed.

- Simulations varying the duty cycle of the forcing and the cavity width reveal the actuator's dominant forcing mechanism is due to it causing a fluid expansion guided by the confining geometry of the cavity. The actuator acts in the same manner as a synthetic (zero-mass-flux) jet by ejecting fluid heated by the plasma model into the boundary layer from the cavity's downstream edge.

- The jetting effect is shown to be enhanced by reducing the cavity width and increasing the duration of the actuator's 'on' time.

- The rapidly-generated high fluid temperatures caused by the plasma are the expected mechanism of actuation, but an alternative actuator model designed to produce significantly lower rises in temperature achieves sufficient control authority on par with the original model that generates substantial heat in the cavity.

- An investigation of the cavity oscillation frequencies reveals that the cavity is not producing resonant tones that are well-predicted by the standard Rossiter model or its variants. Instead, a recently proposed view of the cavity oscillation feedback loop from a signal processing viewpoint is able to predict the dominant features of the complex cavity pressure spectrum accurately even when the actuator is on.

Chapter 5

- The adjoint-based optimization framework previously used successfully for noise control has been extended to three dimensions. The adjoint equations and corresponding characteristic nonreflecting and solid-wall boundary conditions are derived and reported.

- Cost functionals for noise reduction and mixing enhancement based on near-field cross-stream velocity and pressure are formulated and their corresponding gradients are reported.

- Optimizations of a simple internal energy sound source in two dimensions with a solid wall are reported. A simulation with a noise reduction cost functionals without price shows that the control derived reduces as much noise as is available to the control region in one

iteration (86%). The addition of a price term reveals the expected result of diminished ability to reduce noise in the target region.

- Two-dimensional mixing layers with near-wall control are presented with velocity- and pressure-based spreading enhancement cost functionals. Both controls are able to maximize their respective cost functionals by over 50% and increase mixing layer thickness by up to 15% over the optimization time horizon. The controls cause large-structure pairings to occur further upstream than the baseline case and increase the magnitude of the Reynolds stresses in their target regions.

- A three-dimensional, turbulent (spatially-developing) mixing layer is simulated and optimized with a noise reduction cost functional. Inflow turbulence is fed into the simulation with a boundary zone-like forcing term with inflow data from an auxillary temporal simulation. The control successfully reduces the noise on a target plane below the mixing layer by 28% after 4 iterations of the optimization scheme.

Chapter 2

Simulation Techniques

2.1 Governing Equations

The conservation of mass, momentum, and energy equations for a viscous, compressible fluid were solved numerically without modeling assumptions. This technique is commonly referred to as direct numerical simulation (DNS). The mixing layers simulated are planar and were simulated on a Cartesian mesh in three dimensions. We define x as the streamwise coordinate, y as the cross-stream coordinate, and z as the spanwise coordinate with respective velocity components u, v, and w. Flow quantities, denoted by $()^*$, are nondimensionalized as

$$\rho = \frac{\rho^*}{\rho_\infty} \qquad u_i = \frac{u_i^*}{V^*} \qquad p = \frac{p^*}{\rho_\infty (V^*)^2} \qquad T = \frac{T^* C_v^*}{(V^*)^2}, \tag{2.1}$$

where ρ^* is the density, p^* is the pressure, T^* is the temperature, and V^* is a velocity scale. Ambient dimensional quantities are denoted with an ∞ subscript. The velocity scale V^* is chosen as appropriate for the different simulations presented in this dissertation. For the temporally-developing mixing layers in Chapter 3, the velocity $V^* = \Delta U$, the difference between the mean streamwise velocities of the upper and lower streams. It is the ambient speed of sound, $V^* = c_\infty$ in all other simulations presented in this work. The length scale L^* is used to nondimensionalize the independent variables such that

$$x = \frac{x^*}{L^*} \qquad y = \frac{y^*}{L^*} \qquad z = \frac{z^*}{L^*} \qquad t = \frac{t^* V^*}{L^*}. \tag{2.2}$$

The choice of L^* depends on the simulation. In the simulations presented in this work, the momentum thickness at a specified location is usually chosen for L^*. The momentum thickness of

the mixing layer is defined as

$$\delta_{\mathrm{m}}(t) = \int_{-\infty}^{\infty} \frac{\overline{\rho^*}\,\tilde{u^*}}{\rho_\infty \Delta U^*}\left(1 - \frac{\tilde{u^*}}{\Delta U^*}\right)\mathrm{d}y^* \tag{2.3}$$

where $\overline{()}$ and $\tilde{()}$ signify averages in the x (and z where applicable) directions using simple averaging (or Reynolds averaging) and (density-weighted) Favré averaging, respectively, where a Favré averaged quantity $\tilde{a}$ is defined as

$$\tilde{a} = \frac{\overline{\rho a}}{\overline{\rho}}. \tag{2.4}$$

Quantities signified with $()'$ and $()''$ are the perturbations from the Reynolds and Favré-averaged means, respectively. The initial momentum thickness was $\delta_{\mathrm{m}}^0 = \delta_{\mathrm{m}}(t=0)$ for the temporally-developing mixing layers in Chapter 3, and the momentum thickness at the edge of the "nozzle lip" in Chapters 4 and 5. The momentum thickness is commonly chosen since it is less sensitive to statistical convergence as other definitions of layer thickness. The governing equations of mass, momentum, and energy (given in their nondimensionsal form) in index notation are:

$$\frac{\partial \rho}{\partial t} + \frac{\partial}{\partial x_i}(\rho u_i) = 0, \tag{2.5}$$

$$\frac{\partial}{\partial t}(\rho u_i) + \frac{\partial}{\partial x_i}(\rho u_i u_j) = -\frac{\partial p}{\partial x_i} + \frac{\partial \tau_{ij}}{\partial x_i}, \tag{2.6}$$

$$\frac{\partial e}{\partial t} + \frac{\partial}{\partial x_i}[u_i(e+p)] = -\frac{\gamma}{\mathrm{RePr}(\gamma-1)}\frac{\partial^2}{\partial x_i^2}\left(\frac{p}{\rho}\right) + \frac{\partial}{\partial x_i}(\tau_{ij}u_j), \tag{2.7}$$

where e is the total energy per unit volume, and τ_{ij} is the viscous stress tensor for a compressible Newtonian fluid (with zero bulk viscosity) given by

$$\tau_{ij} = \frac{1}{\mathrm{Re}}\left(\frac{\partial u_i}{\partial x_j} + \frac{\partial u_j}{\partial x_i} - \frac{2}{3}\frac{\partial u_k}{\partial x_k}\delta_{kk}\right). \tag{2.8}$$

The total energy is the sum of the internal and kinetic energies

$$e = \frac{p}{\gamma - 1} + \frac{1}{2}\rho u_i u_i, \tag{2.9}$$

where the equation of state

$$p = \rho T \frac{\gamma - 1}{\gamma} \tag{2.10}$$

is used to relate the pressure, temperature, and density of the fluid. The ratio of specific heats at constant pressure and volume is constant and taken to be $\gamma = C_p^*/C_v^* = 1.4$ and the gas is calorically perfect. The internal energy is $e_i^* = \rho^* C_v^* T^*$, which, upon nondimensionalization is $e_i = \rho T/\gamma$. The Reynolds, Mach, and Prandtl numbers are

$$\mathrm{Re} = \frac{\rho_\infty^* V^* L^*}{\mu_\infty^*} \qquad \mathrm{Ma} = \frac{\Delta U^*}{c_\infty^*} \qquad \mathrm{Pr} = \frac{C_p^* \mu_\infty^*}{k_\mathrm{t}^*} = 0.7 \tag{2.11}$$

where k_t^* is the thermal conductivity of the fluid. The temperature variations are assumed to be small and therefore μ_∞^* and k_t^* are assumed to be constant.

2.2 Numerical Methods

2.2.1 Spatial Discretization

Finite differences schemes and Fourier methods were used to evaluate derivatives. In different coordinate directions, different schemes were chosen based upon their resolution and compatibility with efficient implementation on parallel computer systems.

A general finite difference approximation to the first derivative $f_i' = (df/dx)(x_i)$ of a dependent variable f in the interior of the computational domain is

$$\sum_{p=0}^{2} a_p (f'_{i-p} + f'_{i+p}) = \sum_{q=1}^{4} \alpha_q \frac{f_{i+q} - f_{i-q}}{2q\Delta}, \tag{2.12}$$

where Δ is the local mesh spacing, $f_i = f(x_i)$, and i corresponds to the uniformly spaced mesh node where $1 \le i \le N$.

For the first derivative in the cross-stream (y) direction, an implicit compact finite-difference method[30] called the "spectral-like" pentadiagonal scheme was chosen. Although the 9-point stencil for this scheme could yield tenth-order truncation error, its coefficients were optimized to yield

a fourth-order scheme with improved resolution at high wavenumbers. This feature was attained by enforcing constraints on the modified wavenumber

$$k'(k) = \frac{\sum_{q=1}^{4} \alpha_q / q \sin(qk)}{\sum_{p=0}^{2} 2a_p \cos(pk)} \tag{2.13}$$

such that $k'(k_1) = k_1$, $k'(k_2) = k_2$, and $k'(k_3) = k_3$ with $k_1 = 2.2$, $k_2 = 2.3$, and $k_4 = 2.4$. The values of the coefficients a_p and α_q are listed in Table 2.1. With the stencil width of this scheme, alternate schemes had to be implemented for the first and last three points in the domain. The first derivative approximations for these locations were

$$2f'_i + 4f'_{i+1} = \tfrac{1}{\Delta}(-5f_i + 4f_{i+1} + f_{i+2}) \tag{2.14}$$

at $i = 1$,

$$4f'_i + 2f'_{i-1} = \tfrac{1}{\Delta}(5f_i - 4f_{i-1} - f_{i-2}) \tag{2.15}$$

at $i = N_\mathrm{y}$,

$$f'_{i-1} + 4f'_i + f'_{i+1} = \tfrac{3}{\Delta}((f_{i+1} - f_{i-1}) \tag{2.16}$$

at $i = 2$ and $i = N_\mathrm{y} - 1$, and

$$216f'_i + 96(f'_{i+1} + f'_{i-1}) + 6(f'_{i+2} + f'_{i-2}) = \tfrac{1}{\Delta}(160(f_{i+1} - f_{i-1}) + 25(f_{i+2} - f_{i-2})) \tag{2.17}$$

at $i = 3$ and $i = N_\mathrm{y} - 3$. These alternate schemes are applied at points that are away from any significant gradients and in the boundary zones (see §2.2.5) and so are not expected to have any substantial influence on the accuracy of the solution. The resulting matrix of coefficients was pentadiagonal and was numerically inverted via LDU decomposition.

In the streamwise (x) direction, a variant of the Dispersion-Relation-Preserving (DRP) scheme was used to approximate the first derivative. In the original explicit scheme,[31] the coefficients of a seven-point stencil were optimized by minimizing the square of the integrated error of the modified wavenumber between zero and $\pi/2$. Enforcing a 4^{th}-order truncation error allowed for one free parameter to be optimized. By applying the same procedure, a 9-point stencil enforcing

Scheme	a_0	a_1	a_2	α_0	α_1	α_2	α_3	α_4
f', (y-dir)	0.5	0.5771	0.08964	—	1.30252	0.99355	0.0375	—
f', (x-dir)	0.5	—	—	—	1.69949	-1.01339	0.38118	-0.0673
f'', (y-dir)	—	—	—	$-205/72$	$8/5$	$-1/5$	$8/315$	$-1/560$
f'', (x-dir)	—	—	—	$-205/72$	$8/5$	$-1/5$	$8/315$	$-1/560$

Table 2.1: Coefficients for finite difference approximations to interior first and second derivatives. First derivative coefficients are used in (2.12) and second derivatives are used in (2.18).

6^{th}-order truncation error was implemented with the square of the integrated error of the modified wavenumber from zero to $7\pi/16$ minimized. The resulting coefficients are listed in Table 2.1. A plot of the modified wavenumber of the interior schemes shown in Fig. 2.1 shows the resolution properties of the first derivative schemes. For points near a computational boundary, (2.14)–(2.17) are used with N_{y} replaced by N_{x}.

In the spanwise (z) direction, a Fourier spectral scheme was used due to the periodic domain. The FFT of the function is multiplied by the term ik_z (where k_z is the spanwise wavenumber) and then an inverse FFT operation is performed to obtain the first derivative. Although a spectral scheme could have been used in the streamwise direction as well due to its periodicity (for the mixing layers in chapter 3), it was not used to avoid transposing data across processors in parallel implementations of the algorithm.

The second derivative finite difference approximation at node i in the interior of the computational domain, $(d^2f/dx^2)(x_i) = f_i''$ is computed with

$$f_i'' = \alpha_0 f_i + \sum_{q=1}^{4} \alpha_q (f_{i+q} + f_{i-q}). \tag{2.18}$$

In both the streamwise and cross-stream directions, an explicit 6^{th}-order scheme (9-point stencil) with coefficients in Table 2.1 was used. The explicit schemes in x were used to reduce data sharing on multiprocessor systems since the parallel domain decomposition was in that direction.

Due to the computational boundaries in the y direction, lower-order boundary schemes were used for the first and last four points in the domain. The second derivative approximations for

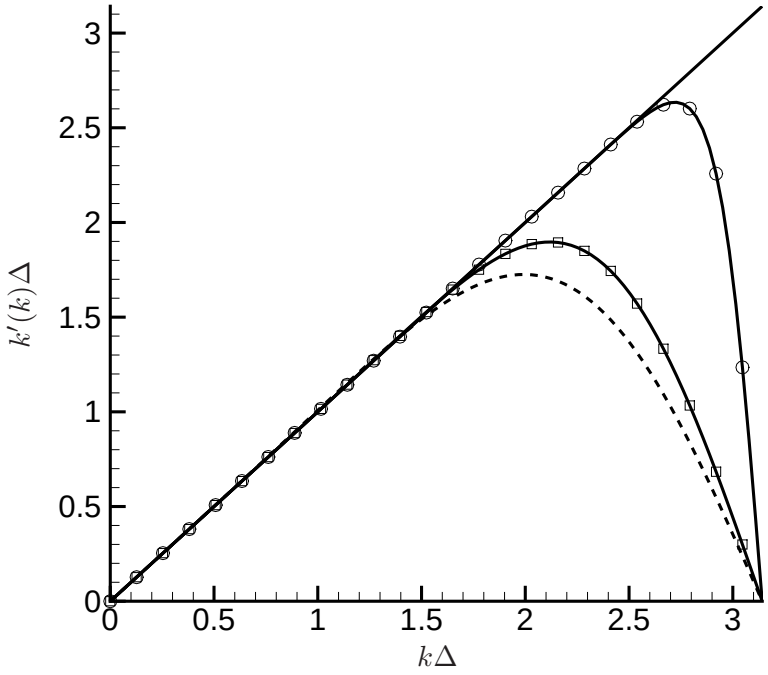

Figure 2.1: Modified wavenumber curves of first derivative finite-difference schemes for the interior computational domain. Exact differentiation (spectral): ——— ; 4^{th}-order DRP scheme[31] - - - - ; optimized 6^{th}-order DRP scheme: - - □ - - ; "spectral-like" pentadiagonal scheme: - - ○ - - .

the endpoints were simply:

$$\begin{aligned} f''_1 &= f''_2 \\ f''_{N_\text{y}} &= f''_{N_\text{y}-1} \end{aligned} \tag{2.19}$$

and the approximations for $i = 2, 3, 4$ and $i = \text{Ny} - 1,\ \text{Ny} - 2,\ \text{Ny} - 3$ were:

$$\begin{aligned} f''_2 &= \tfrac{1}{\Delta^2}\left(f_3 - 2f_2 + f_1\right) \\ f''_3 &= \tfrac{1}{\Delta^2}\left(f_4 - 2f_3 + f_2\right) \\ f''_4 &= \tfrac{1}{\Delta^2}\left(f_5 - 2f_4 + f_3\right) \\ f''_{N_\text{y}-1} &= \tfrac{1}{\Delta^2}\left(f_{N_\text{y}} - 2f_{N_\text{y}-1} + f_{N_\text{y}-2}\right) \\ f''_{N_\text{y}-2} &= \tfrac{1}{\Delta^2}\left(f_{N_\text{y}-1} - 2f_{N_\text{y}-2} + f_{N_\text{y}-3}\right) \\ f''_{N_\text{y}-3} &= \tfrac{1}{\Delta^2}\left(f_{N_\text{y}-2} - 2f_{N_\text{y}-3} + f_{N_\text{y}-4}\right), \end{aligned} \tag{2.20}$$

respectively. Again, these low-order approximations are not expected to effect the solution, since

they are located in boundary zones (see §2.2.5) and far away from the regions of interest in the simulations.

A Fourier spectral scheme was used to compute second derivatives in the z direction where the Fourier transformed function was multiplied by $(ik)^2$ and then an inverse FFT operation performed.

2.2.2 Spatial Discretization Near Walls

For some of the flows simulated in Chapters 4 and 5, solid wall boundaries are embedded into the computational domain. The finite difference boundary schemes in the previous section were implemented on (or near) the computational boundary out of the physical domain of the simulation. To increase the accuracy of the computation near the walls where the flow is physical and of interest, the explicit schemes presented in the section as approximations to the first and second derivatives were used.

For the first derivative, the following 4^{th}-order explicit schemes were implemented:

$$\begin{aligned} f'_1 &= \tfrac{1}{\Delta}\left(-\tfrac{25}{12}f_1 + 4f_2 - 3f_3 + \tfrac{4}{3}f_4 - \tfrac{1}{4}f_5\right) \\ f'_2 &= \tfrac{1}{\Delta}\left(-\tfrac{1}{4}f_1 - \tfrac{5}{6}f_2 + \tfrac{3}{2}f_3 - \tfrac{1}{2}f_4 + \tfrac{1}{12}f_5\right) \\ f'_3 &= \tfrac{1}{\Delta}\left(\tfrac{1}{12}f_1 - \tfrac{2}{3}f_2 + \tfrac{2}{3}f_4 - \tfrac{1}{12}f_5\right) \end{aligned} \tag{2.21}$$

where the boundary is located at $i = 1$, and

$$\begin{aligned} f'_{\mathrm{N}} &= \tfrac{1}{\Delta}\left(\tfrac{25}{12}f_{\mathrm{N}} - 4f_{\mathrm{N}-1} + 3f_{\mathrm{N}-2} - \tfrac{4}{3}f_{\mathrm{N}-3} + \tfrac{1}{4}f_{\mathrm{N}-4}\right) \\ f'_{\mathrm{N}-1} &= \tfrac{1}{\Delta}\left(\tfrac{1}{4}f_{\mathrm{N}} + \tfrac{5}{6}f_{\mathrm{N}-1} - \tfrac{3}{2}f_{\mathrm{N}-2} + \tfrac{1}{2}f_{\mathrm{N}-3} - \tfrac{1}{12}f_{\mathrm{N}-4}\right) \\ f'_{\mathrm{N}-2} &= \tfrac{1}{\Delta}\left(\tfrac{1}{12}f_{\mathrm{N}} - \tfrac{2}{3}f_{\mathrm{N}-1} + \tfrac{2}{3}f_{\mathrm{N}-3} - \tfrac{1}{12}f_{\mathrm{N}-4}\right) \end{aligned} \tag{2.22}$$

where the boundary is located at $i = N$.

For the second derivative approximation, the following 4^{th}-order explicit schemes were im-

plemented:

$$\begin{aligned} f_1'' &= \tfrac{1}{\Delta^2}\left(\tfrac{35}{12}f_1 - \tfrac{26}{3}f_2 + \tfrac{19}{2}f_3 - \tfrac{14}{3}f_4 + \tfrac{11}{12}f_5\right) \\ f_2'' &= \tfrac{1}{\Delta^2}\left(\tfrac{11}{12}f_1 - \tfrac{5}{3}f_2 + \tfrac{1}{2}f_3 + \tfrac{1}{3}f_4 - \tfrac{1}{12}f_5\right) \\ f_3'' &= \tfrac{1}{\Delta^2}\left(-\tfrac{1}{12}f_1 + \tfrac{4}{3}f_2 - \tfrac{5}{2}f_3 + \tfrac{4}{3}f_4 - \tfrac{1}{12}f_5\right) \\ f_4'' &= \tfrac{1}{\Delta^2}\left(\tfrac{1}{90}(f_1 + f_7) - \tfrac{3}{20}(f_2 + f_6) + \tfrac{3}{2}(f_3 + f_5) - \tfrac{49}{18}f_4\right) \end{aligned} \tag{2.23}$$

where the boundary is located at $i = 1$. An additional scheme is added for f_4'' since the interior second derivative scheme has a 5-point stencil. When the boundary is located at $i = N$,

$$\begin{aligned} f_{\mathrm{N}}'' &= \tfrac{1}{\Delta^2}\left(\tfrac{35}{12}f_{\mathrm{N}} - \tfrac{26}{3}f_{\mathrm{N}-1} + \tfrac{19}{2}f_{\mathrm{N}-2} - \tfrac{14}{3}f_{\mathrm{N}-3} + \tfrac{11}{12}f_{\mathrm{N}-4}\right) \\ f_{\mathrm{N}-1}'' &= \tfrac{1}{\Delta^2}\left(\tfrac{11}{12}f_{\mathrm{N}} - \tfrac{5}{3}f_{\mathrm{N}-1} + \tfrac{1}{2}f_{\mathrm{N}-2} + \tfrac{1}{3}f_{\mathrm{N}-3} - \tfrac{1}{12}f_{\mathrm{N}-4}\right) \\ f_{\mathrm{N}-2}'' &= \tfrac{1}{\Delta^2}\left(-\tfrac{1}{12}f_{\mathrm{N}} + \tfrac{4}{3}f_{\mathrm{N}-1} - \tfrac{5}{2}f_{\mathrm{N}-3} + \tfrac{4}{3}f_{\mathrm{N}-3} - \tfrac{1}{12}f_{\mathrm{N}-4}\right) \\ f_{\mathrm{N}-3}'' &= \tfrac{1}{\Delta^2}\left(\tfrac{1}{90}(f_{\mathrm{N}} + f_{\mathrm{N}-6}) - \tfrac{3}{20}(f_{\mathrm{N}-1} + f_{\mathrm{N}-5}) + \tfrac{3}{2}(f_{\mathrm{N}-1} + f_{\mathrm{N}-4}) - \tfrac{49}{18}f_{\mathrm{N}-3}\right). \end{aligned} \tag{2.24}$$

2.2.3 Mesh Considerations

Uniform grids were used in the streamwise and spanwise directions due to the doubly periodic boundary conditions prescribed in temporally-evolving free shear flows in Chapter 3. The cross-stream grid (and streamwise grid for spatial mixing layers in Chapters 4 and 5) was stretched in order to resolve the turbulence near the centerline in all mixing layer calculations. Clustering mesh points in regions containing large flow gradients was done by mapping the stretched mesh on to a uniform mesh via the smooth function mapping $y = g(s)$ where s is a uniform mesh coordinate. Derivatives of an arbitrary function $f(y)$ in the cross-stream direction are thus related to the derivatives on the uniform mesh via:

$$\frac{\partial f}{\partial y} = \frac{1}{g'}\frac{\partial f}{\partial s} \qquad \text{and} \qquad \frac{\partial^2 f}{\partial y^2} = \frac{1}{g'^2}\frac{\partial^2 f}{\partial s^2} - \frac{g''}{g'^3}\frac{\partial f}{\partial s}. \tag{2.25}$$

The mapping function $g(s)$ and its derivatives are:

$$\begin{aligned} g(s) = 2g_0\Bigg[\frac{A_0 s}{2} &+ \frac{A_1}{4\sigma_1}\log(\cosh(\sigma_1 s - \sigma_1 s_1)) + \frac{A_1}{4\sigma_1}\log(\cosh(\sigma_1 s + \sigma_1 s_1)) \\ &+ \frac{A_2}{4\sigma_2}\log(\cosh(\sigma_2 s - \sigma_2 s_2)) + \frac{A_2}{4\sigma_2}\log(\cosh(\sigma_2 s + \sigma_2 s_2))\Bigg] \end{aligned} \tag{2.26}$$

with derivatives

$$g'(s) = 4g_0 \left[\frac{A_0}{2} + \left[\frac{A_1}{4} \tanh(\sigma_1(s - s_1)) - \frac{A_1}{4} \tanh(\sigma_1(s + s_1)) \right] + \left[\frac{A_2}{4} \tanh(\sigma_2(s - s_2)) - \frac{A_2}{4} \tanh(\sigma_2(s + s_2)) \right] \right] \tag{2.27}$$

and

$$g''(s) = 2g_0 \left[A_1\sigma_1 \mathrm{sech}^2(\sigma_1 s - \sigma_1 s_1) - A_1\sigma_1 \mathrm{sech}^2(\sigma_1 s + \sigma_1 s_1) + A_2\sigma_2 \mathrm{sech}^2(\sigma_2 s - \sigma_2 s_2) - A_2\sigma_2 \mathrm{sech}^2(\sigma_2 s + \sigma_2 s_2) \right] \tag{2.28}$$

where

$$g_0 = \frac{L_y}{2} \left[\frac{A_0}{2} + \frac{A_1}{4\sigma_1} \log(\cosh(\sigma_1 - \sigma_1 s_1)) + \frac{A_1}{4\sigma_1} \log(\cosh(\sigma_1 + \sigma_1 s_1)) + \frac{A_2}{4\sigma_2} \log(\cosh(\sigma_2 - \sigma_2 s_2)) + \frac{A_2}{4\sigma_2} \log(\cosh(\sigma_2 + \sigma_2 s_2)) \right]^{-1} \tag{2.29}$$

scaled the functions with the cross-stream domain length, L_y, and s varied from -1 to 1. The shape of the mapping functions in (2.27) and (2.28) are shown in Fig. 2.2. The derivative $g'(s)$ is proportional to the spacing between neighboring mesh points (Δy) and its form shows that the stretched mesh had its highest resolution for $|s| < 0.2$ in the regions where flow gradients were expected to be the greatest. The resolution decreased beyond $|s| > 0.2$ where a dense mesh was no longer needed. The mesh resolution again decreases for $|s| > 0.9$ to implement a buffer zone and outgoing radiation condition (see §2.2.5). The form of $g''(s)$ shows the local point-to-point mesh stretching percentage. For all meshes using these mappings in this work, the maximum stretch between two successive mesh points (in the physical domain of the simulations) occurred near $|s| \approx 0.3$ for all of the mixing layers. The number of grids points and the domain lengths used in each simulation in chapter 3 are tabulated in Table 3.1 along with some mesh parameters. The minimum cross-stream mesh spacing (min Δy) occurs on the centerline and the maximum occurs on the computational boundary.

In simulations of spatially-evolving mixing layers, boundary treatments are prescribed in the inflow and outflow regions and mesh stretching is employed in the streamwise direction as well.

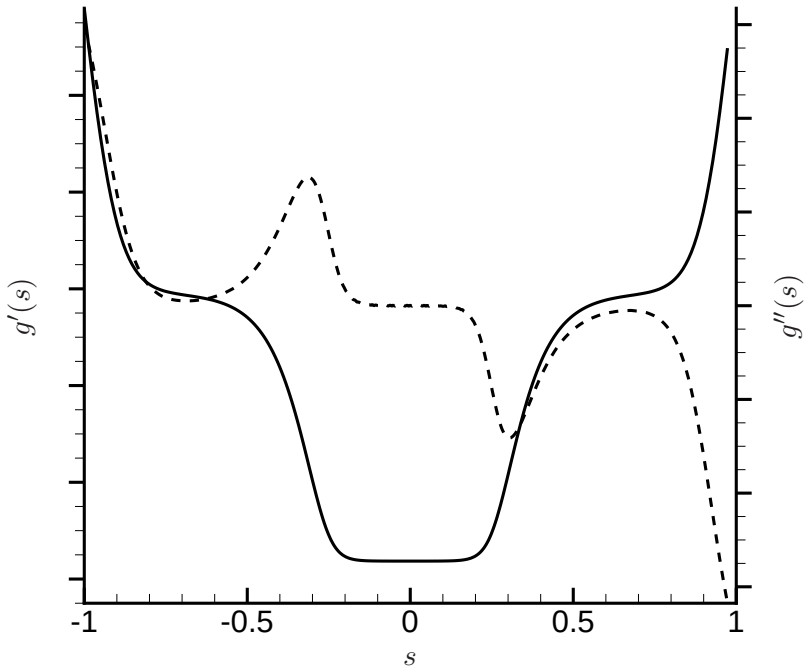

Figure 2.2: Derivatives $g'(s)$ and $g''(s)$ of the cross-stream coordinate mapping function $y = g(s)$. The vertical axis limits are shown with arbitrary scale due to dependence on the computational domain size and mapping parameters. $g'(s)$: —— ; $g''(s)$: - - - - .

For this direction, we consider representing derivatives for an arbitrary function $f(x)$ where $x = h(s)$ in a similar fashion as above. The mapping function $h(s)$ and its derivatives are:

$$h(s) = \frac{L_{\mathrm{x}} s}{h_0} + \frac{(A_1 + A_2) L_{\mathrm{x}} s}{2h_0} + \frac{A_1 L_{\mathrm{x}}}{2h_0 \sigma_1} \log(\cosh(\sigma_1(1-s))) - \frac{A_2 L_{\mathrm{x}}}{2h_0 \sigma_2} \log(\cosh(\sigma_2 s)) \tag{2.30}$$

with first and second derivatives

$$h'(s) = \frac{L_{\mathrm{x}}}{2h_0} \left[1 + A_1(1 - \tanh(\sigma_1(1-s))) + A_2(1 - \tanh(\sigma_2 s))\right] \tag{2.31}$$

and

$$h''(s) = \frac{L_{\mathrm{x}}}{2h_0} \left[A_1 \sigma_1 \cosh^{-2}(\sigma_1(s-1)) - A_2 \sigma_2 \cosh^{-2}(\sigma_2 s)\right], \tag{2.32}$$

respectively, where

$$h_0 = 1 + \frac{A_1 + A_2}{2} - \frac{A_2}{2\sigma_2}\log(\cosh(\sigma_2)). \tag{2.33}$$

For the streamwise coordinate mapping, the uniform coordinate s has values ranging from 0 to 1. Based on the selection of the values of L_x, A_1, A_2, σ_1, and σ_2, this mapping stretches the mesh in the inflow and outflow regions (near $s = 0$ and $s = 1$).

When a cavity is present, such as is the case in the mixing layers presented in chapter 4, the mapping function $h(s)$ is slightly modified to increase the streamwise resolution near the upstream and downstream sides of the cavity walls. The following mapping is used:

$$\begin{aligned} h(s) = \frac{L_\mathrm{x} s}{2h_0}\Big[2 + (A_1 + A_2)s - \frac{A_2}{\sigma_2}\log(\cosh(\sigma_2 s)) - \\ \frac{A_1}{\sigma_1}\log(\cosh(\sigma_1)) + \frac{A_1}{\sigma_1}\log(\cosh(\sigma_1(1-s))) - \\ \frac{A_3}{\sigma_2}\log(\cosh(\sigma_2 s_3)) + \frac{A_3}{\sigma_2}\log(\cosh(\sigma_2 s_4)) + \\ \frac{A_3}{\sigma_2}\log(\cosh(\sigma_2(s_3 - s))) + \frac{A_3}{\sigma_2}\log(\cosh(\sigma_2(s_4 - s)))\Big] \end{aligned} \tag{2.34}$$

with first and second derivatives

$$\begin{aligned} h'(s) = \frac{L_\mathrm{x} s}{2h_0}\big[2 + A_1 + A_2 - A_1\tanh(\sigma_1(1-s)) - \\ A_2\tanh(\sigma_2 s) - A_3\tanh(\sigma_3(s_3 - s)) + A_3\tanh(\sigma_3(s_4 - s))\big] \end{aligned} \tag{2.35}$$

and

$$\begin{aligned} h''(s) = \frac{L_\mathrm{x} s}{2h_0}\big[A_1\sigma_1\mathrm{sech}^2(\sigma_1(1-z)) - A_2\sigma_2\mathrm{sech}^2(\sigma_1 z) + \\ A_3\sigma_3\mathrm{sech}^2(\sigma_3(s_3 - z)) - A_3\sigma_3\mathrm{sech}^2(\sigma_3(s_4 - z))\big], \end{aligned} \tag{2.36}$$

respectively, where

$$\begin{aligned} h_0 = 1 + \frac{A_1 + A_2}{2} - \frac{A_1}{2\sigma_1}\log(\cosh(\sigma_1)) - \frac{A_2}{2\sigma_2}\log(\cosh(\sigma_2)) - \\ \frac{A_3}{2\sigma_3}\log(\cosh(\sigma_3 s_3)) + \frac{A_3}{2\sigma_3}\log(\cosh(\sigma_3(1 - s_3))) + \\ \frac{A_3}{2\sigma_3}\log(\cosh(\sigma_3 s_4)) - \frac{A_3}{2\sigma_3}\log(\cosh(\sigma_3(1 - s_4))) \end{aligned} \tag{2.37}$$

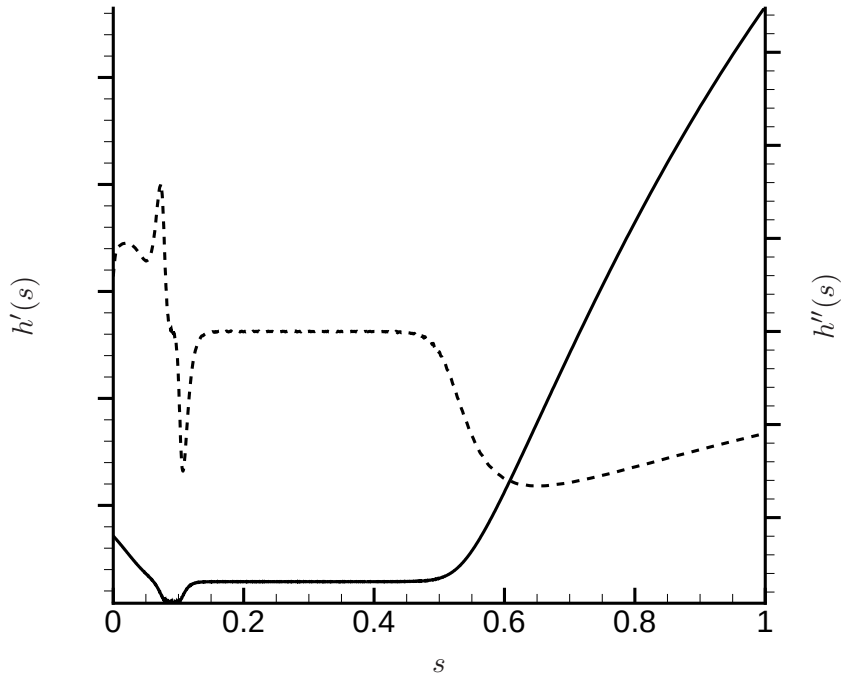

Figure 2.3: Derivatives $h'(s)$ and $h''(s)$ of the streamwise coordinate mapping function $x = h(s)$ when a cavity is present. The vertical axis limits are shown with arbitrary scale due to dependence on the computational domain size and mapping parameters. $h'(s)$: —— ; $h''(s)$: - - - - .

Figure 2.3 shows the derivatives of $h(s)$ for the simulations presented in chapter 4. The physical domain of the simulations (where there are no buffer zones, see explanation of boundary treatments in §2.2.5) is in the range $0.05 < s < 0.5$. The cavity is located in the range $0.06 < s < 0.12$.

2.2.4 Time Advancement

The solution was advanced in time for all mixing layers in chapter 3 using the seven-stage HALE-RK (High-Accuracy Large-Step Explicit Runge–Kutta) scheme,[32] which is optimized to increase the stability limit (instead of accuracy) of the traditional 4^{th}-order Runge-Kutta scheme, was used. The increased stability limits allowed for the CFL limit for stability to be 5.67, which is twice that of the traditional 4^{th}-order Runge–Kutta scheme. This allowed for the numerical time step to also

be doubled, and provided a savings in computation run-time (seven computations of the right-hand side versus eight for the standard Runge–Kutta scheme with a time step twice as small) as well as reducing the amount of data produced by the simulations. The mixing layers in chapters 4 and 5 used the standard 4^{th}-order Runge-Kutta scheme.

2.2.5 Boundary Conditions and Treatments

A radiation boundary condition had to be implemented in the cross-stream direction to model a domain of infinite extent in that direction. This condition was also applied for the stream-wise direction for spatially-evolving mixing layers. Without such a treatment, the computational boundary would create non-physical reflections into the simulation domain. Our non-reflecting boundary treatment has three components.

First, a non-physical zone with a specified width was implemented on upper and lower the cross-stream boundaries. This is a common practice (sometimes referred to as a "sponge" or "buffer" zone) and its effects have been previously studied.[33–35] In this region, the solution is damped towards the base state

$$\mathbf{q}_{\text{bc}} = \begin{bmatrix} \pm\rho_\infty U \\ 0 \\ 0 \\ \rho_\infty \\ \frac{p_\infty}{\gamma-1} + \frac{\rho_\infty}{2}\left(U^2\right) \end{bmatrix} \tag{2.38}$$

by adding the forcing term $-\xi(y)(\mathbf{q}-\mathbf{q}_{\text{bc}})$ to the right hand side of the governing equations. In this section, y is taken to be the coordinate normal to the boundary conditions. The damping function $\xi(y)$ was zero in the physical domain and was quadratic in the buffer zone:

$$\xi(y) = \xi_0 \left(\frac{y \mp y_{\text{p}}\delta^0_{\text{m}}}{L_{\text{b}}\delta^0_{\text{m}}} \right)^2 \qquad \text{for} \qquad y_{\text{p}}\delta^0_{\text{m}} < |y| < L_{\text{y}}/2 - L_{\text{b}}\delta^0_{\text{m}}. \tag{2.39}$$

The value of ξ_0 was 0.4 for the temporal mixing layers in chapter 3 and 0.1 otherwise.

In addition to damping the solution, an explicit low-order, low-pass filter was used in all three

directions in the buffer zone. The flow solution was filtered according to:

$$\mathbf{q}_{\text{filt},j} = (1 - \zeta(y))\mathbf{q}_j + \frac{\zeta(y)}{4}\left(\mathbf{q}_{j+1} + 2\mathbf{q}_j + \mathbf{q}_{j-1}\right) \tag{2.40}$$

where $\mathbf{q}_j = \mathbf{q}(x_j, y, z, t)$ if filtering in the streamwise direction, $\mathbf{q}_j = \mathbf{q}(x, y_j, z, t)$ if in the cross-stream direction, and $\mathbf{q}_j = \mathbf{q}(x, y, z_j, t)$ if in the spanwise direction. The periodic boundaries required no special treatment at the computational boundary when filtering in the x and z directions for the temporal mixing layers. At $j = 1$ and $j = N_{\text{y}}$ in the cross-stream filtering, the condition $\mathbf{q} = \mathbf{q}_{\text{filt}}$ was imposed. The filter strength function $\zeta(y)$ was set to be a linear function with a value of zero at the physical domain boundary and reaching unity at the computational boundary, respectively.

Working in tandem, this filtering along with the damping procedure reduced the fluctuations in the flow field to negligible levels so simple outflow boundary conditions could be applied. At the cross-stream boundaries, the nonreflecting one-dimensional linearized characteristic boundary condition was used. The same conditions were used for the streamwise boundaries in the spatial mixing layer calculations. This condition was applied by specifying a base state as in (2.38) as a reference flow and decomposing the perturbations from the base state into incoming and outgoing components. These were determined by a one-dimensional characteristic analysis of the linearized Euler equations. The components that were incoming were set to zero, thereby forcing all disturbances on the boundary to be outgoing. A similar treatment at the boundaries was done for the adjoint field which is calculated in chapter 5. A one-dimensional characteristic analysis is done for the adjoint equations (shown in Appendix B) to supply boundary conditions. The form of the equation needed for formulating these boundary conditions is reported in Appendix C for nonreflecting boundaries. In the adjoint computation, the field is marched in reverse time, so outgoing characteristics are set to zero. The boundary zone with damping, filtering, and simple outgoing boundary conditions greatly reduces spurious noise from contaminating the physical domain of the calculations.

2.2.6 Solid Wall Boundaries

For the spatial mixing layer simulations in Chapters 4 and 5 which included solid walls, no-slip boundary conditions are, of course, required. In simulations with a wall, the Navier–Stokes Characteristic Boundary Conditions formulated by Poinsot and Lele[36] were used unless otherwise specified. The wall is rigid, does not move, and is isothermal. Adjoint characteristics on the wall are derived and reported in §C.2.3.

2.2.7 Numerical Stabilization

Despite the high resolution with which the simulations in this study were carried out, we will see in §3.3.6 that particularly high Reynolds number simulations could benefit from slight numerical stabilization. The stabilization was done by high-wavenumber filtering as is often used in conjunction with DNS of aeroacoustic flows.[37,38] This filtering does not degrade the solution, however. It should also be made clear that for our DNS, the filtering is not acting as a turbulence model in any way. Its action on the solution field is far further down the wavenumber spectrum than where sub-grid-scale modeling is applied as in typical large-eddy simulation. Its negligible effect on the resolved scales of higher Reynolds number simulations is demonstrated in §3.3.5 and §3.3.6.

The spanwise direction was filtered with a Fourier wavenumber cutoff filter. The solution was Fourier transformed into wavenumber space using an FFT and the Fourier coefficients of the top 15% of the wavenumbers in the spanwise directions were simply set to zero. The solution was then inverse transformed back into physical space.

A filtering procedure similar to that of Visbal & Gaitonde[37] and Bodony & Lele[38] was used to filter in the streamwise and cross-stream directions. It is a variant of the compact pentadiagonal filter of Lele.[30] The coefficients of the scheme were set such that the transfer function $T(k\Delta) = 1.0$ at $k\Delta/\pi = 0.7$ and $T(k\Delta) = 0.95$ at $k\Delta/\pi = 0.85$. Using the notation of Lele[30] (see his equation

C.2.1) the coefficients for this tridiagonal, formally fourth-order filter are

$$\begin{aligned} \alpha &= 0.666606483935696 \\ \beta &= 0.166923313110972 \\ a &= 0.999954862951772 \\ b &= 1.333433554630054 \\ c &= 0.333574934094896 \\ d &= 9.624241661462807 \times 10^{-5}. \end{aligned} \tag{2.41}$$

All flow variables of the DNS solution were filtered in each coordinate direction every five time steps, but only at 60% strength. That is, a linear combination of the filtered and unfiltered fields was used:

$$\mathbf{q}_{\text{new}} = \left[1 - \varrho\left(\frac{y}{\delta^0_{\text{m}}}\right)\right]\mathbf{q} + \varrho\left(\frac{y}{\delta^0_{\text{m}}}\right)\mathbf{q}_{\text{filt}} \tag{2.42}$$

with

$$\varrho\left(\frac{y}{\delta^0_{\text{m}}}\right) = \frac{\varrho_{\max}}{2}\left[\tanh\left(5\frac{\left(\frac{y}{\delta^0_{\text{m}}} + \delta_{\text{f}}/2\right)}{\delta_{\text{f}}/2}\right) - \tanh\left(5\frac{\left(\frac{y}{\delta^0_{\text{m}}} - \delta_{\text{f}}/2\right)}{\delta_{\text{f}}/2}\right)\right], \tag{2.43}$$

where $\varrho_{\max} = 0.6$ and $\delta_{\text{f}} = 1.1\delta_{99}(t)/\delta^0_{\text{m}}$. The physical width of the filtered region, δ_{f}, was set such that filtering effectively only had support in a region 10% larger than the 99% thickness (δ_{99}) of the layer for the simulations in chapter 3. Filtering was applied in the entire physical computation regions in chapters 4 and 5. This filtering procedure is independent of the low-order filtering used in the boundary zones described in §2.2.5.

Chapter 3

The Sound from Mixing Layers Simulated with Different Ranges of Turbulence Scales

3.1 Introduction

The radiated sound spectrum from turbulent jets is broadbanded, having intensity within 10 dB of its peak over two decades in frequency. The role of turbulence scales in generating this broadbanded sound is important for several reasons, large-eddy simulation of turbulent jet noise being perhaps the most obvious. Here, the degree to which noise predictions must rely upon sub-grid-scale modeling of the sound sources is tied, of course, to those that make the sound. Fundamentally different modeling is needed if the only important small scales are, say, the locally largest eddies spanning the thin mixing layer near the jet's nozzle rather than the small-scale turbulence distributed throughout the jet. From a noise control perspective, the largest scales are, naturally, more amenable to control, so their relative contribution to the radiated sound in different parts of its spectrum is likewise important. The role of scales is also important in theoretical jet noise models, which typically require assumptions about the statistics of noise sources. Models for turbulence statistics are expected to be more reliable for smaller scales, which are expected to be closer to homogeneous and therefore more universal.

An interesting observation about the sound spectra from jets might also be related to the role of scales. There is strong empirical evidence that over a wide range of jet operating conditions the spectrum is well-fitted by two spectral shapes.[14,39,40] One has a sharper spectral peak and is more active at radiation angles closer to the jet axis. The other has a broader spectrum and a more uniform directivity. Given the similarity of the sharply peaked spectrum's directivity to that predicted by noise models based upon instability waves,[39] this component is often referred to as the large-scale turbulence spectrum. The other component is thus called the fine-scale turbulence

spectrum. There is no firm theoretical footing for these designations however. Such a decomposition is particularly curious since both spectra have a similar spectral peak frequency, which seems inconsistent with the expectation that finer scales should emit higher frequencies.

Rather than disparate scales, another possible explanation for this two-component character is that the same turbulent noise sources radiate by multiple mechanisms. Goldstein & Leib[41] show that the vector Green's function for a causal solution of an acoustic analogy constructed for a slowly diverging mean flow has two components. Operating on the same noise sources, these Green's function components act as filters which only allow certain components of the source to radiate to the far field. The resulting spectral predictions share some of the key features of experimental observations.[41,42] Still another possibility is that noise from the near-nozzle mixing layers and that which is generated around the closing of the potential core are somehow fundamentally different, yielding different spectra. In summary, it remains unclear whether the two-component character of the spectrum results from different scales, different radiation mechanisms from the same sources, or different noise characteristics of different portions of the jet. In this chapter, our focus on a mixing layer is motivated in part to avoid the additional complexity introduced by the potential core structure of a jet.

It is notoriously difficult to make any direct assessment of the sound-generating role of turbulence scales in a jet. There exists experimental evidence that most (nearly all) of the high-frequency acoustic energy comes from near the nozzle, whereas the sources of low-frequency sound are distributed along the jet axis and peak near the end of the potential core.[26,43,44] Near the nozzle, the locally largest scales are on the order of the shear layer thickness and therefore are small and expected to produce high-frequency sound. This is consistent with the view that the locally largest scales are responsible for most of the radiated sound spectrum and that it is the range of locally largest scale sizes between the nozzle lip and the close of the potential core that gives the radiated spectrum its breadth. Indeed, analysis of large-eddy simulations of jets suggest that representing the thin near-nozzle shear layers is more important than sub-grid-scale modeling.[45]

3.1.1 A Model Turbulent Flow

To examine the relation of near-field turbulence scales to sound field scales, we have designed direct numerical simulations of temporally-developing mixing layers. Geometrically, this configuration provides a model for the shear layers in a jet prior to the close of the potential core. The role of Reynolds number in jets has recently been investigated using large-eddy simulations.[46] Our simulations are designed to avoid the additional complexities introduced by the potential core and the dissipation added to such large-eddy simulations to model (at least functionally) the cascade and dissipation of energy at unresolvable scales. Simulations of several mixing layers with increasing Reynolds numbers allows for the comparison of the sound fields of flows that share the same large turbulence scales, but with an increasing range of smaller scales. Physically, the temporal mixing layer also avoids the ambiguity of spatially-developing flows wherein the locally largest scales from different parts of the flow radiate simultaneously. However, this non-locality in space is traded for non-locality in time for a temporally-developing flow. The non-stationary character of the flow also makes it more convenient to consider the spatial range of scales in the sound field rather than frequency spectra directly.

3.1.2 Temporal Mixing Layer Simulations

Temporally-developing mixing layers are computationally convenient due to their periodicity in both the streamwise and spanwise directions and have been used in many cases to study transition and turbulence.[47–51] However, temporally-developing flows are only a model for their spatially-developing counterpart, and they cannot be expected to exactly match their radiated sound.[52] In some examples,[53,54] the sound from temporally-developing flows appears to be dominated by plane waves traveling perpendicular to the shear layer. This behavior is an artifact of the small size of the periodic domains in those studies. An analysis of the wavenumber components of a model wave equation (see Appendix A for full details) shows that the discrete wavenumber spectrum is only fundamentally restrictive when the dominant sound wavelength is comparable to the size of the periodic domain. When the spectrum is well resolved, its evolution into the sound field should well approximate that of the continuous spectrum case.

Case	$(N_\mathrm{x} \times N_\mathrm{y} \times N_\mathrm{z})$	$(L_\mathrm{x},\ L_\mathrm{y},\ L_\mathrm{z})/\delta^0_\mathrm{m}$	min $\Delta y/\delta^0_\mathrm{m}$	max $\Delta y/\delta^0_\mathrm{m}$
ML1	$340 \times 213 \times 84$	(2000,2000,750)	4.68	26.48
ML2	$680 \times 425 \times 168$	(2000,2000,750)	2.34	13.64
ML3	$2050 \times 1251 \times 512$	(2000,2000,750)	0.79	4.72
ML4	$2050 \times 1251 \times 512$	(2000,2000,750)	0.79	4.72

Table 3.1: Mesh sizes and cross-stream stretching information for all four mixing layers.

3.2 Initial Conditions and Simulation Details

Four temporally-developing compressible mixing layers with varying Reynolds number were simulated in this study. They are referred to as ML1 through ML4, with ML1 being the lowest Reynolds number and ML4 the highest. For reasons that will be explained in §3.3.1, the ML3 simulation was used to create the initial fields for the other three simulations. At $t = 0$, ML3 was initialized with the streamwise mean velocity profile

$$U\left(\mathrm{y}\right) = \frac{\Delta U}{2} \tanh\left(\sigma_\mathrm{y} y\right), \tag{3.1}$$

where $\sigma_\mathrm{y} = 5/\delta^0_\mathrm{m}$ and $\Delta U/c_\infty = 0.9$. No mean flow was specified in the y- and z-directions. The temperature of the upper and lower streams were the same and equal to the ambient temperature, $T_\infty = 1/(\gamma - 1)$. Details about the computational grid and domain sizes are shown in Table 3.1.

The turbulence was seeded via a velocity potential:

$$\begin{aligned}\varphi\left(x,y,z\right) = -e^{-\frac{\sigma_\mathrm{y} y^2}{\delta^0_\mathrm{m}}} \\ \left[\sin\left(\frac{y}{\delta^0_\mathrm{m}}\right) + 2\sigma_\mathrm{y} y \cos\left(\frac{y}{\delta^0_\mathrm{m}}\right)\right] \times \sum_{i,j}^{N_\mathrm{p}} A_{ij} \cos\left(\frac{k^i_\mathrm{x} x}{\delta^0_\mathrm{m}} + \theta_i\right) \cos\left(\frac{k^j_\mathrm{z} z}{\delta^0_\mathrm{m}} + \varrho_j\right).\end{aligned} \tag{3.2}$$

Here θ_i and ϱ_j are random phases between zero and 2π. The mode amplitudes

$$A_{ij} = \frac{\epsilon}{4\pi^2 k^i_\mathrm{x}\, k^j_\mathrm{z}} \tag{3.3}$$

had $\epsilon = 0.15\,\delta_{\mathrm{m}}^0 \Delta U$ and the streamwise and spanwise wavenumbers

$$k_{\mathrm{x}}^i = \frac{2\pi i}{L_{\mathrm{x}}}\delta_{\mathrm{m}}^0 \qquad\qquad k_{\mathrm{z}}^j = \frac{2\pi j}{L_{\mathrm{z}}}\delta_{\mathrm{m}}^0, \tag{3.4}$$

gave decaying spectra in both directions. The longest wavelengths (in each direction) were set to be five times the initial momentum thickness, δ_{m}^0, otherwise stated as equivalent to $L_{\mathrm{x}}/400$ and $L_{\mathrm{z}}/150$. $N_{\mathrm{p}} = 75$ modes were used in each direction. The y-dependence of φ was specified such that the velocity perturbations would not be identically zero but instead have a Gaussian decay profile along the layer centerline. Taking the gradient of (3.2) gives the velocity perturbations

$$\begin{aligned}
u' &= e^{-\frac{\sigma_{\mathrm{y}} y^2}{\delta_{\mathrm{m}}^0}}\left[\sin\left(\frac{y}{\delta_{\mathrm{m}}^0}\right) + 2\sigma_{\mathrm{y}}\frac{y}{\delta_{\mathrm{m}}^0}\cos\left(\frac{y}{\delta_{\mathrm{m}}^0}\right)\right] \times \sum_{i,j}^{N_{\mathrm{p}}} \frac{k_{\mathrm{x}}^i}{\delta_{\mathrm{m}}^0} A_{ij} \sin\left(\frac{k_{\mathrm{x}}^i x}{\delta_{\mathrm{m}}^0} + \theta_i\right)\cos\left(\frac{k_{\mathrm{z}}^j z}{\delta_{\mathrm{m}}^0} + \varrho_j\right) \\
v' &= -e^{-\frac{\sigma_{\mathrm{y}} y^2}{\delta_{\mathrm{m}}^0}}\cos\left(\frac{y}{\delta_{\mathrm{m}}^0}\right) \times \sum_{i,j}^{N_{\mathrm{p}}} A_{ij} \cos\left(\frac{k_{\mathrm{x}}^i x}{\delta_{\mathrm{m}}^0} + \theta_i\right)\cos\left(\frac{k_{\mathrm{z}}^j z}{\delta_{\mathrm{m}}^0} + \varrho_j\right) \\
w' &= e^{-\frac{\sigma_{\mathrm{y}} y^2}{\delta_{\mathrm{m}}^0}}\left[\sin\left(\frac{y}{\delta_{\mathrm{m}}^0}\right) + 2\sigma_{\mathrm{y}}\frac{y}{\delta_{\mathrm{m}}^0}\cos\left(\frac{y}{\delta_{\mathrm{m}}^0}\right)\right] \times \sum_{ij}^{N_{\mathrm{p}}} \frac{k_{\mathrm{z}}^j}{\delta_{\mathrm{m}}^0} A_{ij} \cos\left(\frac{k_{\mathrm{x}}^i x}{\delta_{\mathrm{m}}^0} + \theta_i\right)\sin\left(\frac{k_{\mathrm{z}}^j z}{\delta_{\mathrm{m}}^0} + \varrho_j\right).
\end{aligned} \tag{3.5}$$

A divergence-free field is desirable since it reduces the amount of unphysical sound caused by specifying an initial flow field that is not a solution of the Navier–Stokes equations. This is especially important for temporal mixing layers as unphysical sound waves emanating from the initial conditions propagating the x–z plane will never leave the physical domain due to the periodic boundary conditions. Using (3.5) as the initial velocity field does not result in a fully divergence-free initial flow field, however. To obtain an even quieter initial condition, the velocity components could have been used to solve for corresponding pressure and density perturbations. In a prior simulation, initial velocity perturbations based on sinusoidal functions were generated by a similar means as in (3.5) (but not the gradient of a velocity potential). The average divergence along the centerline was found to be three orders of magnitude larger for the perturbations that were not generated by the velocity potential.

It was found through numerical experimentation that starting with an initial condition outlined above was more expedient in the computational sense than simply exciting the lowest wavenumbers of the flow such as wavelengths that were fractional lengths of the computational

box length as is common. In the latter case, the flow spread faster and the turbulence was not fully developed until later in the time series. Since the layer grows linearly in time, the slower spreading flow allowed for a longer time series of data to be collected. Initializing the mixing layer in the manner shown in (3.2) and (3.3) with longest wavelengths of $5\,\delta_{\mathrm{m}}^0$ allowed for a longer time series to be computed before the shear region of the mixing layer grew beyond the high resolution region of the cross-stream mesh. We will see good development of the turbulence from these initial conditions in §3.3.

3.3 Results

This section presents the near- and far-field quantities of interest of the four mixing layer simulations. First, the initial flow state, which was used as an initial condition, is described in §3.3.1. Next, the growth of the layers is shown and compared with other simulations and experiment, and Reynolds number based upon several pertinent length scales are presented in §3.3.2. Mean flow characteristics and turbulence quantities are presented in §3.3.3 and used to gauge the statistical and similarity properties of the mixing layers. A visualization of the near-field dynamics and sound field are shown in §3.3.4. Near-field one-dimensional kinetic energy and pressure spectra are reported in §3.3.5 and §3.3.7 with an accompanying scaling analysis. The far-field pressure spectra are also compared with the near field in terms of traditionally defined turbulence length scales. The frequency spectra of the mixing layers and a discussion of the effects of viscous attenuation in the far-field pressure spectra are presented in §3.3.8. Energy considerations in the far field are also presented and quantified in §3.3.10. Last, a thorough analysis of a possible link between the near-field vortical structure dynamics and the far-field sound is also presented and discussed in §3.3.11.

3.3.1 Initial Flow

Starting from the initial condition in (3.1) and (3.5), ML3 was marched in time until $t_0 = 540\,\delta_{\mathrm{m}}^0/\Delta U$ (2000 time steps) at which point it had spread to about eight times its initial momentum thickness.

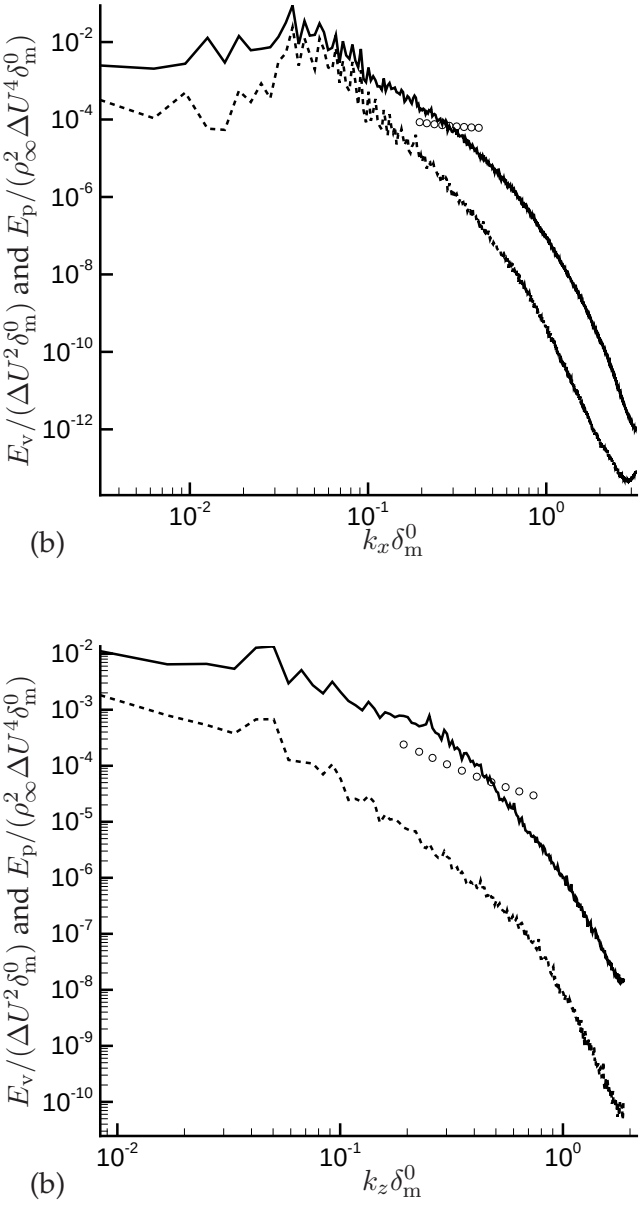

Figure 3.1: One-dimensional kinetic energy and pressure spectra of the ML3 mixing layer at $y = 0$ in the streamwise (a) and spanwise (b) directions. $E_{\rm v}$ at $t = t_0$:—— ; $E_{\rm p}$ at $t = t_0$: ---- ; and $E_{\rm v}$ at $t = 0$: ∘ ∘ ∘ .

At this time, the mixing layer was growing linearly in time. Obvious transients propagating in the $\pm y$ direction created by the initial conditions had passed out of the domain and were absorbed by the boundary buffer zone. Of course, acoustic waves moving in purely periodic directions

Simulation	Initial $\mathrm{Re}_{\delta_\mathrm{m}}$	Final $\mathrm{Re}_{\delta_\mathrm{m}}$	Final $\mathrm{Re}_{\delta_{99}}$	Max $\mathrm{Re}_{\lambda_\mathrm{x}}$	Max $\mathrm{Re}_{\lambda_\mathrm{z}}$
ML1	35	233	2029	148	74
ML2	69	485	4297	171	97
ML3	207	1442	12458	292	177
ML4	414	2848	24376	422	280

Table 3.2: Reynolds numbers based on layer thickness for the temporal mixing layer simulations.

never leave the domain. The initial perturbations in (3.5) were formulated such that these acoustic waves were negligible compared to those generated by the turbulence later in the simulation. The streamwise and spanwise kinetic energy and pressure spectra on the layer centerline ($y = 0$) are shown in Fig. 3.1 for the initial condition and at $t = t_0$ for the ML3 simulation.* Significant energy is found in the lower wavenumbers, which were not excited by the initial perturbations, and the energy cascade of the turbulence appears to have established fully-developed turbulence.

The ML3 field at this time was also then used as the initial flow field for the other three simulations. For the ML1 and ML2 simulations, the field was interpolated onto the smaller meshes using cubic splines in the y direction. In the spanwise and streamwise directions, all variables were Fourier transformed and only the wavenumbers needed for the lower resolution mesh were kept. The ML4 simulation used the same field as ML3 since their meshes were identical. No high-wavenumber filtering was used in the ML1, ML2, or ML3 simulations.

All of the mixing layers were simulated for a time of $2430\,\delta^0_\mathrm{m}/\Delta U$ beyond the initial flow fields generated by the ML3 simulation (t_0). At this point the Reynolds numbers of the ML1, ML2, and ML4 simulations were set such that the initial Reynolds number of ML2 was twice that of ML1, ML3 was initially three times ML2, and ML4 was initially twice ML3. Reynolds number based on several thickness measures at t_0 and the end of the simulations are listed in Table 3.2. The data in Table 3.2 show that these relationships are preserved throughout the simulation.

The Reynolds number based on the Taylor microscale varied. This quantity is defined via the length scale

$$\lambda_\mathrm{x}(t) = \left(\frac{\widetilde{uu}}{\widetilde{\frac{\partial u}{\partial x}\frac{\partial u}{\partial x}}} \right)^{\frac{1}{2}} \tag{3.6}$$

*Throughout this section, the streamwise E_v and E_p spectra are presented after averaging in the spanwise direction and vice versa for the spanwise spectra.

which was computed on the mixing layer centerline. The streamwise Taylor microscale Reynolds number is

$$\mathrm{Re}_{\lambda_\mathrm{x}} = \frac{\rho_\infty (u')_\mathrm{rms} \lambda_\mathrm{x}}{\mu_\infty}, \tag{3.7}$$

with similar definitions for the spanwise direction. The ratio of maximum $\mathrm{Re}_{\lambda_\mathrm{x}}$ between ML4 and ML1 is roughly 3 and about 4 for $\mathrm{Re}_{\lambda_\mathrm{z}}$ while the ratio based on the other Reynolds number definitions is 12. However, the ratio between ML3 and ML4 is around 1.5 while for the others it is 2. The evolution of the Taylor microscales are shown in Fig. 3.2. The Taylor microscale does not have a clear physical interpretation, but is a length scale indicative of the inertial subrange where turbulent motions are determined by inertial effects, not viscous effects, for flows of sufficiently high Reynolds number. It is clear from Fig. 3.2 that this length scale is an increasing function of time and therefore Reynolds number.

3.3.2 Layer Growth

The growth of the mixing layers is shown in Fig. 3.3 with momentum thickness (2.3) and the vorticity thickness:

$$\delta_\omega(t) = \frac{\Delta U}{|\partial U/\partial y|_\mathrm{max}}. \tag{3.8}$$

The layers grow about seven times their initial thickness during the simulation with the relatively viscous ML1 growing at a slightly lower rate than the others. The initial and final Reynolds numbers are reported in Table 3.2. The layers grow with time at an average rate of $\delta'_\mathrm{m}(t)/\Delta U = 0.019$, which is comparable to simulations of planar temporal,[48] annular temporal,[50] and spatial[28,55] mixing layers under similar conditions as well as previous experiments[56] of incompressible spatial mixing layers. The comparison with spatial mixing layer growth rates assumes an informal relationship between the temporal evolution and spatial evolution of the corresponding flows. By normalizing time by δ^0_m and ΔU, we are essentially invoking the often used relationship akin to Taylor's hypothesis.

The momentum thickness and vorticity thickness in Fig. 3.3 both show small regions of time where all four layers suffer periods of slowed (or almost no) growth. This occurs near $t =$

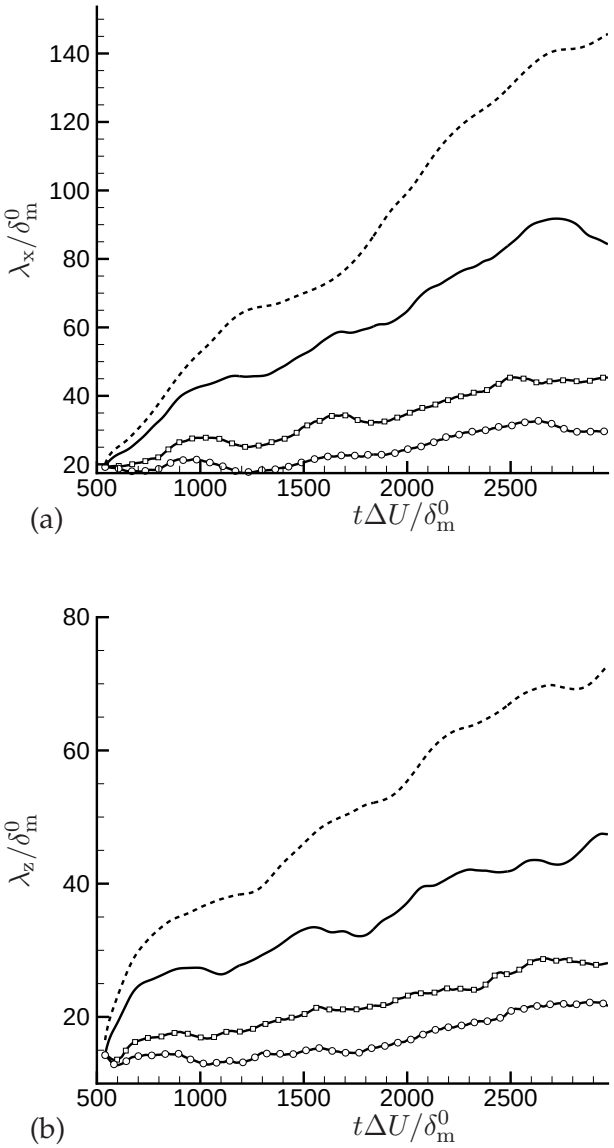

Figure 3.2: (a) Streamwise and (b) spanwise Taylor microscale evolution scaled by the initial momentum thickness: ML1 - - - - ; ML2 —— ; ML3 - □ - ; and ML4 - ○ - .

$800\,\delta^0_m/\Delta U$ and again near $t = 2200\,\delta^0_m/\Delta U$, but the layers revert back to similar growth rates prior to each slow-growth period. Since the slow growth appears in all of the mixing layers regardless of Reynolds number, the effect is expected to be due to the large structures, which are similar in all of the flows. There does not appear to be a reason for this behavior based on visualization of the data, but a clear pairing of large vortical structures does occur near $t = 2200\,\delta^0_m/\Delta U$

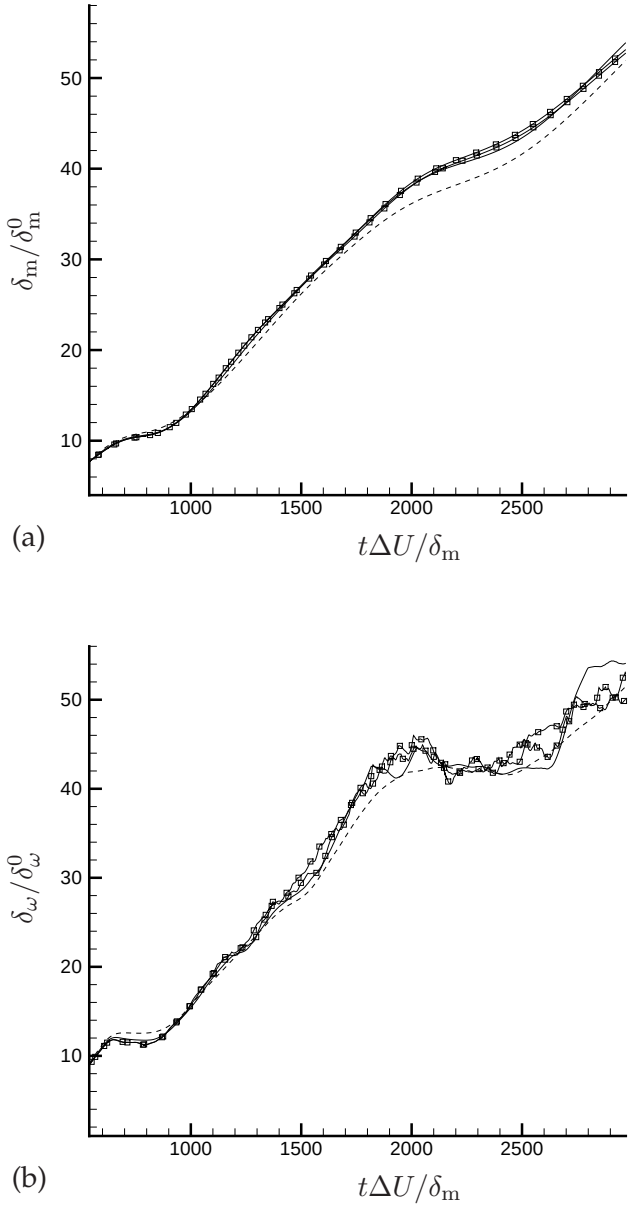

Figure 3.3: (a) Momentum thickness and (b) vorticity thickness evolution scaled by the initial thicknesses $\delta^0_{\rm m}$ and δ^0_ω: ML1 - - - - ; ML2 —— ; ML3 - □ - ; and ML4 - ○ - .

(see Figs. 3.25 and 3.26) which may result in reduced growth. At the later time, it is possible that the simulations are "feeling" the size of the computational domain.

3.3.3 Mean Flow and Reynolds Stresses

We now present the mean flow evolution and Reynolds stresses of the simulation to estimate the degree of self-similarity of the mixing layers. Temporal mixing layers have no laboratory flow counterpart, so computing these often reported quantities (for both temporal and spatial simulations as well as experiments) is necessary for verification of the computed results. Unlike spatial mixing layers, temporally-developing mixing layers are statistically symmetric about $y = 0$ and therefore the profiles are scaled by the similarity variable $y/\delta_{\mathrm{m}}(t)$. The layer thickness is the only length scale associated with a mixing layer, so it should collapse data if the mixing layers computed here have achieved a self-similar equilibrium condition.

The scaled streamwise mean velocity profiles of the ML2 and ML3 simulations are shown in Fig. 3.4 at several times during the simulation. The unequivocal collapse of the profiles are present in the ML1 and ML4 layer data (not shown) as well, thereby ruling out a dependence on Reynolds number, as expected. For all mixing layers, the easier condition for similarity shown by the mean velocity profile is satisfied.

A more difficult condition to satisfy self-similarity is the collapse of Reynolds stress profiles taken at various times during the simulation. To further compare the simulations with the published data and gauge the similarity of the mixing layers, we present the Reynolds stresses of the four mixing layers at $t = \{1080,\, 1620,\, 2160,\, 2700\}\, \delta_{\mathrm{m}}^0/\Delta U$. These times correspond to just after the first slow-growth period, during a period of linear growth, during the more prominent slow-growth period, and near the end of the simulation when the layers are all again growing in a linear fashion, respectively. The $\overline{\rho}\widetilde{u'u'}$, $\overline{\rho}\widetilde{u'v'}$, $\overline{\rho}\widetilde{v'v'}$, and $\overline{\rho}\widetilde{w'w'}$ components of the Reynolds stress tensor for the ML1-ML4 mixing layers are shown in Figs. 3.5-3.8. The effects of non-linear layer growth are present in the stress profiles.

Generally speaking, there exists a collapse in terms of the width of the profiles, but considerable disagreement in the peak magnitudes. The most acute example is the $\overline{\rho}\widetilde{u'v'}$ component, the profiles at later times being the most problematic. The profile at $t = 2160\, \delta_{\mathrm{m}}^0/\Delta U$ deviates significantly in all of the mixing layers. This is the component that is proportional to the most significant production term in the turbulence kinetic energy budget since $U = f(y)$. At this time in the flow,

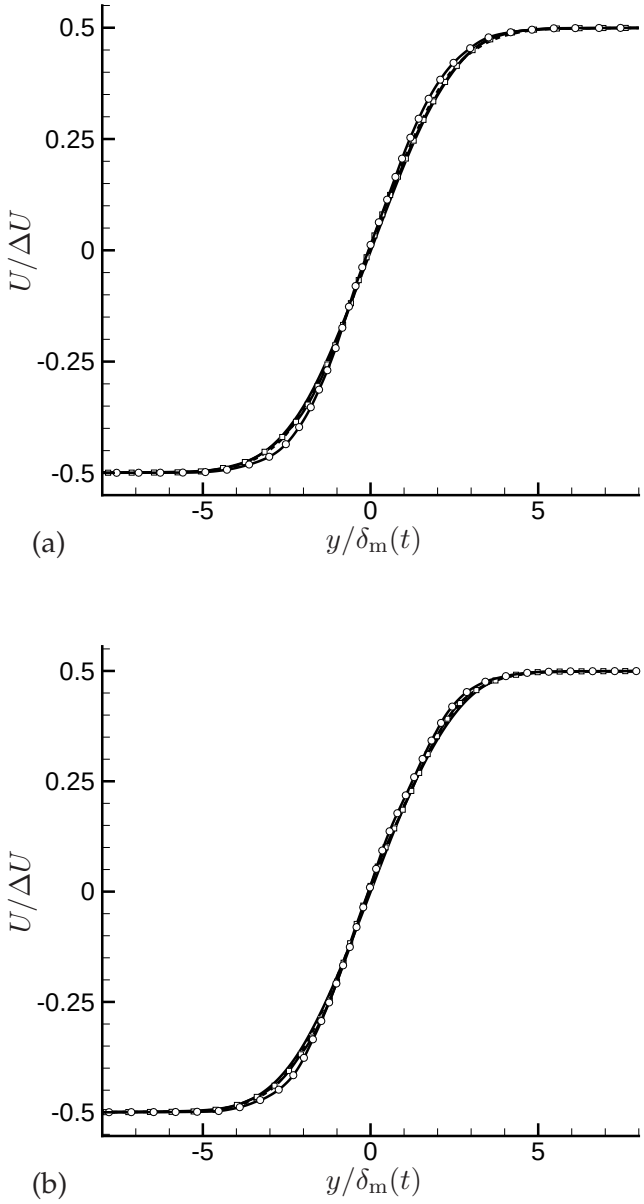

Figure 3.4: Scaled mean streamwise velocity profiles of the (a) ML2 and (b) ML3 mixing layers. $t = 1080\,\delta^0_{\rm m}/\Delta U$: ——— ; $t = 1620\,\delta^0_{\rm m}/\Delta U$: - - - - ; $t = 2160\,\delta^0_{\rm m}/\Delta U$: - □ - ; $t = 2700\,\delta^0_{\rm m}/\Delta U$: - ○ - .

it is probable that the largest structures, which are the size of the flow's width, are beginning to be influenced by the size of the computational domain. The $\widetilde{\overline{\rho}u'u'}$ component reveals perhaps the best collapse of the four stresses with the exception of ML1 in Fig. 3.5. ML1 and ML2 show overshoots at the latest time, but in general this component scales very well. The streamwise and

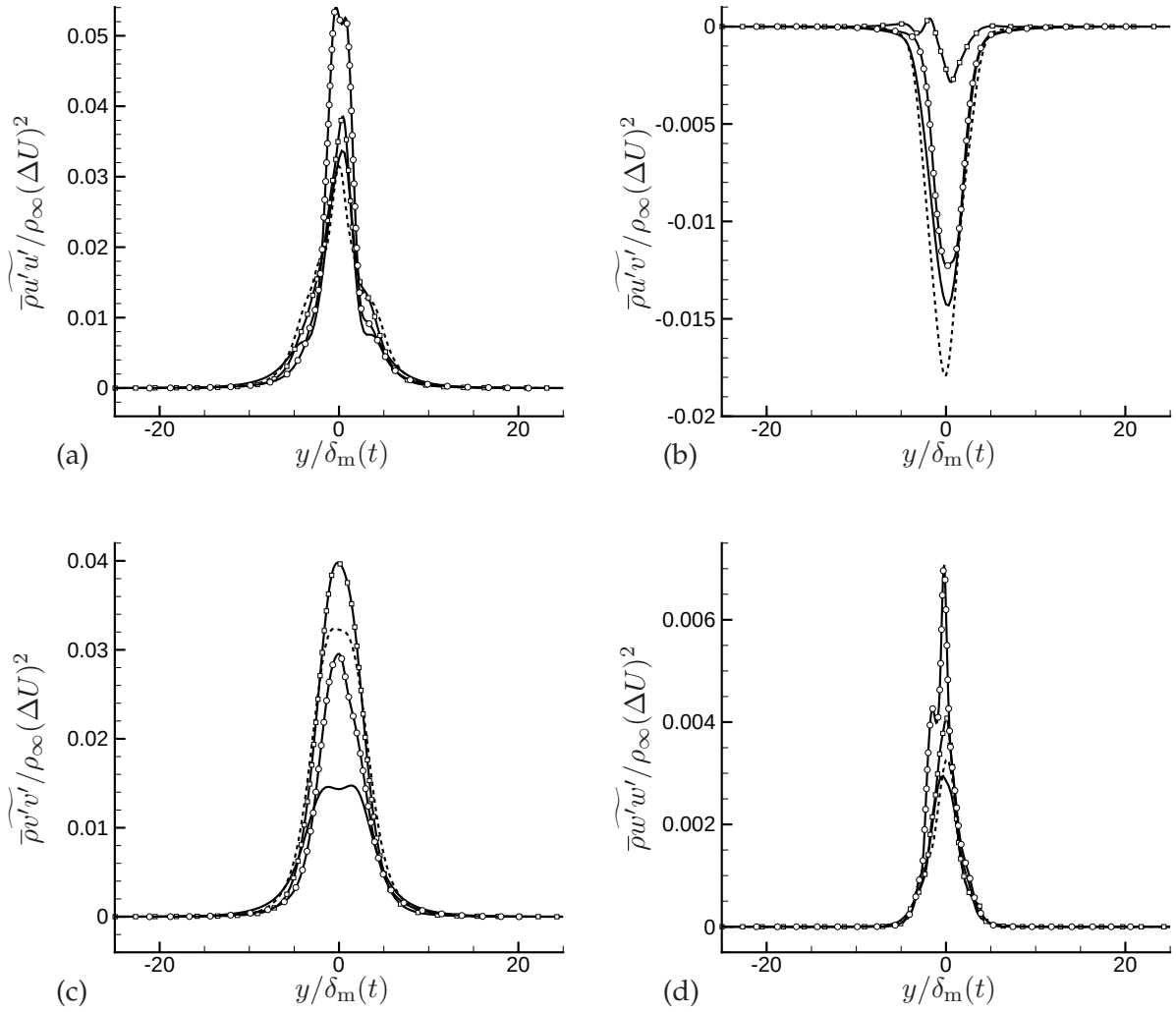

Figure 3.5: Scaled Reynolds stress profiles for the ML1 mixing layer: (a) $\overline{\rho}\widetilde{u'u'}$, (b) $\overline{\rho}\widetilde{u'v'}$, (c) $\overline{\rho}\widetilde{v'v'}$, (d) $\overline{\rho}\widetilde{w'w'}$. $t = 1080\,\delta_{\rm m}^0/\Delta U$: ——; $t = 1620\,\delta_{\rm m}^0/\Delta U$: - - - -; $t = 2160\,\delta_{\rm m}^0/\Delta U$: -▫-; $t = 2700\,\delta_{\rm m}^0/\Delta U$: -○-.

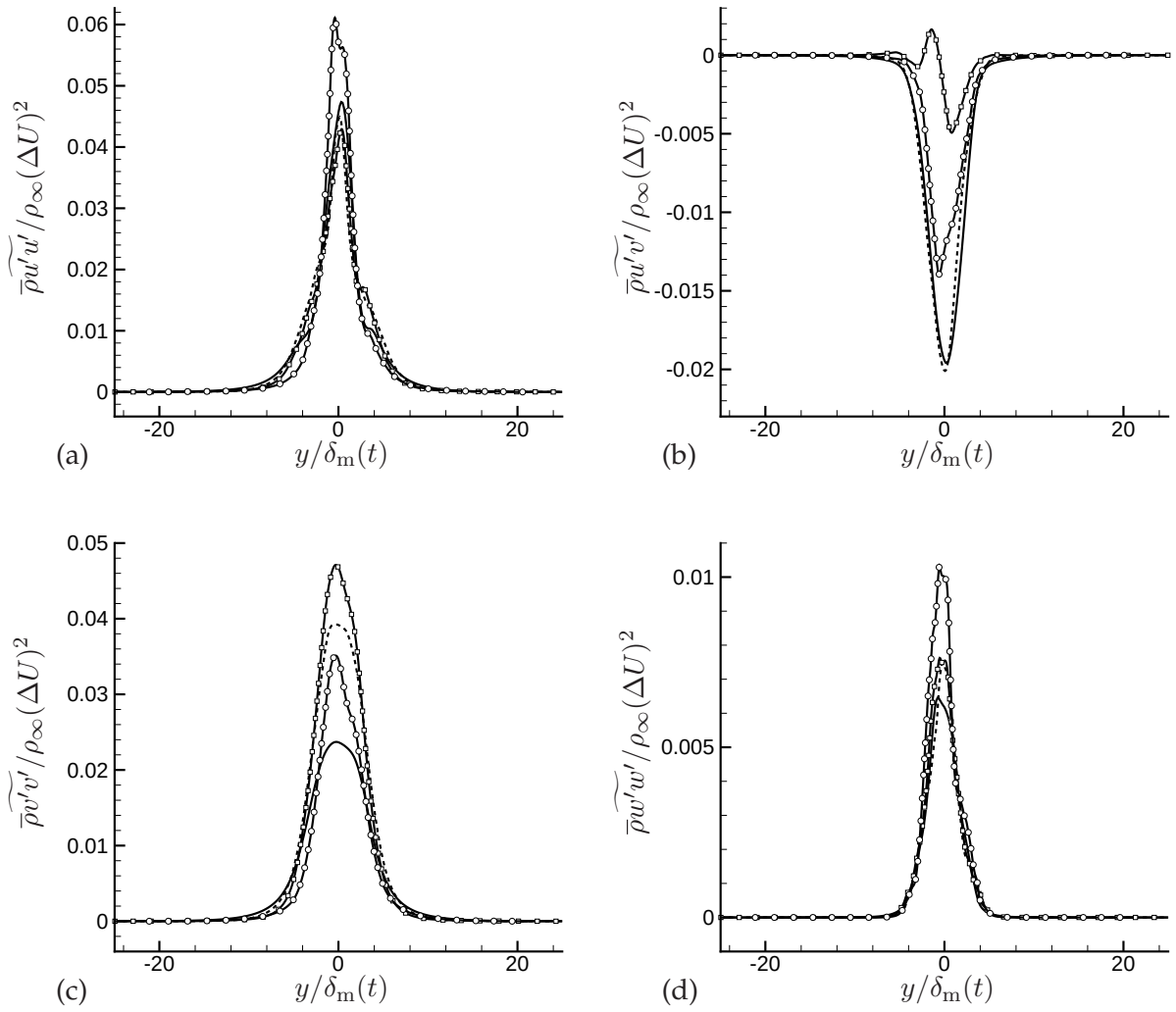

Figure 3.6: Scaled Reynolds stress profiles for the ML2 mixing layer: (a) $\widetilde{\overline{\rho}u'u'}$, (b) $\widetilde{\overline{\rho}u'v'}$, (c) $\widetilde{\overline{\rho}v'v'}$, (d) $\widetilde{\overline{\rho}w'w'}$. See Fig. 3.5 for legend.

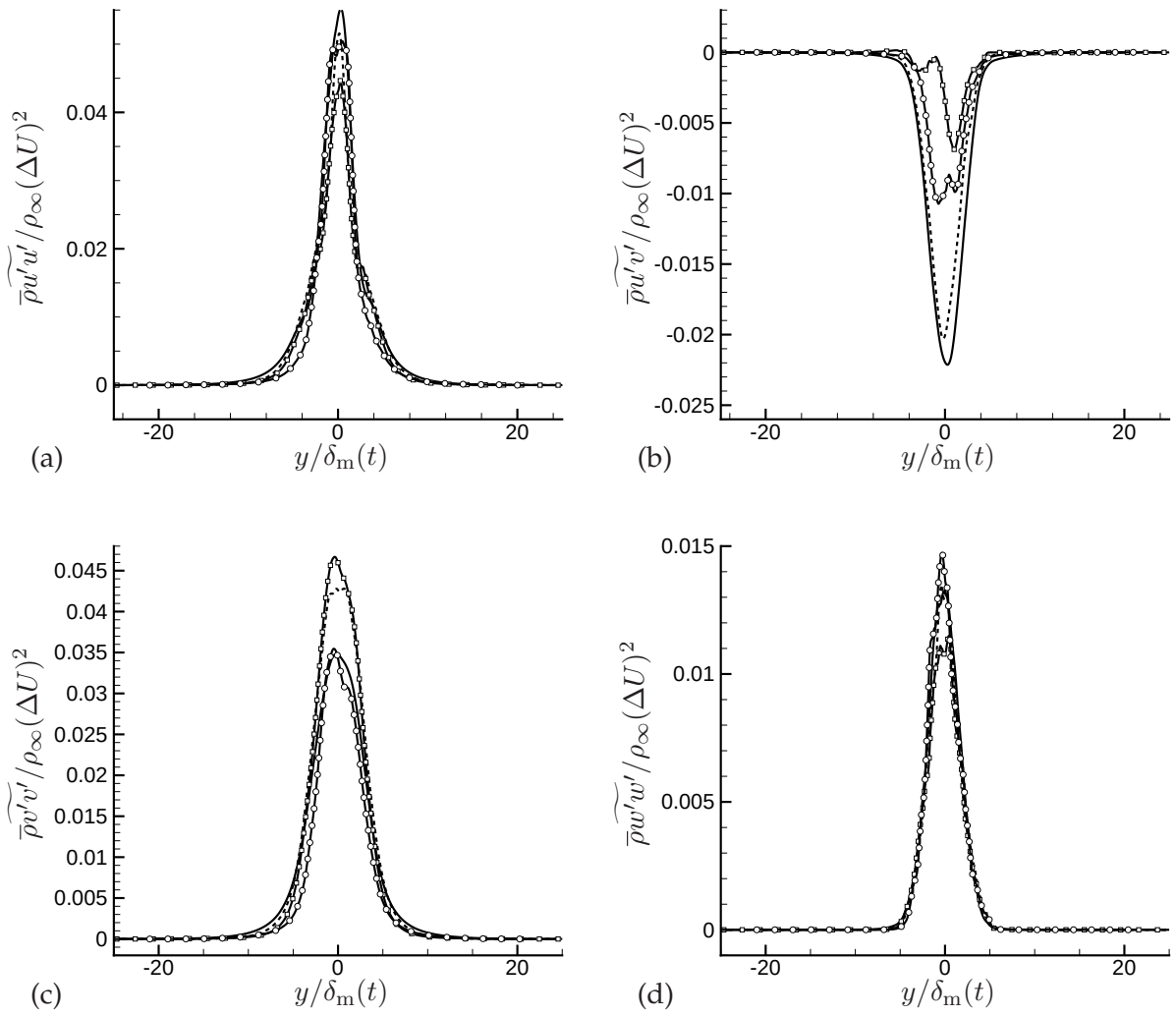

Figure 3.7: Scaled Reynolds stress profiles for the ML3 mixing layer: (a) $\overline{\rho}\widetilde{u'u'}$, (b) $\overline{\rho}\widetilde{u'v'}$, (c) $\overline{\rho}\widetilde{v'v'}$, (d) $\overline{\rho}\widetilde{w'w'}$. See Fig. 3.5 for legend.

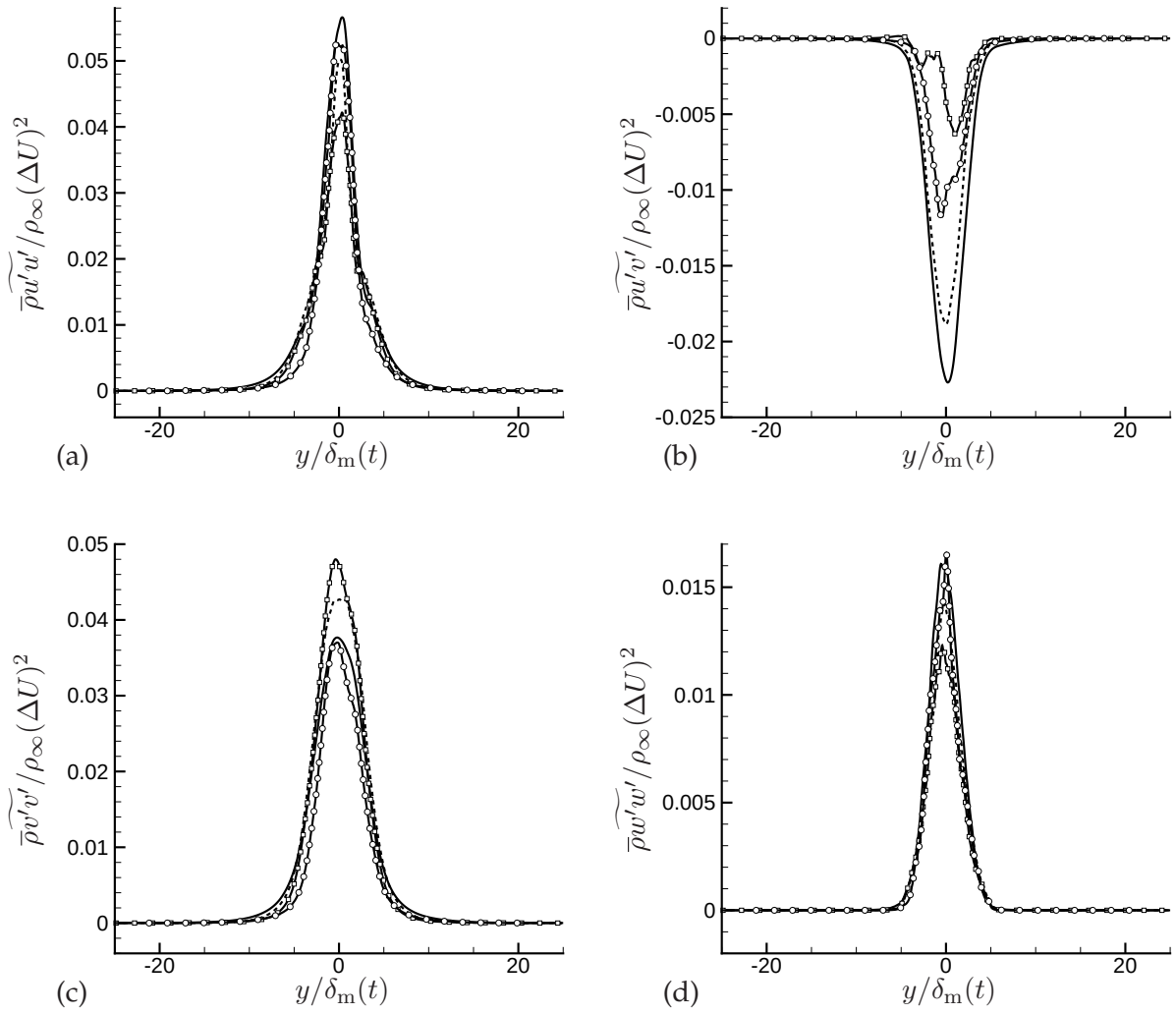

Figure 3.8: Scaled Reynolds stress profiles for the ML4 mixing layer: (a) $\overline{\rho}\widetilde{u'u'}$, (b) $\overline{\rho}\widetilde{u'v'}$, (c) $\overline{\rho}\widetilde{v'v'}$, (d) $\overline{\rho}\widetilde{w'w'}$. See Fig. 3.5 for legend.

cross-stream normal stresses ($\widetilde{\overline{\rho}u'u'}$ and $\widetilde{\overline{\rho}u'v'}$) are of similar magnitude in all four mixing layers. The $\widetilde{\overline{\rho}v'v'}$ and $\widetilde{\overline{\rho}w'w'}$ components collapse better as the Reynolds number increases. ML1 and ML2 collapse poorly, but this is removed for both ML3 and ML4.

Comparing these profiles to existing simulations and experiments shows reasonable agreement. The maximum values at early times (during linear growth) of $\widetilde{\overline{\rho}u'v'}$ are in agreement with many experiments and simulations.[50,57,58] However, the magnitudes of the streamwise and cross-stream normal stresses are between 10 and 30% higher than the spatial experimental results of Bell & Mehta[56] and Samimy & Elliot[58] as well as other temporal and spatial DNS,[48,55] but are reasonable compared to the compressible annular mixing layer simulation of Freund *et al.*[50] at $\mathrm{Ma} = 0.9$. The spanwise normal stress $\widetilde{\overline{\rho}w'w'}$ is seldom reported, but is of similar magnitude to the results of Freund *et al.*[50]

We conclude that during the times of linear growth, all four mixing layers appear to be be well developed but strictly self similar. The periods of slowed growth are manifested in the $\widetilde{\overline{\rho}u'v'}$ Reynolds stress, an indication of retarded production of turbulent kinetic energy near the end of the simulation and possibly effects due to the finite size of the computational domain. This is more striking in the two lower Reynolds number simulations. For this reason, we will view near-field turbulence spectra at times prior to $t = 2160\,\delta^0_{\mathrm{m}}/\Delta U$ in later analysis. The goal of this study, however, was not to simulate strictly self-similar mixing layers. Indeed, the initial shear layers of jets are not self-similar. The continuity of results from the four simulations again suggests that the large scales are similar among them and they dominate the flow dynamics.

3.3.4 Visualization

A visualization in Fig. 3.9 shows the vorticity magnitude in the shear layers and pressure perturbations from the ambient pressure p_∞ at $t = 2160\,\delta^0_{\mathrm{m}}/\Delta U$ on the $z = 0$ plane. Over the range of Reynolds numbers, the pressure fields appear to have similar features despite an obvious increase in the range of turbulence scales in the shear layer with increasing Reynolds number. Figure 3.10

also shows divergence of velocity in place of pressure in the sound field. Since

$$\nabla \cdot \mathbf{u} \propto -\frac{\mathrm{d}p}{\mathrm{d}t} \tag{3.9}$$

in the acoustic limit, for visualization purposes this augments the higher frequencies (smaller scales) in the sound field. The visualizations at $z = 0$ are representative of each layer's large-scale structures throughout the spanwise domain. In general, the vortical structure pairing events are not localized in this direction and the large rollers of spanwise vorticity cover almost the entire spanwise domain. A visualization of an x-z plane at $y = 0$ of the vorticity magnitude is shown in Fig. 3.11 which shows this behavior. No attempt was made to decorrelate the turbulent structures in this direction.

3.3.5 Kinetic Energy Spectra

We now present one-dimensional turbulence kinetic energy spectra calculated at $y = 0$ to quantify the range of scales present in each of the mixing layers and assess the resolution of the DNS. The spectra are shown in Fig. 3.12 at $t = 2160\,\delta^0_\mathrm{m}/\Delta U$ scaled by the momentum thickness. By this point in time only the peak wavenumber is changing substantially, progressing to lower wavenumbers as the layer grows and the vortical structures pair. This suggests that the turbulence is fully developed. The spectra show that all of the mixing layers are well resolved with the streamwise spectra dropping at least eight decades and the spanwise spectra, which has a higher-resolution discretization in the solver, dropping at least seven. For the stabilized ML4 simulation which was filtered by the method of §2.2.7, the vertical line in Fig. 3.12(a) labeled "T_{999}" marks the wavenumber for which the stabilizing filter's transfer function was $T(k_\mathrm{x}\delta^0_\mathrm{m}) = 0.999$. The sudden drop in the spanwise spectra of ML4 in Fig. 3.12(b) shows the effect of the Fourier cutoff filter used in that direction. A full assessment of the filtering of ML4 is given in §3.3.6.

As expected, the spectra are have similar kinetic energy in the lowest wavenumbers since they share the same large scales. ML1 has energy in only the first few streamwise wavenumbers before decaying quickly and is even narrower in the spanwise spectra as reported in Fig. 3.12. Only ML3 and ML4 have spectra suggestive of an inertial range, and their spectra collapse in this

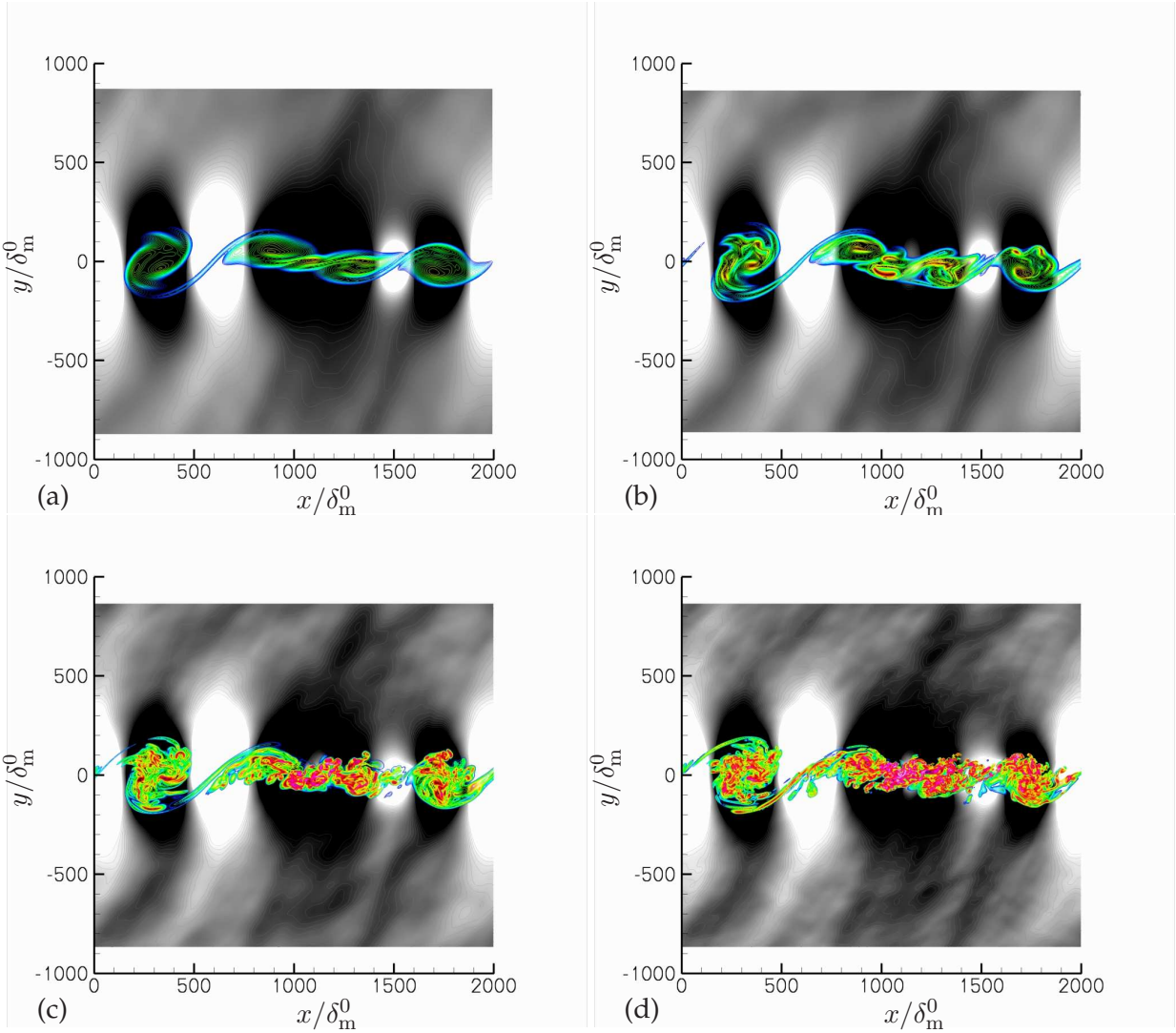

Figure 3.9: Visualizations of $x-y$ plane at $z=0$ of pressure fluctuations and vorticity magnitude. Twenty-two evenly-spaced contours between -0.02 and 0.02 are shown for pressure, and 45 evenly-spaced contours between 0.015 and 2 are shown for the vorticity magnitude. (a) ML1, (b) ML2, (c) ML3, and (d) ML4.

region when scaled by the streamwise Taylor microscale, $\lambda_{\rm x}$, which is computed on the mixing layer centerline using (3.6). This is shown in Fig. 3.13(a). The spectra of ML1 and ML2 lie slightly below that of ML3 and ML4 and do not collapse with this scaling, which is consistent with their apparent lack of an inertial range. This fact is not surprising since as the Reynolds number is lowered, the large scales will begin to overlap with the scales affected by viscosity, which are becoming larger and subsequently removing the inertial range. Similar scaling results are found

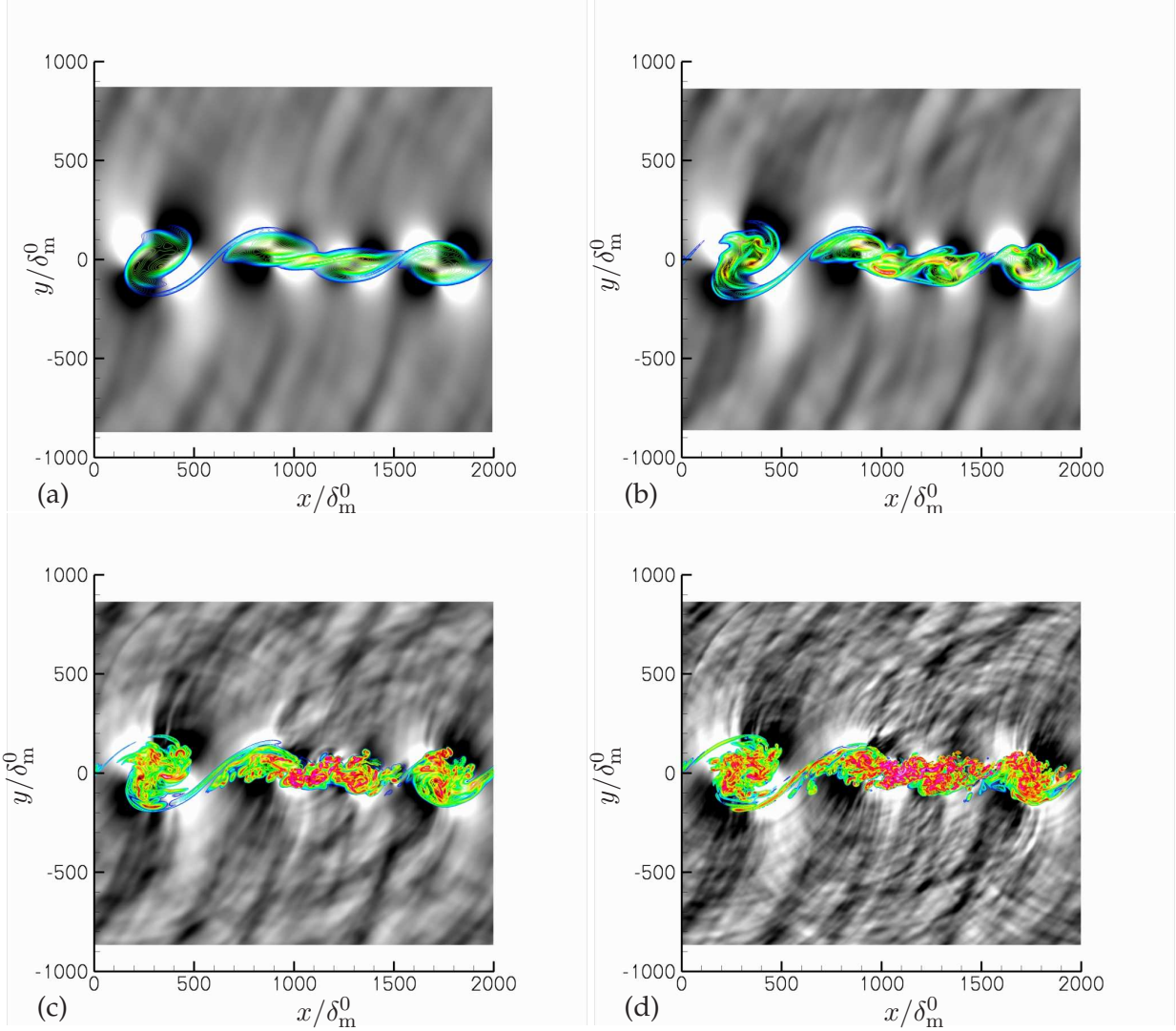

Figure 3.10: Visualizations of $x-y$ plane at $z=0$ of dilatation of velocity and vorticity magnitude. Twenty-two evenly-spaced contours between -0.002 and 0.002 are shown for dilatation and 45 evenly-spaced contours between 0.015 and 2 are shown for the vorticity magnitude. (a) ML1, (b) ML2, (c) ML3, and (d) ML4.

with the spanwise kinetic energy spectra in Fig. 3.13(b) when scaled by λ_z, where the spanwise Taylor microscale is defined in the same manner as (3.6). It is also worth mentioning in light of Table 3.2 that the Reynolds numbers based on δ_{m} follow the initial prescribed Reynolds numbers, which vary among the layers by a factor of twelve. The Reynolds numbers based on the Taylor microscales vary less by this measure.

Kolmogorov scaling collapses the streamwise spectra of ML3 and ML4 at high wavenumbers

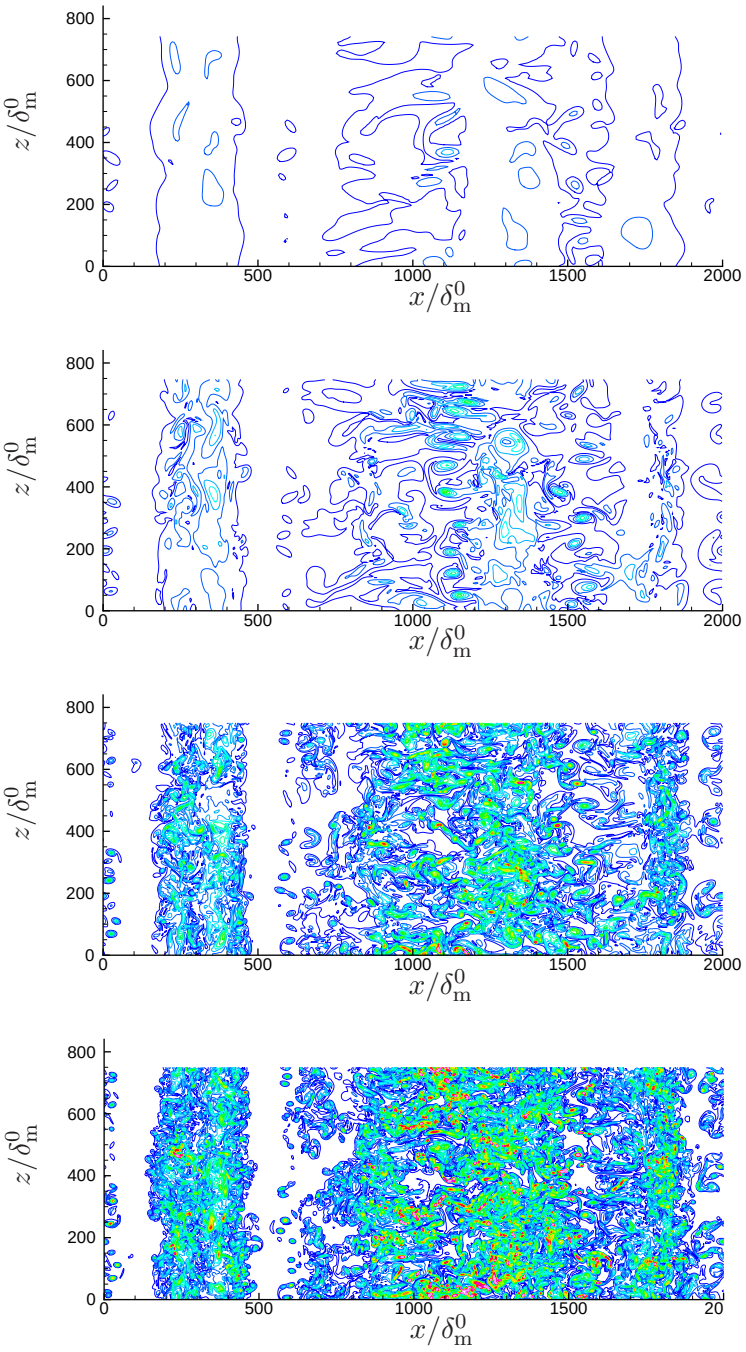

Figure 3.11: Visualizations of $x-z$ plane at $y=0$ of vorticity magnitude. Seventeen evenly spaced contours between 0.05 and 1.8 are shown.

as seen in Fig. 3.14(a) and in the spanwise spectra up until the filtering cutoff wavenumber as seen in Fig. 3.14(b). To compute the Kolmogorov scale for this figure, we use the usual definition

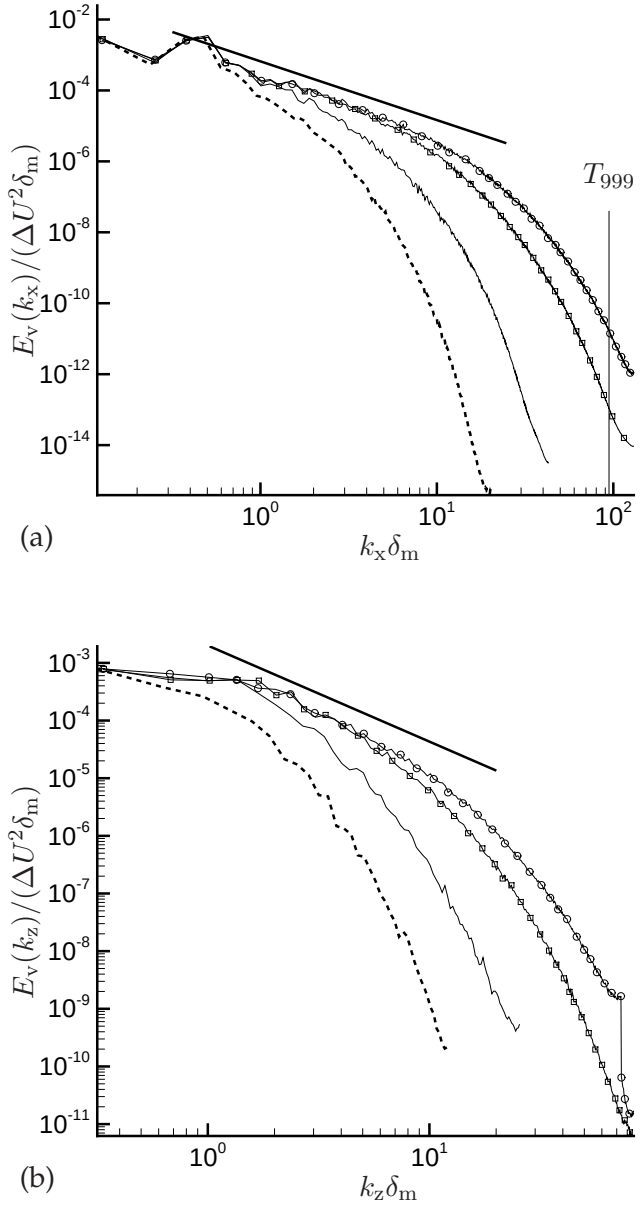

Figure 3.12: One-dimensional kinetic energy spectra at $y = 0$ in the (a) x and (b) z directions. Curves indicate: ML1:- - - - ; ML2: —— ; ML3: -□-; and ML4: -○-. The straight solid lines have a slope of $-5/3$.

$$\eta = \left(\frac{\nu^3}{\varepsilon}\right)^{\frac{1}{4}}, \tag{3.10}$$

but it has been assumed that the dissipation in each of the layers is equal. The structure of the

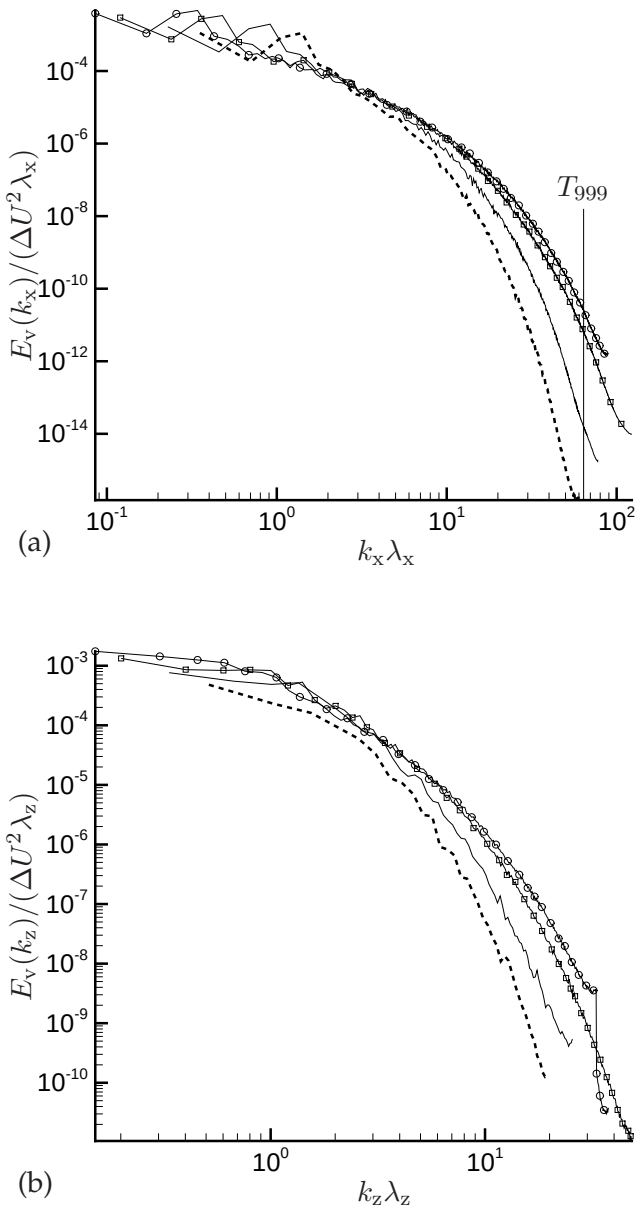

Figure 3.13: One-dimensional streamwise velocity spectra at $y = 0$ in the (a) x and (b) z direction scaled by the Taylor microscale. T_{999} is placed at the wavenumber where $T(k_{\rm x}\lambda_{\rm x}) = 0.999$. Curves indicate: ML1 - - - - ; ML2 —— ; ML3 - □ - ; and ML4 - ○ - .

largest scales are certainly similar in all cases (except perhaps in the most viscous case, ML1). If the turbulence in all the cases is in equilibrium, the assumption of equal dissipation should provide a good estimate of the Kolmogorov scaling. Using the actual dissipation might yield a

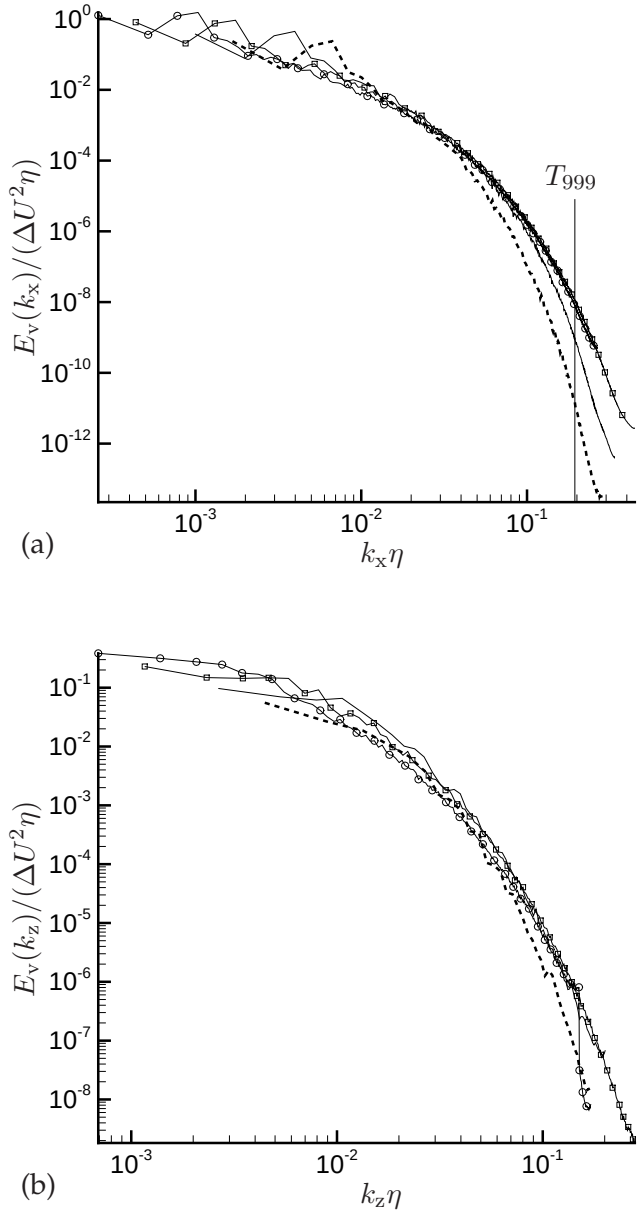

Figure 3.14: One-dimensional streamwise velocity spectra at $y = 0$ in the (a) x and (b) z direction scaled by the Kolmogorov length scale, η. T_{999} is placed at the wavenumber where $T(k_x\eta) = 0.999$. Curves indicate: ML1 - - - - ; ML2 —— ; ML3 - □ - ; and ML4 - ○ - .

somewhat different numerical value for the Kolomogorov scale, but should not change the scaling with Reynolds number. In conclusion, the near-field turbulence spectra show that, compared to ML4, ML1 and ML2 share only a portion of the largest scales, and ML3 shares all scales of ML4

except the highest wavenumbers where the effects of viscosity are dominant.

3.3.6 Numerical Stabilization via Filtering

In §2.2.7 high-order wavenumber filters were formulated to provide numerical stabilization to high Reynolds number DNS. We can now assess the impact of the filtering scheme on the resolved scales on the highest Reynolds number simulation, ML4, which was the only simulation that was filtered. To do this, an additional simulation was carried out. Given the well-resolved direct numerical simulation of ML3, its field was filtered and interpolated onto a mesh with half the points in each direction ($N_{\mathrm{x}} \times N_{\mathrm{y}} \times N_{\mathrm{z}} = 1025 \times 626 \times 256$) in the same manner as for the ML1 and ML2 initial conditions discussed in §3.3.1. The Reynolds number was left unchanged, but the same filtering procedure used for the ML4 simulation was applied. This allowed for a direct comparison of filtered fields with the corresponding direct numerical simulations, which should reveal any of the same kinds of errors caused by the stabilization of ML4.

The energy spectra and pressure spectra of the two cases are compared and show essentially no difference up to the T_{999} point for the streamwise spectra in Fig. 3.15(a) and likewise for the spanwise spectra in Fig. 3.15(b). The stabilization procedure causes no significant effect on the near-field quantities or on the far-field pressure spectra. The resolution of the turbulence in the simulations in this work is far better than typical large-eddy simulations, and the stabilizing filtering is restricted to only the highest wavenumbers. This is particularly important since the filtering procedure provides no physical model for the unresolved scales; it simply removes them and neglects the effects of the small scales on the large and inertial range scales. It would therefore be expected to fail as a sub-grid scale model if applied closer to the energetic scales. However, as seen in the kinetic energy of §3.3.5 as well as Fig. 3.15, the slight effects of the filter are evident far from the energetic scales and only in the dissipative range. We regard it as successfully providing a minimal amount of numerical stabilization to a direct numerical simulation.

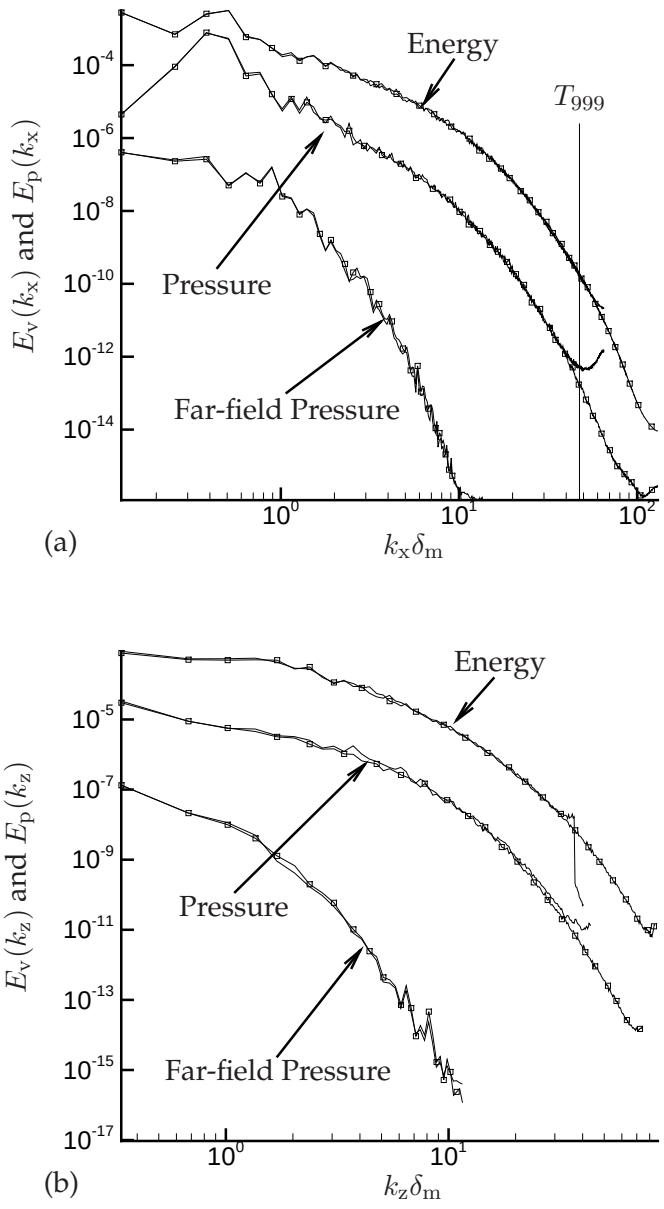

Figure 3.15: One-dimensional streamwise (a) and spanwise (b) energy and pressure spectra computed at $y = 0$ and $y = -850\,\delta_{\rm m}^0$ (denoted as "Far-field Pressure"). T_{999} is placed at the wavenumber where $T(k_{\rm x}\delta_{\rm m}^0) = 0.999$. Curves indicate: stabilized coarser mesh simulation —— and ML3 -□-.

3.3.7 Pressure Spectra

To investigate the increasing range of turbulence scales at higher Reynolds numbers, we compare near- and far-field pressure spectra. All spectra were calculated at $t = 2160\,\delta_{\rm m}^0/\Delta U$, the same time

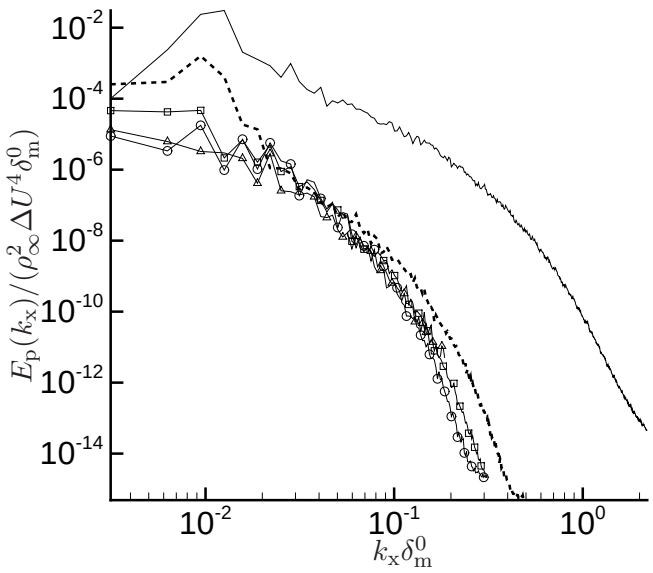

Figure 3.16: One-dimensional x-direction pressure spectra of ML3 simulation at several y locations at propagation adjusted times. Curves indicate: $y = 0$ ——— ; $y = -250\,\delta_{\rm m}^0$ - - - - ; $y = -550\,\delta_{\rm m}^0$ - - □ - - ; $y = -850\,\delta_{\rm m}^0$ - - ○ - - ; and $y = -1850\,\delta_{\rm m}^0$ - - △ - - .

of the simulation as the visualizations in §3.3.4 and the kinetic energy spectra presented in §3.3.5. One-dimensional pressure spectra in the streamwise and spanwise directions were calculated at $y = 0$ and $|y| = 850\,\delta_{\rm m}^0$. The pressure spectra at $y = -850\,\delta_{\rm m}^0$ and $y = 850\,\delta_{\rm m}^0$ were computed and averaged together to provide a measure of sound in the far field.

A suitable location of the far field was determined via an extrapolation using data from the $y = -550\,\delta_{\rm m}^0$ plane from the direct numerical simulations as a boundary condition for an Euler equations solution beyond the Navier-Stokes domain. The same simulation methodology of §2.2 used for the DNS was used to compute the Euler equations. The viscous terms were simply omitted and no high-order filtering was done. This result is shown in Fig. 3.16 for one-dimensional streamwise pressure spectra of ML3 at several cross-stream locations below the shear layer. The far-field pressure spectra at $y = -550\,\delta_{\rm m}^0$ and $y = -850\,\delta_{\rm m}^0$ calculated by the direct numerical simulations showed no significant differences with the spectrum computed with the Euler solver at $y = -1850\,\delta_{\rm m}^0$. The spectra in Fig. 3.16 are evaluated at a time which is adjusted taking into account the time it takes for an acoustic wave to propagate to the specific y locations, thus viewing

the spectrum of a wave as it propagates in the $-y$ direction. The Euler solver used fewer mesh points since it was far from the shear layer and therefore the highest wavenumber in Fig. 3.16 is less than the other spectra obtained from the direct numerical simulation data. A slight variation is seen from the $y = -250\,\delta_{\mathrm{m}}^0$ location to those further away. The structures of the mixing layer grow into this region at this time in the simulation which is seen in the low wavenumber components of Fig. 3.16. These results also counter previous arguments[54] against the use of the current direct numerical simulations of temporal mixing layers to study far-field sound. As per the discussion in Appendix A, the energy in any particular streamwise wavenumbers (and spanwise, not shown) do not decay away from $y = -250\,\delta_{\mathrm{m}}^0$ and therefore do not result in purely planar waves in the far field.

Figure 3.17(a) shows the streamwise near- and far-field pressure spectra scaled by the momentum thickness. The lowest wavenumbers of all four mixing layers scale with the momentum thickness, as was the case with the kinetic energy spectra. The effect of Reynolds number is similarly clear here. ML1 and ML2 depart near $k_{\mathrm{x}}\delta_{\mathrm{m}} \approx 1$, whereas ML3 and ML4 continue on together at a constant slope until $k_{\mathrm{x}}\delta_{\mathrm{m}} \approx 10$ where the ML3 curve begins to decay. This region of constant slope corresponds to the $k^{-7/3}$ inertial range scaling for mean-square pressure fluctuations for homogeneous turbulence.[59] George *et al.*[60] extended the scaling analysis to turbulent shear flows and suggested a switch from a $k^{-7/3}$ scaling (turbulence-turbulence interactions) to a $k^{-11/3}$ scaling (turbulence-mean shear interaction) at lower wavenumbers. These scalings appear to explain a kink in the spectra of an axisymmetric, incompressible jet[60] and a similar change in slope has been observed in large-eddy simulations of compressible jets.[38] In the current study, ML3 and ML4 exhibit the $-7/3$ slope over almost a decade of wavenumbers and a kink in the spectra show the possible transition to the $-11/3$ slope, though the limited size of the computational domain prevents forming any strong conclusions in this regard.

Far-field streamwise spectra are also shown in Fig. 3.17(a). When scaled by the layer thickness, ML2, ML3, and ML4 collapse well in lower wavenumbers, with ML1 showing slightly lower values. The far-field spectra of ML2, ML3, and ML4 all diverge at about the same wavenumber — near the wavenumber of the beginning of the apparent near-field inertial range in the centerline spectra. The far-field spectra also decay much faster after the beginning of the inertial range than

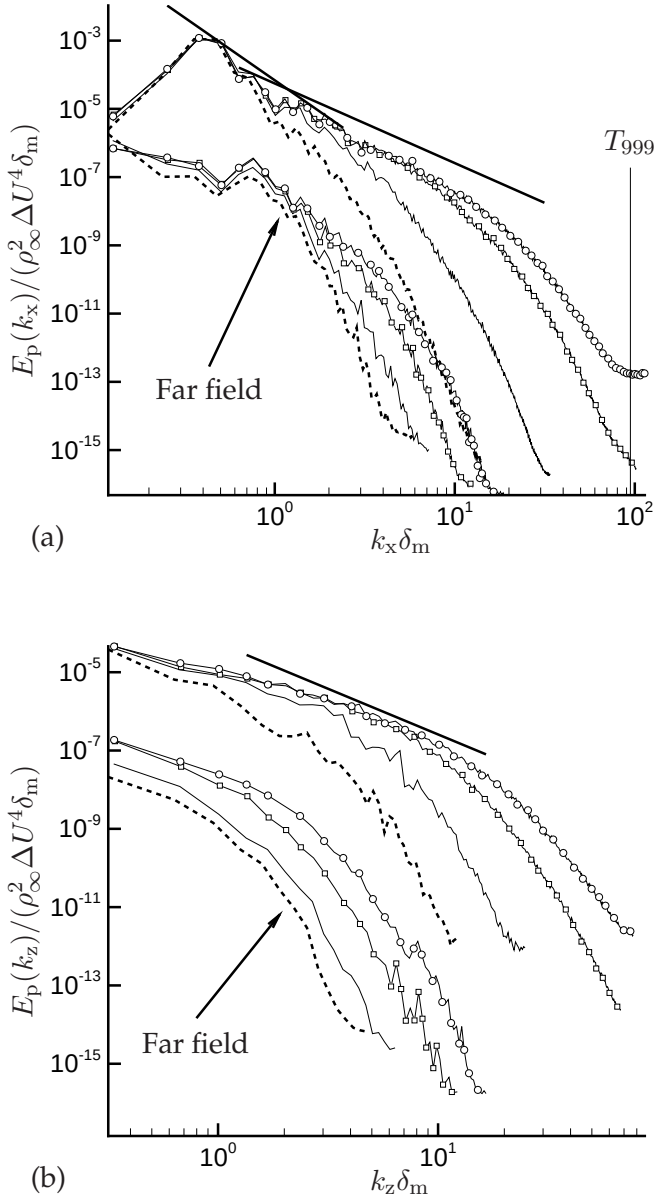

Figure 3.17: One-dimensional pressure spectra at $y = 0$ and $y = \pm 850\,\delta_{\rm m}^0$ (denoted as "Far field") scaled by the momentum thickness. (a) x-direction, with straight solid lines have slopes $-11/3$ and $-7/3$, and (b) z-direction with the straight solid line having slope $-7/3$. Curves indicate: ML1 - - - - ; ML2 —— ; ML3 - □ - ; and ML4 - ○ - .

the near-field spectra, especially for the ML3 and ML4 cases. Figure 3.17(b) shows the spanwise near- and far-field pressure spectra scaled by the layer momentum thickness. The far-field spectra decay in the same manner as the streamwise far-field spectra — well before the centerline spectra

decay. However, in contrast to the streamwise spectra, the spanwise spectra do not collapse in any region of wavenumbers when scaled by the layer thickness.

The narrow character of the far-field spectra compared to the source spectra in the near field at $y = 0$ is expected from the acoustic analogy of Lighthill.[7] It is well known that only components of the source with streamwise supersonic phase velocity are capable of radiating to the far field.[9,61–63] The radiation-capable portion of a $k - \omega$ plane and the turbulence spectrum in this same plane is expected of itself to limit the radiation to the far field, effectively narrowing the far-field spectra.

Figure 3.18(a) shows the streamwise pressure spectra scaled by the Taylor microscale, λ_x. The near-field spectra in the streamwise direction collapse in a similar manner as the energy spectra. ML3 and ML4 scale together for a decade in wavenumber. The far-field spectra show that all the spectra are moved together for the ML3 and ML4 cases over almost the entire spectrum except at the lowest wavenumbers, where it scaled well with the layer momentum thickness. The lower-Reynolds-number cases do not collapse with the higher cases. The centerline spanwise spectra in Fig. 3.18(b) show the ML3 and ML4 cases collapsing in a similar fashion as the streamwise. The maximum values of the spanwise Taylor Reynolds number Re_{λ_z} are reported in Table 3.2 and are all 1.5–2 times smaller than their streamwise counterparts. However, the ML2 case in the spanwise direction also collapses well with the higher-Reynolds-number simulations.

The near- and far-field pressure spectra scaled by the Kolmogorov length are shown in Fig. 3.19. The streamwise spectra at both locations show no collapse of the curves in the far field and ML3 and ML4 collapse for a small range near $k_x\eta \approx 10^{-1}$. The spanwise centerline spectra scale with the Kolmogorov length over the wavenumber range shown in Fig. 3.19, but in the far field only ML3 and ML4 collapse.

3.3.8 Far-field Frequency Spectra

It is, of course, challenging to compute frequency spectra for time-developing flows, but the time spectra show essentially the same behavior as the wavenumber spectra. Far-field frequency spectra of the four mixing layers at $y = -850\,\delta_m^0$ are presented in Fig. 3.20. To compute the spectra the time series of pressure data between $t = 765\,\delta_m^0/\Delta U$ and $t = 2970\,\delta_m^0/\Delta U$ was used. These

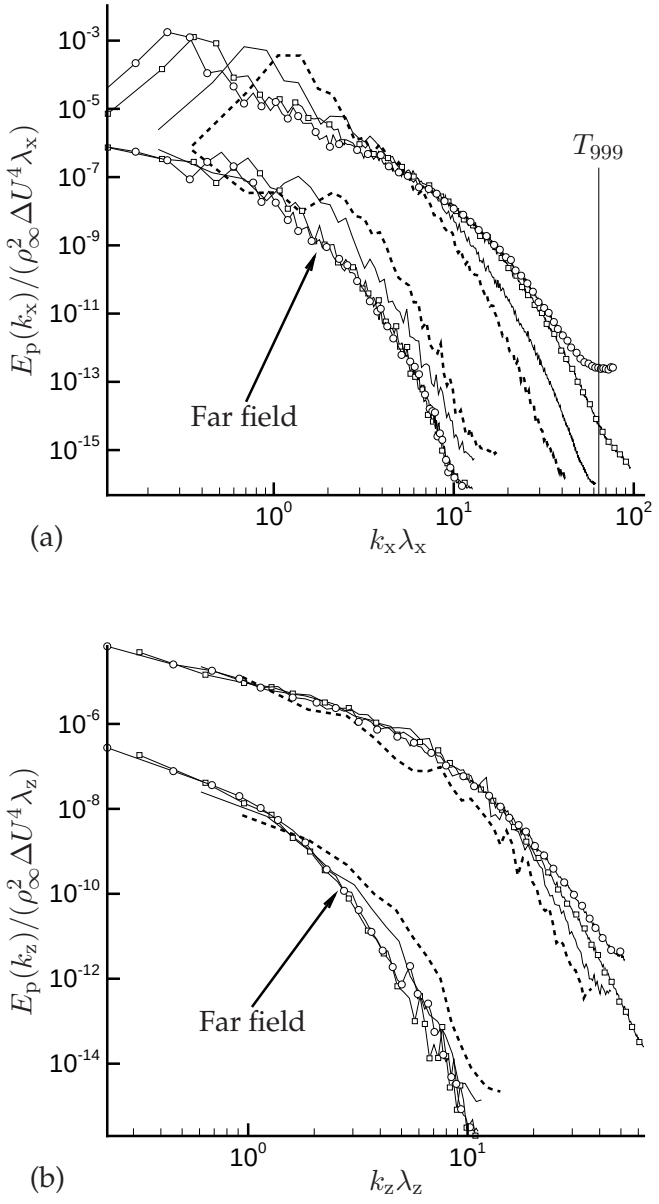

Figure 3.18: One-dimensional pressure spectra at $y = 0$ and at $y = \pm 850\,\delta_{\rm m}^0$: (a) x-direction scaled by the streamwise Taylor microscale $\lambda_{\rm x}$, and (b) z-direction scaled by the spanwise Taylor microscale $\lambda_{\rm z}$. Curves indicate: ML1 - - - - ; ML2 —— ; ML3 - □ - ; and ML4 - ○ - .

times corresponded to slightly after pressure fluctuations from the initial field of the mixing layers reached the $y = -850\,\delta_{\rm m}^0$ plane and to the end of the data set, respectively. Spectra were calculated at every sixth data point in x and every other data point in z, averaged together, and binned to

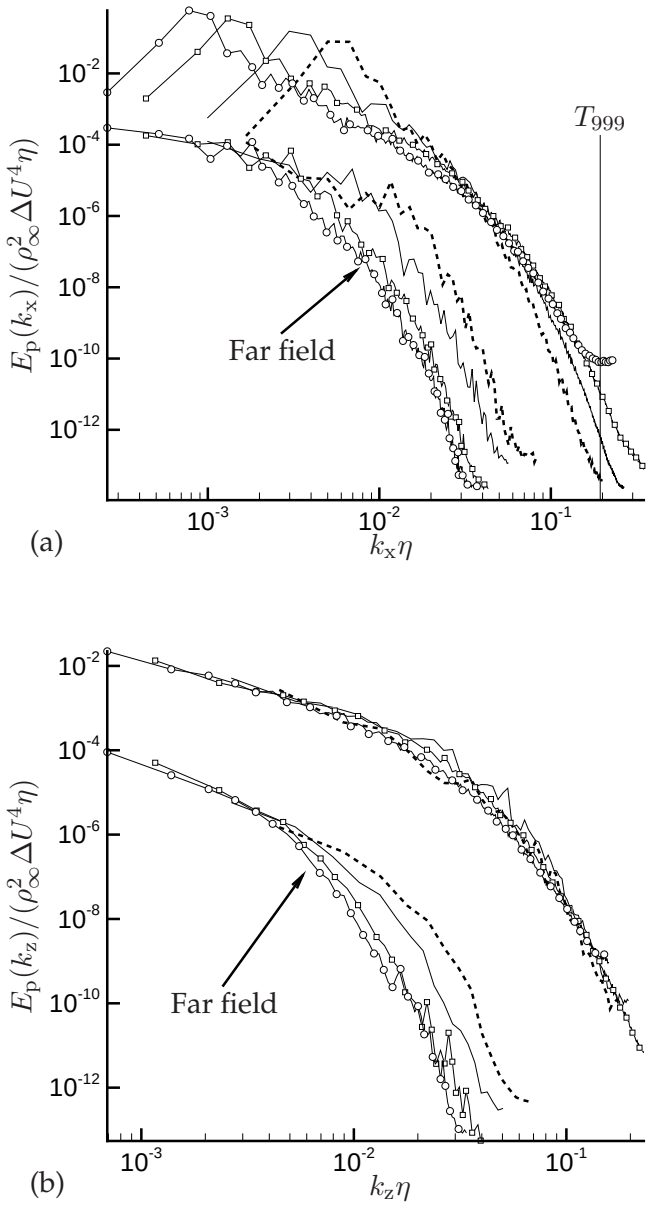

Figure 3.19: One-dimensional pressure spectra at $y = 0$ and at $y = \pm 850\,\delta_{\rm m}^0$: (a) x-direction and (b) z-direction scaled by the Kolmogorov scale, η. Curves indicate: ML1 - - - - ; ML2 —— ; ML3 -▫-; and ML4 -○-.

create the $1/3$-octave averaged spectra shown. The mean pressure was subtracted and the data was windowed with a Bartlett (triangle) function before Fourier transforms were carried out since the time data is not periodic.

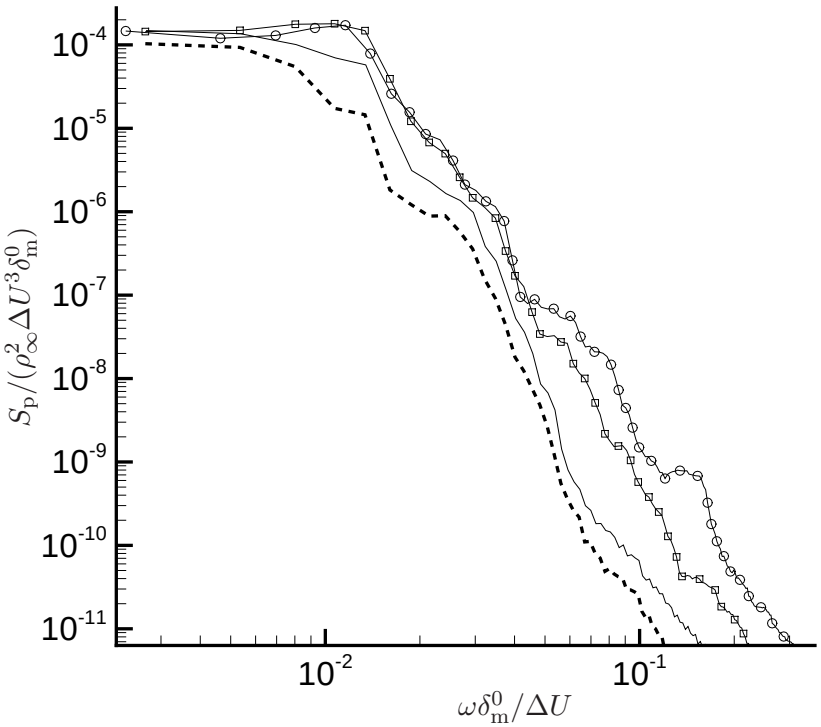

Figure 3.20: $1/3$-octave frequency spectra at $y = -850\,\delta_{\rm m}^0$. Curves indicate: ML1 - - - - ; ML2 ——— ; ML3 - □ - ; and ML4 - ○ - .

All of the mixing layers have a broad band of frequencies, but similar magnitude only in the lowest frequencies, with ML3 and ML4 being almost identical. A rapid decay is seen after $\omega = 0.01\Delta U/\delta_{\rm m}^0$ especially in the low Reynolds number cases. ML3 and ML4 follow each other closely until about $\omega = 0.04\Delta U/\delta_{\rm m}^0$, where both have decayed three decades. That the simulations are similar in the lowest frequencies confirms that their shared turbulence scales, namely the largest scales, are responsible for the majority of the sound emission. For ML3 and ML4, the addition of the smaller scales appears to only affect frequencies above $\omega = 0.04\Delta U/\delta_{\rm m}^0$ at magnitudes significantly below the levels of the lower frequencies. The trend is more evident when comparing ML1 and ML2 to the higher-Reynolds-number simulations at higher frequencies.

3.3.9 Pressure Wave Attenuation

It is important to establish that it is not dissipation of acoustic waves that affects the spectra in the acoustic region. Pressure waves are attenuated as they travel from their source due to the effects of viscosity. The extent of the dissipation is related to the distance the waves have traveled, the frequency/wavenumber of the disturbances, and the properties of the fluid. Based on the standard estimates,[64,65] the pressure spectrum of a plane wave propagating in the $+y$ direction with frequency ω and wavenumber k at a distance y from some reference point decays by the classical attenuation factor

$$\alpha_{\mathrm{cl}} = -\frac{\mu_\infty}{\rho_\infty}\frac{\omega^2}{c_\infty^3}\left(\frac{4}{3} - \frac{\gamma - 1}{\mathrm{Pr}}\right). \tag{3.11}$$

The percentage of attenuation due to α_{cl} along with far-field streamwise pressure spectra of the four mixing layers are shown in Fig. 3.21.

The attentuation factor does not reach a significant magnitude until after the far-field pressure spectrum of each mixing layer has decayed significantly. At eight decades below their respective peaks, the four mixing layers have attenuations of around 60%, 50%, 40%, and 40% for ML1, ML2, ML3, and ML4, respectively. The inset of Fig. 3.21 shows a closer view of the far-field spectra, E_{p}, and $E_{\mathrm{p}}/\exp\left[-\alpha_{\mathrm{cl}}\, y\right]$ at high wavenumbers. The four spectra separate only slightly in this range. If the waves had travelled a distance ten times longer than y_{b}, the attenuation four decades below the peak of the ML4 spectra would still only be 50%.

In the analysis of the streamwise pressure spectra, the assumption was made that $\omega \approx k_{\mathrm{x}} c_\infty$ for simplicity. This was to show the effect of viscous dissipation on already presented spectra and because determining the full wavenumber is difficult in this situation. The same analysis can be done using (3.11) without the k_{x} approximation for the frequency spectra in §3.3.8. Figure 3.22 shows the results of comparing the attenuated frequency spectra with the spectra originally shown in Fig. 3.20. When comparing with the streamwise wavenumber spectra, the attenuation is less pronounced for most of the frequency range included in the analysis. Near six decades below the peak of the frequency spectra, the attenuation is less than 20% for all of the mixing layers. Based on these results, we conclude that the attenuation due to viscous effects on the wavenumber

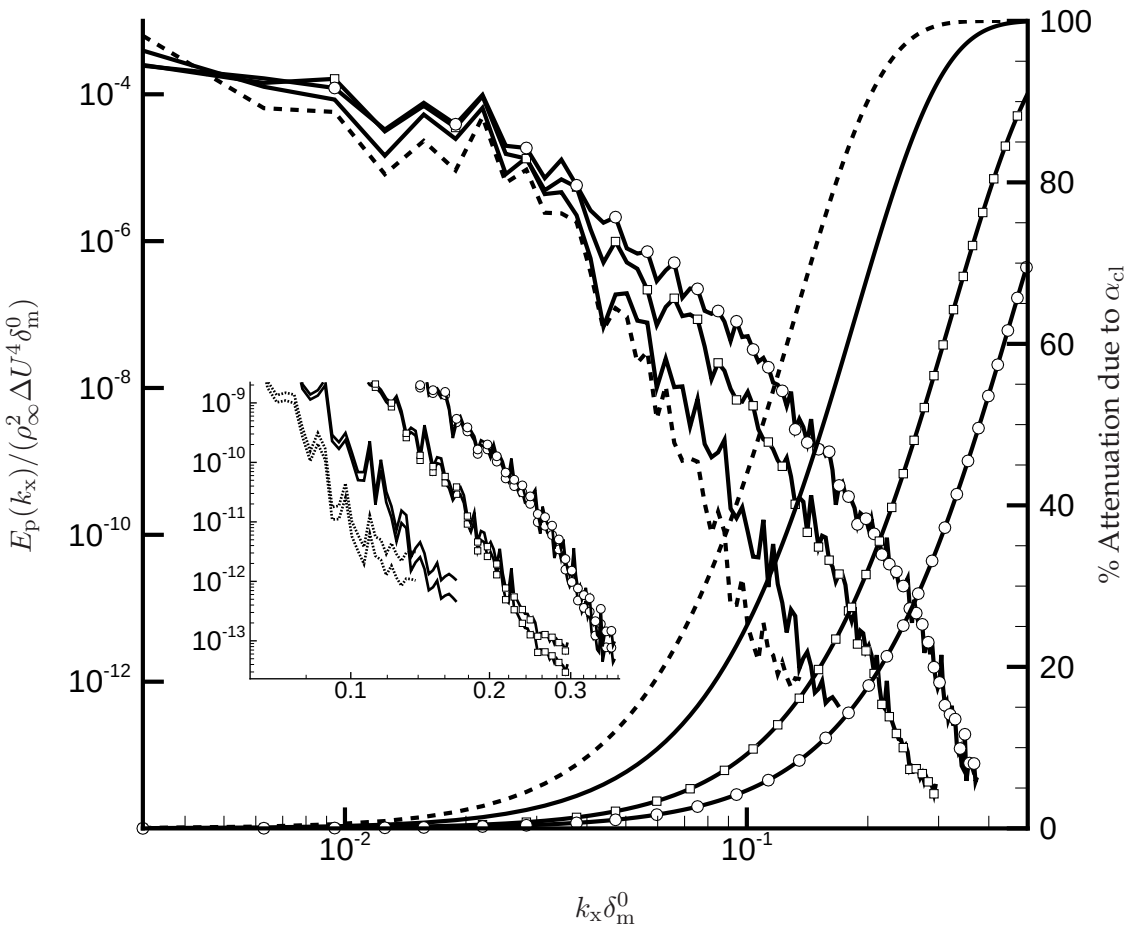

Figure 3.21: One-dimensional streamwise pressure spectra at $y = -850\,\delta_{\rm m}^0$ and the percentage of attenuation as a function of streamwise wavenumber. Inset: one-dimensional streamwise pressure spectra at $y_{\rm b}$ zoomed in on the high wavenumber region. Spectra corrected by the attenuation factor, $\alpha_{\rm cl}$, are plotted along with the original data. Curves indicate: ML1 - - - - ; ML2 —— ; ML3 -▫-; and ML4 -○-, with similar convention for $\alpha_{\rm cl}$.

and frequency ranges of interest at $|y| = 850\,\delta_{\rm m}^0$ for all of the mixing layers does not alter the conclusions of the previous sections.

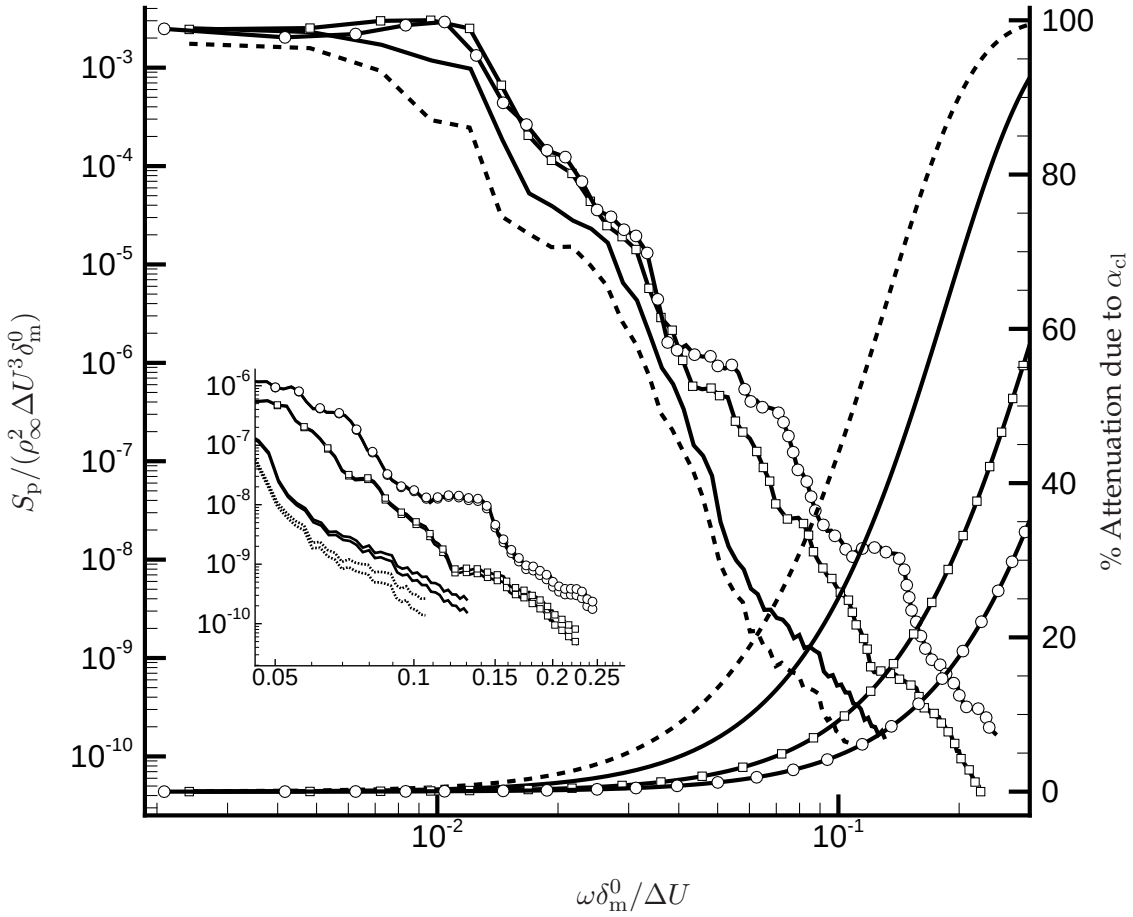

Figure 3.22: Frequency spectra at $y = -850\,\delta_{\rm m}^0$ and the percentage of attenuation as a function of frequency. Inset: frequency spectra at $y_{\rm b}$ zoomed in on the high frequency region. Spectra corrected by the attenuation factor, $\alpha_{\rm cl}$, are plotted along with the original data. Curves indicate: ML1 - - - - ; ML2 —— ; ML3 - □ - ; and ML4 - ○ - , with similar convention for $\alpha_{\rm cl}$.

3.3.10 Acoustic Power and Energy

The net radiated acoustic power (area-integrated acoustic intensity) is defined as

$$\mathcal{P}(t) = \frac{1}{\rho_\infty c_\infty}\int_0^{L_z}\int_0^{L_x}[p(x,y_{\rm b},z,t)-\overline{p}(y_{\rm b},t)]^2\,{\rm d}x\,{\rm d}z, \tag{3.12}$$

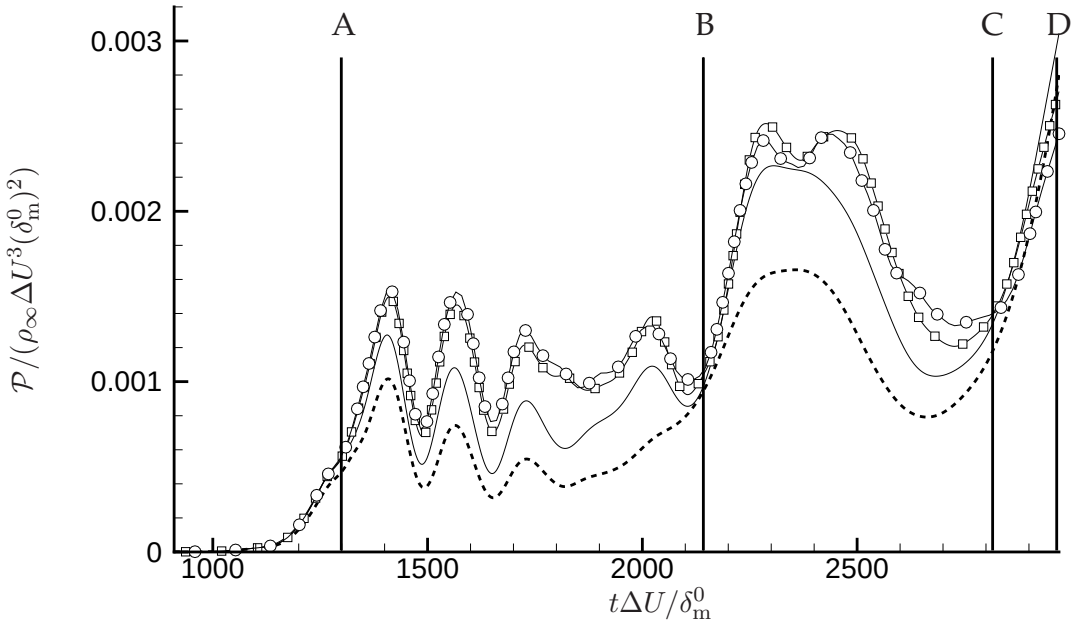

Figure 3.23: Acoustic power $\mathcal{P}(t)$ at $y = y_{\rm b}$. The vertical lines correspond to the times where acoustic energy is compared via (3.13). Curves indicate: ML1 - - - - ; ML2 —— ; ML3 -▫-; and ML4 -○-.

where $y_{\rm b} = \pm 850\,\delta^0_{\rm m}$, the location of the far-field spectra calculated in §3.3.7. The curves of $\mathcal{P}(t)$ at $y = -850\,\delta^0_{\rm m}$ and $y = 850\,\delta^0_{\rm m}$ have been averaged together and are shown in Fig. 3.23. As smaller scales are introduced to the flow by increasing the Reynolds number, the net effect on the acoustic power is minimal. The curves of $\mathcal{P}(t)$ are coincident at the beginning due to all of the mixing layers being started from the same initial condition. As the Reynolds number is doubled from ML1 to ML2, there is a marked increase in $\mathcal{P}(t)$. ML1's contribution follows the same trends as the other three layers at a lower magnitude, but near the end of the time series joins the other curves. At $t = 2810\,\delta^0_{\rm m}/\Delta U$ where the ML1 curve joins the others, $\mathrm{Re}_{\delta_m} = 215$ for ML1, which is near the initial value of ML3 (see Table 3.2). The same trend is true for ML2, which initially is far from the almost coincident ML3 and ML4 curves, but joins them in almost half the time as ML1. The doubling of Reynolds number from ML3 to ML4 has little effect on the values of $\mathcal{P}(t)$.

	$\mathcal{E}_{\mathrm{A}\to\mathrm{D}}$	$\mathcal{E}_{\mathrm{B}\to\mathrm{D}}$	$\mathcal{E}_{\mathrm{C}\to\mathrm{D}}$
ML1	1.596	1.102	0.278
ML2	2.110	1.412	0.312
ML3	2.458	1.557	0.299
ML4	2.480	1.538	0.274

Table 3.3: Net acoustic energy $\mathcal{E}$ between labeled points A, B, C, and D in Fig. 3.23.

To quantify this result further, integrating with respect to time gives

$$\mathcal{E}_{\mathrm{A}\to\mathrm{B}} = \int_{t=\mathrm{A}}^{t=\mathrm{B}} \mathcal{P}(t)\mathrm{d}t, \tag{3.13}$$

the total average acoustic energy through the $y_b = \pm 850\,\delta^0_{\mathrm{m}}$ planes over the time horizon of the four simulations. Four points of interest in the time series are marked in Fig. 3.23. Point A is the approximate location where the four curves begin to "forget" the initial condition ($t = 1295\,\delta^0_{\mathrm{m}}/\Delta U$). Point B is the location where ML2's curve joins ML3 and ML4 ($t = 2140\,\delta^0_{\mathrm{m}}/\Delta U$). Point C is the location where the same happens for ML1 ($t = 2810\,\delta^0_{\mathrm{m}}/\Delta U$), and point D marks the end of the time series ($t = 2970\,\delta^0_{\mathrm{m}}/\Delta U$). Table 3.3 shows the results of integrating between points A→D, B→D, and C→D.

The integration from A→D shows that ML3 and ML4 have equivalent $\mathcal{E}$ despite showing minor visual differences in $\mathcal{P}(t)$ in Fig. 3.23. This suggests that the additional small scales included in ML4 had little contribution to the net acoustic energy radiated. As ML2 grows in time and reaches a Reynolds number similar to the initial Reynolds number of ML3 at point B, the results of the integration from B→D show ML2 being roughly the same despite differences in the curves of $\mathcal{P}(t)$. From C→D, where all of the curves lie near each other, the integrations shows similar values of energy for each mixing layer. For $\mathrm{Re}_{\delta_{\mathrm{m}}} \gtrsim 300$, all four mixing layers seem to radiate the same net acoustic energy.

3.3.11 The Role of Vortex Pairing

An interesting behavior of the radiated acoustic power in Fig. 3.23 arises which may be related to the large scales in the shear layer. The existence of sharp peaks and valleys at various points

in $\mathcal{P}(t)$ may suggest that the merging of specific events are responsible for the spikes of radiated acoustic power. There have been several studies devoted to investigating the noise due to vortex pairing in free shear flows.[8,66–68] It is believed that a connection exists between the radiated noise and the action of vortices rolling up and pairing. In these studies, the radiated sound is usually produced by flows which were forced with a single frequency or harmonically excited throughout. Although the mixing layers presented here were initially forced with sinusoidal disturbances, any resemblance of the flow structures to the initial condition had disappeared by $t = 540\,\delta^0_{\mathrm{m}}/\Delta U$, the beginning of the time series considered. There have also been investigations of roll-up and pairing noise from two-dimensional[53] and three-dimensional[54] temporally-developing mixing layers. However, the radiated noise in these simulations may be contaminated due to small streamwise domains (see the discussion in §3.1.2 and Appendix A), which restrict the range of wavelengths that may radiate and little to no evidence is given that the noise is directly related to pairing.

A recent noise control study is also relevant to vortex pairing generated noise.[28] A randomly-excited two-dimensional mixing layer was controlled via adjoint-based optimization and the radiated noise in a region of the far field was reduced by over 90% compared to the uncontrolled case. Comparison of the large structures using the same method as presented below showed that the control dramatically reduces the sound without suppressing pairing or altering the vortex structure fundamentally. The simulations presented in the current work, although three-dimensional, are expected to bear a closer resemblance to the randomly-excited case than the previously mentioned harmonically-driven studies since no harmonic (or otherwise) forcing is done and the turbulent nature of the flow is inherently random.

To investigate the possible connection of vortex pairing to radiated noise, we present Fig. 3.24, which shows the net radiated acoustic power (as in Fig. 3.23) of the four mixing layers in the far field. Time intervals over which significant peaks in acoustic power occur are shaded with gray and labeled as t_{p_1} through t_{p_5} and are listed in Table 3.4. The width of the intervals was determined by taking the time at which the midpoint peak-to-valley value of $\mathcal{P}(t)$ occurred for the ML3 simulation. When a value could not be taken from the data, such as with the left side of the peak in t_{p_1}, the value on the other side of the peak was chosen. The fifth time interval, t_{p_5}, was included since another spike in acoustic power appeared to be approaching at the end of the time

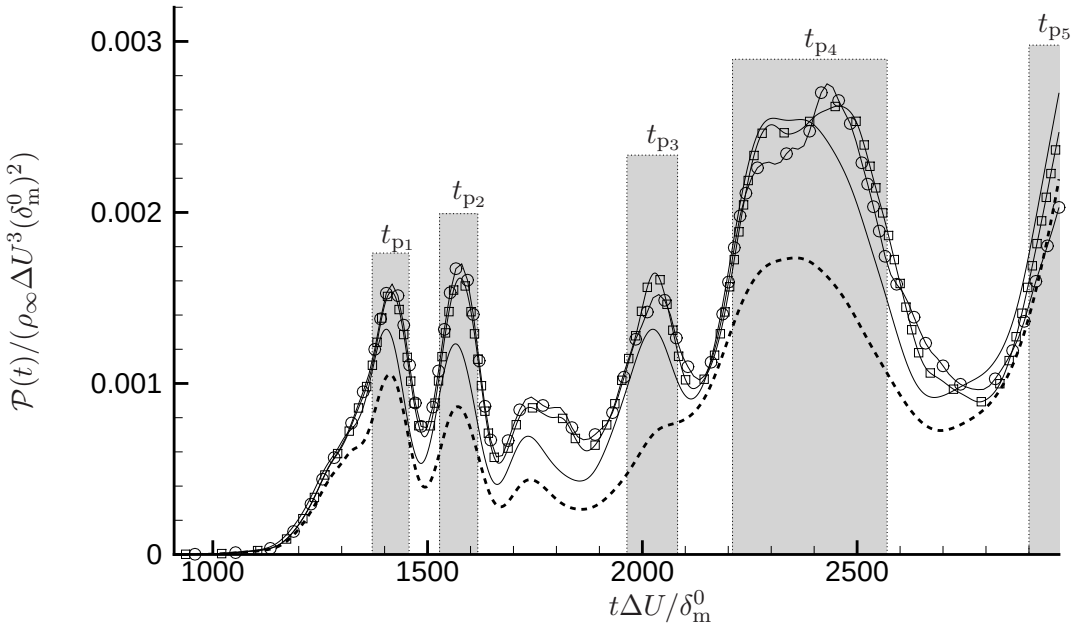

Figure 3.24: Acoustic power $\mathcal{P}(t)$. Time intervals surrounding five peaks of acoustic power are shaded in gray (see Table 3.4 for times). Curves indicate: ML1 - - - - ; ML2 —— ; ML3 - □ - ; and ML4 - ○ - .

Time Interval	Start – End @ $y_{\rm b}$	Start – End @ $y = 0$
$t_{\rm p1}$	1371–1455	521– 605
$t_{\rm p2}$	1528–1617	678– 767
$t_{\rm p3}$	1967–2082	1114–1232
$t_{\rm p4}$	2210–2570	1360–1720
$t_{\rm p5}$	2900–2970	2050–2120

Table 3.4: Nondimensional time intervals shown shaded in gray in Fig. 3.24 at $y_{\rm b}$ and propagation-adjusted time intervals in Figs. 3.25, 3.26 and 3.28.

series of the data at $y_{\rm b} = -850\,\delta^0_{\rm m}$. The end of $t_{\rm p5}$ occurs at the end of the time series. Differences in the shape of $\mathcal{P}(t)$ between mixing layers make the width of the time intervals around each peak only an approximation to when pairing events may have occurred. All four mixing layers show significant peaks during these time intervals with the exception of ML1 at $t_{\rm p3}$, where $\mathcal{P}(t)$ is increasing until the $t_{\rm p4}$ interval.

To compare the acoustic power at $y_{\rm b}$ with the near-field vortical structures, we present in Fig. 3.25 the pressure fluctuations associated with large structures at $y = z = 0$ for the time history

of the four mixing layers. The black areas in Fig. 3.25 represent low pressure regions and vortex merging occurs when branches converge. Also shown are the time intervals (shaded in gray) corresponding to t_{p_1} through t_{p_5} in Fig. 3.24. These time intervals are also listed in Table 3.4. The times of the intervals are adjusted for propagation time of a sound wave traveling on a direct path (in the cross-stream direction) from the centerline to y_{b}. This adjustment represents the shortest path that a sound wave generated at $y = 0$ could take in order to contribute to $\mathcal{P}(t)$ and does not take into account waves that do not propagate purely in the y direction. The width of the time intervals around the peaks of $\mathcal{P}(t)$ relaxes this restriction.

Over the first time interval, t_{p_1}, all four mixing layers show pairing events in Fig. 3.25. This result may be suspect since the beginning of t_{p_1} adjusted for propagation time occurs before $t = 540\,\delta^0_{\mathrm{m}}/\Delta U$, the time when the initial condition given of ML3 was used to start ML1, ML2, and ML4. Interval t_{p_2} is far enough after the initial condition and pairings are seen in all mixing layers. ML3 and ML4 show delayed pairings (compared to pairings at similar locations in ML1 and ML2) at $x = 1888\,\delta^0_{\mathrm{m}}$ and $x = 362\,\delta^0_{\mathrm{m}}$ which happen slightly before and after t_{p_2}, respectively. ML1 has a pairing at the very end or slightly after t_{p_3}, but the other three mixing layers show two delayed pairings just afterwards between t_{p_3} and t_{p_4}. The most distinct peak in $\mathcal{P}(t)$ occurs during t_{p_4} and two pairing events are seen in the ML3 and ML4 mixing layers. No pairings are present in ML1 and ML2 during t_{p_4} despite ML2 having $\mathcal{P}(t)$ values similar to ML3 during this time and ML1 showing a large increase to its peak as well. Instead, Fig. 3.25 shows black "finger" regions which abruptly stop without converging with another branch. These "fingers" occur when a structure has moved out of the $z = 0$ plane or has been raised or lifted from the $y = 0$ plane during the course of roll-up. Viewing the pressure fluctuations at $z = L_{\mathrm{z}}/2$ in Fig. 3.26 reveals that pairing does happen for both ML1 and ML2 during t_{p_4}. Figure 3.26 also provides evidence of several pairing events not shown at $z = 0$ in Fig. 3.25 during t_{p_3}. Finally, the pressure fluctuations at both z-locations reveal the merging of four main structures into three shortly after the last time interval, t_{p_5}. It seems reasonable to conclude that, if the large increase in $\mathcal{P}(t)$ during t_{p_5} is due to vortex pairing, this large pairing which is soon to come in addition to the pairings seen shortly before and during t_{p_5} is responsible.

While it would appear that many pairing events correspond to the peaks in $\mathcal{P}(t)$ associated

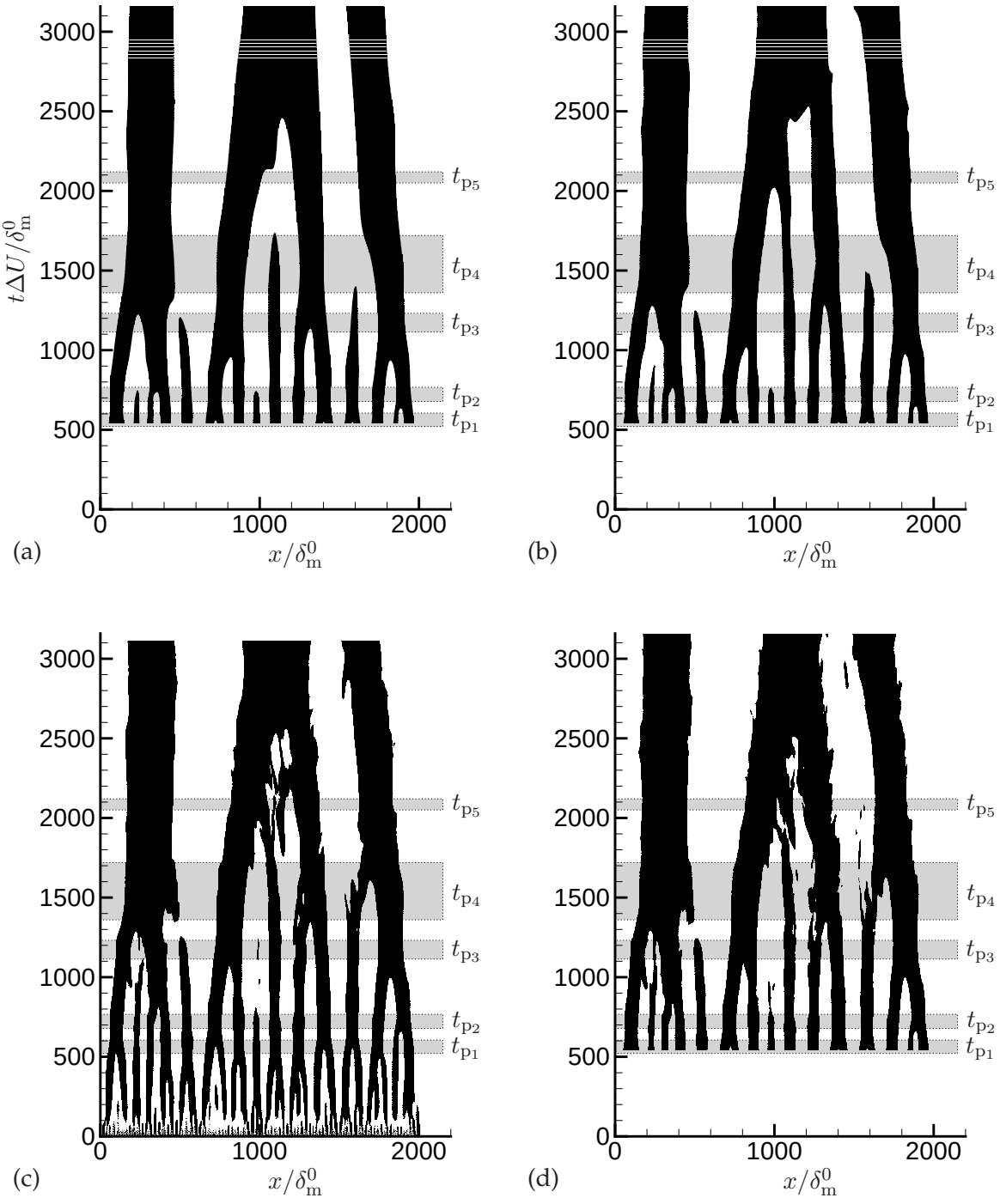

Figure 3.25: Pressure evolution at $y = z = 0$ of the (a) ML1, (b) ML2, (c) ML3 and (d) ML4 mixing layers. Propagation-time adjusted time intervals (see Table 3.4) surrounding peaks of acoustic power (t_{p_1} through t_{p_5}) in Fig. 3.24 are shaded in gray. Black denotes $(p - p_\infty)/(\rho_\infty \Delta U^2) < 0$ and white $(p - p_\infty)/(\rho_\infty \Delta U^2) > 0$.

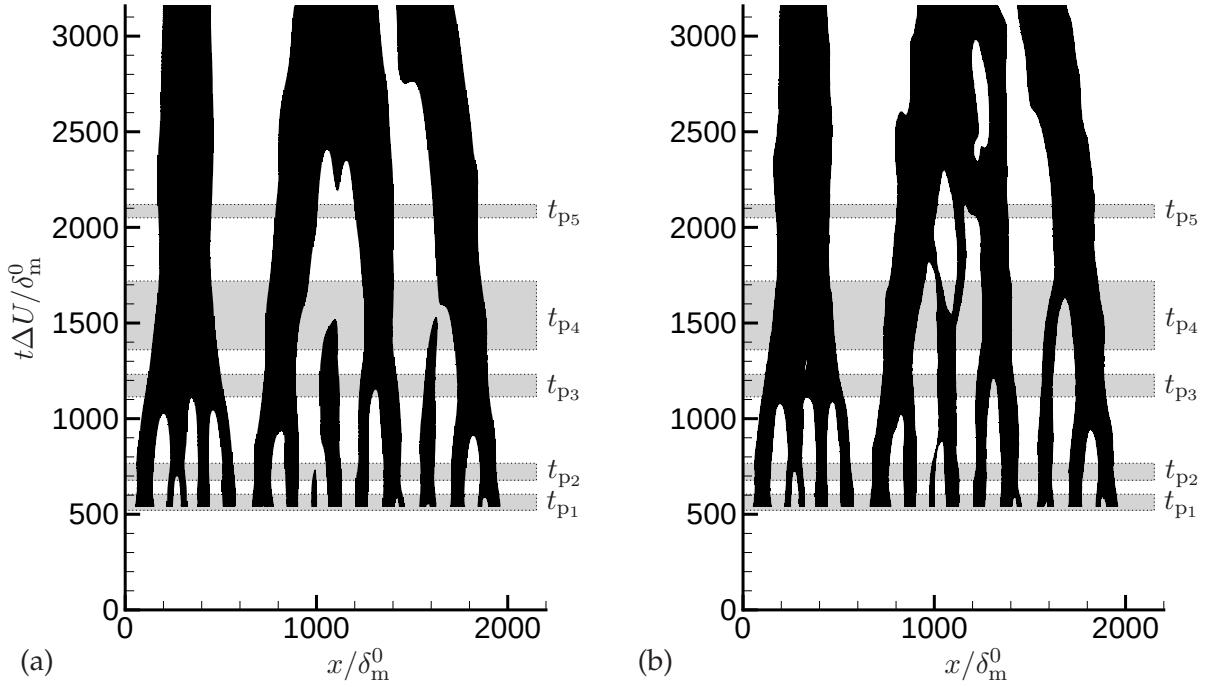

Figure 3.26: Pressure evolution at $y = 0$ and $z = L_z/2$ of the (a) ML1 and (b) ML2 mixing layers. Propagation-time adjusted time intervals (see Table 3.4) surrounding peaks of acoustic power (t_{p_1} through t_{p_5}) in Fig. 3.24 are shaded in gray. Black denotes $(p - p_\infty)/(\rho_\infty \Delta U^2) < 0$ and white $(p - p_\infty)/(\rho_\infty \Delta U^2) > 0$.

with the time intervals t_{p_1} through t_{p_5}, there are just as many instances for which the opposite is true. Of course, adjusting the time intervals to include more of the peaks in Fig. 3.24 captures more pairing events, but again does not account for all pairings. A view of the pressure evolution data in Figs. 3.25 and 3.26 at only these two spanwise locations reveals the complex three-dimensional structure of the pairing and merging vortices in the shear region. This situation further complicates the ability to connect a pairing event with a spike in acoustic power in the far field, a feat which appears to be difficult in two dimensions as well.

Another qualitative investigation can be done by viewing the pressure perturbations at y_{b} to see if evidence of pairing manifests itself in the far field. If pairings are significant contributors to the far-field sound, we would expected to see larger amplitudes and longer wavelengths in the far-field pressure as more vortical structures paired in the mixing layer. Figure 3.27 presents pressure traces (with the mean extracted) in the far field at $z = 0$ and $z = L_{\mathrm{z}}/2$ over the simulated times

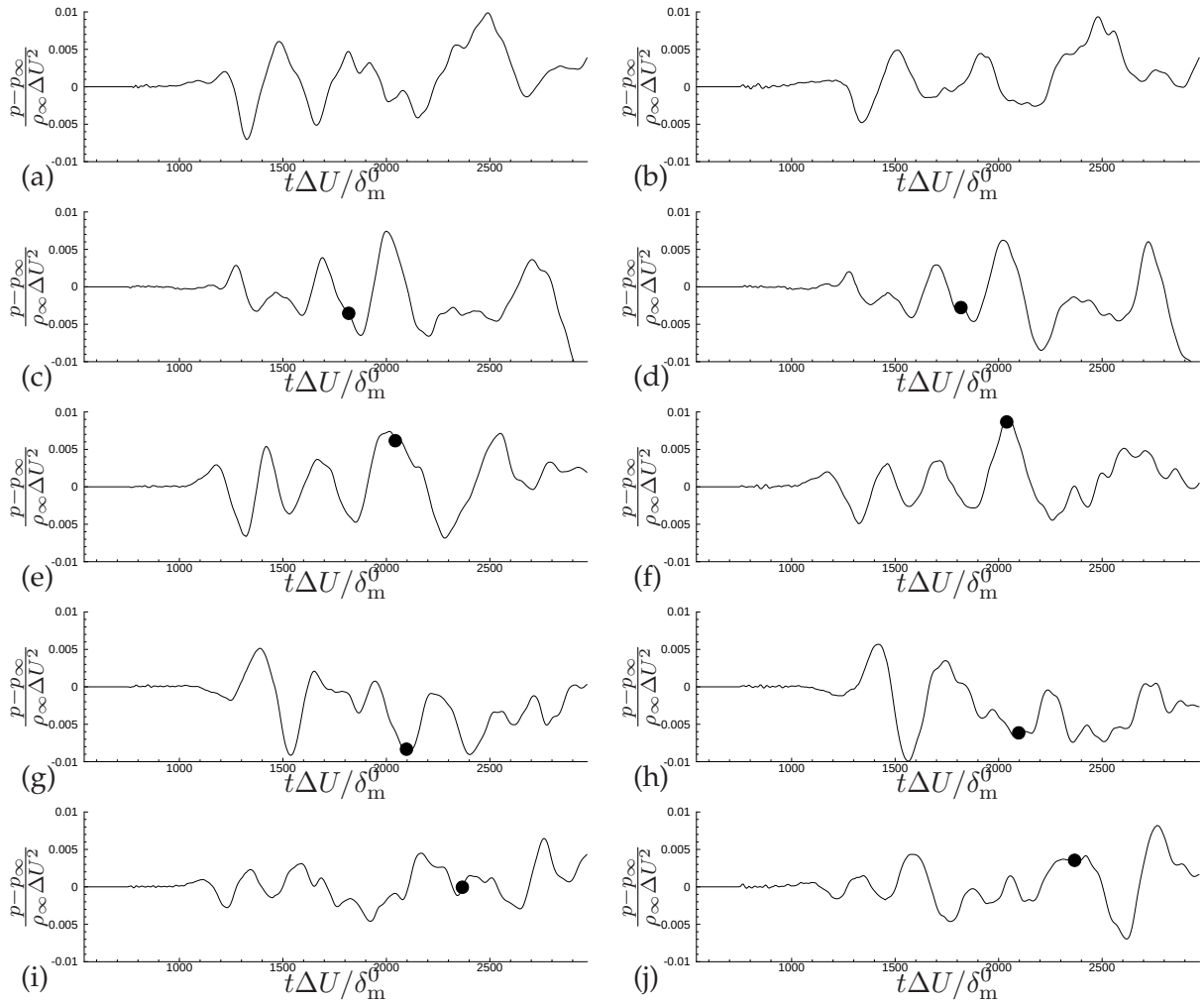

Figure 3.27: Pressure traces of ML3 taken at $y_{\rm b}$ at spanwise locations $z = 0$ (a, c, e, g, i) and $z = L_{\rm z}/2$ (b, d, f, h, j). (a-b): traces at $x = 0$, where no pairings take place; (c-d) traces at $x = 810\,\delta^0_{\rm m}$; (e-f) traces at $x = 230\,\delta^0_{\rm m}$; (g-h) traces at $x = 1320\,\delta^0_{\rm m}$; (i-j) traces at $x = 1700\,\delta^0_{\rm m}$. Black dots denote the propagation-time adjusted times when a pairing event occurred at $y = 0$ (see Fig. 3.25(c)).

of ML3 at five specifically chosen streamwise locations. The first location chosen was located at $x = 0$, where it is evident from Fig. 3.25(c) that no pairings occur over the time of the simulation. The following four locations were chosen such that a pairing occurred at each streamwise location, and the black dot corresponds to the earliest propagation-time adjusted time when the sound from each pairing could arrive. The pressure traces are presented such that the associated pairings occur at earlier times at the top of the Fig. 3.27 and later at the bottom.

As with the previous analysis comparing pairing events with peaks of $\mathcal{P}(t)$, their comparison

with the raw pressure data is ambiguous. The pressure traces in Fig. 3.27(c), (d), (e), (f), and (j) seem to support connection to pairings as they show greater amplitudes and evidence of longer wavelengths that earlier in their respective time series. However, Fig. 3.27(g), (h), and (i) do not share these qualities. Figures 3.27(a) and (b), where no pairing event supposedly occurred, do show a possibility of pairing-related behavior, which they should not. This method of attempting to connect pairing to sound is less powerful than the previous analysis using $\mathcal{P}(t)$. The acoustic power, which was an integrated quantity over the streamwise and spanwise domains, should capture the general characteristics of at least the amplitude changes in the far field pressure better than simply viewing the pressure at certain locations. Still, this method does not appear to correlate vortex pairings with the radiated sound.

Another test was undertaken by simply counting the number of vortical structures (the number of black "branches" in Fig. 3.25) and comparing them with the peaks in acoustic power in Fig. 3.24. The results of this quantification of structures at $y = 0$ is shown in Fig. 3.28. We expect to see significant reductions in the number of structures as vortices pair during the gray-shaded time intervals if pairing events are indeed responsible for a significant portion of the noise in the far field.

Examining the data, the number of structures roughly follows a exponentially decreasing trend (note the logarithmic horizontal axis in Fig. 3.28) for all four mixing layers until t_{p_4} ($\sim 1500\,\delta^0_{\mathrm{m}}/\Delta U$). All four mixing layers have the same number of structures until the beginning of t_{p_2} where they diverge soon thereafter, suggesting as in Figs. 3.25 and 3.26 that the initial fields of ML1 and ML2 interpolated from the ML3 simulation have not been forgotten. It is evident from counting of the structures that pairing events occur during the highlighted time intervals and pairings do not happen during these times. Of particular note is the reduction in structures between t_{p_2} and t_{p_3} which do not appear to correspond to a peak in $\mathcal{P}(t)$. The similarities in the location of $\mathcal{P}(t)$ peaks between all four layers do not appear to correlate to similarities in pairing in this quantitative measure of the near-field structures. There also is a noticeable lead in the reduction of structures with time in ML1 over ML2 and ML3 and ML2 over ML3. This leading of pairing events in ML1 does not correspond to a leading of peaks of $\mathcal{P}(t)$ in the far field. All of the peaks during the intervals t_{p_1} through t_{p_5} are aligned in time.

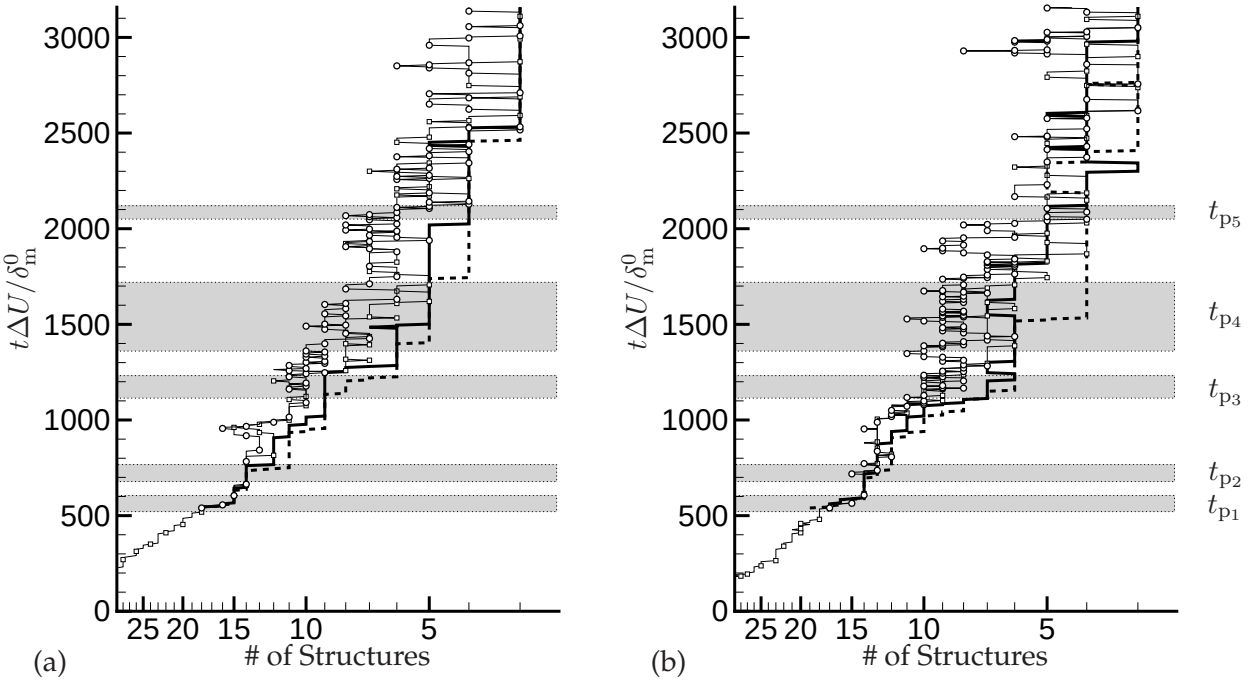

Figure 3.28: Number of black regions in Fig. 3.25 showing the progression of pairing events at (a) $y = z = 0$ and (b) $y = 0$, $z = L_{\mathrm{z}}/2$ in the ML1: - - - - , ML2: ——— , ML3:-▫-and ML4:-○-mixing layers. The horizontal axis is shown with a logarithmic scale. Propagation-time adjusted time intervals (see Table 3.4) surrounding peaks of acoustic power ($t_{\mathrm{p_1}}$ through $t_{\mathrm{p_5}}$) in Fig. 3.24 are shaded in gray.

In conclusion, we have presented three analyses of the connection between pairing events in the shear layers of the four simulations. Each analysis shows evidence that vortex pairing is not conclusive to firmly link these events to radiated sound. The simulations were not excited by any type of periodic forcing (or otherwise) which would allow for more educated guesses of when sound possibly created by a vortex pairing would arrive at a prescribed listening station. The inherent three-dimensionality of the flow also creates a significant hurdle for drawing definite connections without an involved visualization of the large structures in the shearing region. However, the general conclusion presented here suggests evidence in each of the three methods of analysis that does not link pairings to peaks of acoustic power. There appears to be no pairing pattern that corresponds to the fluctuations in radiated acoustic energy. The data does not lead to the conclusion or definite result that the peaks in far-field acoustic power are the result of

near-field vortex pairing events.

3.4 Discussion

The far-field sound is seen to have a streamwise wavenumber spectrum that is invariant to Reynolds number over the same range of wavenumbers as the near-field turbulence. Nearly all the radiated acoustic energy is in this range, which is consistent with Lighthill's statistical estimates of stress-tensor correlations.[69] Based on the net radiated power, more than 85 percent of the acoustic energy that would apprarently be radiated in the high-Reynolds-number limit is radiated for $\mathrm{Re}_{\delta_m} \gtrsim 300$. This result suggests that there should be a low burden in large-eddy simulations to represent noise from turbulence scales that are not explicitly represented, though any importance weighting of the spectrum such as for gauging annoyance could, of course, complicate this conclusion. This is also consistent with the conclusions of Bodony & Lele[45] deduced from the relative success of large-eddy simulations. They conclude that the fidelity of the radiated sound prediction is most dependent upon representing the locally largest turbulence scales near the nozzle. The frequency spectra we were able to estimate for the non-stationary flow suggest a similar behavior. In contrast to large-eddy simulation, modeling approaches that require assumptions about the statistical properties of the turbulence (e.g. isotropic, homogeneous,[70] axisymmetric[71]) will be most challenged by the need to model the statistics of the largest scales, which are never universal.

Interestingly, the spanwise structure of the sound field does not show a similar collaps of low wavenumbers despite the low wavenumber Reynolds number insensitivity of the spanwise spectra in the near field. This is consistent with the notion that the largest, instability wave structures in the flow radiate in a special fashion as they propagate downstream. This line of thinking is the basis for the designation of the more peaked empirical sound spectrum component as being associated with the large turbulence structures[14] and consistent with detailed analysis of the role of instabilities in generating far-field sound.[41] In simple analytical models, instability wave structures can have a highly downstream directive (so-called superdirective) character.[72] This type of directivity and near-field sources have been educed via spectral analysis of low-Reynolds-number

jet turbulence.[9]

The spectra for the Reynolds-number-sensitive higher wavenumbers of the streamwise spectra and all the wavenumbers for the spanwise spectra collapse reasonably well with the turbulence microscale scaling. This suggests that only this low-energy part of the sound derives from scales smaller than the most energetic. Though the acoustic energy in this range is much less than the spectral peaks, it could conceivably be important in some cases when weighting the sound for human annoyance. The highest two Reynolds number mixing layers, both of which showed evidence of an inertial range, show better collapse of their spectra via this scaling. There is no evidence that viscosity itself directly affects any part of the radiated sound spectra.

3.5 Conclusions

Direct numerical simulation of the compressible Navier-Stokes equations was used to study the role of turbulence scale in sound generation. Four temporally-developing mixing layers with Reynolds numbers varying from 50 to 600 based on the velocity difference between the streams and the momentum thickness were simulated to model the near-nozzle initial shear layers of a jet. This approach allowed for the comparison of the sound fields of each mixing layer of flows that share the same large scales, but an increasing range of smaller turbulence scales. The far-field sound spectra and acoustic power show that most of the sound field is derived from the shared larger scales. The small scales (smaller than the Taylor microscale), if they make noise at all, do not contribute significantly to the far field.

One motivation for this work was to explore two hypotheses related to scale contribution and the observed two-component spectra. Using data from a vast collection of jet noise experiments, Tam *et al.*[39] generated two similarity spectra with different shapes and broad, overlapping frequency ranges. The authors attributed each spectrum individually to sound radiated by "large" and "fine" flow scales with the jet diameter being the delineating length scale.[73] The conclusions of the current study supply evidence that this interpretation is problematic since most of the sound appears to come from larger scales, that is, scales larger than the Taylor microscale.

On the other hand, Lighthill[69] suggested that *"...it is eddies of scales only slightly smaller than the main energy-bearing eddies that generate most of the acoustic radiation."* The far-field data presented here are compatible with his analysis and support the notion of the *locally* largest scale being the main noise contributer to the sound field. If this is true, one would expect that the locally largest scale is the most important for simulation using large eddy simulation, rather than absolute scales in any given flow. Since the near-nozzle shear layers are growing in space until reaching the potential core, it follows that one should expect to see higher frequencies near the nozzle and lower nearer to the potential core. The increasing locally largest scale will also be responsible for the observed breadth and broadbandedness of jet noise. Experiments in noise-source localization support these expectations.[26,43,44]

An obvious future extension to this work would be to conduct the same Reynolds number parameter study using spatially-developing mixing layers or round jets. Admittedly, the temporal simulations presented here are only a model of their spatial counterpart. A particular challenge associated with extending this study to a spatial flow is the non-locality in time which did not allow for frequency spectra to be computed directly. Therefore, far-field sound data was not able to be compared with experiments and simulations previously studied. Simulations of spatially-developing flows will allow for greater validation—especially of the sound field.

Spatial mixing layers are probably the better candidate for a next step for a scale contribution study since they will be less expensive to simulate than round jets and they remove the complications of the potential core as temporal mixing layer simulations do. However, several issues arise which were simplified due to the design of the simulations in this study. First, since spatial mixing layers are radiating a broad range of scales at any time instant due to the growth of the layer in the domain, it will be impossible to pinpoint the contribution from a particular turbulence scale. Still, varying the Reynolds number will allow for each simulation to include a progressively larger subset of scales as in this study. Second, spatial mixing layers must be provided with realistic streamwise inflow conditions upstream of the splitter plate (nozzle exit). This can be done by extending the upstream domain at great computational cost and allowing a boundary layer to form. An alternate method is to simulate auxillary temporal shear layers or boundary layers which are "fed" into the spatial compuatation's domain.[29,74] Another very popular method sim-

ilar to this but with spatially-developing generation capability is the rescaling/recycling method originally of Lund *et al.*[75] Most, if not all, of the computational tools necessary to go forward with a study of turbulence scale contribution using spatial mixing layers are currently in place.

Chapter 4

Numerical Modeling of Localized Arc-filament Plasma Actuators

4.1 Introduction

Passive controls involving geometry modification of the exit nozzle such as vortex generators (e.g. tabs and chevrons) have recently shown success in delaying flow separation[76] and reducing the radiated noise from jets.[19–22,77,78] However, these methods often introduce unacceptable drag or thrust penalties at certain flow conditions. Active control technologies for flow control such as fluidic-based actuators (synthetic or zero net-mass-flux jets) and plasma actuators by their time-dependent nature offer the promise of increased control authority with a reduction in the adverse effects at these conditions.[79,80] Recent work on the development and characterization of plasma actuators has shown that they offer significant control authority, and provide an advantage over fluidic-based actuators by having no moving parts.[27]

Therefore, plasma actuation of different types are gaining in popularity and being considered for a wide range of flow control objectives. Dielectric barrier discharge (DBD),[81] DC and RF glow discharge,[82,83] and arc-filament discharge[27,80,84,85] plasmas are all being actively researched for applications in boundary layer separation control, shock wave control, noise mitigation, and shear-flow mixing enhancement. The primary mechanisms by which these types of plasmas interact with the flow make each type best suited for different control objectives in different flow regimes. For example, DBD actuators produce electrohydrodynamic interactions by accelerating charged molecules via a Coulomb force and in that way can locally accelerate a flow. This technology has been used effectively for boundary layer separation control in airfoils.[86]

However, it does not appear that DBD and glow discharge actuators have sufficient authority to force high-speed (near-sonic or above) flows such as a turbulent jet,[87] which is the topic of

interest in this work and a control objective in chapter 5. Arc-filament discharge actuators seem to be the better suited to this case. They are thought to generate pressure perturbations via rapid thermal (Joule) heating by the ionized gas established in their vicinity. This effect has been shown to be strong enough to produce shock waves and flow separation in supersonic boundary layers.[88] Arc-filament actuators have also demonstrated the capability to excite strongly amplified instabilities in high-speed jets,[27] making them a promising technology in aeroacoustic control and jet noise reduction.

The specific localized arc-filament plasma actuators (LAFPA) under consideration here are under continued development at The Ohio State University (OSU) by Professor M. Samimy and colleagues with the intent of controlling subsonic and supersonic jets[27] and cavity flows.[89] By targeting the instabilities in a jet, power requirements are relatively low, around 20 Watts average power (for each actuator) in laboratory jet experiments. LAFPA also have the advantage of being able to force at a wide range of frequencies: from a few Hz up to 200 kHz.[27] This flexibility and high control authority makes them potentially useful in a wide range of flow control applications. Depending on the forcing applied, the actuators have increased downstream mixing[27] and slightly reduced far-field noise relative to an unforced baseline jet.[90]

These successful demonstrations are highly encouraging, but it is still unclear how the LAFPA might be designed and used most effectively since the detailed mechanism by which they act on a flow remains unclear. Determining this mechanism is the primary motivation for this chapter. The generated plasma is known to quickly create a local high-temperature region, which is thought to be the root forcing mechanism.[27,85] What is not known is how this thermal source (an 'entropy mode' in a linear sense) alters the flow and drives the observed downstream response ('vorticity mode') in the jet's initial shear layers.

Experiments have suggested that the local geometry in the neighborhood of the plasma arc may be an important factor. In the OSU jet experiments the array of electrode pairs that create the plasma is recessed in a rectangular cross-section cavity near the nozzle outlet as represented by the schematic in Fig. 4.1. This cavity forms a ring-shaped groove around the inner circumference of the jet nozzle. It was added to stabilize the plasma by shielding it from the flow, which

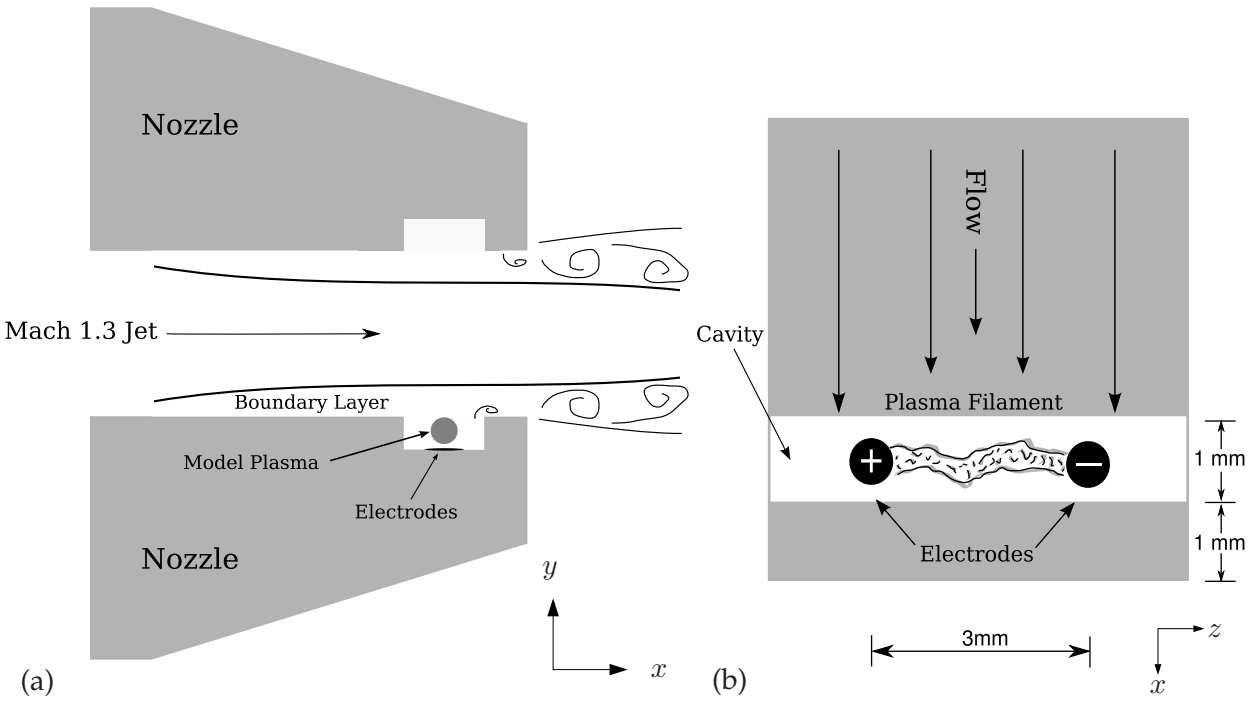

Figure 4.1: Drawings of the OSU Mach 1.3 jet nozzle exit region and the plasma actuator cavity geometry. (a) Side view of the nozzle exit showing the cavity in the near-nozzle exit region of the jet where the actuator model is implemented. (b) Top view (from the nozzle interior) of a planar representation of the cavity showing the actuator electrodes and mock-up of the arc-filament plasma within the cavity. The cavity is 0.5 mm deep, 1 mm wide, and situated 1 mm from the nozzle exit. Note: this schematic is not drawn to scale.

was observed to advect the plasma away from the electrodes. The flow caused a stretching and subsequent breakdown of the plasma filament that in turn weakened the downstream effects of the actuation on the jet flow.[84] It remains unclear what, if any, effect the cavity itself has on the interaction between the arc-filament discharge and the flow.

Experimental diagnostics of the actuation are difficult for several reasons. First, the plasma emits strong electromagnetic radiation that interferes with the electronic equipment that might be used to measure pressure in the vicinity of the cavity. Second, the relatively small dimensions of the nozzle and its exit region (see Fig. 4.1) compared to measuring equipment prohibits gathering information that could be gained via standard methods of flow visualization. Finally, the LAFPA system operates in a particularly harsh high-speed and high-temperature environment. Therefore, in this work we have designed a simulation model to supplement and extend the observations of

experiments to identify the forcing mechanisms leading to excitation of the flow downstream. This will facilitate future optimization and effective use of the LAFPA technology in a range of flow control applications, especially jet noise control.

Specifically, we have developed a simple numerical model of the plasma and implemented it in a high-fidelity compressible flow solver that includes the cavity and the near-nozzle shear layer of the jet. Our simulations of the near-nozzle region of a Mach 1.3 jet match the actuator geometry and the Reynolds number based upon the boundary layer momentum thickness of the OSU experiments. However, at present the model is two dimensional, but includes some key elements of the actuation; a more realistic fully three-dimensional simulation at the jet Reynolds number is prohibitively expensive using direct numerical simulation, though large-eddy simulations may be able to capture a realistic actuation response. Regardless, the key features of the flow are represented: the injection of thermal energy due to the plasma, the cavity, the nozzle edge, and the early development of the shear layer. Validation against multiple experimental observations support this. Variation of forcing and geometric parameters is then used to study the detailed mechanisms of the actuation.

The organization of this chapter is as follows. Details of the experimental parameters of the jet and the LAFPA system at OSU are given in §4.2. A full description of the numerical model of the LAFPA is described in §4.3. Simulation details and numerical methods used specifically for the simulation of the flow in this study are presented in §4.4.1 and §4.4.2, respectively. The results of the simulations are presented and discussed in §4.5 through §4.10. Finally, concluding remarks are given in §4.11.

4.2 Experimental Characterization of LAFPA

The LAFPA system is implemented on a high-speed, high-Reynolds-number jet in ongoing experiments at OSU. Relevant details of the flow facility and experimental conditions are described briefly here, but a full description is provided by Samimy *et al.*[27] The standard experiments consist of a Mach 1.3 axisymmetric jet with a Reynolds number of $\mathrm{Re_D} = 1.1 \times 10^6$ based on the jet

exit diameter $D_\mathrm{j} = 2.54$ cm and the jet centerline velocity. The jet is operated as near to an ideally expanded condition as possible.

A boron nitride nozzle extension attached to the nozzle houses the plasma actuators as shown schematically in Fig. 4.1(a). A rectangular cross-section groove of width $L_\mathrm{c} = 1$ mm and depth $D_\mathrm{c} = 0.5$ mm (an aspect ratio of $L_\mathrm{c}/D_\mathrm{c} = 2$) is machined into the nozzle extension 1 mm upstream of the exit. The plasma is generated between two high-voltage steel or tungsten pin electrodes spaced 3 mm apart (in the azimuthal direction) in the bottom of the groove as seen in Fig. 4.1(b). Visual observation during experiments confirms that the plasma glow is always located inside the cavity. In laboratory experiments, eight such pairs of electrodes are evenly spaced along the circumference of the nozzle extension in the ring groove.

The actuation is created using a high-voltage plasma generation system developed at OSU to enable simultaneous operation of up to eight actuators with independently variable frequency, duty cycle, and phase. The time dependence of a pulse is approximately a square wave, so only its fraction of time 'on' (its duty cycle) can be set. The current is limited to 250 mA, so multiplying by the voltage difference across the electrodes the maximum power is approximately 100 W while the actuator is on. The time-averaged power depends on the specified duty cycle.

4.3 Numerical Plasma Heating Model

Numerical models of several different plasmas have been formulated using a combined Navier–Stokes/Maxwell equations approach.[91] In many cases, these models are necessarily complex due to the complexity of the underlying plasma physics. However, the principal effect of the present arc discharge on the surrounding flow is thought to be a rapid and intense localized heating, which we can model simply as a time-varying, spatially-distributed source of internal energy. A similar forcing approach was followed in the one-dimensional model of Utkin *et al.*[85] In their work, an axisymmetric compressible Navier–Stokes simulation with a cylindrical heating power source was used to estimate the pressure and temperature fields due to the plasma filament, neglecting any effects of the cavity. We have extended the cylindrical power source model to two

dimensions and incorporated it into direct numerical simulations of a model mixing layer flow representing the near-nozzle exit region of a jet.

Our model is parameterized based on the available experimental data for these specific LAFPA actuators.[27,84,85,92] The plasma is assumed to be a cylindrical heat source with length $L_{\mathrm{act}} = 3$ mm (assuming a planar representation of the nozzle) and a radius of $r_0 = 0.25$ mm based on the spacing of the electrodes and observations of the plasma. The thermal source added to the right-hand side of the governing energy equation (2.7) is

$$S_{\mathrm{act}}(r(x,y),t) = w(t)\frac{f(r(x,y))}{f_{\mathrm{V}}}\frac{P_{\mathrm{act}}}{\pi r_0^2 L_{\mathrm{act}}}, \tag{4.1}$$

where the spatial distribution is

$$f(r(x,y)) = \frac{1}{2}\left[\tanh\left(-\sigma_{\mathrm{xy}}\left(r(x,y) - \frac{2}{3}r_0\right)\right) + 1\right] \tag{4.2}$$

and the distance is $r(x,y) = \sqrt{(x-x_{\mathrm{act}})^2 + (y-y_{\mathrm{act}})^2}$ with x and y the streamwise and cross-stream coordinates as shown in Fig. 4.1. The source is centered at $(x_{\mathrm{act}}, y_{\mathrm{act}})$, the geometric center of the cavity. The constant $\sigma_{\mathrm{xy}} = 10/r_0$ controls the sharpness of the model's distribution function such that $f(r(x,y))$ decreases towards zero prior to reaching the cavity walls. The power imparted to the flow by the plasma ($P_{\mathrm{act}} = 100$ W) is divided by the volume of the 3 mm long cylinder, as it would be in three dimensions. The constant

$$f_{\mathrm{V}} = \int_0^\infty f(r)\mathrm{d}r \tag{4.3}$$

ensures that the spatial distribution function does not provide additional energy to S_{act} beyond the input power P_{act}.

The time-varying portion of the source term models the square-wave input signal as

$$w(t) = \frac{1}{2}\left[\tanh\left(\frac{t-t_{\mathrm{i}}}{t_{\mathrm{r}}}\right) - \tanh\left(\frac{t-t_{\mathrm{f}}}{t_{\mathrm{r}}}\right)\right], \tag{4.4}$$

which allows for a variable duty cycle. This form for $w(t)$ was chosen over a simple pulse-train

square wave to facilitate discretization with the numerical solver described in §4.4.2. The constants are as follows. The time $t_{\mathrm{r}} = 1\ \mu s$ is the rise time of the actuator signal (the time for the input signal to go from zero to one). This parameter is determined by the power supply used in the experiments. The parameter $t_{\mathrm{i}} = 10\ \mu s * f_{\mathrm{act}}$ is the time delay of the actuator signal from its driving controller, and $t_{\mathrm{f}} = t_{\mathrm{i}} + p_{\mathrm{dc}} T_{\mathrm{act}}$ governs the actuator 'off' time and is based on the duty cycle p_{dc}. Of the timing parameters in the simulations in this model, only the duty cycle is varied, not f_{act}, the frequency of actuation.

4.4 Simulation Details

4.4.1 Flow Domain and Parameters

The numerical plasma model of the previous section is incorporated as an internal energy source in the compressible flow equations in two dimensions as in (2.5)–(2.7). No modeling is used in the fluid flow solution. The equations are nondimensionalized by the speed of sound $c_\infty = 343$ m/s ($= V^*$ in §2.1), density $\rho_\infty = 1.2$ kg/m^3, viscosity $\mu_\infty = 1.87 \times 10^{-5}$ kg/(m·s), temperature $T_\infty = 300$ K, and the experimentally estimated momentum thickness at the exit of the jet $\delta_{\mathrm{m}}^0 = 0.1$ mm ($= L^*$ in §2.1). Based on these values, the momentum thickness Reynolds number is $\mathrm{Re} = 3330$. The Prandtl number is $\mathrm{Pr} = 0.7$. Despite the locally high temperatures we shall see near the actuator, the ideal gas equation is chosen to close the system of equations.

The simulation domain covering the near-nozzle region of the OSU experimental jet is shown schematically in Fig. 4.2. The basic flow is a Mach 1.3 compressible boundary layer above a solid (no slip) wall located at $y = 0$ with fixed wall temperature equal to T_∞. There is no flow ($\mathrm{Ma} = 0$) downstream of the nozzle exit for $y \ll 0$. All wall boundaries are isothermal. With the inclusion of the thermal source from §4.3, some amount of heat transfer from the cavity fluid to the boron nitride nozzle extension is expected, but we do not model this beyond recognizing that the thermal conductivity of the nozzle is high and that the actuators are small thermal sources relative to the size of the whole nozzle. An isothermal model of the actuator cavity is therefore expected to be reasonably accurate for our purposes.

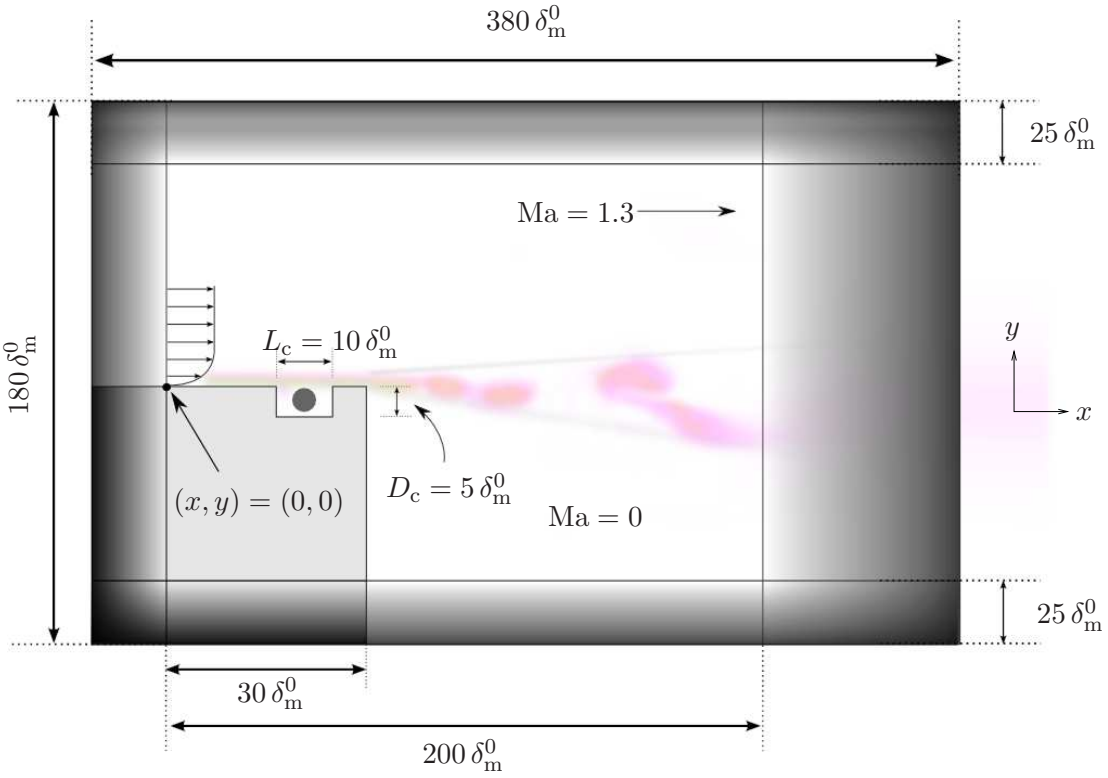

Figure 4.2: Schematic of the computational domain of the direct numerical simulations. Dimensions are presented in terms of the momentum thickness at the nozzle exit, δ_{m}^0. The light grey area denotes computational space treated as a solid, isothermal wall. The shaded area on all four sides of the domain denotes the computational boundary (buffer) zones. The black circle located in the cavity shows the location of the internal energy source in (4.1). Note: this schematic is not drawn to scale.

The laminar inflow boundary layer is specified above the wall using the method outlined by Lui.[93] The actual boundary layer leaving the nozzle lip at these conditions is too thin for its profile to be accurately measured. Estimates from experiments using a nozzle with similar length but at different flow conditions suggest[94] that the boundary layer is turbulent with a momentum thickness of around $\delta_{\mathrm{m}} = 0.1$ mm, but there is also some evidence that it may actually be laminar. Based on the acceleration parameter $K = \nu/U^2 \partial U/\partial x$ employed by Viswanathan and Clark[95] and a RANS solution of the jet mean flow gradient near the nozzle, the boundary layer in this flow is expected to be laminar. Regardless, a laminar boundary layer is used in the present investigation of mechanisms. The non-dimensional momentum thickness of the layer ($\delta_{\mathrm{m}}/\delta_{\mathrm{m}}^0$) was specified to be equal to unity at the nozzle exit ($x = 30\,\delta_{\mathrm{m}}^0$ in Fig. 4.2). The downstream physical simulation domain extends to $x = 200\,\delta_{\mathrm{m}}^0$ so that we can study the near-nozzle response of the shear layers.

Direction	s_1	s_2	s_3	s_4	σ_1	σ_2	σ_3	A_0	A_1	A_2	A_3
x	—	—	0.43	0.05	20.0	25.0	40.0	—	38.0	3.0	0.7
y	0.38	0.75	—	—	6.0	10.0	—	1.0	0.27	0.68	—

Table 4.1: Mesh stretching constants for the actuator simulation domain. The streamwise parameter values correspond to (2.34)–(2.37), and the cross-stream parameter values correspond to (2.26)–(2.29).

The cross-stream physical domain extends out to $y = \pm 65\,\delta_{\mathrm{m}}^0$. For reference, in terms of the experimental jet dimensions, the streamwise domain extends to about $x = 0.8 D_{\mathrm{j}}$ and the cross-stream domain from $y = \pm 0.25 D_{\mathrm{j}}$. A computational absorbing buffer zone of width $25\,\delta_{\mathrm{m}}^0$ is present above and below the cross-stream physical domain, and $30\,\delta_{\mathrm{m}}^0$ and $150\,\delta_{\mathrm{m}}^0$ upstream and downstream of the streamwise physical domain, respectively.

4.4.2 Numerical Methods

A full description of the numerical schemes is given in chapter 2 and summarized briefly here in the context of the actuator simulations. The flow equations are solved using high-resolution explicit and compact finite difference schemes. The optimized finite difference schemes described in §2.2.1 are used for the interior points of the computational mesh. Fourth-order biased schemes are used at the walls and the edges of the computational domain and are outlined in §2.2.2. The mesh is Cartesian and stretched in both coordinate directions so as to cluster points in the cavity and the shear layer. The functional mappings used to stretch the mesh are found in §2.2.3 and the values used in the simulations are given in Table 4.1. The mesh size was $N_{\mathrm{x}} \times N_{\mathrm{y}} = 3000 \times 1001$. A standard fourth-order Runge–Kutta time algorithm was used for time integrating the flow equations and the numerical time step was $\Delta t c_\infty / \delta_{\mathrm{m}}^0 = 0.005$ (~ 1.45 ns).

The Navier–Stokes characteristic boundary conditions[36] with the viscous correction of Yoo and Im[96] were used for boundary conditions on the isothermal walls. One-dimensional characteristics are used on the computational domain edges as a radiation boundary condition to disallow non-physical reflections back into the physical domain. Fig. 4.2 shows shaded areas indicating the boundary "buffer zones". Low-order, low-pass filtering is also implemented in these zones to

reduce any numerical artifacts generated at these outer boundaries and temper the flow moving towards the boundary. Lastly, numerical stabilization of the flow solutions is provided by high-order, high-wavenumber filtering in the physical domain of the solution[30] as formulated in §2.2.7. The flow solution is filtered in both coordinate directions once every five time steps in the physical domain of the simulation. A linear combination of the filtered solution (40%) is combined with the unfiltered solution (60%) at that time step and taken as the new simulation solution. The filtering is purely for numerical stabilization and is confirmed not to alter the physical behavior of the flows simulated here as well as in other flows (see §3.3.6). The present results were also confirmed to be mesh independent.

4.4.3 Actuator Forcing Parameters

The simulations incorporating the actuator model in this work are performed with a forcing frequency of $f_{\mathrm{act}} = 20$ kHz. This frequency was chosen because experiments showed the development of actuation-induced perturbations at this frequency occurred closer to the nozzle exit than lower frequencies and were stronger in general (see Samimy, *et al.*, figure 4).[27] The perturbations also decayed quickly downstream and therefore 20 kHz forcing allowed for the strongest mixing layer response to be captured in the relatively small computational domain. Settings of 5%, 10% and 20% duty cycle are presented in this chapter as data were also available for these parameters from experiments. For 10% duty cycle, the actuator is 'on' for 5 μs of the actuator's $T_{\mathrm{act}} = 50\,\mu$s period. Using these forcing parameters, the time series (4.4) and the corresponding frequency spectra of the forcing are shown in Fig. 4.3.

4.5 Results and Discussion

Results of the simulations are presented in the following sections beginning with validation of the numerical plasma heating model. We first focus on the cavity region where the actuator model is implemented to understand the mechanism by which it affects the flow. Then, we examine the subsequent downstream evolution of the shear layer including frequency spectra resulting from

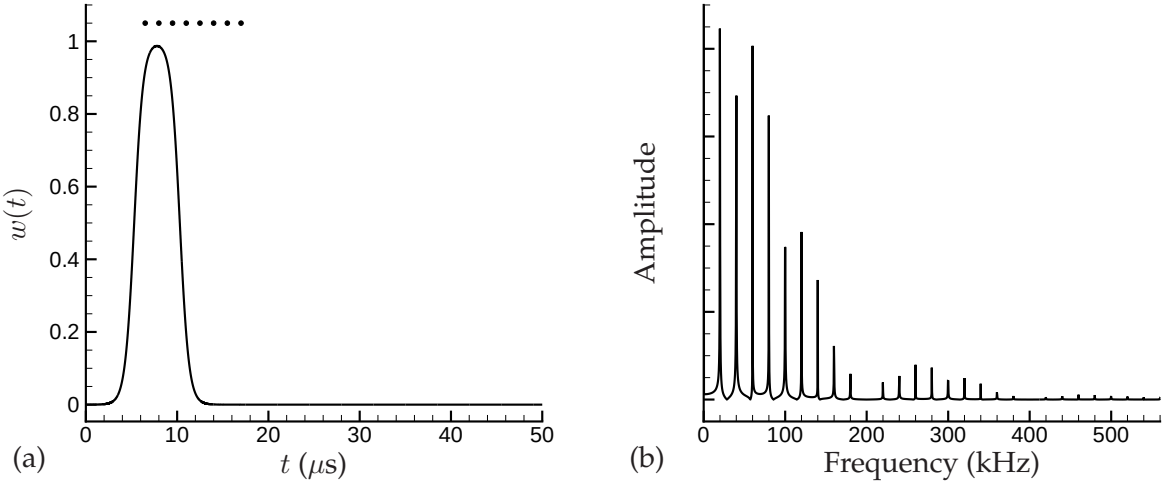

Figure 4.3: (a) Time series of $w(t)$ for 20 kHz forcing with 10% duty cycle for one actuation period. The dots in the figure represent the times in the actuation period that are represented with visualizations in §4.9.1. (b) Corresponding frequency spectrum of $w(t)$ showing the 20 kHz forcing frequency and harmonics.

the actuated cases.

Each simulation presented here is advanced in time from the initial condition for one-million time steps to allow for initial flow transients to convect out of the domain. The actuator model is active during this initial simulation. Statistical data is then collected during the following two-million time steps. This corresponds to 33 domain flow-through times (based on the velocity difference of the upper and lower streams, $0.65U_\infty$) and 58 actuator forcing periods. Phase-averaged quantities presented in the following sections are averaged over all of these 58 forcing periods.

4.6 Actuator Model Validation

As mentioned in the Introduction, detailed experimental characterization of the cavity and near-nozzle region is limited. However, there are two available points of comparison with the experiments that allow us to assess whether or not the simulations are at least qualitatively in line with the actuators in the experiment. Estimates are available of the temperature of the plasma in the cavity and the sound pressure level (SPL) at a location slightly downstream of the nozzle exit.

4.6.1 Near-field Pressure

The pressure amplitudes measured for the ideally expanded Mach 1.3 jet are compared with the results of the simulations presented here. The actuation was axisymmetric (i.e. 8 actuators firing simultaneously) for a 20kHz forcing with a 20% duty cycle. The pressure measurement was made at a location where the probe just grazed the edge of the shear layer, half a jet diameter downstream ($x/D_\mathrm{j} = 0.5$) of the nozzle lip. This corresponds in the simulation to $(x,\, y) = (127,\, -20)\, \delta^0_\mathrm{m}$. The experiments report an amplitude of 172 dB at $x/D_\mathrm{j} = 0.5$, but the trend shows the amplitude decreasing sharply afterwards, suggesting a higher reading closer to the nozzle. Our corresponding SPL was 173 dB, which is in close agreement with the experimental data.

Figure 4.4(a) shows the SPL along the streamwise coordinate (x) at the nozzle lip ($y = 0$). This location is within the shear layer at all streamwise locations and is therefore expected to have a higher perturbation amplitude than the experiments for this region close to the nozzle exit. At 20 kHz forcing, the simulation and actuator model correctly capture the behavior of the pressure perturbations saturating shortly downstream of the nozzle exit, but the computational domain ends before any decrease can be seen.

4.6.2 Cavity Temperature

The second model validation comes from comparing the reported peak plasma temperature and the corresponding maximum temperature of the fluid in the model simulations. The temperature in the experiments is calculated from emission spectroscopy since it was not feasible to it measure with probes. A least-squares fit was then used to compare the measured spectrum and the synthetic spectra from the second positive band system of nitrogen calculated numerically using temperature as a free parameter. Results of this calculation suggest that the plasma reaches temperatures near 2000 K,[97] although depending on the type of power supply the temperature could be as low as 1200 K.[92] The one-dimensional model of Utkin *et al.*[85] suggests a maximum temperature near 1800 K for this particular set of actuation parameters. The maximum temperature in the cavity for the current model is shown in Fig. 4.4(b). The phase-averaged temperature in the cavity for 20 kHz forcing at 20% duty cycle is shown to have a maximum temperature of around

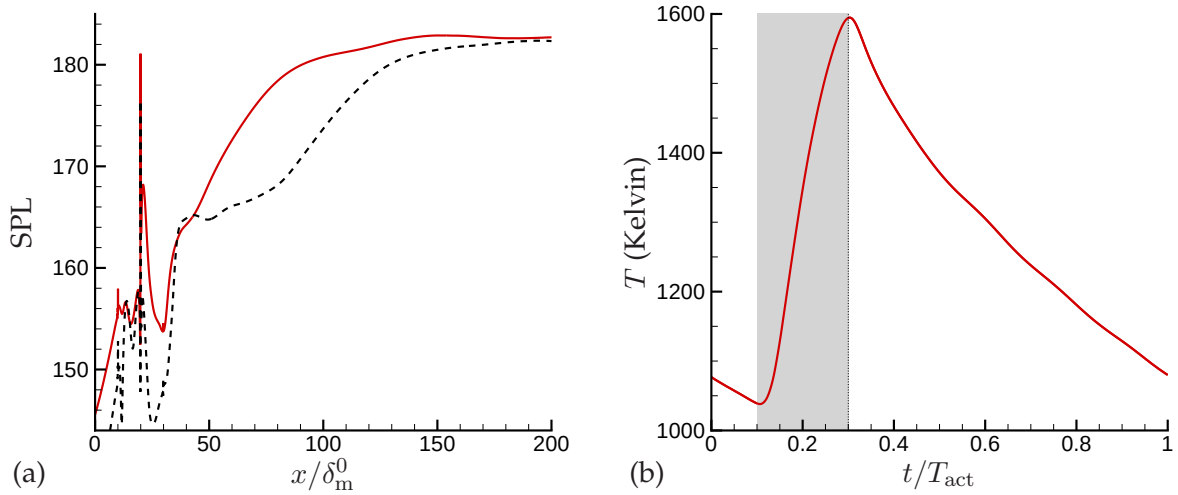

Figure 4.4: (a) Sound pressure level of the actuator-in-cavity mixing layer simulation (——) and baseline (no actuation, - - - -) simulation at the lipline ($y = 0$) as a function of streamwise distance. (b) Phase-averaged maximum temperature in the cavity for 20kHz forcing and 20% duty cycle. The shaded region denotes the time where the actuator model is 'on'.

1600 K. When the temperature is not phase-averaged, the maximum temperatures of the fluid in the groove do reach slightly over 1800 K at the peak of the actuator's 'on' time. Overall, this appears to be a reasonable agreement, especially given the simplicity of our actuator model.

4.7 Cavity Oscillation Dynamics – Baseline Simulation

4.7.1 Background

A key aspect of our study is the role played by the cavity designed to house the plasma. It was included to shield the plasma from the flow, but our simulations suggest that it might be fundamental to the working of the actuator. Even without actuation, cavities such as the actuator groove have been shown to possess interesting dynamics.

Over the past several decades, many detailed investigations have been performed that involve such cavity flows. The main classification of a cavities is based on their length-to-depth ratio, where $L_{\rm c}/D_{\rm c} > 1$ is deemed to correspond to a shallow cavity and $L_{\rm c}/D_{\rm c} < 1$ is said to be

deep. Cavities are also defined by whether the shear layer that forms over the cavity reattaches at the trailing edge (called an 'open' cavity flow) or on the cavity floor (a 'closed' cavity flow). Cavities are found to be associated with large-amplitude discrete tones (as high as 150 dB for supersonic flows) in scramjet engine combusters,[98] weapon payload bays, and landing gear bays.[99] The generation of tones is thought to be the result of one of several mechanisms based on the cavity geometry and surrounding flow, which are important to understand given that the actuation also will impose discrete frequencies.

For a large $L_{\mathrm{c}}/\delta_{\mathrm{m}}$ at the leading edge, the cavity is said to be operating in what is known as wake mode.[100,101] In this regime, a high drag is associated with the cavity due to vortices generated and ejected from the cavity of similar dimensions as the cavity itself. The actuator cavity recess flow in this study is open and $L_{\mathrm{c}}/\delta_{\mathrm{m}} = 10$, a relatively low value. The cavity dynamics are not expected to resemble the wake mode.

At certain low Mach numbers ($\mathrm{Ma} < 0.2$), the shear layer over the cavity is capable of exciting acoustic modes within it.[102,103] This regime is typically encountered for cavities deeper than the $L_{\mathrm{c}}/D_{\mathrm{c}} = 2$ cavity presented here.[104,105] At higher Mach numbers, a complex feedback mechanism involving the shear layer that forms over the mouth of the cavity and acoustic waves within the cavity is believed to cause broadband pressure spectra in conjunction with the large amplitude resonant tones. Rossiter[106] was the first to propose this feedback mechanism, and therefore the tones created are generally referred to as Rossiter frequencies which correspond to the "Rossiter modes" of the cavity. The cavity in this study is expected to behave in this manner.

The generation of these modes is thought to occur by the following mechanism. First, small perturbations present at the leading edge of the cavity are convected by the shear layer towards the trailing edge. Second, the layer grows over the width of the cavity due to the mismatch of velocities above the cavity and within it. The Kelvin-Helmholtz mechanism amplifies a set of the initial instabilities and the familiar vortical structures appear. Third, these vorticies convect downstream and impinge on the trailing edge of the cavity creating a pressure perturbation (an upstream-propagating acoustic wave). Finally, the wave excites the receptive shear layer at the leading edge. When in phase, the cycle of shear layer excitement and acoustic wave generation

develops a set of resonant tones that radiate from the cavity.

The frequency of the Rossiter modes generated by this cycle can be predicted via

$$\frac{L_\mathrm{c}}{U_\mathrm{c}} + \frac{L_\mathrm{c}}{c_\infty} + \frac{\alpha}{f} = \frac{n}{f}, \tag{4.5}$$

where U_c is the convection velocity of the shear layer, α is a phase delay constant, f is the frequency, and n is the oscillation mode number. The first term, $L_\mathrm{c}/U_\mathrm{c}$, is the estimated time required for a perturbation in the shear layer to travel from the cavity's leading edge to the trailing edge. Likewise, L_c/c_∞ is the time required for an acoustic wave to propagate from the trailing edge back to the leading edge of the cavity. The phase lag term α/f represents the time delay in fractions of a wavelength between the impingement of a vortex on the trailing edge and the generation of an acoustic wave. This quantity is defined empirically. For resonance, the sum on the left-hand side of (4.5) must equal n/f, an integer multiple of the period of oscillation. Only in this way can the feedback loop be complete.

Rossiter[106] used this reasoning to develop his equation for the oscillation frequency of mode "n"

$$f_\mathrm{n} = \frac{U_\infty}{L_\mathrm{c}} \frac{n - \alpha}{\mathrm{Ma}_\infty + 1/k_\mathrm{c}}, \tag{4.6}$$

where U_∞ and Ma_∞ are the freestream velocity and Mach number, respectively. A second quantity that is empirically-defined is the velocity ratio $k_\mathrm{c} = U_\mathrm{c}/U_\infty$. The empirical constants were measured by Rossiter to be $\alpha = 0.25$ and $k_\mathrm{c} = 0.57$ for a $L_\mathrm{c}/D_\mathrm{c} = 4$ cavity at low Mach number.[106] These values substituted into (4.6) reasonably predict oscillation frequencies and have been used widely in previous studies over a wide range of cavity length-to-depth ratios and Mach numbers.[107]

However, more recent data have shown that the values of these constants depend on the freestream Mach number and cavity geometry,[103,108–110] especially for supersonic cavity flows. Equation (4.6) assumes that the speed of sound in the cavity is constant and equal to the freestream speed of sound, which can lead to large errors for high-Mach-number flows. Heller and Bliss[108] modified Rossiter's equation for the modes by assuming that the sound speed in the cavity is

equal to the sound speed in a stagnating free stream such that

$$f_{\mathrm{n}} = \frac{U_\infty}{L_{\mathrm{c}}} \frac{n - \alpha}{\mathrm{Ma}_\infty \left(1 + \frac{\gamma-1}{2}\mathrm{Ma}_\infty^2\right)^{-\frac{1}{2}} + \frac{1}{k_{\mathrm{c}}}}, \tag{4.7}$$

or in the form of (4.5) as

$$\frac{L_{\mathrm{c}}}{U_{\mathrm{c}}} + \frac{L_{\mathrm{c}}}{c_\infty \left(1 + \frac{\gamma-1}{2}\mathrm{Ma}_\infty^2\right)^{\frac{1}{2}}} + \frac{\alpha}{f} = \frac{n}{f}. \tag{4.8}$$

4.7.2 Cavity Pressure Spectrum – Baseline

Using (4.6) and (4.7) and the common values of $k_{\mathrm{c}} = 0.57$ and $\alpha = 0.25$ proposed by Rossiter,[106] the first oscillation mode is calculated for the parameters of this flow to be $f_1 = 109$ kHz and $f_1 = 116$ kHz, respectively. The baseline (no actuation) frequency spectrum for the $L_{\mathrm{c}}/D_{\mathrm{c}} = 2$ cavity calculated in this study is shown in Fig. 4.5 where the pressure data is collected at $(x, y) = (15, -5)\,\delta_{\mathrm{m}}^0$. This is the streamwise center of the cavity on its bottom surface. The data was sampled every 25 time steps (a sampling rate of 27 MHz), windowed with a triangle function as in §3.3.8, and then Fourier transformed to yield the power spectrum. The most prominent frequency of the cavity from the data in Fig. 4.5 is $f = 131.3$ kHz with associated harmonics at $2f$, $3f$, and $4f$. If this peak is assumed to be the first Rossiter mode (f_1), then the frequency calculated by (4.6) represents an error of 17% and the modified equation (4.7) prediction gives an error of 12%.

Tuning the velocity ratio parameter to $k_{\mathrm{c}} = 0.69$ to match $f = 131.3$ kHz and using (4.7) to predict higher modes, we calculate $f_2 = 301$ kHz and $f_3 = 473$ kHz. The parameter α is kept at 0.25 as is common practice in the literature[106,108] for cavities of this length-to-depth ratio. Although in typical experiments not all Rossiter modes are necessarily apparent in cavity spectra,[105,110] there are clearly higher resonances in Fig. 4.5 that do not in any way match with the predictions of (4.7). In fact, there is no tuning of either k_{c} or α which result in (4.6) or (4.7) being able to describe the rich frequency content of the spectrum in Fig. 4.5 assuming that the peak at $f = 131.3$ kHz is f_1 with associated harmonics. Previous cavity flow experiments have shown cavity pressure spectra with non-Rossiter peaks.[110–112] The dominant spectral peaks in Fig. 4.5 at $f = 131.3$ kHz and its harmonics are not Rossiter peaks, since they are nonharmonic and are separated by constant

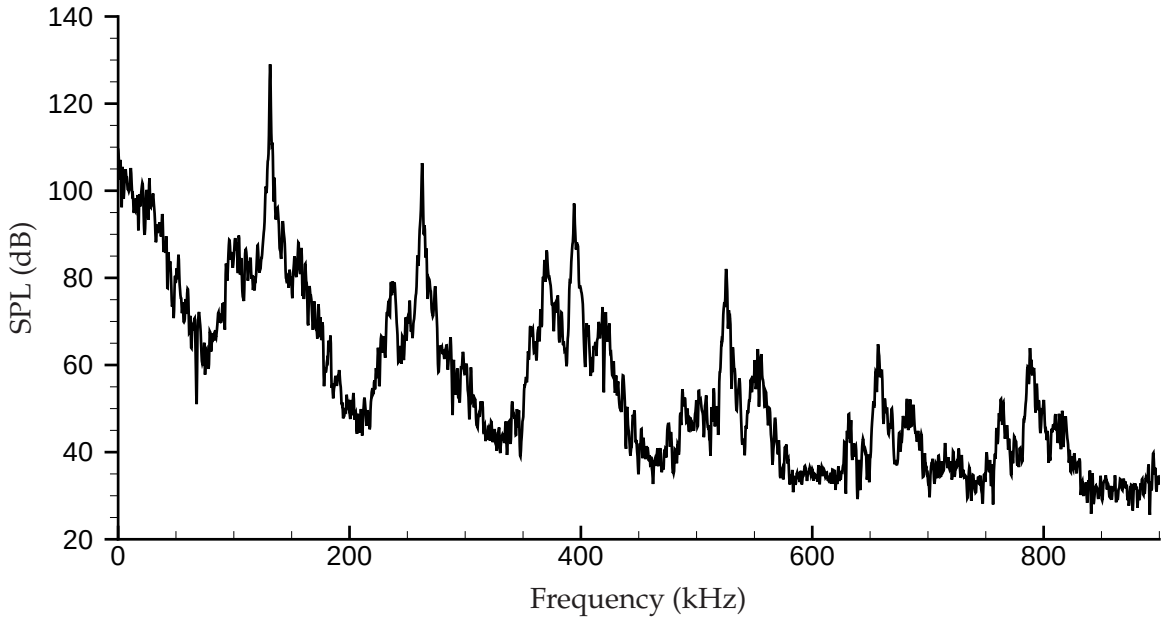

Figure 4.5: Sound pressure level computed at $(x, y) = (15, -5)\,\delta_{\mathrm{m}}^{0}$ for the $L_{\mathrm{c}}/D_{\mathrm{c}} = 2$ cavity of the baseline (no actuation) simulation.

frequency intervals whereas the peaks in the baseline spectrum are harmonic. The longitudinal acoustic modes are ruled out since for this two-dimensional cavity geometry the acoustic resonance is $f = c_{\infty}/2L_{\mathrm{c}} = 171.5$ kHz.

To explain the structure of the frequency peaks of the baseline cavity pressure spectra in Fig. 4.5, we introduce the signal processing viewpoint of cavity resonance proposed by Delprat.[113] This viewpoint introduces the idea that the cavity resonances observed by Rossiter and initially predicted by (4.6) are considered a "spectral signature". That is, they are the result of an underlying amplitude modulation of cavity resonances by a second wave of differing frequency associated with the overall dynamics of the cavity flow. From this perspective, the Rossiter modes are one, or possibly more, nonharmonic frequency components separated by constant frequency intervals. This is as opposed to a harmonic case, where the dominant frequencies occur at intervals equal to the first harmonic. The dynamics of the cavity are deduced *a posteriori* by selecting dominant peaks in a particular spectrum and determining the interactions between them.

Delprat's approach begins with (4.5) with $\alpha = 0$ and $n = 1$ so that

$$\frac{L_\mathrm{c}}{U_\mathrm{c}} + \frac{L_\mathrm{c}}{c_\infty} = \frac{1}{f_\mathrm{a}}, \tag{4.9}$$

where f_a is defined as the *fundamental aeroacoustic loop frequency*. The period of this relation corresponds to the time for a disturbance carried by the shear layer to travel from the leading edge to the trailing edge and an acoustic wave generated at this point to return to the leading edge without the phase delay proposed by Rossiter. The period of the aeroacoustic loop T_a is related to the frequency difference of two Rossiter modes such that

$$\frac{1}{T_\mathrm{a}} = f_{\mathrm{n}+1} - f_\mathrm{n} \tag{4.10}$$

which by substituting into Rossiter's equation (4.6) gives the constant frequency difference

$$f_{\mathrm{n}+1} - f_\mathrm{n} = \frac{U_\infty}{L_\mathrm{c}} \frac{1}{\mathrm{Ma}_\infty + 1/k_\mathrm{c}}. \tag{4.11}$$

A second frequency is defined as $f_\mathrm{b} = \alpha f_\mathrm{a}$ where α is now considered to be a frequency ratio instead of the phase lag interpretation of (4.5) and (4.6). Combining this frequency ratio with (4.6) and (4.11) and incorporating the mode number n gives an alternate expression for the traditional Rossiter modes as

$$\begin{aligned} f_{\mathrm{n}+1} - f_\mathrm{n} &= \frac{U_\infty}{L_\mathrm{c}} \frac{1}{\mathrm{Ma}_\infty + 1/k_\mathrm{c}} \\ f_\mathrm{a} &= \frac{U_\infty}{L_\mathrm{c}} \frac{1}{\mathrm{Ma}_\infty + 1/k_\mathrm{c}} \\ (n-\alpha) f_\mathrm{a} &= \frac{U_\infty}{L_\mathrm{c}} \frac{n-\alpha}{\mathrm{Ma}_\infty + 1/k_\mathrm{c}} \\ (n-\alpha) f_\mathrm{a} = (n f_\mathrm{a} - f_\mathrm{b}) &= f_\mathrm{n}. \end{aligned} \tag{4.12}$$

Essentially the Rossiter modes are now viewed as difference components of a fundamental frequency (f_a or one of its harmonics) of the cavity resonance process with its amplitude modulated by a low-frequency wave (f_b) through a nonlinear process. A canonical example of this process

occurs when considering the multiplication of two harmonic signals of differing frequency or, equivalently, the convolution of their respective spectra. The modulation causes a nonharmonic spectrum due to a spectral shift equal to the frequency difference (often referred to as a "beat" frequency). Along with the Rossiter frequencies (the difference components of f_a and f_b in (4.12)) are the corresponding sum components

$$f_{\mathrm{n}+} = nf_\mathrm{a} + f_\mathrm{b}. \tag{4.13}$$

The sum and difference components are revealed directly when considering the example just mentioned of the nonlinear interaction of two harmonic signals. For example, given the two harmonic signals $\sin(2\pi f_\mathrm{a} t)$ and $\sin(2\pi f_\mathrm{b} t)$, their product is

$$\sin(2\pi f_\mathrm{a} t)\sin(2\pi f_\mathrm{b} t) = \frac{\cos(2\pi t(f_\mathrm{a} - f_\mathrm{b})) - \cos(2\pi t(f_\mathrm{a} + f_\mathrm{b}))}{2},$$

which will show peaks at $f_\mathrm{a} - f_\mathrm{b}$ (the difference component) and $f_\mathrm{a} + f_\mathrm{b}$ (the sum component). Such sum and difference frequencies of a dual-frequency acoustically excited free shear layers have indeed been observed in experiments.[112,114] The resulting sound spectrum of this type of forcing includes numerous "intermodulation" modes at $nf_\mathrm{a} \pm mf_\mathrm{b}$ for $n \geq 0$ and $m \geq 0$.

Using this approach, we can educe the effective f_a and f_b from the cavity spectrum. In Fig. 4.5, the spectral peaks can be easily identified. We begin by choosing the fundamental aeroacoustic loop frequency to be $f_\mathrm{a} = 131.3$ kHz since this frequency is clearly the frequency difference between the dominant peaks and the first dominant peak itself in the spectrum in Fig. 4.5. Using (4.9) and assuming $U_\mathrm{c} = 0.5U_\infty$ for this flow, the calculated f_a is in agreement with a value of 135 kHz. The choice of $f_\mathrm{b} = 23.5$ kHz was made because it was the frequency difference between $2f_\mathrm{a}$ and the prominent peak at $f = 238.7$ kHz labeled f_2 in Fig. 4.6 as well as the difference between $3f_\mathrm{a}$ and the prominent peak below it at $f = 369.8$ kHz labeled as f_3. Since f_b is proposed to be a modulating frequency, the peaks at $2f_\mathrm{a} - f_\mathrm{b}$ and $3f_\mathrm{a} - f_\mathrm{b}$ are certainly good candidates to choose to estimate f_b for this spectrum.

The calculated values of the Rossiter modes using (4.12) as shown in Table 4.2 match well with

n	$(n \cdot f_\mathrm{a})$	f_b	f_n	$f_{\mathrm{n}+}$	f_n from (4.6)	f_n from (4.7)
1	131.3	23.5	107.8	154.8	109.5	116.1
2	262.2	23.5	239.1	285.7	255.5	271.1
3	393.3	23.5	369.8	416.8	401.4	426.0
4	525.2	23.5	501.7	548.7	547.5	581.0
5	656.5	23.5	633.0	680.0	693.4	735.9
6	787.8	23.5	764.3	811.3	839.4	890.8

Table 4.2: Rossiter modes and cavity oscillation frequencies (in kHz) as computed by (4.12) and (4.13) for the baseline $L_\mathrm{c}/D_\mathrm{c} = 2$ simulation shown in Figs. 4.5 and 4.6.

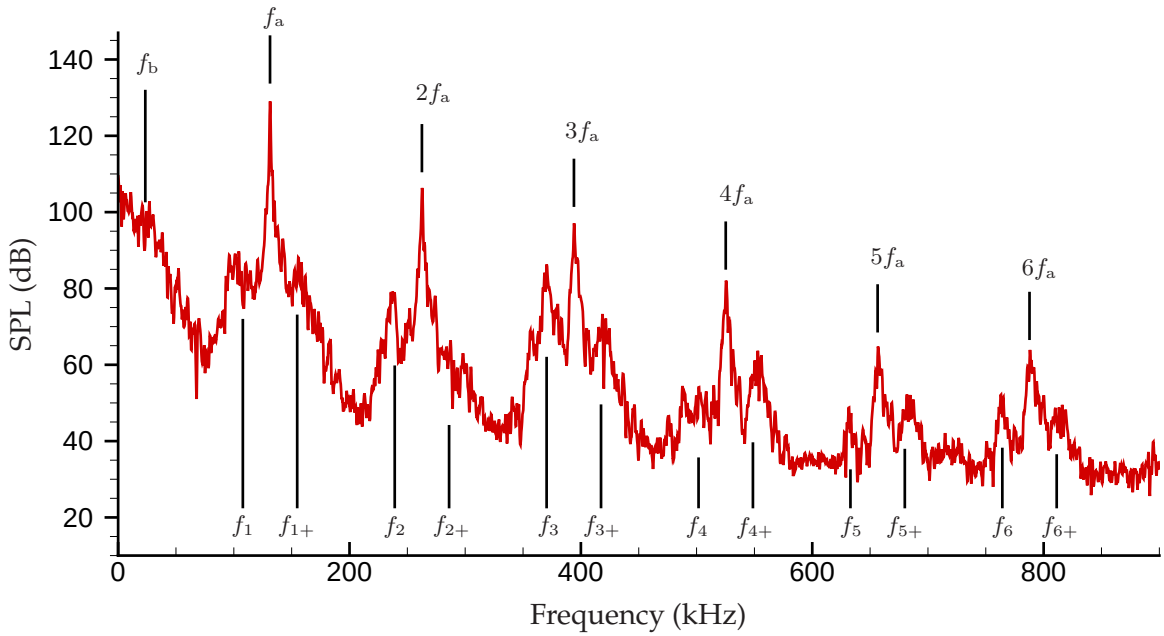

Figure 4.6: Sound pressure level computed at $(x, y) = (15, -5)\,\delta^0_\mathrm{m}$ showing cavity resonance frequencies for the $L_\mathrm{c}/D_\mathrm{c} = 2$ cavity of the baseline (no actuation) simulation. Lines pointing to spectral peaks are those calculated by (4.12) and (4.13) and listed in Table 4.2.

the spectrum in Fig. 4.5. The spectrum is shown again in Fig. 4.6 with the calculated frequencies marked and labeled for comparison. Along with the harmonics of f_a are several peaks corresponding to the Rossiter modes for $n = 2$, 3, 5, and 6 (labeled as f_2, f_3, etc. in Fig. 4.6), although all have smaller magnitudes than the fundamental aeroacoustic loop frequency harmonic each is associated with. The first Rossiter mode f_1 is also visible albeit not as prominently as the others just mentioned. The sum components from (4.13) are labeled in Fig. 4.6 and f_{3+}, f_{4+}, f_{5+}, and

f_{6+} are discernible in the spectrum at lower amplitudes than dominant peaks as seen in similar experiments.[112,113] There also appears to be a 'bump' in the spectrum at 23.5 kHz as would be expected corresponding to the modulating frequency, f_{b}.

Delprat[113] comments that f_{a} and its harmonics are usually missing or at very small amplitudes in experiments. However, we see them clearly in our two-dimensional simulations, which is in agreement with recent experiments reported by Malone *et al.*[110] of cavity flows with a freestream Mach number ranging from 0.20 to 0.65. Although those experiments were of subsonic cavity flows, f_{a} and its harmonics became more visible (and dominant compared to the Rossiter modes) as the Mach number increased, with f_{a} reaching a SPL of 25 dB greater than f_1 for Mach 0.60 (see Malone *et al.*[110] figure 11). The experiments reported by Malone also categorized the dominant frequency peaks within the amplitude modulation process proposed by Delprat and followed here. It is expected that numerous cavity experiments might have encountered the fundamental aeroacoustic loop frequency but that they were not identified as such. Delprat[113] provides one such example[115] where a visible harmonic of f_{a} was considered to be the result of nonlinear interaction of various Rossiter modes.

4.7.3 Rossiter Parameter Comparisons with Experiment

The values of f_{a} and f_{b} used in (4.12) predict all of the significant frequency peaks in the spectrum. But, it also important to see if these correspond to reasonable values of the empirical Rossiter parameters k_{c} and α deduced from experiments. The velocity ratio parameter using the freestream sound speed in (4.9) and f_{a} is $k_{\mathrm{c}} = 0.48$. This is lower than reported initially by Rossiter.[106] It is generally accepted that for $L_{\mathrm{c}}/D_{\mathrm{c}} = 2$ and $L_{\mathrm{c}}/D_{\mathrm{c}} = 1$ cavity ratios changing the value of k_{c} to 0.61 or 0.66 provides a good approximation to the Rossiter modes.[113] Some researchers have suggested that over the Mach number range 0.4–2.0 the value of k_{c} increases with Mach number and can vary from 0.4 to 0.75 and up to 0.9 for supersonic cavity flows ($\mathrm{Ma} \approx 5$).[108,109] On the other hand, Malone *et al.*[110] provides evidence of a decreasing downward trend of k_{c} with Mach number based on a semi-empirical equation formulated to match the occurrence of f_{a} and Rossiter modes in their data. They suggest the trend is physically realistic indicating that for higher Mach number,

the presence of the cavity causes the shear layer structures to tend to move toward the cavity as opposed to the higher momentum freestream. Our data agree with the findings of Malone *et al.*[110] which also is the only experimental study we are aware of that originally interpreted cavity resonance frequencies in the framework proposed by Delprat.

The frequency ratio $\alpha = f_\mathrm{b}/f_\mathrm{a} = 0.179$ is lower than the nominal reported value $\alpha = 0.25$ of Rossiter, but as previously mentioned his original experiments were on low subsonic flows with larger cavity length-to-depth ratios. Rossiter[106] predicted the trend of decreasing α with smaller $L_\mathrm{c}/D_\mathrm{c}$. Experiments[105] and corresponding large-eddy simulations[104] of high subsonic flows ($\mathrm{Ma} = 0.8$) over a deep cavity $L_\mathrm{c}/D_\mathrm{c} = 0.42$ show $\alpha \approx 0$ and Rossiter modes appearing harmonic, as if the spectrum were dominated by f_a and therefore unmodulated by f_b. With this lower frequency ratio, the structure of the baseline spectrum suggests the cavity oscillations are quasi-harmonic and only weakly modulated such that f_n is approaching nf_a. This appears to explain why the harmonics of f_a are dominant in the present simulation, though a few of the Rossiter and sum component modes are identifiable in the spectrum. The data of Malone *et al.*[110] shows α trending lower as Mach number is increased with values between 0.1 and 0.2 for $0.2 < \mathrm{Ma} < 0.65$. The baseline simulation is also lower than the traditional values taken, but remains above the range reported by Malone *et al.*

It is interesting to note that without the introduction of spectral signature, the spectrum in Fig. 4.6 would imply the presence of a single Rossiter mode with several harmonics of that mode present, but no firm explanation of the existence of the other significant spectral bumps at f_2 and f_3, for instance. If the assumption was made that f_a was actually f_1 for the spectrum presented in Fig. 4.5, using (4.7) would give $k_\mathrm{c} = 0.69$ and be within the range reported in the literature. The amplitude modulation process proposed by Delprat's signal processing approach predicts that $f_1 = 107.8$ kHz (see Table 4.2) with $\alpha = 0.179$ and $k_\mathrm{c} = 0.47$ derived from the spectrum. This is close to the $f_1 = 109.5$ and 116.1 kHz computed by (4.6) and (4.7) using the nominal values for the tunable parameters. Even though the spectrum is not dominated by the Rossiter modes, the Rossiter-based predictions appear to provide reasonable estimates of f_1 for the higher Mach number and lower cavity length-to-depth ratio in the present simulation. However, as Table 4.2 shows, the predictions for higher f_n would be less accurate for larger n.

4.7.4 Cavity Oscillation Frequency Evolution

The pressure spectrum in Fig. 4.5 shows that the dominant frequencies in the cavity are the harmonics of f_{a} with evidence of several Rossiter modes and sum components at lower amplitudes of up to 40 dB. Experiments[115] and large-eddy simulations[116] have observed that the dominant cavity mode can change in time. When one mode shifts energy to another (or others) over a period of time, the phenomenon is referred to as "mode-switching". The most common means of presenting cavity oscillation modes is via a Fourier transformation of the unsteady pressure data and squaring the result to get the power spectrum as was done in Figs. 4.5 and 4.6. However, this operation essentially time-averages the signal by discarding the phase information and removes the ability to distinguish intermittent and nonstationary features as would occur in mode-switching. Given the evidence that f_{a} and its harmonics can coexist and be of similar magnitude as Rossiter modes (for example, see Malone *et al.*,[110] figure 11 and f_3 and $3f_{\mathrm{a}}$ which differ in Fig. 4.6 by only 10 dB), it is informative to determine if a similar mode-switching phenomenon is occurring between the dominant harmonics and modes in the current baseline simulation.

To determine the possible nonstationary features of the cavity spectrum, we introduce a joint time-frequency analysis. The simplest such decomposition is the short-time Fourier transform (STFT), which is defined as

$$\mathrm{STFT}(f,t) = \int_{-\infty}^{\infty} p(\tau) W^*(\tau - t) e^{-2\pi i f t} \mathrm{d}\tau, \tag{4.14}$$

where $p(t)$ is an unsteady pressure signal and $W^*(t)$ is the complex conjugate of a user-chosen windowing function, which has a shorter time duration than $p(t)$. The convolution of the shorter window function with the signal produces Fourier transforms of subsets of the full time series. The result is a two-dimensional mapping in the frequency-time domain that provides a measure of the time evolution of the power spectrum. The square of the magnitude is plotted and is referred to as the pressure spectrogram. The STFT computed for the baseline $L_{\mathrm{c}}/D_{\mathrm{c}} = 2$ cavity was obtained with a Fourier transform and window function size of 18293 points and the signal was split into segments with 95% overlap. This resulted in the STFT frequency resolution being $\Delta f = 1.5$ kHz. A Hanning window was used for $W(t)$.

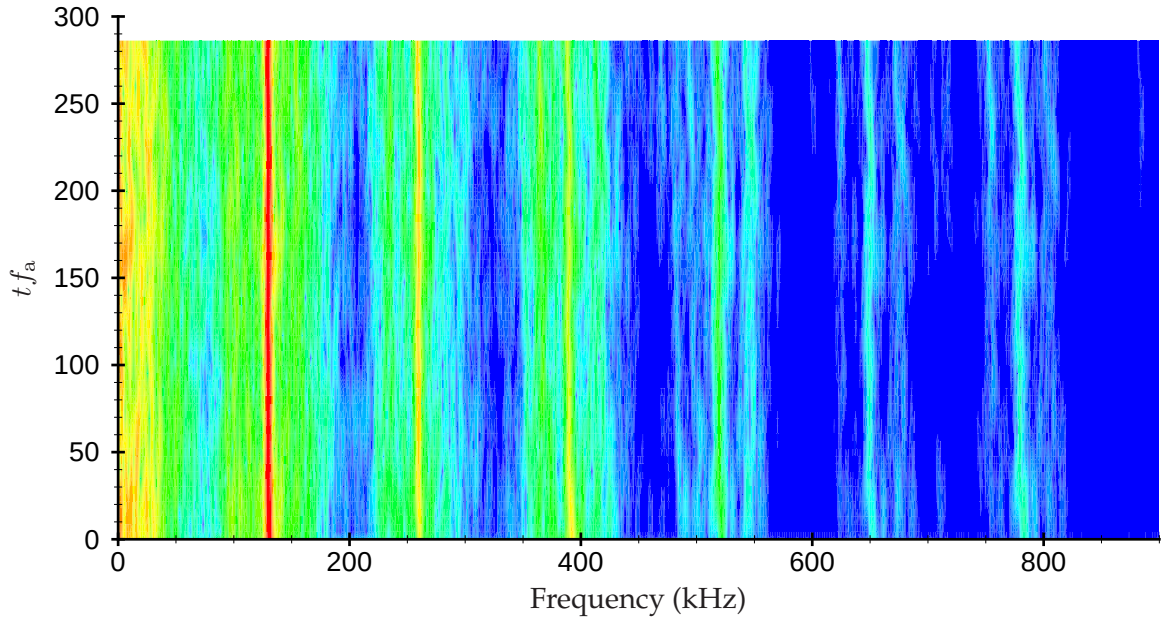

Figure 4.7: Pressure spectrogram computed at $(x, y) = (15, -5)\,\delta_m^0$ for the $L_c/D_c = 2$ cavity of the baseline simulation. The vertical axis is plotted with respect to the number of periods of f_a. The colors vary continuously between 40 dB (blue) and 130 dB (red).

The result of the joint-time frequency analysis of the $L_c/D_c = 2$ baseline cavity simulation is shown in Fig. 4.7. The spectrogram reveals no strong evidence of time-evolution of the dominant frequencies of the cavity pressure. The harmonics of f_a are dominant throughout the entire time series of the pressure data and show no significant swapping of energy with each other or with the Rossiter modes. The more visible presence of f_b from $tf_a = 200$ until the end of the time series loosely coincides with the appearance of f_3, f_5, and f_6 during the same interval, suggesting the amplitude modulation by f_b may be more pronounced during this period. The sum components that are discernible in the spectrum also are steady in the spectrogram. As with the power spectrum, there does not appear to be a strongly distinguishable peak in amplitude at the first Rossiter mode in the spectrogram.

4.7.5 Conclusions

Overall, the pressure in the baseline cavity seems to be resonating in a stable fashion at frequencies dominated by f_{a} and its harmonics. Several Rossiter modes and corresponding frequency sum components are visible in the cavity pressure spectrum, but most are at significantly lower amplitudes than f_{a}. The values of the empirical parameters in Rossiter's original equation for the baseline cavity simulation are comparable to experimental values. All of the natural cavity resonance frequencies are significantly higher than the actuator forcing frequency, $f_{\mathrm{act}} = 20$ kHz, which will be implemented in the simulation in the next section.

4.8 Cavity Oscillation Dynamics – Actuated Simulation

We now proceed with the investigation of cavity oscillations when the plasma heating model formulated in §4.3 is activated.

4.8.1 Observations

The addition of the model actuator forcing changes several features of the flow in the cavity region affecting the self-sustained oscillation feedback loop described in §4.7. First, as a consequence of the actuator model design, a high-temperature region is created in the cavity. As heat is generated by the model source $S_{\mathrm{act}}(r(x, y), t)$ through successive firings, a point is reached where the amount of heat that diffuses or is convected out of the cavity balances that which is deposited by the source over the period of the actuation. A rise in mean temperature will result in an increased mean speed of sound in the cavity. For our nondimensional equation of state (2.10), the speed of sound is

$$c = \sqrt{\frac{\gamma p}{\rho}} = \sqrt{(\gamma - 1)T}. \tag{4.15}$$

The "hot spot" that is generated in the cavity is seen in the mean temperature field shown in Fig. 4.8(a). The mean temperature spans a range of over 600K from the cavity wall to the center of

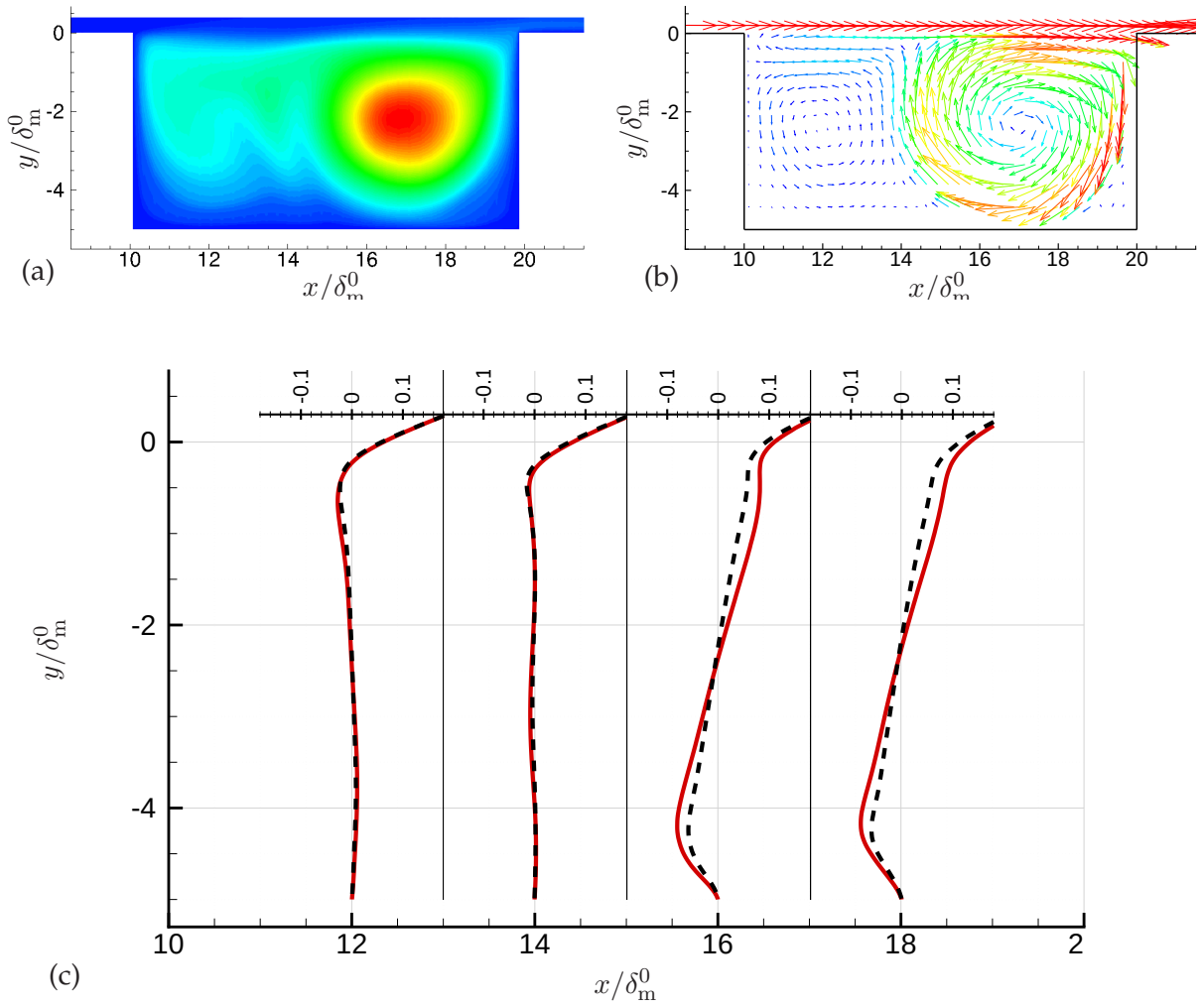

Figure 4.8: Mean quantities in the actuated $L_c/D_c = 2$ cavity with 10% duty cycle forcing. (a) Mean temperature in the cavity. The color in the temperature field varies continuously from 300K (blue) and 900K (red). (b) Mean velocity vectors showing the two counter-rotating recirculation regions in the cavity. The vector lengths are proportional to the magnitude of mean velocity and are colored accordingly. (c) Profiles of mean streamwise velocity at four streamwise stations in the cavity. The curves at different stations are displayed with the same grid scaling. Baseline simulation (- - - -) and actuated simulation (——).

the highest temperature location. Instantaneous temperature differences can range up to 1500 K from the center of the cavity to the wall while the actuator is on.

Although the actuator model's spatial distribution is centered at $x = 15\,\delta_{\mathrm{m}}^0$, the location of the center of the high temperature fluid is biased towards the trailing edge of the cavity. The position of the hot spot coincides with one of two recirculation zones common in cavities of this length-to-

depth ratio. The recirculation in the present flow is shown by vectors of the mean velocity in the cavity in Fig. 4.8(b). The downstream half of the cavity shows the stronger recirculation, which encompasses the hottest fluid while a weaker, counter-rotating zone of low temperature fluid appears in the upstream portion. Profiles of the mean streamwise velocity at several streamwise locations in Fig. 4.8(c) show the relative strengths and the opposite rotation of the two recirculating areas. The high temperature spot is centered at a location where the flow velocity is approaching zero as is seen in the profiles at $x = 16\,\delta_{\mathrm{m}}^0$ and $x = 18\,\delta_{\mathrm{m}}^0$ around $y = -2.5\,\delta_{\mathrm{m}}^0$. Also plotted with the actuated profiles are the baseline curves that show the same two recirculating regions. The baseline profiles at the downstream half of the cavity show the mean velocity switching from positive to negative at the same cross-stream location, but the velocities are lower. The two upstream profiles show only minor differences.

Despite the baseline and actuated cavities having two nearly identical rotating regions, a high temperature region is localized in the latter recirculation zone of the actuated case as stated above. We can expect that if self-sustaining oscillations are present in the cavity in addition to the artificial spectrum introduced by the forcing, the frequency of these oscillations will be shifted higher than those found in the baseline modes. The speed of sound was assumed to be constant in the cavity in Rossiter's equation (4.5), Heller's variant (4.8), and in the calculation of the fundamental aeroacoustic loop frequency in (4.9). The flow-acoustic interaction mechanism described by these three equations is now slightly altered. As noted by Delprat,[113] time variations in Ma (and thus c) and k_{c} (and thus U_{c}) may cause frequency modulations of f_{a}, in which case its harmonic peaks will not necessarily be equally spaced.

We can still attempt to estimate the difference in travel time of the trailing-to-leading edge acoustic wave by integrating the mean speed of sound $\overline{c}(x, y)$ along a simple path. The speed of sound field with the actuator turned on now varies considerably compared to the baseline flow so the time for an acoustic wave generated at the trailing edge to reach the leading edge of the cavity (previously L_{c}/c_∞) should be sufficiently different between the baseline and actuated simulations. For simplicity, we choose to integrate over the width of the cavity along a horizontal line located at $y = -2.5\,\delta_{\mathrm{m}}^0$, the middle of the cavity and also the lateral position roughly corresponding to the

location of the highest temperature in the cavity. Numerically integrating

$$t = \int_{L_c} \frac{1}{\overline{c}(x,y)}\, dx = \int_{20\delta_m^0}^{10\delta_m^0} \frac{1}{\overline{c}(x,-2.5\,\delta_m^0)}\, dx \tag{4.16}$$

gives the travel time in the upstream direction as $2.2\,\mu$s compared to $L_c/c_\infty = 2.9\,\mu$s, a difference of 24%. Correspondingly, we can use (4.9) to estimate f_a for this flow, assuming there is no change in the convective velocity, to be $f_a = 145$ kHz.

Second, we observe that the derivation of Rossiter's equation in §4.7 is based on acoustic waves generated at the trailing edge traveling upstream and seeding new instabilities over the cavity lid. The proposed mechanism by which the LAFPAs force a flow is through a pressure perturbation generated by the rapid heating of the fluid in the vicinity of the plasma filament. It is possible that the perturbation could be large enough to break or alter the feedback loop by disrupting the formation of vorticies in the shear layer represented by the L_c/U_c term in (4.9). This will be investigated further in this section and by visualization of the cavity in §4.9.1.

Third, we note that the set of harmonic frequency peaks created by the actuator forcing function $w(t)$ as shown in Fig. 4.3(b) have a periodic variation in amplitude that may be important in understanding the frequency content of the cavity pressure spectrum when the actuator forcing is present. To further describe this quantitatively, we can approximate $w(t)$ as a simple pulse-train square wave with constant amplitude and variable duty cycle with the piecewise-defined function

$$x(t) = \begin{cases} 0 & \text{for } 0 < t < t_i \\ \mathcal{A} & \text{for } t_i < t < t_i + p_{dc} T_{act} \\ 0 & \text{for } t_i + p_{dc} T_{act} < t < T_{act} \end{cases} \tag{4.17}$$

where t_i is the time when the signal jumps in amplitude from 0 to $\mathcal{A}$ as in (4.4) (see §4.3). This approximation of $w(t)$ is made to provide an analytical result for the Fourier coefficients. The Fourier series is defined in the usual manner

$$x(t) = a_0 + \sum_{n=1}^{\infty} \left[a_n \cos\left(\frac{2\pi n t}{T_{act}}\right) + b_n \sin\left(\frac{2\pi n t}{T_{act}}\right) \right] \tag{4.18}$$

where n/T_{act} are the harmonics of f_{act} and the coefficients are defined as

$$a_0 = \frac{1}{T_{\text{act}}} \int_0^{T_{\text{act}}} x(t)\, dt \tag{4.19}$$

$$a_{\text{n}} = \frac{1}{T_{\text{act}}} \int_0^{T_{\text{act}}} x(t) \cos\left(\frac{2\pi n t}{T_{\text{act}}}\right) dt \tag{4.20}$$

$$b_{\text{n}} = \frac{1}{T_{\text{act}}} \int_0^{T_{\text{act}}} x(t) \sin\left(\frac{2\pi n t}{T_{\text{act}}}\right) dt. \tag{4.21}$$

Substituting in the function $x(t)$ to the equations for the coefficients gives

$$a_0 = \frac{1}{T_{\text{act}}} \int_{t_{\text{i}}}^{t_{\text{i}}+p_{\text{dc}}T_{\text{act}}} \mathcal{A}\, dt$$

$$a_{\text{n}} = \frac{1}{T_{\text{act}}} \int_{t_{\text{i}}}^{t_{\text{i}}+p_{\text{dc}}T_{\text{act}}} \mathcal{A} \cos\left(\frac{2\pi n t}{T_{\text{act}}}\right) dt$$

$$b_{\text{n}} = \frac{1}{T_{\text{act}}} \int_{t_{\text{i}}}^{t_{\text{i}}+p_{\text{dc}}T_{\text{act}}} \mathcal{A} \sin\left(\frac{2\pi n t}{T_{\text{act}}}\right) dt,$$

which can be evaluated to yield

$$a_0 = \mathcal{A} p_{\text{dc}} T_{\text{act}} \tag{4.22}$$

$$a_{\text{n}} = \frac{\mathcal{A}}{n\pi} \sin\left(n\pi p_{\text{dc}}\right) \cos\left(\frac{2\pi n t_{\text{i}}}{T_{\text{act}}} + n\pi p_{\text{dc}}\right) \tag{4.23}$$

$$b_{\text{n}} = \frac{\mathcal{A}}{n\pi} \sin\left(n\pi p_{\text{dc}}\right) \sin\left(\frac{2\pi n t_{\text{i}}}{T_{\text{act}}} + n\pi p_{\text{dc}}\right). \tag{4.24}$$

Figure 4.9 shows the power spectrum of the actuator model forcing function $w(t)$ and a plot of the Fourier series coefficients of $x(t)$ in (4.17) where the amplitude factor $\mathcal{A} = 1$ for convenience. The approximation $x(t)$ has a power spectrum that captures the main features of the forcing power spectrum used for the actuator model in the simulation. Since the coefficients vary sinusoidally, there are frequencies at 200 kHz, 400 kHz, 600 kHz, etc. that have zero amplitude for a duty cycle of 10%. The harmonics of f_{act} undergo an amplitude modulation related to the duty cycle of the signal. In general, the coefficients of $w(t)$ also decay faster than those of $x(t)$. There also appears to be a higher frequency creating further modulation in $w(t)$ in addition to those defined by a_{n} and b_{n}. Both of these deviations are attributable to the subtle differences between the piecewise functional form of $x(t)$ and smooth form of $w(t)$ at the signal's rise from zero to one and vice versa.

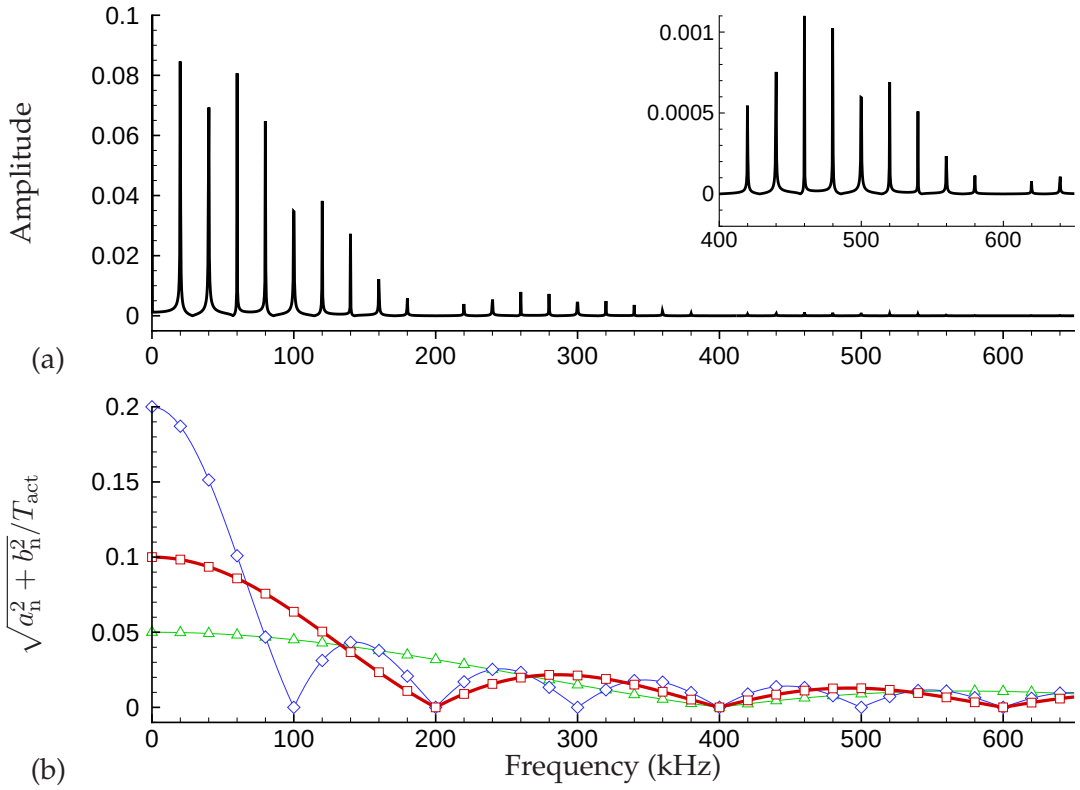

Figure 4.9: (a) Power spectrum of the time-varying actuator forcing $w(t)$ from (4.4) for $f_{\text{act}} = 20$ kHz with 10% duty cycle. Inset: Zoomed-in view of the power spectrum of $w(t)$ at higher frequencies. (b) Amplitude of the Fourier series coefficients of the pulse train $x(t)$ in (4.22)-(4.24) at 20 kHz with $\mathcal{A} = 1$. The symbols are located at the harmonics of f_{act} and correspond to $n = 1, 2, 3, \ldots$ The following duty cycles are plotted: 5% (— △ —), 10% (— □ —), and 20% (— ◇ —).

The decay and additional amplitude modulation are sufficiently minor in importance compared to the enveloping nature captured by the coefficients of $x(t)$ in Fig. 4.9(b). The approximation of $w(t)$ by $x(t)$ reveals that the actuator forcing has significant amplitude at harmonics of f_{act} which vary in a sinusoidal fashion. The harmonics of f_{act} will retain significant amplitude at higher frequencies to interact with the natural oscillations of the cavity.

It is also observed from Fig. 4.9(b) that the choice of duty cycle has an important effect on the overall spectrum of the forcing. The enveloping character of the power spectra for 5%, 10%, and 20% duty cycles shown in the figure reveals that the choice of p_{dc} creates very different frequency profiles. Using a higher duty cycle, where the actuator is "on" for a greater portion of the actuator period, the zero frequency component (the signal average component) is necessarily higher and

therefore results in higher peak temperatures in the cavity. This choice of duty cycle places a large fraction of the spectral power into a smaller subset of frequencies at the low end of the spectrum. Contrast this with the 5% duty cycle, which decays much slower spreading relatively constant (lower) amplitude actuation over a wider range of frequencies.

4.8.2 Cavity Pressure Spectrum – Actuated

The pressure spectrum of the actuated case provides a measure of how the flow is altered by the forcing. The full pressure spectrum is shown in Fig. 4.10(a) up to 700 kHz and split into two sections in Fig. 4.10(b) for viewing in greater detail. It was computed at $(x, y) = (15, -5)\,\delta_{\mathrm{m}}^{0}$ and the entire time series of pressure data was used to compute the spectrum just as was done for the baseline case presented in the previous section.

In Fig. 4.10, it is clear that the spectrum of the actuation function $w(t)$ is prevalent throughout the entire frequency range of the cavity pressure spectrum shown. The actuation spectrum in Fig. 4.9(a) shows the first few harmonics of f_{act} having high amplitudes, and this behavior of the forcing is carried through to the cavity pressure. The first harmonic is the strongest at 119 dB. Superimposed on Fig. 4.10(a) is the curve showing the amplitude of the Fourier coefficients of the analytical model $x(t)$. The zero-amplitude frequencies in $x(t)$ at 200 kHz, 400 kHz, etc. are seen to have no amplitude peaks as predicted by the model. Despite the decrease in amplitude of the harmonics of forcing, the cavity pressure spectrum begins an amplitude increase from 100 kHz to 160 kHz before decreasing again. Upon closer inspection, the peak amplitude of 121 dB of the entire cavity pressure spectrum occurs not at the eighth harmonic of f_{act} at 160 kHz, but at 156 kHz.

The peak at 156 kHz suggests a similar spectral pattern to that of the baseline spectrum. In the baseline spectrum (Fig. 4.6), the harmonics of the fundamental aeroacoustic loop frequency f_{a} were the dominant peaks, with Rossiter modes and sum components at equidistant frequency intervals prior to and after f_{a}, respectively. Each set of peaks in the baseline spectrum gradually decreased in amplitude as the frequency increased. It appears from the spectrum in Fig. 4.10(a) that the cavity is still oscillating "naturally" in the Rossiter (flow-acoustic) sense in the presence

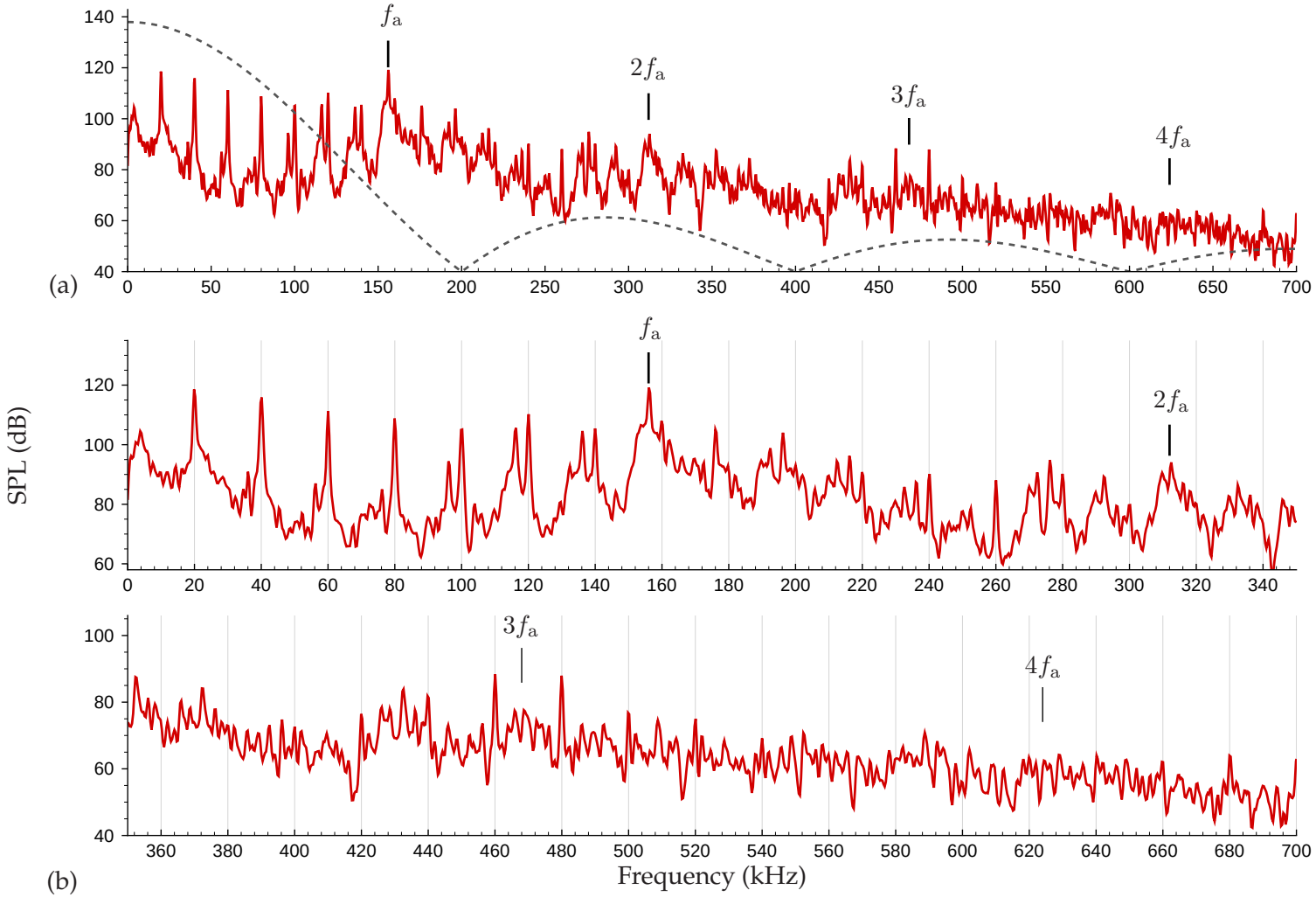

Figure 4.10: Sound spectra computed at $(x, y) = (15, -5)\,\delta_m^0$ showing the cavity pressure spectrum for the $L_c/D_c = 2$ cavity of the actuated 20 kHz simulation with 10% duty cycle. The spectrum has been split into three separate curves to illuminate its details. The vertical axes span different ranges. For the sake of clarity, the spectrum has been smoothed to remove residual noise. (a) Pressure spectrum from 0 to 700 kHz (——) and amplitude coefficients of $x(t)$ model function spectrum in (4.22)-(4.24) (- - - -). (b) Pressure spectrum from 0 to 350 kHz (top) and from 350 kHz to 700 kHz (bottom).

of the model actuator forcing with $f_\mathrm{a} = 156$ kHz and a clear harmonic at $2f_\mathrm{a}$. The spectrum shows a gradual amplitude decrease between f_a and the next set of peaks near $2f_\mathrm{a}$ and repeats the decrease with regularity at a constant frequency interval equal to f_a just as in the baseline cavity spectrum. The areas of higher amplitude at and surrounding f_a in the actuated pressure spectrum that would correspond to sum and Rossiter frequency peaks are not as pronounced as in the baseline spectrum as the actuator forcing adds considerable complexity to the cavity spectrum. Additionally, $3f_\mathrm{a}$ and $4f_\mathrm{a}$ are labeled in the figure but are not distinguishable.

The appearance of a spectral peak at $f_\mathrm{a} = 156$ kHz in the actuated flow spectrum is consistent not only with the general similarities in frequency peaks between the baseline and the actuated spectra, but also with the transition of the cavity oscillations when the actuation is switched on. Figure 4.11 shows the joint time-frequency analysis of an additional simulation started with an already developed baseline flow transitioning to the actuated flow. The actuator model was turned on one-third of the way through the time series and remained on until the end of the simulation. The pressure data used to create Fig. 4.11 are thus not the same data used to create the pressure spectrum in Fig. 4.10, but the simulation and actuation parameters are identical.

The pressure spectrogram initially shows the baseline cavity spectrum oscillating as observed in the previous section. As the actuation commences, the harmonics of the baseline f_a shift to the harmonics of $f_\mathrm{a} = 156$ kHz present in the actuated pressure spectrum of Fig. 4.10. The shift is especially visible for the third baseline harmonic of f_a and higher, since the actuator forcing spectrum is sufficiently weaker at higher frequencies, and the frequency differences between the actuated and baseline harmonics are greater. By $tf_\mathrm{a} = 50$, the gradual drift of the harmonics ceases.

Also shown with the spectrogram is the spatially-averaged temperature in the cavity, which increases and then begins oscillating about a fixed temperature for $tf_\mathrm{a} \gtrsim 30$. Based on the earlier predictions in this section, higher frequencies of self-sustained oscillation are expected because of the actuator adding heat to the cavity. We expect $f_\mathrm{a} \approx 145$ kHz based only on the change in the mean cavity speed of sound. Figures 4.10 and 4.11 confirm the shift to higher frequencies in the actuated cavity pressure spectrum.

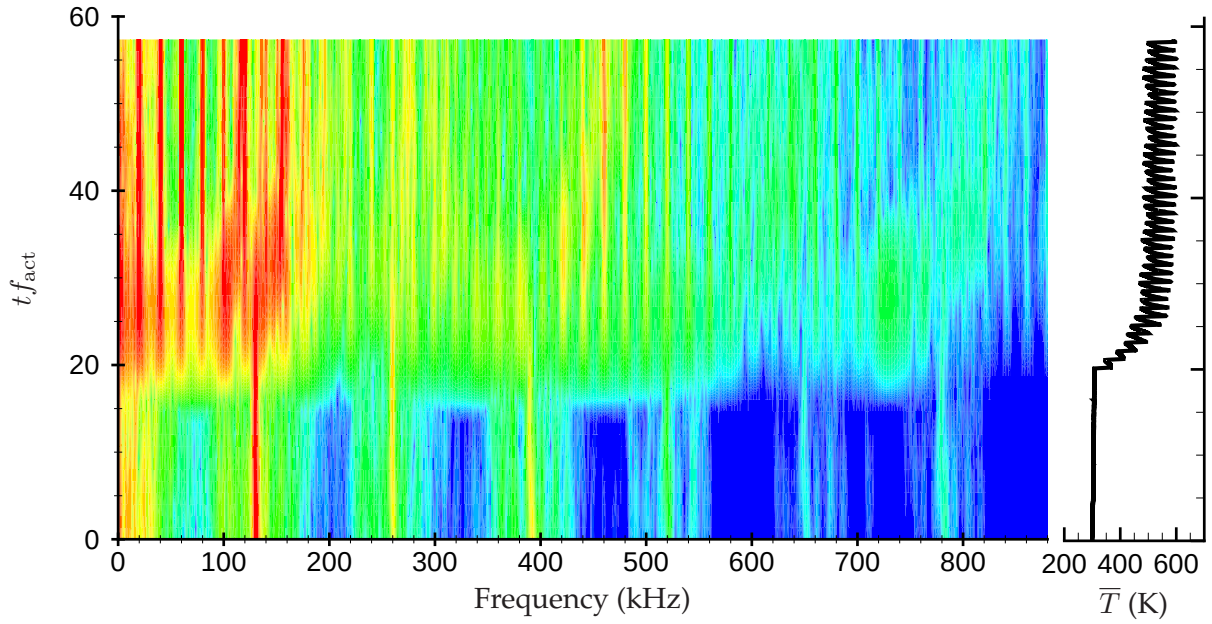

Figure 4.11: Pressure spectrogram computed at $(x, y) = (15, -5)\,\delta_{\mathrm{m}}^{0}$ for the $L_{\mathrm{c}}/D_{\mathrm{c}} = 2$ cavity of the baseline simulation transitioning to 20 kHz, 10% duty cycle forcing. The vertical axis is plotted with respect to the number of periods of f_{act}. The colors vary continuously between 40 dB (blue) and 130 dB (red). The temperature of the fluid averaged over the cavity is also plotted for reference on the right of the figure.

The effect of the forcing on the velocity of the shear layer perturbations, which account for the other portion of the calculation of f_{a}, can also be determined. Figure 4.12 shows the path of structures traveling along the top of the cavity via the fluctuating pressures to compare the baseline flow and the actuator-forced flows. The line in the figure traces the convection velocity of one such structure in between an actuator firing (the whiter regions in Figs. 4.12(b), (c), and (d)) and at the same simulation time in the baseline simulation. The convection velocity of the actuated case is approximately 13% higher than the baseline for both the 5% and 10% duty cycle forcing, giving $k_{\mathrm{c}} = 0.53$ and 19% higher for 20% forcing giving $k_{\mathrm{c}} = 0.57$. Using this k_{c} value and (4.9) along with the previous estimate for the increased speed of sound due to the heated cavity gives $f_{\mathrm{a}} = 155$ kHz, which is in agreement with the observed value in the actuated simulation's pressure spectrum. Equation (4.9) shows that increases in the convection velocity of the shear layer perturbations and increases in the speed of sound will also increase f_{a}. The forcing appears

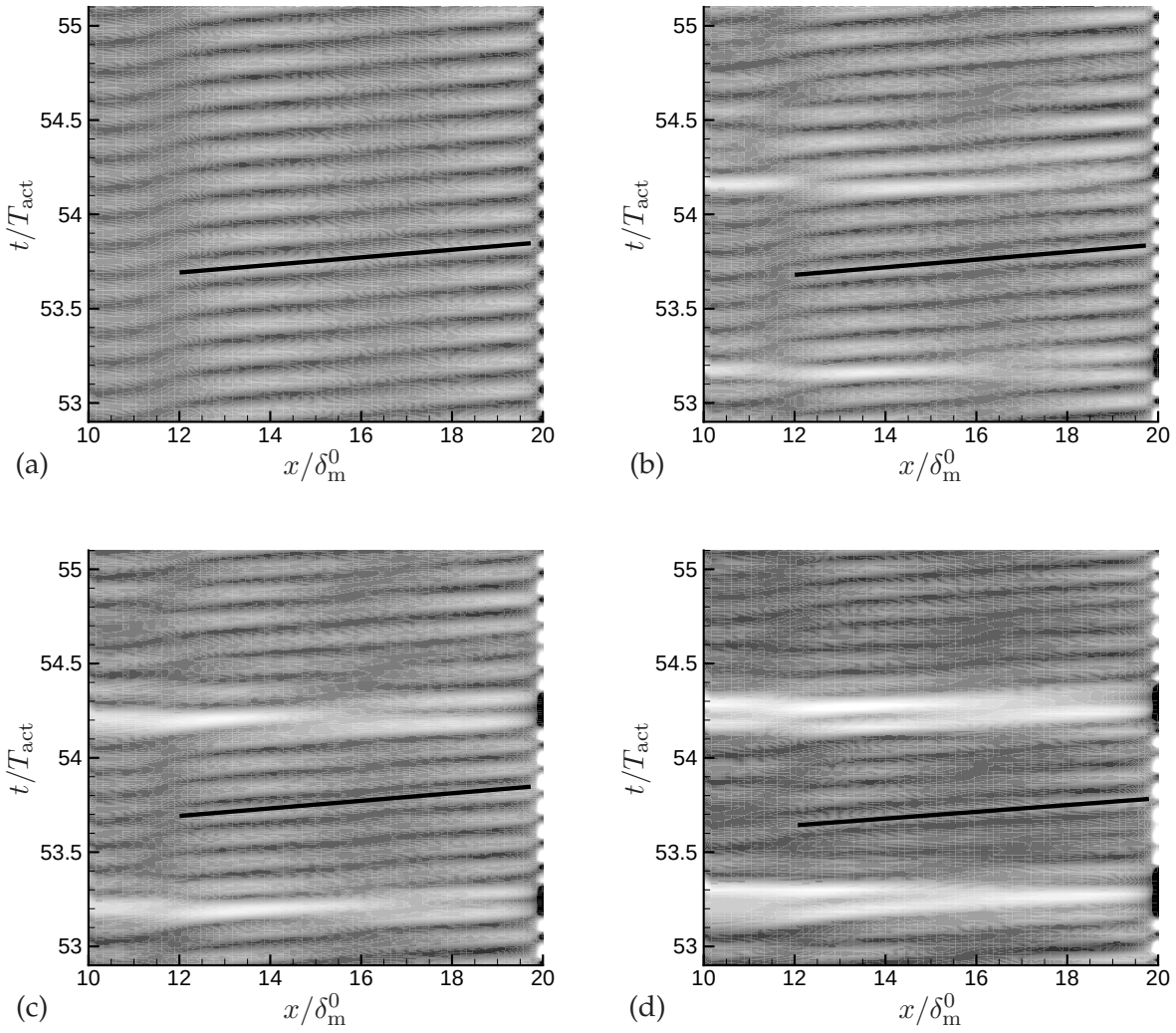

Figure 4.12: Pressure evolution at $y = 0$ for the (a) baseline and the actuated $L_{\rm c}/D_{\rm c} = 2$ cavity for two periods of actuator forcing $T_{\rm act}$ near the end of the entire simulation time series for (b) 5%, (c) 10%, and (d) 20% duty-cycle forcing. Contour levels of the fluctuating pressure over the interval $-0.03 < (p - p_\infty)/\rho_\infty c_\infty^2 < 0.03$ are shown with darker-shaded regions corresponding to $(p - p_\infty)/\rho_\infty c_\infty^2 < 0$. The lines in each pressure field trace the path of a vortical structure traveling over the cavity.

to be affecting both portions of the cavity oscillation feedback loop.

Deciphering the value of the modulating frequency $f_{\rm b}$, if it exists, to determine the possibility of Rossiter modes and sum components is hampered by the notable presence of what appear to be intermodulation modes in Fig. 4.10. These are seen as spectral peaks located at sum and difference frequencies between the cavity oscillation harmonics and the actuation frequency har-

monics. These interactions generate significant amplitude modulations at frequencies not related to the cavity or the spectrum of $w(t)$ and thus further complicate the analysis. The close proximity of f_{a} to $8f_{\mathrm{act}}$ (a 4 kHz difference) is possibly the reason for the many harmonics of f_{act} showing significant peaks offset by the same interval. The peak at f_{a} appears to be augmented by several dB due to one of these interaction peaks centered at 156 kHz. A low-frequency peak is visible in Fig. 4.10(b) at exactly 4 kHz and appears to be the frequency responsible for the majority of the modulation in the spectrum.

Figure 4.10 does provide some evidence of f_{b} in the cavity pressure spectrum. There are several frequency bands that show the spectrum increasing in amplitude between the harmonics of f_{a}, temporarily halting the steadily decreasing amplitude trend. These locations are most visible near 275 kHz, 430 kHZ, and 585 kHz and correspond to frequency differences of 37 kHz, 38 kHz, and 39 kHz, respectively, from the next highest harmonic of f_{a}. Considering the average difference to be $f_{\mathrm{b}} \approx 38$ kHz and reasonable similarity of these values leads us to label 275 kHz, 430 kHZ, and 585 kHz the second, third, and fourth Rossiter modes of the cavity under 10% duty cycle forcing. Using this f_{b} would suggest that $f_1 \approx 118$ kHz, which is reasonable since the frequency peaks at 116 kHz and 120 kHz are higher amplitude than the harmonics of f_{act} at 100 kHz and 140 kHz. Choosing this f_{b} also gives $\alpha = 0.24$, which is very close to the commonly accepted value of the phase-lag constant although varying slightly higher compared to the baseline case.

4.8.3 Cavity Pressure Spectra for Varying Duty-cycle Forcing

Figure 4.13 shows the cavity pressure of actuated simulations with forcing of 5% and 20% duty cycle, with 10% repeated for comparison. The spectra are computed by the same process and at the same location as the baseline and 10% duty cycle forcing in previous sections. As with the 10% duty cycle forcing already presented, the harmonics of f_{act} dominate the pressure spectra of the 5% and 20% cases for frequencies below 100 kHz. The actuation produces the strongest pressure response in the 20% case where the SPL reaches about 142 dB at f_{act}. Despite the actuator being 'on' for a smaller fraction of the forcing period, the 5% case shows a maximum SPL of 135 dB whereas the 10% case shows the weakest amplitude at f_{act} with 125 dB.

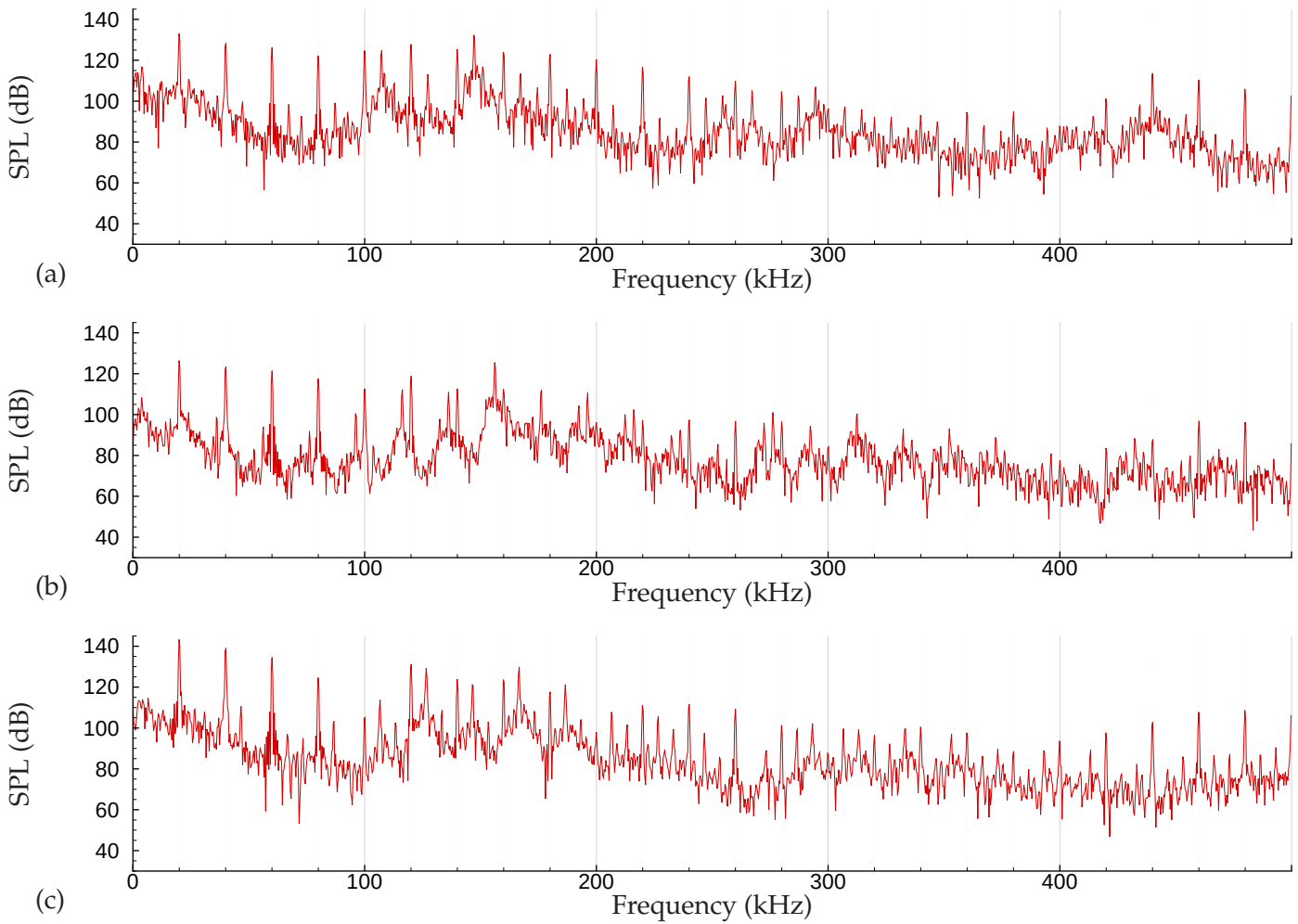

Figure 4.13: Sound pressure levels computed at $(x, y) = (15, -5)\,\delta_{\mathrm{m}}^{0}$ showing the cavity pressure spectrum for the $L_{\mathrm{c}}/D_{\mathrm{c}} = 2$ cavity of the actuated 20 kHz simulation. (a) 5% duty cycle forcing, (b) 10% duty cycle forcing, and (c) 20% duty cycle forcing.

Above 100 kHz, intermodulation modes between the cavity oscillation modes and actuator harmonics become significant in amplitude for all three cases. For the 5% case, the interaction frequencies occur at 7 kHz above the harmonics of f_{act} and about 6.6 kHz above for the 20% duty-cycle forcing case. These frequencies appear to be the result of nonlinear interactions with significant peaks that we interpret as the fundamental aeroacoustic loop frequency. Beginning with the 5% case, broad yet significant peaks occur in pairs at 108 kHz and 147 kHz, 255 kHz and 296 kHz, and 400 and 441 kHz in Fig. 4.13(a). Since the second frequency of these three pairs are harmonics, we assume $f_{\mathrm{a}} = 147$ kHz with $f_{\mathrm{b}} = 40$ kHz and the first frequency of the three pairs to be f_1, f_2, and f_3, respectively.

Determining f_{a} and the Rossiter modes of the 20% case is not as clear as the other two cases. Figure 4.13(c) shows bumps in the spectra centered around 124 kHz, 145 kHz, 166 kHz, and 188 kHz. We can expect that f_{a} will be higher than 156 kHz in the 10% case since the longer actuator 'on' time corresponds to a higher temperature in the cavity region. Using the same technique of integrating the mean speed of sound in the cavity as presented in (4.16) and the observed convection velocity in Fig. 4.12(d), we calculate $f_{\mathrm{a}} = 169$ kHz. Taking this calculation as a guide, it is reasonable to suggest $f_{\mathrm{a}} = 166$ kHz with $f_{\mathrm{b}} = 42$ kHz. Assuming this gives $f_1 = 124$ kHz and follows the trend of higher oscillation frequencies for higher temperatures in the cavity region. The spectrum does not show recognizable cavity oscillation frequencies above 200 kHz.

4.8.4 Conclusions

Table 4.3 summarizes the results of calculating f_{a} using values from the simulation data for the three duty cycles and the resulting Rossiter mode parameters. Several major effects on the cavity oscillation frequencies are introduced by the actuator model. First, the actuation increases the apparent convective velocity of the large-scale structures in the shear layer. The convection velocity, and correspondingly k_{c}, increases by 13% with up to 10% duty-cycle forcing and 21% with 20% duty cycle forcing as summarized in Table 4.3. Second, heating from the actuation raises the speed of sound resulting in a faster acoustic communication between the trailing and leading edges of the cavity. Both the increase in convection velocity and speed of sound combine to shift the funda-

p_{dc}	$L_{\mathrm{c}}/U_{\mathrm{c}}$ (μs)	L_{c}/c (μs)	calculated f_{a} (kHz)	observed f_{a} (kHz)	% Error in f_{a}	k_{c}	α
baseline, 0%	4.67	2.92	—	131	—	0.47	0.17
5%	4.23	2.34	152	147	3.4%	0.53	0.27
10%	4.23	2.21	155	156	0.6%	0.53	0.24
20%	3.93	1.98	169	166 (?)	1.8% (?)	0.57	0.25 (?)

Table 4.3: Calculated values of the fundamental aeroacoustic frequency for the baseline and actuated cases. The convective and acoustic travel times from (4.9) are calculated from the k_{c} value acquired from Fig. 4.10 and via the mean speed of sound as in (4.16), respectively. The values of f_{a} are from Figs. 4.6 and 4.13.

mental aeroacoustic loop frequency to higher frequencies. The frequency ratio f_{b}, as interpreted from the viewpoint proposed by Delprat,[113] increases with the introduction of the actuation but does not appear to be affected significantly by changes in duty cycle.

4.9 Actuator Forcing Mechanisms

In this section we present the investigation of the actuator forcing mechanisms that drive the downstream response observed in experiments.

4.9.1 Cavity Region Visualization – A Jetting Effect

In this section several visualizations of the cavity region are presented in order to begin the description of the mechanisms by which the actuator forcing creates a perturbation that causes the downstream mixing layer to respond accordingly. We will focus on the actuation with $f_{\mathrm{act}} = 20$ kHz and a duty cycle of 10% as presented in §4.8.2, but will also present some results of simulations with varying duty cycle. We begin by stepping through several discrete times while the actuator is 'on' (the time instants are marked with dots in Fig. 4.3(a)) and viewing the response of the fluid in the cavity region to the forcing.

Visualizations of the instantaneous velocity vector fields in Fig. 4.14(a)–(h) show the two recirculation regions in the cavity, as might be expected for any cavity of aspect ratio $L_{\mathrm{c}}/D_{\mathrm{c}} = 2$. These zones were also seen in the mean velocity field in Fig. 4.8(b). The recirculation is driven, in

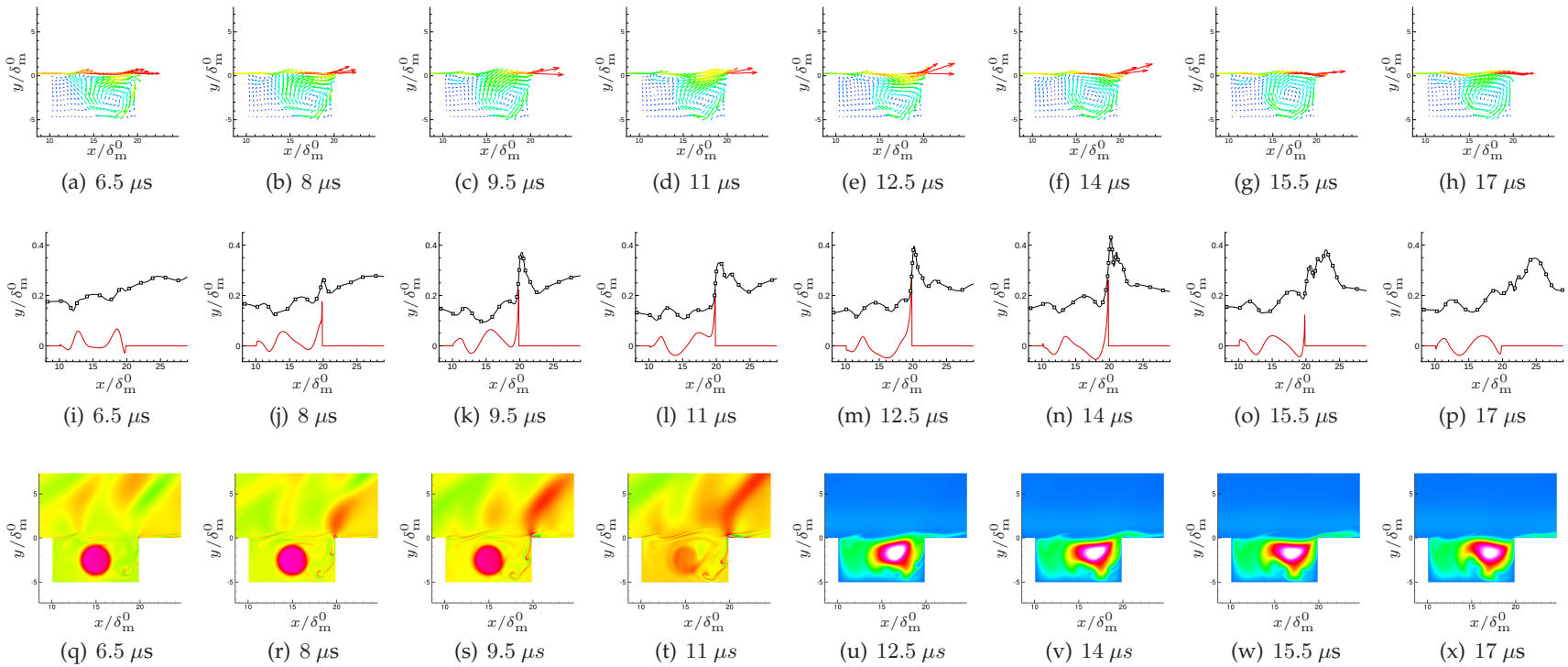

(a) 6.5 μs (b) 8 μs (c) 9.5 μs (d) 11 μs (e) 12.5 μs (f) 14 μs (g) 15.5 μs (h) 17 μs

(i) 6.5 μs (j) 8 μs (k) 9.5 μs (l) 11 μs (m) 12.5 μs (n) 14 μs (o) 15.5 μs (p) 17 μs

(q) 6.5 μs (r) 8 μs (s) 9.5 μs (t) 11 μs (u) 12.5 μs (v) 14 μs (w) 15.5 μs (x) 17 μs

Figure 4.14: Time series of instantaneous velocity, dilatation, and temperature in the $L_c/D_c = 2$ simulation with 10% duty cycle forcing. For reference, the dots in Fig. 4.3(a) mark the times in the forcing period which correspond to the vector fields shown. (a–h) Velocity vector field of the cavity during actuation. Each vector's length is proportional to its magnitude. (i–p) Cross-stream velocity v/c_∞ at $y = 0$ from $x = 10\,\delta_m^0$ to $x = 30\,\delta_m^0$, i.e. the top of the cavity along its width to the end of the "nozzle" (——) and the streamwise velocity at $y = 0.2\,\delta_m^0$ (- - ▫ - -). (q–t) Dilatation of velocity with colors varying between $-0.05\delta_m^0/c_\infty < \nabla \cdot \mathbf{u} < 0.05\delta_m^0/c_\infty$ The circular region of positive dilatation corresponds to the actuator model forcing. (u–x) Temperature fields in the cavity region with colors varying between 235 K (blue) and 1080 K (white). The times denoted in each figure represent the time after the beginning of the actuator period.

a sense, by the shear layer above the cavity, which forms at the leading edge where the upstream boundary layer detaches. As the actuator turns on starting at $t = 6.5$ μs, the upward fluid motion in the middle of the cavity, which is the upward part of the stronger, clockwise-recirculating flow, appears to be accentuated. A trace of the vertical velocity at $y = 0$ at this same time instant is shown in Fig. 4.14(i). The v-velocity shows two positive regions at $x = 13\,\delta^0_{\rm m}$ and $x = 18\,\delta^0_{\rm m}$. These locations correspond to the two vorticies forming over the cavity in the growing shear layer, and their spacing corresponds to the cavity oscillation frequency of $f_{\rm a} = 156$ kHz as reported in §4.8.2. The velocity vector field begins to show the characteristics of the fluid expanding radially outward from the cavity center. This is seen most clearly by the vectors pointing to the left and up in the top left quadrant of the cavity ($x < 15\,\delta^0_{\rm m}$ and $y > -2.5\,\delta^0_{\rm m}$). The cavity is known to be circulating in the counter-clockwise direction in this area (see the mean velocity vectors in Fig. 4.8(b)), and the velocity induced by the actuator accentuates this recirculation zone.

At $t = 8$ μs as shown in Figs. 4.14(b) and (j), the velocity vectors show the upward action of the recirculating flow and the forcing providing a net movement directly up and out of the cavity. The two vortices have convected further downstream with the first now over the center of the cavity and the second reaching the trailing edge. A spike in both u/c_∞ and v/c_∞ is seen at the trailing edge suggesting that the shear-layer vorticity there is also being displaced up and outwards (downstream) by the expanding flow. The velocity vectors confirm this. The circular region of high expansion (shown by positive dilatation of velocity) located in the center of the cavity, which corresponds to the actuator forcing in Figs. 4.14(q)–(t), drives the ejection of fluid out of the cavity.

By $t = 9.5$ μs, as seen in Figs. 4.14(c) and (k), cavity fluid is being ejected from the downstream edge of the cavity in what appears to be a jetting motion. At $t = 12.5$ μs, as seen in Figs. 4.14(e) and (m), this ejected fluid has a cross-stream velocity component that is a significant fraction of its streamwise component. Since the shear layer over the top of the cavity is a significant fraction of the cavity size, the ejected fluid is only pushed into the middle of the downstream boundary layer profile. The fluid does not penetrate far and is contained between the wall and $y = 1\delta^0_{\rm m}$. At this time the ejected fluid moves at higher velocities (both u and v) than the surrounding fluid. The streamwise velocity in Figs. 4.14(k–m) shows that the fluid not only is sent upward by the

expansion driving it from below, but it is also displaced forward by the boundary layer velocity pushing it from behind. Because of the thermal input from the actuator over several cycles, the fluid ejected from the cavity is hot and therefore can be clearly seen the temperature fields shown in Figs. 4.14(u)–(x). Even with obvious stretching and deformation of this ejected fluid by the boundary layer, by $t = 14$ μs there appears in Fig. 4.14(v) a nearly $\delta^0_{\rm m}$ thick layer of hot fluid on the wall just downstream of the cavity.

We also note that the analysis of the cavity pressure spectrum concluded that the actuation did not appear to disrupt the natural pressure oscillations of the cavity. This is consistent with what is seen in Figs. 4.14(g) and (h), which shows that another Kelvin-Helmholtz roll-up is already beginning to form over the top of the cavity just after the actuator has shut off.

The ejection of the hot fluid from the cavity suggests that part of the actuator's forcing mechanism may resemble more of a fluidic rather than a thermal actuator. The forcing cycle of the actuator is similar to a synthetic jet in the sense that no net mass is injected, but unlike typical synthetic jet actuators it is driven by the thermal expansion of the local fluid rather than a prescribed mechanical wall motion. Devices similar to LAFPA that cause rapid Joule heating by an electric arc discharge located at the bottom of a finite volume chamber with an orifice at the top also cause an ejection of hot fluid at high velocity.[80] We can therefore anticipate that if the actuator were more confined, as in a narrower cavity, a stronger ejection might be formed by the thermally-induced expansion. This was tested by decreasing $L_{\rm c}$ from $10\,\delta^0_{\rm m}$ down to $5\,\delta^0_{\rm m}$, thus making it one-half the width of the OSU cavity with a length-to-depth ratio of $L_{\rm c}/D_{\rm c} = 1$. In this configuration, the plasma model nearly fills the cavity recess.

Velocity visualizations of this narrow-cavity actuator are shown in Fig. 4.15. The recirculation in this case is now centered in the cavity. When the actuator is inactive as seen in Fig. 4.15(h), there are no obvious instabilities seen in the velocity field of the detached shear layer of the kind that were evident for the wider cavity as presented in Fig. 4.14(h), presumably because there is less distance for their amplification. However, when the actuator turns on, Fig. 4.15(c) shows that there is an even more prominent expulsion of fluid from the downstream edge of the cavity. If this jetting is important for the downstream evolution of the shear layer, we expect there to be a

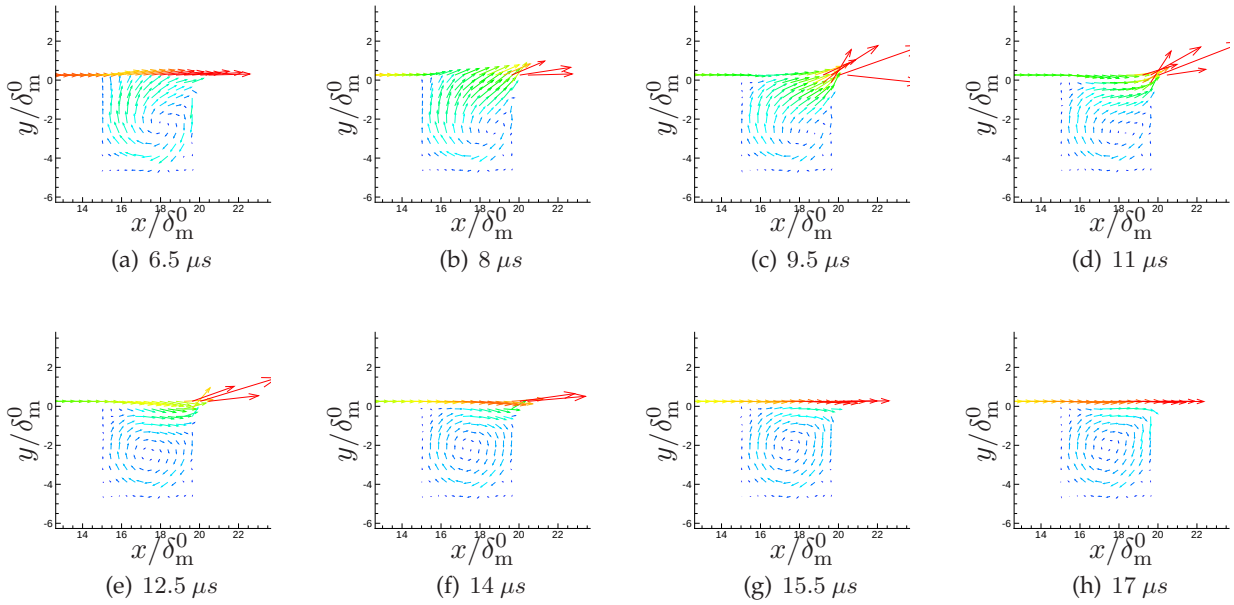

(a) 6.5 μs (b) 8 μs (c) 9.5 μs (d) 11 μs

(e) 12.5 μs (f) 14 μs (g) 15.5 μs (h) 17 μs

Figure 4.15: A time series of the velocity vector field of the narrower cavity ($L_c/D_c = 1$) during actuation. Each vector's length is proportional to its magnitude. For reference, the dots in Fig. 4.3(a) mark the times in the forcing period that correspond to the vector fields shown.

stronger response for this narrower cavity. We investigate this quantitatively in §4.9.3.

The amount of fluid mass expelled from the cavity when the actuator activates is shown in Fig. 4.16(a) for both the $L_c/D_c = 2$ and $L_c/D_c = 1$ cavities. Nearly the same amount of mass is expelled in both cases, peaking just after the end of the period of activation of the actuator despite the $L_c/D_c = 1$ cavity being one half of the width. The visualizations show that this ejection is also more focused by the narrower geometry of the cavity. The subsequent oscillations after the ejection as seen in Fig. 4.16 are the natural instabilities of the cavity and coincide with the dominant fundamental aeroacoustic loop frequency presented in §4.8.2. These cavity frequencies are not significant in the pressure spectra of the downstream flow region (see §4.10). The wider cavity has significantly stronger fluctuations, presumably because the instabilities of the shear layer can amplify to high levels before reaching the downstream edge.

Changing the duty cycle of the actuation only weakly affects the peak mass ejection. Ejected mass fluxes for the wider ($L_c/D_c = 2$) cavity are shown in Fig. 4.16(b) for 5%, 10%, and 20% duty cycles. There is more effective mass ejected from the cavity for the larger duty cycles while the

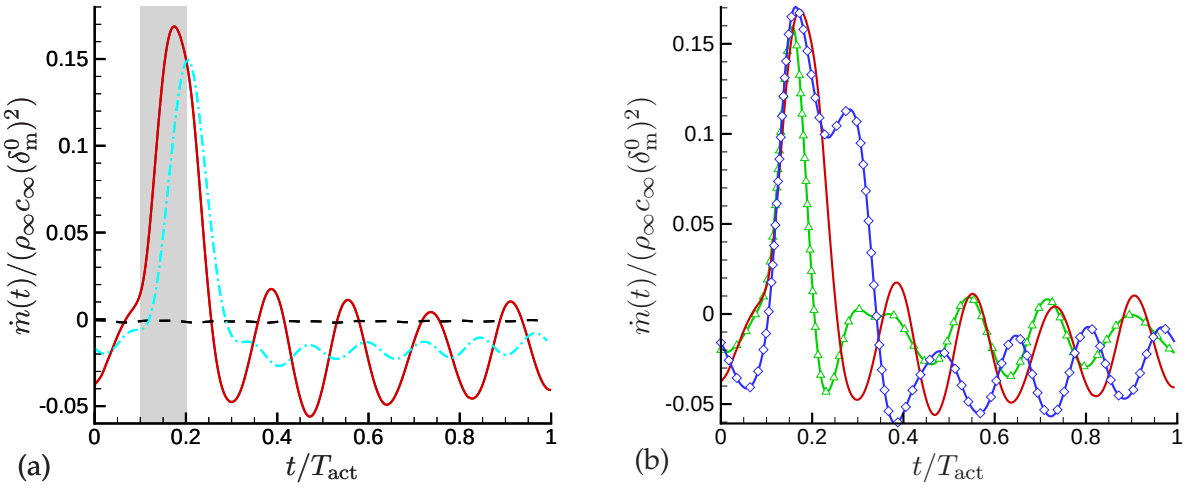

Figure 4.16: (a) Mass flux (per unit depth) out of the cavity calculated at $y = 0$ of the baseline (----), $L_c/D_c = 2$ (——), and $L_c/D_c = 1$ (—·—) cavities phase averaged over the forcing frequency, f_{act}. The grey region indicates the time the actuator was turned 'on' for 10% duty cycle forcing. (b) Mass flux (per unit depth) as in (a) but for three different duty cycles for the $L_c/D_c = 2$ cavity: 5% (— △ —), 10% (——), and 20% (— ◇ —).

actuator is on, but switching from 5% to 10% changes the overall mass ejection relatively little. At 20% duty cycle, it seems that the ejection interacts with the instabilities excited by the dominant cavity oscillation mode, giving the principal ejection another "bump" and putting the subsequent cavity oscillation 180° out of phase with those for the lower duty cycle cases. The 20% duty cycle is long enough for two of the vortical roll-ups advecting over the top of the cavity to be pushed upward by the actuation. We will see the ejection of these roll-ups for the 10% duty cycle case in §4.9.2.

4.9.2 Vorticity Generation in the Near-nozzle Region

While it is clear from the OSU experiments that the actuators are indeed effective at exciting the initial shear layers of an axisymmetric jet,[27] the precise mechanisms of this excitation have been difficult to anticipate. As discussed in §4.1, the principal effect of the actuator is thought to be thermal heating, so the question of how the actuator works is really how the thermal source comes to alter the vortical development of the downstream shear layer. A baroclinic torque is an obvious

candidate, wherein non-parallel pressure and density gradients, for example, can lead to the generation of vorticity and presumably thereby the vortical structures seen in a mixing layer. Still, the visualizations of the cavity region during actuation described in the previous section reveal what appears to be an important effect of the forcing in the cavity. The jetting of fluid from the cavity suggests perhaps a more direct interaction of the actuator with the boundary before it travels past the nozzle edge. We see a clear lifting of the boundary layer in Fig. 4.14, for example. The plasma heating in the cavity space caused a portion of cavity fluid to be ejected from the downstream side of the cavity as we see in the temperature fields of Fig. 4.14. In this section, we focus on the effect of the actuation on the downstream flow. We again focus on the $L_c/D_c = 2$ cavity geometry with 10% duty cycle forcing at 20 kHz.

To investigate the conversion of the imparted thermal energy into vortical disturbances, we appeal to the vorticity evolution equation for a two-dimensional, viscous, compressible fluid. The only non-zero component in two space dimensions is ω_z, which we simply call ω. The governing equation for ω is

$$\frac{\partial \omega}{\partial t} = -\underbrace{(\mathbf{v}\cdot\nabla)\omega}_{\dot{\omega}_A} - \underbrace{\omega(\nabla\cdot\mathbf{v})}_{\dot{\omega}_C} + \underbrace{\frac{1}{\rho^2}\nabla\rho\times\nabla p}_{\dot{\omega}_B} + \underbrace{\nabla\times\left(\frac{\nabla\cdot\boldsymbol{\tau}}{\rho}\right)}_{\dot{\omega}_D}. \tag{4.25}$$

The terms on the right-hand side are as follows. The first term ($\dot{\omega}_A$) corresponds to vorticity advection via the local flow velocity. The vorticity-dilatation term ($\dot{\omega}_C$) is the product of velocity dilatation ($\nabla\cdot\mathbf{v}$) with vorticity, and describes vorticity intensification due to the compressibility of the fluid. The $\dot{\omega}_B$ term is the baroclinic torque and contributes to vorticity generation when density and pressure gradients do not align. The last term is the vorticity diffusion term ($\dot{\omega}_D$) and accounts for diffusion due to viscous effects with $\boldsymbol{\tau}$ from (2.8).

Fluid Injection into the Boundary Layer

We begin by visualizing the terms of the vorticity evolution equation as well as the flow density, temperature, pressure, and dilatation in Fig. 4.17. The time chosen here, $t = 15.5$ μs matches the beginning of the actuation cycle and corresponds to the cavity visualizations in Fig. 4.14(g).

The effect of the actuation is the production of significant gradients of vorticity, density, and temperature in the boundary layer above the wall. The induced thermal expansion of the fluid in the cavity along with the upward flow of the recirculation region cause hot, low density fluid to be ejected from the corner of the cavity into the boundary layer over the wall downstream of the cavity. This process was described by the velocity vector visualizations and mass flux curves presented in the previous section. As visible in the plot of ω in Fig. 4.17(a), the ejected fluid is relatively irrotational and is forced into the boundary layer in seemingly the same fashion as seen in simulations of synthetic jets actuating flat-plate boundary layers.[117] Peak streamwise velocity at this time in Fig. 4.14(o) reaches nearly double the free-stream streamwise velocity at this time and location above the wall. The actuation pushes the hot cavity fluid up into the boundary layer and also forward at a locally higher velocity. The boundary layer is now stratified with colder, denser, high vorticity fluid above and below the ejected fluid. An irrotational layer exists between the shearing mean flow above and the high-shear region below due to the no-slip wall.

The baroclinic torque ($\dot{\omega}_{\mathrm{B}}$) in Fig. 4.17(b) shows the results of the cross-stream density gradient and a streamwise pressure gradient in the region $20 < x/\delta^0_{\mathrm{m}} < 25$. However, it is worth mentioning that $\dot{\omega}_{\mathrm{B}}$ is mostly absent beyond this region. We see vorticies beginning to form in ω beyond the nozzle edge ($x/\delta^0_{\mathrm{m}} > 30$) at a spacing determined by the vortex shedding frequency of the cavity. The high rates of change in vorticity at times before the ejected cavity fluid reaches the nozzle edge is mainly the result of the advection term $\dot{\omega}_{\mathrm{A}}$. Note that the vorticity presented here is negative for clockwise rotation. Therefore, negative dilatation (black regions in Fig. 4.17(f)) produces negative vorticity in the vorticity-compressibility term in Fig. 4.17(c) and negative regions of the vorticity-advection term in Fig. 4.17(d) produce negative vorticity.

We also observe from in Fig. 4.17(a) that the timing of the ejection of fluid by the actuator coincides with the fluid that is periodically ejected by the natural cavity resonance mechanism. The phase-averaged mass flux profiles presented in Fig. 4.16 also indicate that fluid mass ejected by the natural forcing of the cavity oscillations and by the actuator's external forcing tend to coincide. The fluid ejected by the cavity naturally is seen as a higher (more negative) vorticity spot at $(x,\, y) = (24,\, 1.5)\delta^0_{\mathrm{m}}$, just above and to the right of the actuator-ejected fluid and labeled as vortex 'A' in the figure. Of the sources of vorticity in (4.25), only the $\dot{\omega}_{\mathrm{A}}$ term is active at this

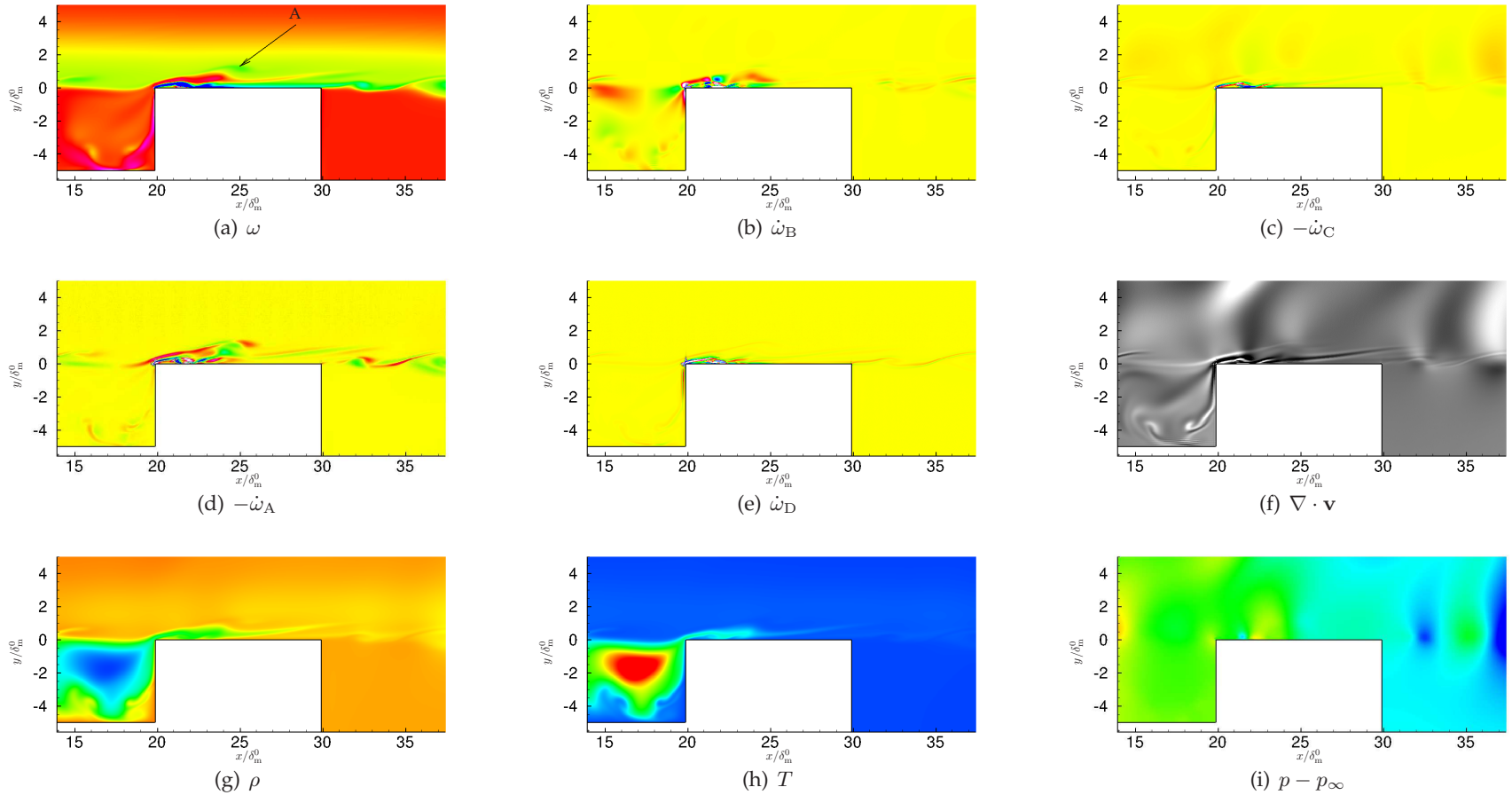

Figure 4.17: $L_{\mathrm{c}}/D_{\mathrm{c}} = 2$ cavity and near nozzle region 15.5 μs after the start of the actuation. (a) ω with colors varying between -1.3 (blue) and 0.7 (white) (red $= 0$) . Negative vorticity corresponds to rotation in a clockwise direction. (b) $\dot{\omega}_{\mathrm{B}}$ with colors varying between -0.05 and 0.05. (c) Negative of $\dot{\omega}_{\mathrm{C}}$ with colors varying between -0.05 and 0.05. (c) Negative of $\dot{\omega}_{\mathrm{A}}$ term with colors varying between -0.5 and 0.5. (d) $\dot{\omega}_{\mathrm{D}}$ with colors varying between -0.3 and 0.3. (e) Dilatation with colors varying between -0.01 (black) and 0.01 (white). (f) Density with colors varying between 0.2 and 1.1. (g) Temperature with colors varying between 250 K and 1000 K. (h) Pressure perturbation with colors varying between -0.1 and 0.1. For (b)–(d) and (f)–(h): maximum values in (red) and minimum values in (blue).

spot, suggesting that the vorticity is being redistributed by the local flow velocity. There is no baroclinic torque associated with vortex A, since it is not fluid ejected from the cavity interior due to the actuator, and thus is of temperature close to the ambient fluid above the cavity. This reveals that the actuation is, in a sense, lifting the boundary layer up and inserting much hotter fluid (about 40% hotter) than what is carried out of the cavity by the shear layer instabilities forming above it while the actuator is off.

Boundary Layer and Nozzle Edge Interaction

The flow at $t = 20\ \mu$s after the beginning of the actuation shows the downstream evolution of the nearly irrotational ejected fluid. It is stretched and elongated rapidly by action of the boundary layer's shear. The shearing has the effect of decreasing the overall wall-normal extent of the ejected fluid, but the low density, high temperature streak now extends further in the streamwise direction. The maximum temperature of the fluid above the wall downstream of the cavity has decreased to about $T = 400$ K, with a peak of $T = 497$ K at $t = 15\,\mu$s. The dilatation is strongly negative in the center of the ejected fluid because of this cooling.

At this time, the baroclinic torque is beginning to make more substantial contributions to the vorticity transport at the nozzle edge. The small positive and negative torque region is visible in Fig. 4.18(b) just above the edge due to the cross-stream density gradient in the ejected fluid as it reaches this point downstream. The torque is created when the ejected fluid interacts with the pressure difference located at the nozzle edge due to the vorticies forming there. As with the visualization in Fig. 4.17, the time rate of change of the vorticity is still dominated by the vorticity advection term. The growth of the instability waves in the mixing layer along with the gradual increase in entrained fluid causes the layer to thicken and spread. The $\dot{\omega}_{\mathrm{C}}$ term plotted in Fig. 4.18(c) does not become significant until locations downstream of the ejected fluid.

Perhaps the largest effect seen here in the visualization is ω in Fig. 4.18(a). Near $x = 33\,\delta^0_{\mathrm{m}}$ we see the ejected cavity fluid behind the spot of higher vorticity fluid (vortex 'A' in Fig. 4.17(a)) that was initially an instability wave forming over the cavity by the cavity oscillation feedback loop. With the ejection catapulting this spot into the boundary layer, it was placed into higher

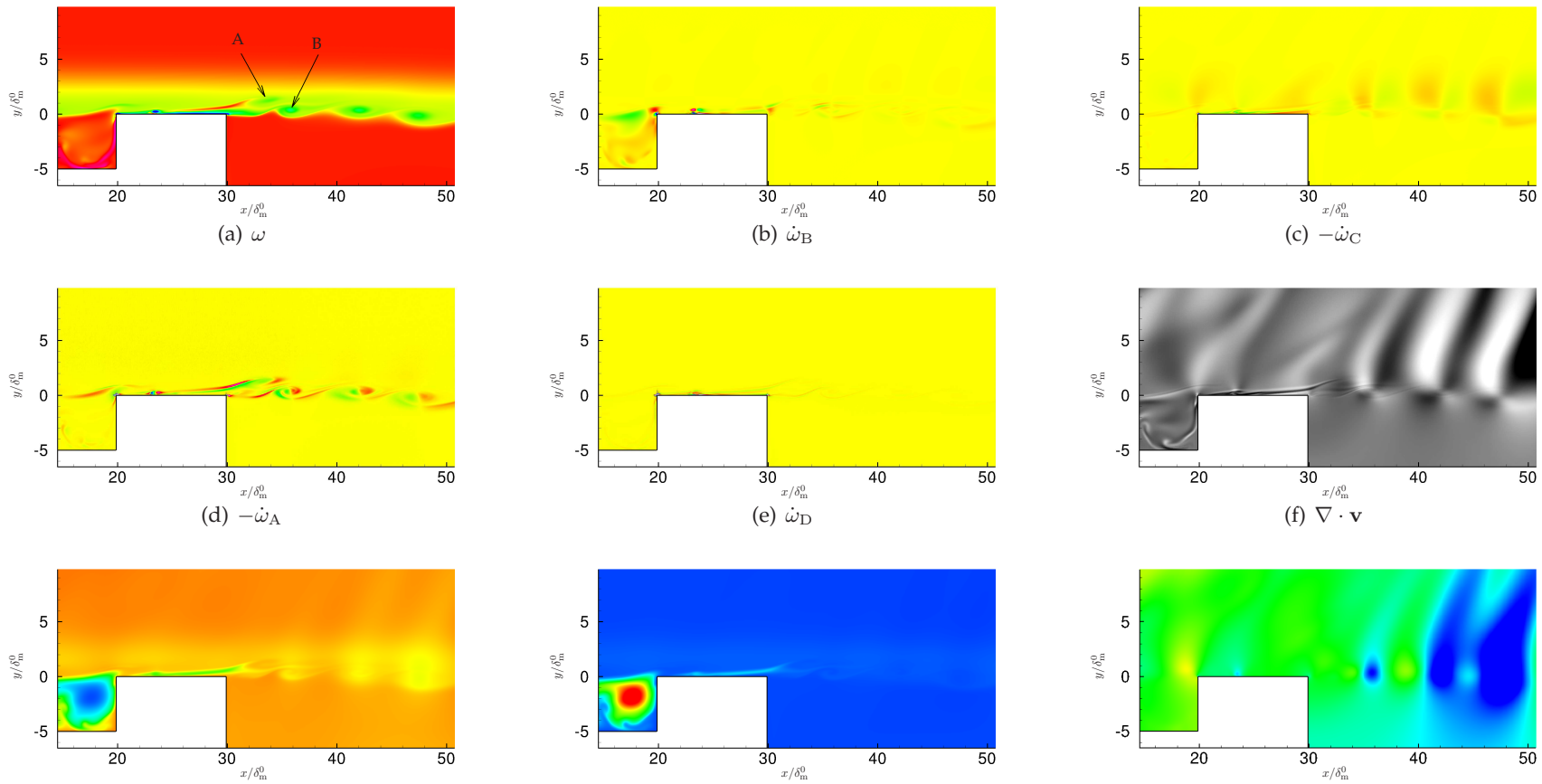

(a) ω (b) $\dot{\omega}_{\mathrm{B}}$ (c) $-\dot{\omega}_{\mathrm{C}}$

(d) $-\dot{\omega}_{\mathrm{A}}$ (e) $\dot{\omega}_{\mathrm{D}}$ (f) $\nabla \cdot \mathbf{v}$

(g) ρ (h) T (i) $p - p_\infty$

Figure 4.18: $L_{\mathrm{c}}/D_{\mathrm{c}} = 2$ cavity and near nozzle region 20 μs after the start of the actuation. See Fig. 4.17 for legend and contour values of the fields shown.

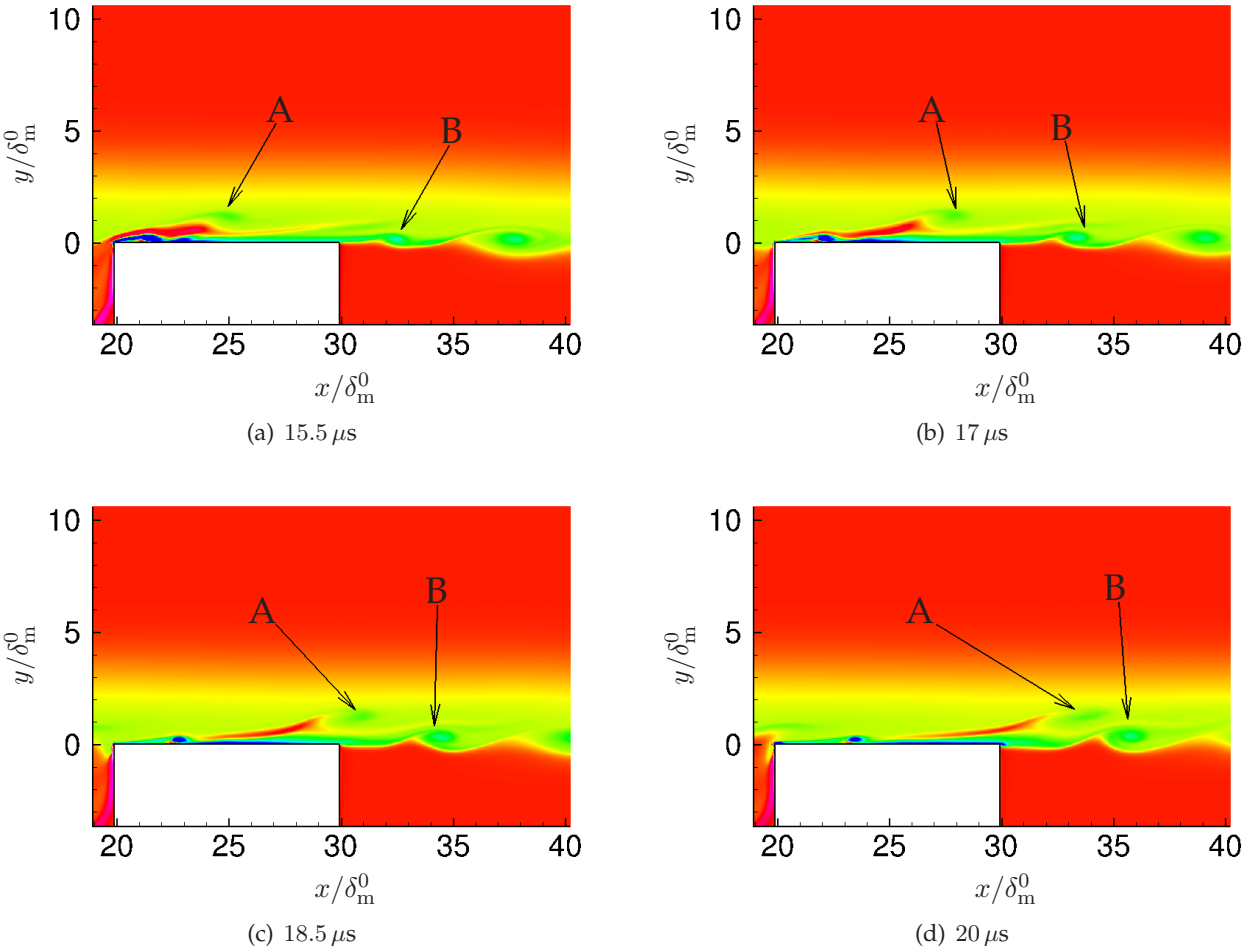

(a) 15.5 μs (b) 17 μs

(c) 18.5 μs (d) 20 μs

Figure 4.19: Visualization of the $L_c/D_c = 2$ cavity and near nozzle region for several times after the start of the actuation cycle. ω is shown with colors varying between -1.3 (blue) and 0.7 (white) (red $= 0$). Negative vorticity corresponds to rotation in a clockwise direction. See text for description of labeled vorticies A and B.

streamwise velocity fluid and pushed out in front of the ejected hot cavity fluid. We now observe this spot being sheared by the boundary layer and moving over the top of one of the vortices forming in the mixing layer. The actuation appears to be causing a forced merging of vortical structures: one that was forming over the cavity (labeled 'A' in the figure). Vortex A was forced forward to interact with a separate vortex forming in the initial region of downstream mixing layer (labeled 'B' in the figure). Figure 4.19 shows the progression of vortex A as it travels to come into the influence of vortex B for time snapshots between Fig. 4.17(a) and Fig. 4.18(a).

Vortex Roll-up and Merging

At $t = 26\ \mu$s after the beginning of the actuation cycle, the effects of the actuation is clearly causing the mixing layer beyond the nozzle to roll-up in a manner different than it does naturally. Visualizations in Fig. 4.20 show that the hot ejected cavity fluid has been rolled-up upon itself and has formed a single vortex centered at $x = 34\,\delta^0_{\mathrm{m}}$. The density and temperature fields show that this vortex is relatively low density and high temperature because it contains fluid expelled from the cavity. The baroclinic torque experiences its highest magnitudes at this time. This suggests that the subsequent roll-up, not the formation, of this vortex is due to the temperature imparted to the boundary layer by the ejected fluid from the actuation. While the baroclinic torque appears to play an important role at this instant, we see in Fig. 4.18(a) that this vortex was already beginning to separate from vortex B when the baroclinic torque was not a significant factor in the vorticity transport equation as seen in Fig. 4.18(b).

The formation of this single vortex appears to be due mainly to the actuation causing the pairing of vortex A and vortex B because of the jetting effect. Vortex A and vortex B denoted in Fig. 4.18(a) are shown to have reversed order in Fig. 4.20(a) with vortex B now trailing A. The high velocity fluid created by the actuation that pushed vortex A into the boundary layer has caused it pass over the top of vortex B. Both of these vorticies are now merging with the vortex previously downstream of them and beginning to coalesce into one structure. In addition, we also note that between $35 < x/\delta^0_{\mathrm{m}} < 40$ a braid region appears where the vortex closest to the nozzle edge with high baroclinic torque magnitude is separating from the group of three vorticies downstream which include vortex A and B.

In summary, the effect of the actuator in the near field of the nozzle exit appears to be realized by the combination of two factors. First, there is a "forced" pairing caused by the thermally-induced expansion in the confined cavity, which lifts one of the high vorticity spots (vortex A) associated with the cavity shear layer instability. This region of high vorticity is displaced into the higher-velocity fluid of the boundary layer and interacts with two vorticies rolling up in the mixing layer beyond the nozzle exit causing all three structures to merge together. Second, vorticity is generated by a baroclinic torque just after the nozzle edge which intensifies on the fluid that has

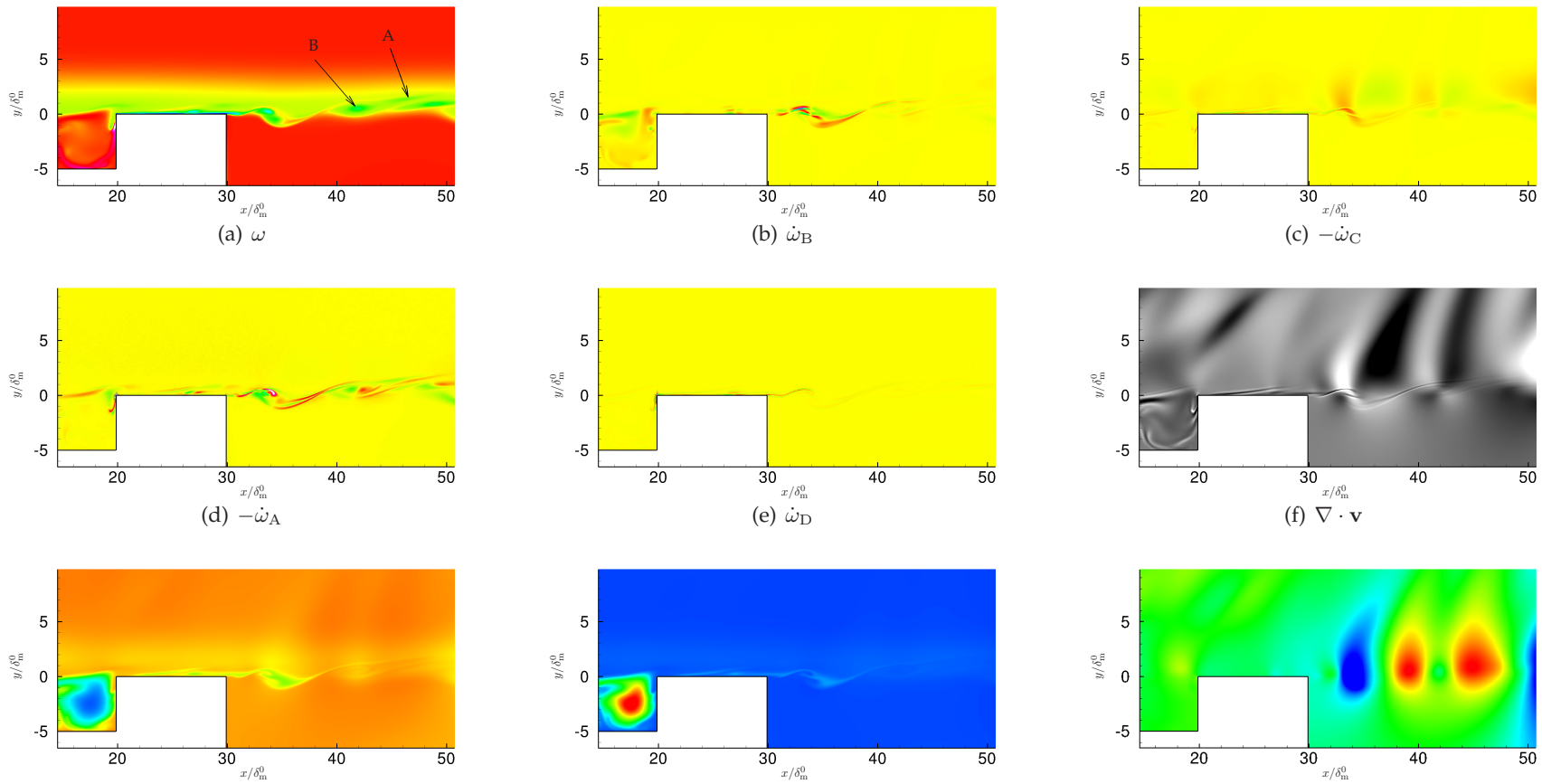

(a) ω (b) $\dot{\omega}_{\mathrm{B}}$ (c) $-\dot{\omega}_{\mathrm{C}}$

(d) $-\dot{\omega}_{\mathrm{A}}$ (e) $\dot{\omega}_{\mathrm{D}}$ (f) $\nabla \cdot \mathbf{v}$

(g) ρ (h) T (i) $p - p_\infty$

Figure 4.20: $L_{\mathrm{c}}/D_{\mathrm{c}} = 2$ cavity and near nozzle region 26 μs after the start of the actuation cycle. See Fig. 4.17 for legend and contour values of the fields shown.

rolled up and separated from the three merging structures just downstream.

We can contrast this with the vortex pairing of the baseline. Figure 4.21 shows the space-time evolution of the pressure at $y = 0$ (with the mean pressure removed) near the nozzle exit. Recall that the intersection of black regions in the figure correspond to the pairing/merging of vortical structures. The pressure is plotted for the actuation period visualized in the current section (0 to 50 μs) and the next actuation (50 to 100 μs) afterwards.

The baseline simulation shows a regular pattern of pressure perturbations just after the nozzle with a vortex shedding frequency equal to the cavity oscillation frequency. Pairing of the developing vortical structures is seen only rarely and sporadically for $x < 100\,\delta^0_{\rm m}$, but the majority of pairings occur much farther downstream. On the other hand, the actuated simulation shows a considerable number of pairings even before $x = 50\,\delta^0_{\rm m}$ including that of vortex A and vortex B with the vortex immediately downstream of them. These three vorticies are marked with the solid line in Figure 4.21(b) corresponding to the their location in Fig. 4.20(a). The actuation causes pairing to occur far upstream of where they would have occurred without external forcing as indicated by the previous vorticity visualizations.

4.9.3 Temperature and Cavity Effects

The previous section illuminated two apparent mechanisms by which the actuator affected the cavity and near nozzle flow. In this section we assess the relative importance of the higher fluid temperatures created by the actuator forcing versus their mass-source-like effect due to thermal expansion. The former is responsible for baroclinic torque effects, while the latter is responsible for the ejection behavior we observe. We proceed by introducing several reduced actuator models that are designed to remove either the temperature or the cavity from the full actuator model.

The first model we have developed we refer to as the alternative actuator source model and use it to study the actuator mechanisms with the cavity but in absence of the high temperatures. Using the conservation equations, we aim to provide a similar cavity forcing as $S_{\rm act}$ in (4.1), but instead manipulate sources in the equations to produce a comparable pressure response as $S_{\rm act}$,

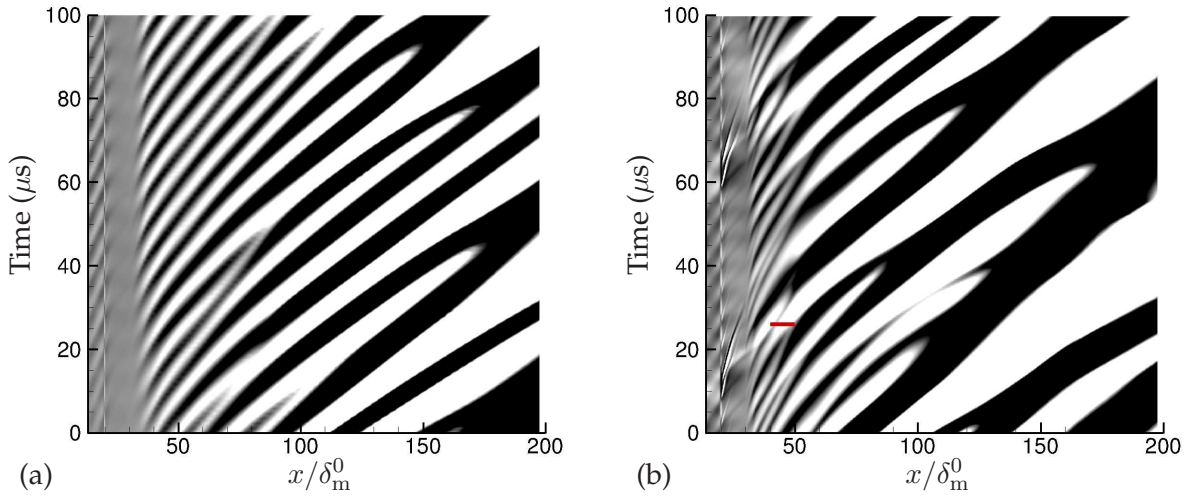

Figure 4.21: Pressure evolution at $y = 0$ for the (a) baseline and (b) actuated $L_{\rm c}/D_{\rm c} = 2$ cavity for two periods of actuator forcing. Contour levels of the fluctuating pressure over the interval $-0.03 < (p - p_\infty)/\rho_\infty c_\infty^2 < 0.03$ are shown with darker-shaded regions corresponding to $(p - p_\infty)/\rho_\infty c_\infty^2 < 0$ and lighter regions vice-versa. The solid horizontal line in (b) corresponds to the location and time of vortex A and vortex B (see text) merging in Fig. 4.20(a).

but without a rise in temperature. This, of course, requires manipulation of the governing equations, which is described as follows. The conservation equations for the flow density, momentum, and total energy with respective mass, body, and internal energy sources M, F_i, and E are

$$\begin{aligned} \frac{\partial \rho}{\partial t} + \frac{\partial}{\partial x_j}(\rho u_i) &= M \\ \frac{\partial \rho u_i}{\partial t} + \frac{\partial}{\partial x_j}(\rho u_i u_j) + \frac{\partial p}{\partial x_i} &= F_i \\ \frac{\partial e}{\partial t} + \frac{\partial}{\partial x_i}[u_i(e+p)] &= E. \end{aligned} \tag{4.26}$$

To reach our stated objective, we combine and manipulate these equations to get corresponding

equations for the density, pressure, and temperature. The result of this manipulation is

$$\begin{aligned}
\frac{\partial \rho}{\partial t} + u_j \frac{\partial \rho}{\partial x_j} &= -\rho \frac{\partial u_j}{\partial x_j} + M \\
\frac{\partial p}{\partial t} + u_j \frac{\partial p}{\partial x_j} &= -\gamma p \frac{\partial u_j}{\partial x_j} + (\gamma - 1)\left[E - u_j F_j + \frac{1}{2} u_j u_j M\right] \\
\frac{\partial T}{\partial t} + u_j \frac{\partial T}{\partial x_j} &= -\frac{(\gamma - 1)}{T} \frac{\partial u_j}{\partial x_j} + \frac{\gamma}{\rho}\left[E - u_j F_j - \frac{MT}{\gamma} + \frac{1}{2} u_j u_j M\right].
\end{aligned} \tag{4.27}$$

Our stated objective is to match the pressure that results from S_{act}, but without generating significant temperatures. That is, we should like to have

$$T_{\text{s}} = \frac{\gamma}{\rho}\left[E - u_j F_j - \frac{MT}{\gamma} + \frac{1}{2} u_j u_j M\right] = 0 \tag{4.28}$$

where the pressure source

$$P_{\text{s}} = (\gamma - 1)\left[E - u_j F_j + \frac{1}{2} u_j u_j M\right] \tag{4.29}$$

is modeled to generate the pressure from the actuated simulation. By choice, we set the body-force source $F_j = 0$ preferring to work with just M and E. Setting $T_{\text{s}} = 0$ gives

$$\frac{\gamma}{\rho}\left[E - u_j F_j - \frac{MT}{\gamma} + \frac{1}{2} u_j u_j M\right] = 0 \tag{4.30}$$

and substituting P_{s} to remove of E according to (4.29) gives

$$\frac{\gamma}{\rho}\left[\frac{P_{\text{s}}}{(\gamma - 1)} - \frac{MT}{\gamma}\right] = 0. \tag{4.31}$$

This we can solve for M and then use in (4.30) to solve for M and E in terms of P_{s}, with the result

$$\begin{aligned}
M &= \frac{\gamma P_{\text{s}}}{(\gamma - 1)T} \\
E &= \frac{P_{\text{s}}}{(\gamma - 1)} - \frac{1}{2} u_j u_j \frac{\gamma P_{\text{s}}}{(\gamma - 1)T}.
\end{aligned}$$

We assume that P_{s} has the same functional form as the actuator forcing source term S_{act}. This way P_{s} will have the same dominant pressure spectrum harmonics of f_{act} imparted by the time-dependent portion of the source $w(t)$. S_{act} in the full actuator model is implemented as an internal

(a) basic configuration (b) above wall (c) wall boundary condition on v and/or T

Figure 4.22: Basic (a) and reduced actuator models (b) and (c).

energy source, so from (2.9) it is natural to specify the pressure in terms of internal energy as $S_{\rm act} = P_{\rm s}/(\gamma - 1)$. With this, the mass and internal energy sources in the alternative actuator source model are

$$M = \frac{\gamma S_{\rm act}}{T} \tag{4.32}$$

$$E = S_{\rm act} - \frac{1}{2} u_j u_j \frac{\gamma S_{\rm act}}{T}. \tag{4.33}$$

These sources are now added to the governing equations for density (2.5) and total energy (2.7), and the simulation using the alternate actuator source is carried out in the same manner as the original actuator simulations.

Besides the alternative actuator source model just described, we also have developed three reduced actuator models to estimate the relative importance of the cavity, the jetting, and the effect of thermal heating on the downstream development of the mixing layer. Instead of specifying a new source model, these reduced models are reduced in the sense that they involve removing the cavity geometry from the simulation completely. In the first, the actuator is placed above the wall, in the experimental configuration for which the plasma appeared to break down as it was advected downstream of the electrodes by the flow.[85] Of course, in the simulation the thermal source does not advect away or break down like an actual plasma. This configuration is shown schematically in Fig. 4.22(b) where the actuator forcing $S_{\rm act}$ is placed directly in the boundary layer flow, centered at $(x_{\rm act}, y_{\rm act}) = (15,\, 5)\delta^0_{\rm m}$.

In the two other cases, both shown schematically in Fig. 4.22(c), the $L_{\rm c}/D_{\rm c} = 2$ cavity is re-

placed with a wall boundary condition with either the wall-normal v velocity or both v and temperature T taken from the full actuator simulation. For this boundary condition actuation, the needed data from the full cavity simulation was saved every one hundred time steps and cubic splines were used to interpolate it to provide the time-dependent wall boundary conditions. The Navier–Stokes characteristic boundary conditions were used to solve for the density on the wall in the same manner as it is solved everywhere else on the wall (see §4.4.2). However, the streamwise velocity, u, was set to zero as per the no slip condition. Imposing only v on the wall is loosely thought of as imposing a blowing/suction type boundary condition while omitting the effects of heating and the cavity. The advecting v-velocity fluctuations associated with the forming instabilities over the cavity are present in the boundary condition data, so this forcing is not simple stationary mass flux changes as a traditional blowing/suction boundary condition would provide. Prescribing v and T was done to remove the cavity effects but still maintain the jetting effect and heating components of the actuation.

We begin comparing these various actuator models and geometry configurations in Fig. 4.23(a) by presenting the momentum thickness of the downstream mixing layer for all of the simulations in Fig. 4.23 along with the baseline case. As expected, all of the actuated cases spread more than the baseline, but none of the reduced or alternative actuators match the spreading caused by the full actuator with the cavity. The fastest spread is for the narrow-cavity case, for which we anticipated improved response based upon the apparently stronger ejection of fluid out of the cavity. The narrow cavity increases the spreading by nearly 50% over the baseline case.

The actuator placed above the wall is seen to be the least effective of all. This behavior suggests that the cavity geometry is indeed necessary for eliciting a mixing layer response, beyond its role in stabilizing the plasma. This configuration does not allow for high temperatures to be retained from one actuation cycle to the next since all of the fluid heated by S_{act} is swept immediately downstream. The maximum fluid temperature generated by the actuation in this forcing configuration is 355 K at $(x_{\mathrm{act}}, y_{\mathrm{act}})$, or about 18% higher than T_∞. This is opposed to the simulation with the cavity, where the majority of the heated fluid remains to be reheated in the cavity from cycle-to-cycle with a small amount being expelled by the thermally-induced fluid ejection. The v-only case yields almost an identically weak response downstream to placing the actuator

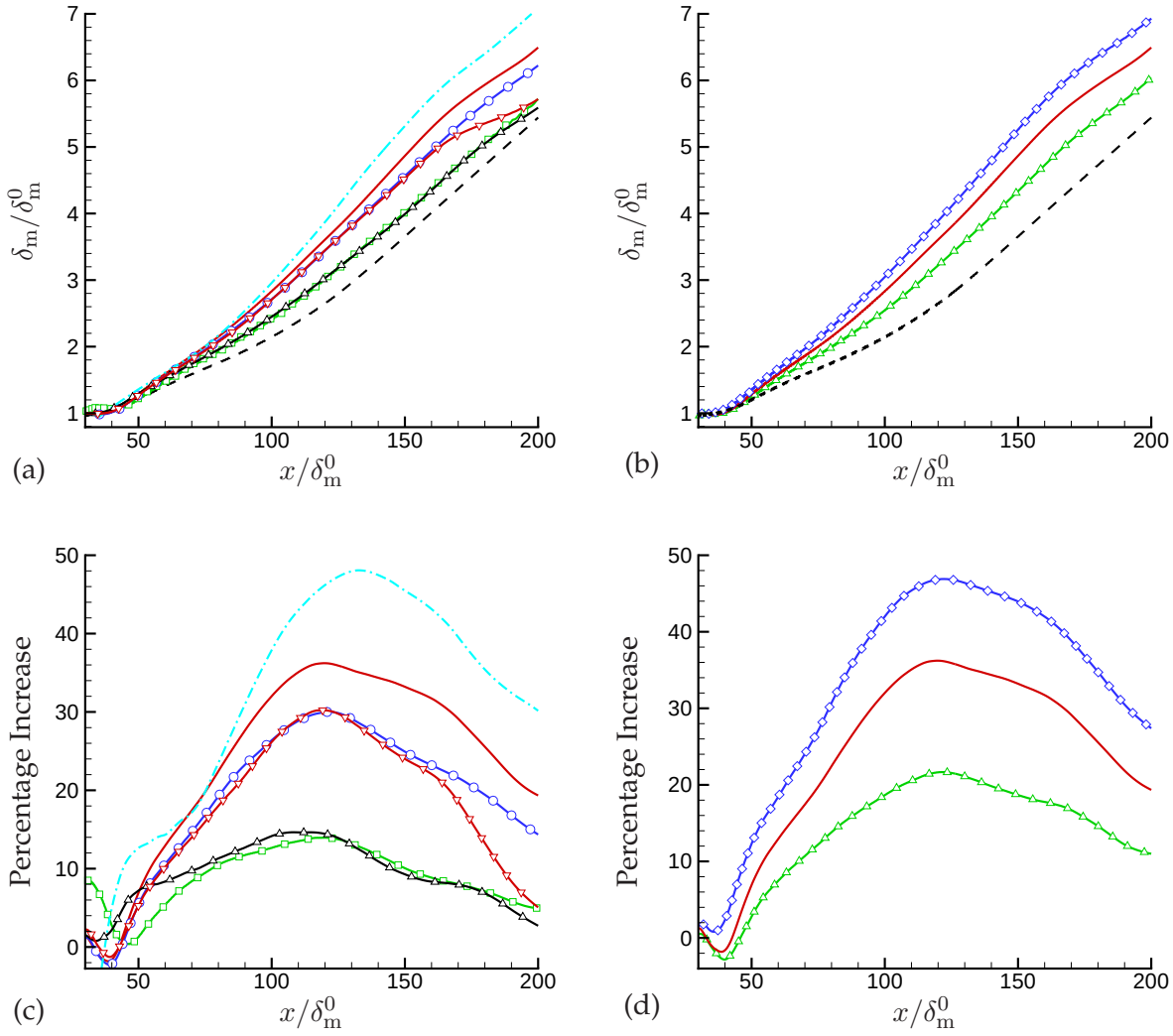

Figure 4.23: (a) Momentum thickness of the various simulations with and without the cavity with 10% duty cycle forcing. Curves indicate: baseline (- - - -), full cavity simulation (———), no cavity with v imposed (- □ -), no cavity with temperature and v imposed (- ○ -), narrow cavity ($L_c/D_c = 1$) simulation (— · —), actuator above wall (- △ -), and alternative actuator source (- ▽ -). (b) Momentum thickness for simulations with three different duty cycles for the $L_c/D_c = 2$ cavity: 5% (- △ -), 10% (———), 20% (- ◇ -), and baseline (no actuation) for comparison (- - - -). Percentage increase in momentum thickness over the baseline case for the 10% duty cycle cases (c) and for three duty cycles (d).

above the wall.

The mixing layer responds more strongly with both v and T wall forcing, suggesting some explicit thermal or density role in the subsequent amplification of the disturbances. The alternative

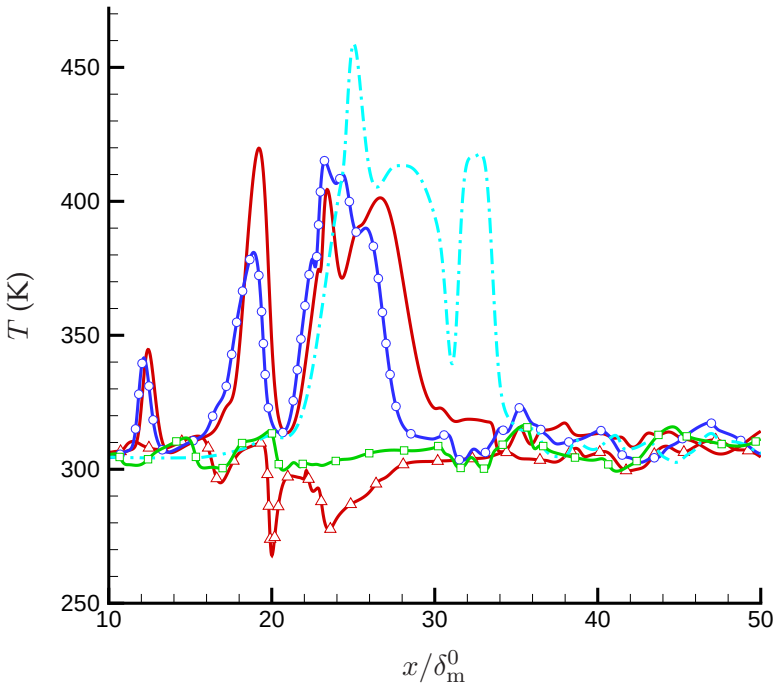

Figure 4.24: Fluid temperature of the simulations with 10% duty cycle forcing with and without the cavity just above the nozzle wall at $y = 0.25\delta^0_{\rm m}$ and $20\,\mu$s after actuation. Curves indicate: full cavity simulation (——), no cavity with v imposed (-▫-), no cavity with temperature and v imposed (-○-), narrow cavity ($L_{\rm c}/D_{\rm c} = 1$) simulation (—·—), and alternative actuator source (-▽-).

actuator source causes almost the same mixing layer growth response as only specifying v and T up until $x = 150\,\delta^0_{\rm m}$, where the alternative source simulation encounters a decrease in growth rate. It seems that this downstream growth-rate suppression is due to a difference in the dominant frequencies in the mixing layer. This appears to affect the vortex pairing behavior and growth rate as we will see in §4.10.

The alternative source and the full actuator source have similar growth responses even though the alternative source was designed to not produce the high temperatures created by $S_{\rm act}$. Figure 4.24 shows the fluid temperature evolution over the cavity and nozzle edge for all of the simulations at $20\,\mu$s after actuation (the same time as Fig. 4.18). The temperature is reduced by approximately 30% between the alternative source and the v and T reduced actuator above the

nozzle wall. We see that the alternative source model is successful in suppressing high temperatures associated with the full actuator model. It is also interesting to note that the rapid Joule heating that creates high temperatures in the cavity is the expected dominant mechanism the actuator forcing.[27] From Fig. 4.24 it is clear that the high fluid temperature (as high as 1800 K) in the cavity is significantly reduced by the time it is ejected from the cavity and begins to interact with the surrounding flow.

The disparity in temperature between the alternative source and simulations with a cavity suggests that the effectiveness of the actuator forcing in causing the downstream growth increase of the mixing layer is not directly due to its thermal forcing. Instead, the strength of the generated baroclinic torque appears to have a relationship with the observed growth response downstream. Figure 4.25 shows the baroclinic term of the cavity, narrow cavity, and other model simulations just as the first roll-up generated by the actuation (in the full cavity simulations) occurs. The snapshots of $\dot{\omega}_{\mathrm{B}}$ are ordered from (a) to (f) from highest torque magnitude ($\sqrt{\dot{\omega}_{\mathrm{B}}^2}$) occurring after $x = 30\,\delta_{\mathrm{m}}^0$ to the lowest, respectively. For most of the cases, the higher $\dot{\omega}_{\mathrm{B}}$ have the strongest downstream spreading in the mixing layer and decreasing torque is correlated with a decreased downstream growth. However, the maximum torque magnitude for the alternative source is about two and a half times smaller than the maximum torque magnitude in the v-and-T case, suggesting again that the thermal component of the actuator forcing is a secondary mechanism to the jetting fluid exiting the cavity. While greater baroclinic torques appear to correlate to larger growth rates for the simulations with the cavity, the alternative source and the v and T wall forcing grow with almost identical rates.

The essential difference between the v and T wall forcing and the full actuator simulation of the $L_{\mathrm{c}}/D_{\mathrm{c}} = 2$ cavity is the removal of the streamwise velocity component above the cavity. Not including it causes a reduction in growth rate on par with not ejecting fluid from the cavity at high temperature according to Fig. 4.23(a). In Fig. 4.26, we see the instantaneous cross-stream and streamwise velocity traces for the 10% duty cycle simulations just above the wall. These traces occur just as the fluid ejected out of the cavity by the actuator is pushed above the nozzle wall and before the boundary layer flow significantly deforms it. We have seen in §4.9.1 from the velocity vector visualizations and mass flux profiles that the vertical velocity is an indicator

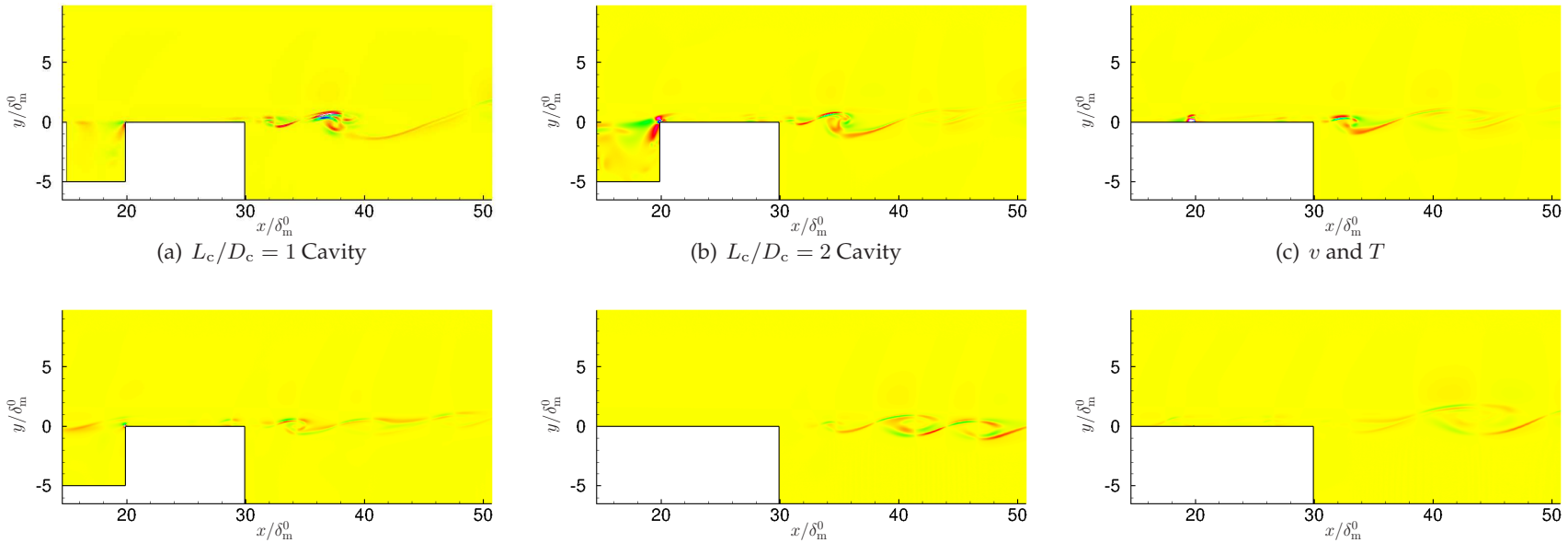

(a) $L_{\mathrm{c}}/D_{\mathrm{c}} = 1$ Cavity (b) $L_{\mathrm{c}}/D_{\mathrm{c}} = 2$ Cavity (c) v and T

(d) Alternative Source (e) Actuator above wall (f) v only

Figure 4.25: Baroclinic torque ($\dot{\omega}_{\mathrm{B}}$) in the near nozzle region 26 μs after the start of the actuation cycle for the actuated simulations with 10% duty cycle. Colors vary between 0.05 in red and -0.05 in blue (yellow $= 0$).

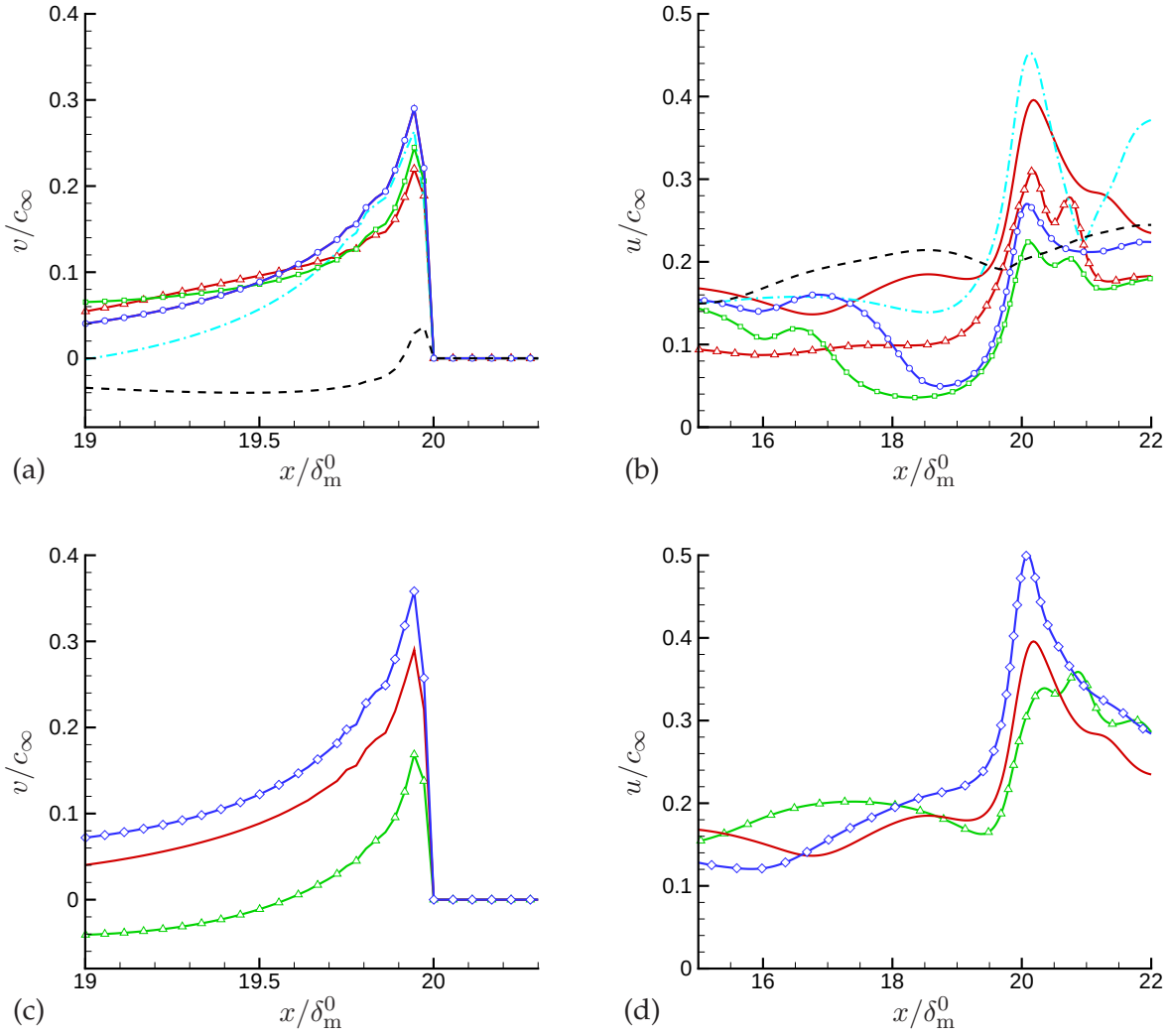

Figure 4.26: Profiles of v-velocity (a, c) at $y = 0$ and u-velocity (b, d) at $y = 0.25\delta^0_{\rm m}$ at $t = 12.5\,\mu$s after actuation. For the curves in (a) and (b): baseline (- - - -), full cavity simulation (———), no cavity with v imposed (-▫-), no cavity with temperature and v imposed (-○-), narrow cavity ($L_{\rm c}/D_{\rm c} = 1$) simulation (—·—), and alternative actuator source (-▽-). For the curves in (c) and (d): 5% duty cycle (-△-), 10% (———), 20% (-◇-).

of the cavity's fluid ejection, and now Fig. 4.26(b) shows that the actuation provides significant streamwise velocity augmentation as well. The trend of u-velocity magnitude follows the same trend of downstream mixing layer growth. While the v and T wall forcing and the full $L_{\rm c}/D_{\rm c} = 2$ cavity simulation have identical v velocities (by design), the streamwise velocity is reduced for the wall forcing to levels below that of the alternative source.

The effect of duty cycle on momentum thickness for the full actuator in the $L_c/D_c = 2$ cavity is shown in Fig. 4.23(b). We see an increase in response with increasing duty cycle, and the mechanisms for this follow the same trends revealed with the different actuator models. As the length of actuator 'on' time increases, the velocities that eject the fluid also increase and cause the mixing layer to grow faster. The 20% duty cycle forcing and the narrower $L_c/D_c = 1$ cavity forced at 10% spread at almost the same rates suggesting that the narrow cavity would provide similar control response for lower input power requirements.

4.9.4 Conclusions

The perturbation to the boundary layer is primarily due to the fluid ejected from the cavity recess. Mixing layers have long been known to be highly susceptible to this type of upstream forcing with modest responses realizable with $u'/U_\infty \approx 10^{-2}$ for a perturbation velocity u' and as low as 10^{-7} if the forcing is near the natural frequency of the layer.[25] From the instantaneous values shown in Fig. 4.26, the forcing provided by the actuator model is about $u'/U_\infty = 10^{-1}$ for both the v and u velocity increases above the baseline. The hot ejected fluid is deformed by the boundary layer and a region of high vorticity is concentrated just after the nozzle wall resulting in an immediate roll-up and the first sign of mixing layer response to forcing.

The baroclinic term in the vorticity evolution equation is active in the nozzle edge region due to the temperature difference between the ejected fluid and the surroundings. However, the alternative actuator source , which was designed to force at similar but lower temperatures, still causes the immediate roll-up as seen by vorticity snapshots in Fig. 4.27 despite significantly smaller baroclinic torque magnitude (see Fig. 4.25(d)). Reduced actuator models which forced with only v-velocity and v-velocity and temperature without the cavity yield a diminished mixing layer response downstream. Figure 4.26 suggests that the cavity is essential in producing both u and v to achieve maximum mixing layer response. Increasing the actuation duty cycle and reducing the cavity length increase the mixing layer spreading through higher perturbation velocities suggesting again that the magnitude of baroclinicity generated by the actuator is not as critical as the jetting effect.

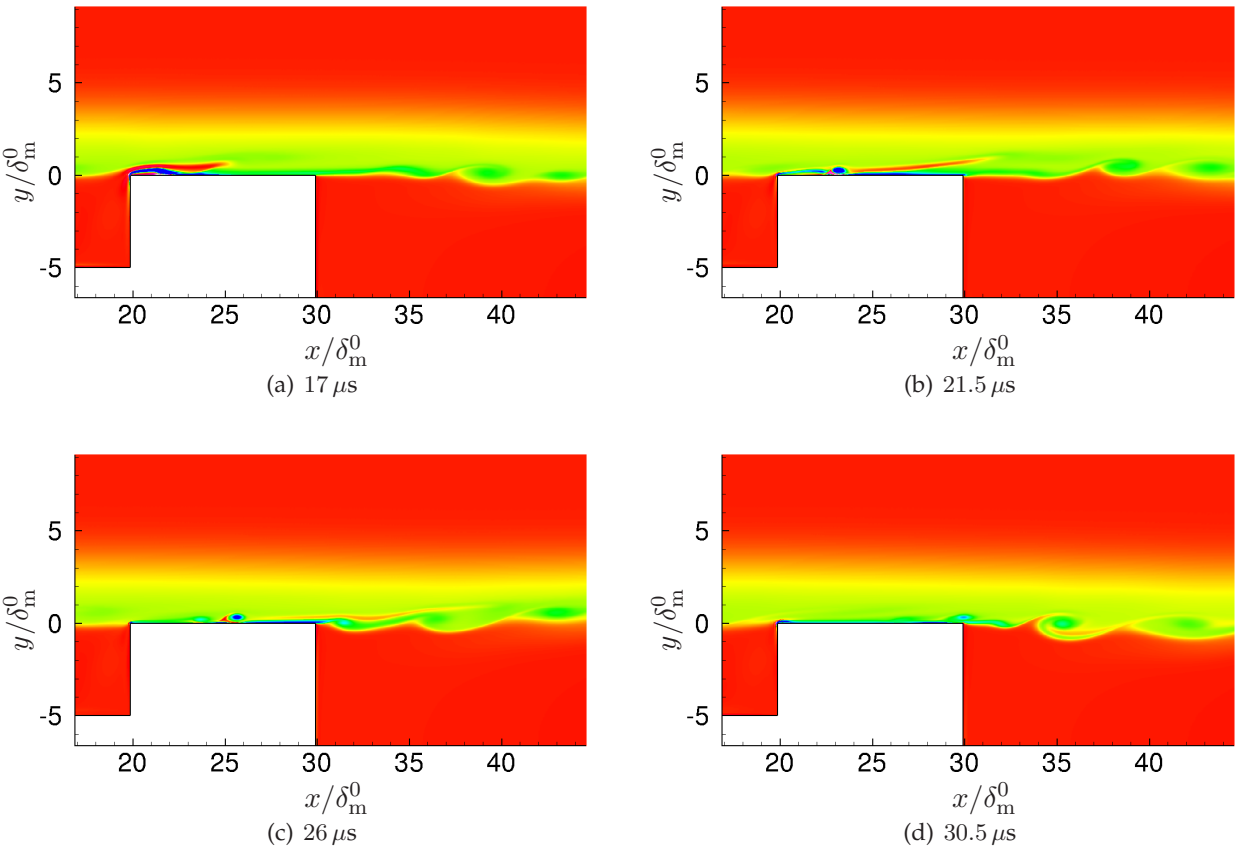

(a) 17 μs (b) 21.5 μs

(c) 26 μs (d) 30.5 μs

Figure 4.27: $L_{\mathrm{c}}/D_{\mathrm{c}} = 2$ cavity and near nozzle region at several times after the start of the actuation cycle for the alternative actuator source. ω with colors varying between -1.3 (blue) and 0.7 (red $= 0$). Negative vorticity corresponds to rotation in a clockwise direction.

4.10 Frequency Spectra

While the spreading of the mixing layer is an important measure of its response to the actuation, especially for mixing enhancement efforts, a principal concern and driving force for the development of the LAFPA technology is noise reduction, which has different objectives. In a related active noise-control study by Wei and Freund,[28] adjoint-based methods were used to find optimal actuations for suppressing radiated sound. These did not change the growth of the mixing layer, however. Instead, it seemed that their principal effect was to organize the flow structures so that they advected with more uniform velocity in the downstream direction. The 20 kHz actuation in the present study is also expected to also organize the unsteady flow structures. We assess how the actuation achieves this and compare the spectral response from this actuator to the reduced

and alternative actuator models.

Figure 4.28(a) shows the evolution of the pressure spectra downstream at $y = 0$ for the baseline simulation. There is energy in a broad range of frequencies, but even at $x = 200\,\delta_{\mathrm{m}}^{0}$, most of it is at frequencies higher than 20 kHz. The highest energy frequency, which also appears relatively far upstream, occurs at 55 kHz. We calculate from inviscid parallel-flow linear stability theory[118] that the most amplified mode is 57 kHz. By the end of the simulation domain, this peak has begun to decrease as the mixing layer pairs showing energy near the first subharmonic.

The effect of the actuator forcing in the full $L_{\mathrm{c}}/D_{\mathrm{c}} = 2$ cavity simulation in Fig. 4.28(b) is obvious and striking. The flow seems to be nearly perfectly organized into harmonics of the 20 kHz baseline forcing up to 80 kHz. Note that since the actuation has a square-wave like form, the nominally 20 kHz signal is indeed strongly dominated by harmonics of this frequency (recall Fig. 4.3(b)) in the mixing layer as it was in the cavity pressure spectrum. As with the pressure spectrum at $y = 0$, we see f_{act} and its harmonics with high amplitudes further upstream when the actuator is on compared to the baseline case. Figure 4.21 showed this to be the result of earlier pairing of vorticies caused by the actuator forcing. This result is also seen in the frequency distribution.

The sound pressure level of the baseline and actuated simulations is compared in Fig. 4.29 at $(x,\, y) = (200,\, -70)\,\delta_{\mathrm{m}}^{0}$. This denotes the bottom, downstream edge of the simulation domain. As mentioned earlier, Wei and Freund[28] showed that flow organization similar to what is seen here, without increasing amplitude, can suppress noise in the downstream acoustic field. Because the simulation domain was designed to capture the cavity and initial mixing layer forming after the nozzle edge, the location of the data presented in Fig. 4.29 cannot be considered the acoustic far field. It corresponds to $0.8D_{\mathrm{j}}$ downstream from the nozzle and only $0.25D_{\mathrm{j}}$ below it in experiments. Inspection of the pressure field show the hydrodynamic features of the mixing layer extend near to the edge of the simulation domain. Therefore, it is reasonable to expect that the actuation produces a louder response at this close location to the nozzle as is seen. Similar forcing parameters in experiments[27] show that the pressure amplitude is increased due to the actuation in this area. We see that the sound pressure level is increased over the entire frequency range. There are slight increases at the harmonics of f_{act} for the actuated simulation. No significant peaks are

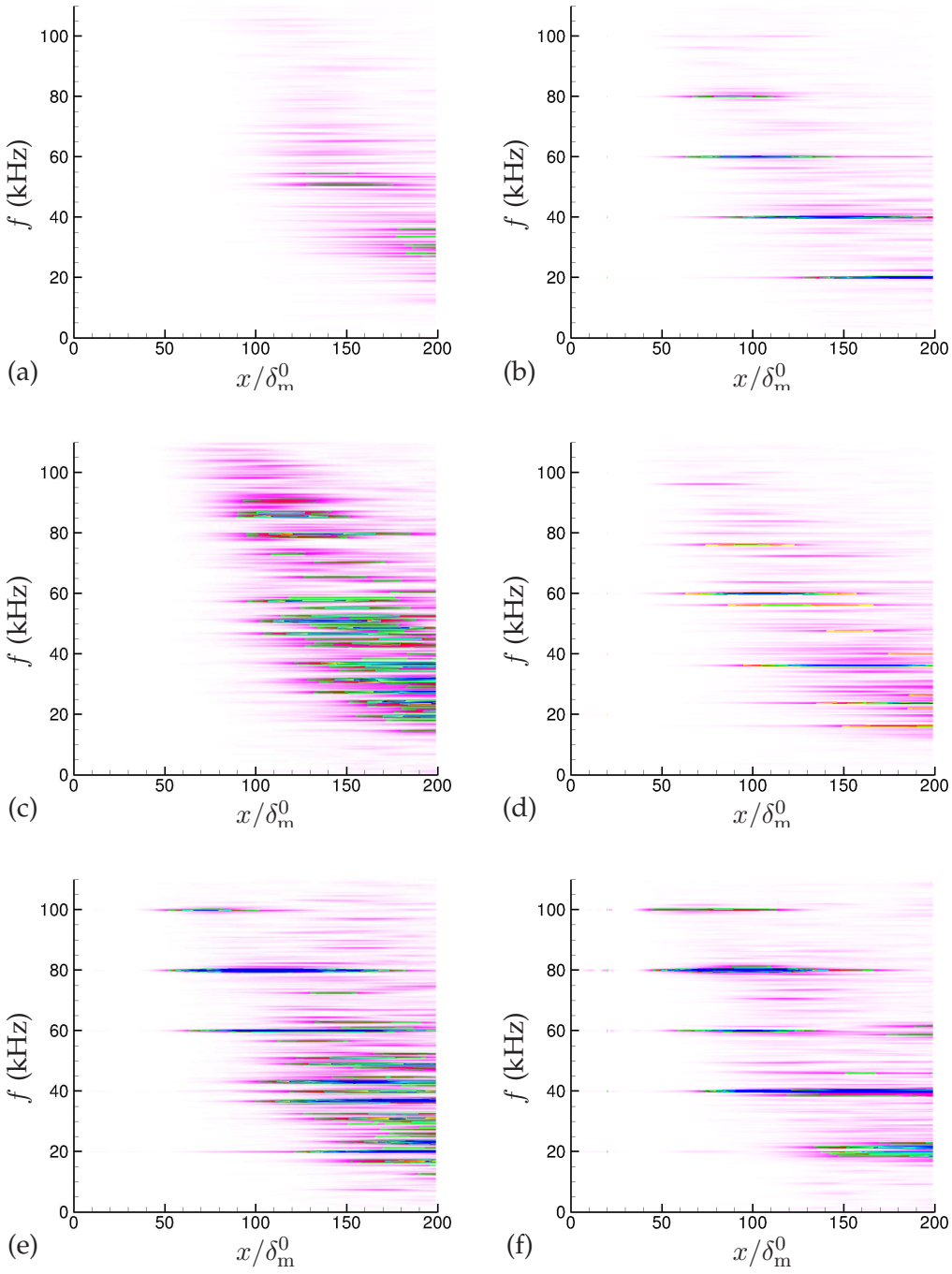

Figure 4.28: Pressure amplitude along $y = 0$ for the following simulations with 10% duty cycle forcing: (a) baseline (no actuation), (b) full cavity simulation, (c) v wall forcing, (d) v and T wall forcing, (e) actuator above wall, and (f) alternative actuator source model. Pressure is shown as a function of frequency (in kHz) and streamwise distance.

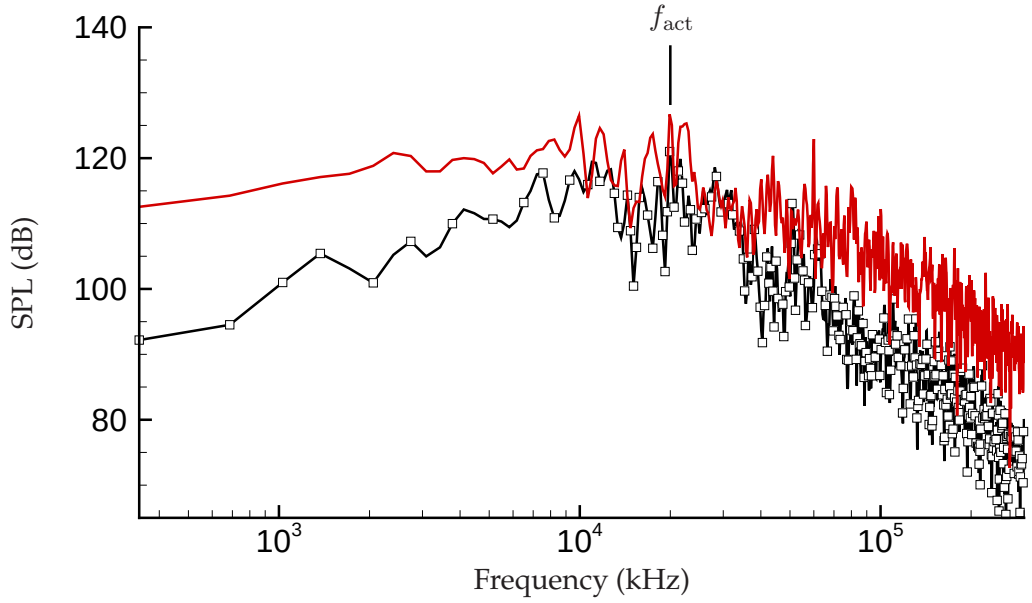

Figure 4.29: Sound pressure level of baseline (-▫-) and $L_c/D_c = 2$ cavity with 10% duty cycle forcing (——) simulations computed at $(x, y) = (200, -70)\delta_m^0$.

seen at any of the dominant cavity oscillation frequencies for the baseline or actuator-forced flow.

Focusing again on the frequencies on the centerline, for the v and the v and T boundary condition control cases, the spectral response shown in Fig. 4.28 is very different from the full actuator. The v-only boundary condition control fails to organize the pressure into tones, as seen in Fig. 4.28(c). The lack of organization by the v-only wall forcing again stresses the primacy of jetting effect mechanism caused by u and v velocity augmentation. Adding T input to this, improves the apparent organization, but nowhere near to the same degree as the cavity actuator control. The alternative source model, which includes a cavity and produces a similar jetting response as the original actuator, also organizes the structures in a similar manner to the full cavity simulation although slight differences are visible. This again suggests the temperature-related forcing mechanism to be secondary in the downstream response. Placing the 'plasma' actuator above the wall without a cavity, excites a response in the mixing layer at higher harmonics of f_{act} in Fig. 4.28(e), but the lower frequencies remain broad banded, again supporting the importance of the cavity recess.

For the cavity actuation, which organizes the flow into discrete frequencies downstream very effectively, it is interesting to track the development of the highest energy modes. Figure 4.30 shows that all of the disturbances grow up slowly from the relatively small perturbation provided by the actuator. For reference, the amplitudes of the harmonic frequencies of f_{act} are shown for the baseline case in Fig. 4.30(a), but it is clear from the scale of the figure that they have only a small fraction of the flow's energy. This baseline case also shows highest amplitude for 60 kHz, which is close to the expected most amplified natural frequency of 57 kHz.

When actuation is turned on, comparing the baseline to the actuated cases shows that the forcing creates dominant pressure amplitudes at the actuation frequency and its harmonics. The trend shows that as the duty cycle is increased, these frequencies become even stronger in the downstream shear layer. All four simulations show that f_{act} is still growing at the downstream end of the physical domain. The 5% duty cycle case has the strongest 80 kHz harmonic, though the reasons for this are unclear as it does not follow the same behavior as the other cases. The 80 kHz tone is shifted downstream and peaks at $x = 100\,\delta^0_{\mathrm{m}}$, well after the 10% and 20% cases. The 60 kHz and 80 kHz tones peak at the same location while the 40 kHz data has a relatively weak contribution. It is possible that the differences in the structure of the actuator forcing spectra shown in Fig.4.9 for each duty cycle may play a role in this observed difference in downstream frequency for the 5% duty cycle case. As seen in Fig.4.9(b), the magnitude of the 80 kHz harmonic for the 5% duty cycle forcing function approximated by $x(t)$ is almost the same magnitude as the lower harmonics, which is not the case for the 20% duty cycles for which f_{act} is almost four times as strong as the 80 kHz peak in $x(t)$. In the 5% duty cycle forcing case, with the amplitudes being essentially equal for the first four harmonics of forcing, the mixing layer apparently responds more to the 80 kHz mode.

As the duty cycle is increased, the progression of growth and subsequent decay of the harmonics with distance from the nozzle exit becomes closer to what is expected from linear stability analysis. Both the 10% and 20% simulations have a steady progression of stronger, lower frequency amplitude peaks as distance from the nozzle exit is increased. The ordering of these harmonics compared to the baseline translates into more efficient spreading (cf. Fig. 4.23). The higher duty cycle pairing appears to create a more orderly roll up of the large structures in the shear layer.

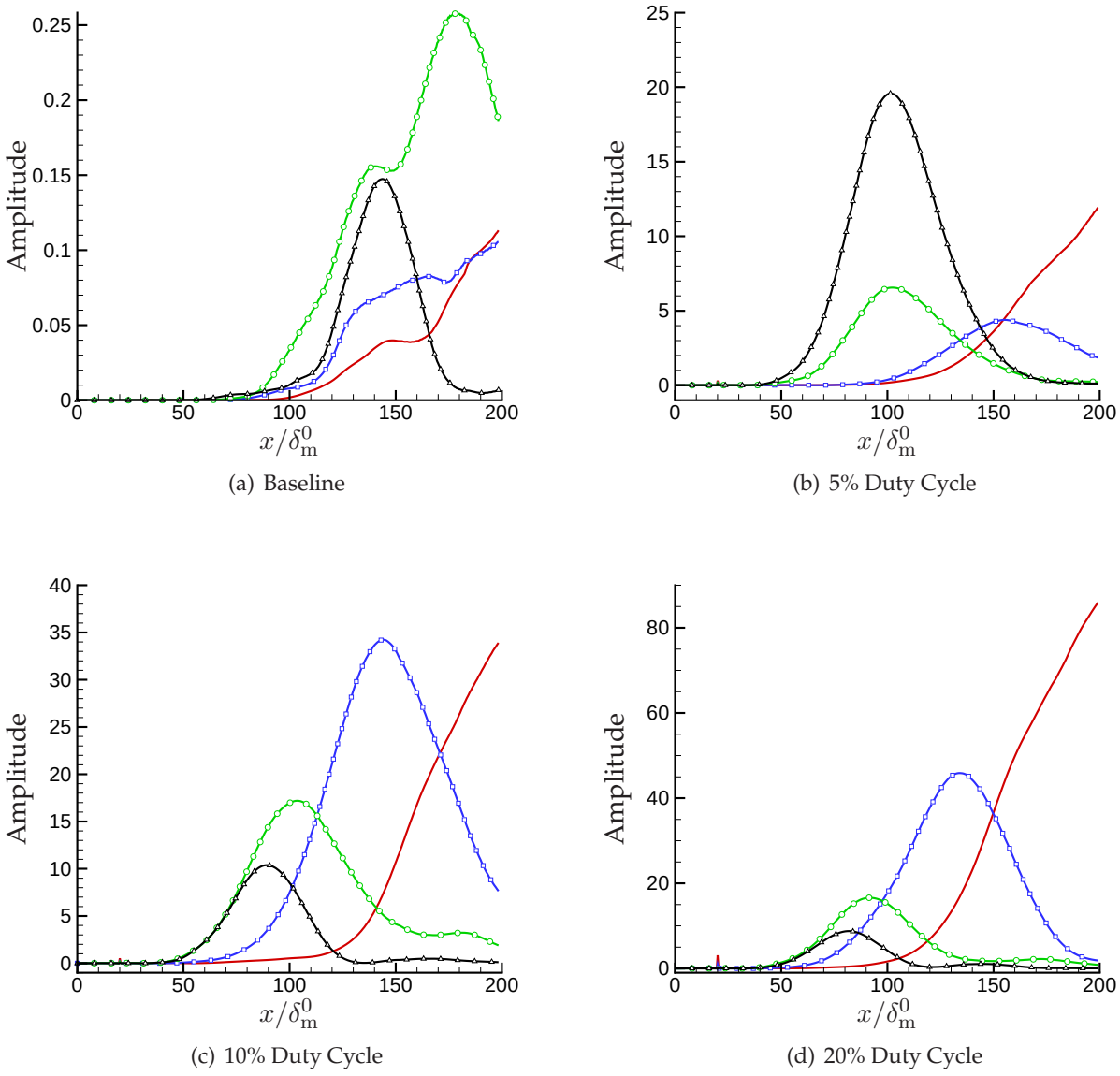

(a) Baseline

(b) 5% Duty Cycle

(c) 10% Duty Cycle

(d) 20% Duty Cycle

Figure 4.30: Streamwise variation of harmonics of forcing shown by pressure amplitude along $y = 0$ for the cavity simulations with (a) baseline (no actuation), (b) 5% duty cycle, (c) 10% duty cycle, and (d) 20% duty cycle. Curves indicate: 20 kHz (——), 40 kHZ (–▫–), 60 kHz (–○–), and 80 kHz (–△–). Note: the vertical scales differ in each figure.

4.11 Conclusions

In this study, direct numerical simulations coupled with a numerical plasma heating model have been used to simulate localized arc-filament plasma actuators (LAFPA). These actuators have been developed by researchers at The Ohio State University and have shown sufficient control author-

ity for use in high Reynolds number and high-speed flow regimes.[27] Enhancements to jet mixing, increased spreading, and modest reductions in the radiated far-field sound from jets have been displayed in experiments. Despite the successful demonstration of these actuators, the dominant mechanisms by which the arc-filament plasma actuates the flow are not entirely known. While experiments have verified the existence of a pressure wave and locally high-temperature region that are due to the plasma formation, it was not known how these features translate into the observed alterations to the baseline flow downstream of the actuation. Experiments showed that when the plasma was placed in the boundary layer prior to the nozzle exit in a jet, the plasma was blown off and destabilized. A recess was added to stabilize and house the plasma forming a cavity upstream of the nozzle exit that increased the response of the downstream flow. Because of the conditions of the flow and size of the features, a detailed explanation of the actuator forcing mechanisms by experimental means is not available. The numerical simulations and actuator model designed in this work were designed to provide insight into the mechanisms of forcing including determining the effects of the plasma temperature and the inclusion of the cavity. Knowledge of these mechanisms will facilitate future optimization and effective use of the LAFPA technology in jet and cavity flow applications.

The results of simulations, including the validated numerical plasma heating model, have illuminated several features of the actuation. The forcing supplied by the plasma actuator model causes a locally high-temperature recirculating region of fluid centered in the cavity. When the actuation begins, a sudden fluid expansion occurs in the cavity, which lifts the shear layer that has formed over the cavity and injects hot fluid into the boundary layer. The cavity is thus essential for producing this effect.

The principal effect of the actuator in the cavity is this jetting of fluid, which is similar to the action of synthetic jets used to perturb mixing layers and jets. Despite a similar forcing mechanism, the advantage of the LAFPA technology over synthetic jets appears to be its increased control authority over a wide range of forcing capability that does not depend on mechanical actuation. A simulation with a narrower cavity than what has been used in experiments showed that this jetting effect is even stronger, and it causes an even greater downstream flow response. The actuation promotes earlier pairing in the mixing layer and organizes the flow structures more

effectively than the baseline flow without actuation. Increasing the duty cycle of forcing and decreasing the cavity size both provide greater control authority. As the LAFPA system is scaled up to geometries of engineering interest, these simulations suggest that minimizing the cavity recess width will allow for decreased power requirements for effective forcing.

The jetting effect provides the perturbation to the flow that causes the main response downstream of the nozzle exit. Higher temperatures created by the plasma appear to be correlated with the increased response of the downstream flow. However, the high temperatures do not appear to be necessary for strong forcing. Forcing with larger duty cycles and with the narrower cavity also produced stronger jetting effects. An alternative actuator source was designed to provide a similar pressure response in the cavity as the full plasma model source, but without strong temperature excitation. A simulation with this alternative actuator model still provided sufficient control authority and organized downstream flow structures to a similar degree but at temperatures close to the ambient flow. The downstream spectra closely resembled that of the full actuator model. It appears that the increased temperatures cause conditions that generate vorticity via a baroclinic torque, however the alternative source showed significantly reduced magnitudes of this quantity but still with strong control authority. This leads us to conclude that the jetting promoted by the cavity is the primary means by which the actuator incites flow response.

The LAFPA technology is also applicable to the control of cavity flows, which are found in many engineering applications. The increased temperature caused by the plasma actuator is very important in this case as it fundamentally alters the natural oscillation frequency of the cavity. Simulations with the plasma model formulated in this work verify that the increased mean temperature of the cavity subsequently increases the speed of sound and shifts the cavity oscillation frequencies higher. A recently proposed signal processing viewpoint[113] was able to explain the complex frequency distribution of the cavity for both the baseline and actuator simulations. There was no obvious controllability to reduce the pressure levels of the cavity oscillations frequencies in this flow regime, however. The peak magnitudes of the resonant tones in the actuated cavities were not higher than the peaks of the baseline case. However, the actuation itself created higher amplitude peaks in the cavity at lower frequencies that are of greater engineering interest.

The simulations presented here have provided a detailed view of the actuation mechanisms and flow response in the near-nozzle region. Future extensions of this study should focus on expanding the simulation domain presented in this study to capture more of the downstream flow response and simulating an array of actuators situated in an axisymmetric jet geometry. These actuators have shown the capability to reduce the radiated noise from jets, however, the simulation domain was designed to focus on the near-nozzle region. As more detailed characterizations of the cavity region and the plasma itself become available by experiments, the simple plasma model formulated here can be extended to a more realistic form. This is especially important for providing a three-dimensional view of the actuation. Because the plasma is believed to form somewhat of a cylindrical shape, the induced fluid expansion shown here in two dimensions will likely introduce a three-dimensional character to the actuation that may be important in the evolution of the response downstream.

Chapter 5

Adjoint-based Optimization of Compressible Mixing Layers

5.1 Introduction

Scaling laws such as Lighthill's that show the acoustic power being proportional to the eighth power of jet velocity[7] have been successfully used in reducing jet noise by up to 20dB. This reduction was manifested through the development of high-bypass ratio engines which decreased the exit velocity. However, little information that is useful for further noise reduction is gained from such scaling laws beyond simply dropping the exit velocity. There is no guidance that is suitable for decreasing radiated noise using active control strategies, which take into account the time-varying nature of the jet and attempt to manipulate the large flow structures near the nozzle exit. As mentioned in Chapter 1, it is well known that predictive tools for designing quieter jets are lacking and that current successful control efforts typically involve some degree of trial-and-error iterations. The complexity of available theoretical noise sources[7,12] and the subtle connections between the turbulent fluctuations in the flow and the radiated sound are the principle causes of this difficulty. Even in the loudest civilian near-sonic jet engines, the overall noise contribution is a tiny fraction ($< 10^{-3}$) of the total flow energy. Predicting this small fraction of the energy that "leaks out" as sound is challenging.

In light of the relatively unclear understanding of the mechanisms of jet noise generation, we have designed a means to circumvent the complexity of a given flow and investigate jet noise control directly. A control optimization framework has been developed and is based on an adjoint formulation, which possesses the ability to optimize an extremely large set of control parameters. (This set is usually only restricted by computational limitations.) Adjoint-based formulations have been used in many recent optimization problems including magnetohydrodynamic control

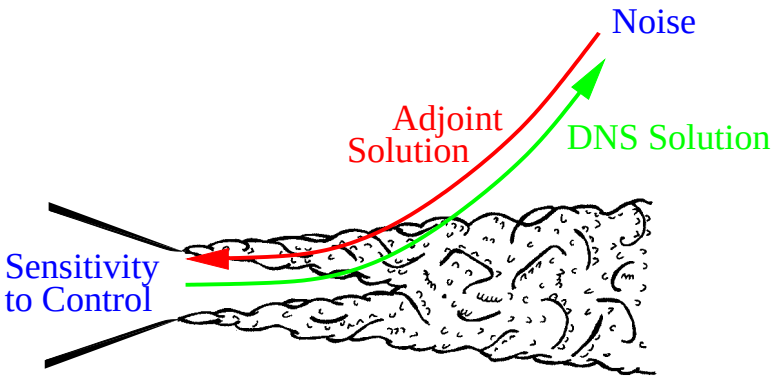

Figure 5.1: Schematic of the adjoint-based procedure for determining sensitivity for a sound reduction control.

in hypersonic applications,[119] error estimation for discontinuous Galerkin approximations of hyperbolic systems,[120] shape optimization for airfoil design,[121] flutter control in aeroelastic interactions,[122] studies of drag reduction in a turbulent channel flow,[123] analysis of mean flow refraction effects on sound radiated by localized sources in jets,[124] and some attempts to control unsteady compressible flow.[125–127] The use of adjoint methods is fairly new in the realm of fluid mechanics because of the already large computational burden of simulating flows even in simple geometries. The availability of high-speed computational resources along with the adjoint approach, by nature of simultaneous optimization of control parameters, reduces this burden.

In this work, the adjoint formulation is used to derive controls relevant to jet noise mitigation and increasing spreading, which is related to mixing enhancement. The latter is an important goal especially in military applications since increased mixing reduces the infrared signature of heat-generating aircraft and thus reduces detectability.[50] Jet noise reduction is somewhat more challenging problem than a majority of the applications just mentioned since the underlying mechanisms of turbulence-generated noise are not well understood. Our computational approach using the adjoint method for the reduction of far-field sound, for example, is shown schematically in Fig. 5.1. Given a numerical solution of the compressible flow equations, the adjoint of the linearized perturbed equations is solved numerically backward in time to give the sensitivity, as defined by the appropriate metric, to changes in the control at the nozzle. The sensitivity is used to update control parameters to satisfy the control objective. A control strategy for increasing the

spreading of a mixing layer is similar to the sound control approach in Fig. 5.1 given an appropriate control objective in the mixing region.

Because the approach is in essence a linearization, multiple iterations are necessary to improve controls of nonlinear, turbulent flows. This is computationally intensive since numerous solutions of the flow equations and their adjoint are necessary for each iteration. Flows to be controlled are thus relegated to model flows at low Reynolds numbers or require some degree of modeling to represent the turbulence. The adjoint method of control is also not suitable for implementation in hardware due to the iterative scheme and the unrealistic need for prior knowledge of the unsteady flow field. Instead, a flow successfully controlled by this method provides information on the flow physics unattainable through other means. It can also act as a guide to identifying suitable actuation for the development of active control technologies and reduce the trial-and-error aspect of current control efforts.

The adjoint control procedure applied to noise reduction has been previously implemented by Wei and Freund[28] and Wei,[128] and the results have been discussed. In that study the noise from a two-dimensional, randomly-excited mixing layer was reduced by up to 90% in a region targeted for control. The mechanism responsible for the resulting quieted flow was found to be a subtle changing of the most energetic flow structures by the control into a more orderly configuration. Given the considerable promise of the adjoint methodology for aeroacoustic control previously shown, the present work extends the control procedure to three dimensions and incorporates simple geometries. These objectives are necessary for several reasons:

1. While the structure of the three-dimensional shear layers in the near-nozzle region of a jet are essentially two-dimensional, their dynamics are much more chaotic. Streamwise correlation lengths are smaller and the sound spectra of three-dimensional turbulent jets are broader. The higher frequencies present are those particularly annoying to the human ear.

2. The effectiveness of the control in three-dimensional flows compared to the success of the previous two-dimensional flows needs to be established. Demonstration of the adjoint control procedure in more realistic, turbulent flows is a necessary step if the method is to be used in future control efforts associated with actuator technologies.

3. Current actuator technologies are associated with and often interact with the geometry that places them in the flow. It is necessary to develop and implement the needed numerical tools (such as adjoint boundary conditions) to demonstrate controls which can be placed in similar configurations as model actuators.

The organization of this chapter is as follows. The derivation of the control and how it is implemented in the governing equations is presented in §5.2. Control objectives (cost functionals) for sound reduction and mixing enhancement are formulated in §5.2.2 and their sensitivities to control in §5.2.3. The adjoint equations and the gradients of the cost functionals are derived in §5.2.4 and §5.2.5, respectively, and the control optimization procedure is explained in §5.2.6. Numerical methods used specifically for the simulation of the flows in this study are presented in §5.3. Both two- and three-dimensional spatially-developing mixing layers and simple anti-sound test problems in simple geometries for various control objectives are simulated and the results are reported in §5.5 and §5.6. Concluding remarks are given in §5.7.

5.2 Control Derivation and Implementation

5.2.1 Governing Equations

The flows in this study are governed by the compressible, viscous-fluid flow equations and were solved by direct numerical simulation as outlined in §2.1. For brevity, equations (2.5)-(2.7) can be expressed in the nonlinear operator form

$$\mathcal{N}(\mathbf{q}) = \mathbf{0}, \tag{5.1}$$

where

$$\mathbf{q} = \begin{bmatrix} \rho & u & v & w & p \end{bmatrix}^T \tag{5.2}$$

is solution of the governing equations with appropriate initial and boundary conditions. In deriving the control framework, it is also necessary to introduce two additional vector fields: the

perturbation about the DNS flow solution,

$$\mathbf{q}' = \begin{bmatrix} \rho' & u' & v' & w' & p' \end{bmatrix}^T, \tag{5.3}$$

and the adjoint field,

$$\mathbf{q}^\dagger = \begin{bmatrix} \rho^\dagger & u^\dagger & v^\dagger & w^\dagger & p^\dagger \end{bmatrix}^T, \tag{5.4}$$

which will be used later in §5.2.4.

The actuation is implemented as a general source term $\phi(\mathbf{x}, t)$ with compact support in the *control region*, $\mathcal{C}$:

$$\mathcal{N}(\mathbf{q}) = \mathbf{F}\phi(\mathbf{x}, t), \tag{5.5}$$

where the vector $\mathbf{F}$ places the control's action into the different equations of $\mathcal{N}(\mathbf{q})$. Mass, momentum (body force), and internal energy controls are selected based on the form of $\mathbf{F}$ (see Wei & Freund[28]) and it ensures that the controls are placed into the equations consistently. We will only utilize an internal energy-type control, which is thought to be the most appropriate model for arc-filament plasma actuators. These types of plasma actuators are thought to act primarily as a thermal source due to Joule heating effects in the vicinity of the plasma[85] (see Chapter 4). The control ϕ can remain unconstrained within $\mathcal{C}$ or have spatial and/or temporal forms specified to model-specific details of the plasma actuators. For example, ϕ could be constrained to a time-harmonic function with a prescribed spatial form such as

$$\phi(\mathbf{x}, t) = A(\mathbf{x}) \sin(\omega t + \varphi).$$

In this case the frequency ω and phase φ are optimizable parameters. Leaving ϕ unconstrained will result in each spatial grid location in $\mathcal{C}$ at every time step in the simulation acting as a control parameter to be optimized. While this presumably maximizes the control effectiveness, it is probable that the control derived will not be physically realizable in hardware and greatly increases the dimensionality of the optimization problem to be considered.

5.2.2 Cost Functionals

Our control formulation begins with specifying a cost functional be minimized that represents the control objective The cost functional is a function of the state of the system, the flow solution, and the control variables, ϕ. In this study, we are interested mainly in the reduction of the sound radiated by the mixing layer, but will also consider mixing enhancement through increasing growth rate of the layer. The cost functional is defined over a region of space where it is to be minimized (the *target region*, $\mathcal{T}$) and over some length of time called the control time horizon, $(0, T_\phi)$.

For sound control, our choice of cost functional was

$$\mathcal{J}_{\text{sound}}(\phi(\mathbf{x},t)) = \int_0^{T_\phi} \int_{\mathcal{T}} [p(\phi(\mathbf{x},t),\mathbf{x},t) - \langle p(\mathbf{x})\rangle]^2 \, \mathrm{d}\mathbf{x} \, \mathrm{d}t + c_{\text{p}} \int_0^{T_\phi} \int_{\mathcal{C}} \phi^2 \, \mathrm{d}\mathbf{x} \, \mathrm{d}t, \tag{5.6}$$

where p is the pressure in the target region, which depends on $\phi(\mathbf{x},t)^*$ and $\langle p\rangle$ is the time-averaged pressure in $\mathcal{T}$ before the control is applied, and not exactly the same as the ambient. Wei & Freund[28] found that since the mean pressure is not constrained, it can drift due to the control even though such a drift would be penalized since it would increase $\mathcal{J}_{\text{sound}}$. It can also vary in space and slightly reflect the entrainment flow. $\mathcal{T}$ is chosen to be far from the mixing region so that it resides in the sound field, which is loosely defined as the irrotational flow region far from the shear layer. This cost functional aims to minimize the acoustic energy in the target region. The second term in (5.6) represents the price of the control with the tunable price factor c_{p} which is commonly chosen via trial and error. It penalizes the control for being too "costly" (i.e. adding excessive energy into the flow) and is added to constrain ϕ to more realizable conditions for actuation in practical applications.

For mixing layer spreading, the cost functional is formulated with the goal of maximizing the spreading in the mixing layer. While this may be achieved with formulations based on layer thickness, such an approach is not preferred due to complexity of the thickness definitions (integrals for displacement and momentum thickness) or definitions that are not well-defined analytically, such as the "visual" thickness. The motivation for a simple cost functional will become apparent

*The spatial and temporal dependence of ϕ is omitted for clarity from this point forward and will be declared only when explicitly needed.

when we derive the cost functional gradient in §5.2.3. Instead, a simple cost functional can be created by differentiating the momentum thickness (2.3) with respect to time to give

$$\delta' = -\frac{1}{\rho_\infty (\Delta U)^2} \int_{-\infty}^{\infty} \frac{\partial \widetilde{\overline{\rho} u u}}{\partial t} \, \mathrm{d}y. \tag{5.7}$$

We would like to maximize δ' but with a simpler function form. Following Vreman *et al.*,[49] the term in the integrand is twice the mean flow kinetic energy and its evolution is governed by

$$\frac{\partial}{\partial t}(\widetilde{\overline{\rho} u u}) = \frac{\partial}{\partial y}(-\widetilde{\overline{\rho} u u}\tilde{v} + 2\tilde{\tau_{\mathrm{xy}}}\tilde{u} - 2\widetilde{\overline{\rho} u' v'}\tilde{u}) + 2\widetilde{\overline{\rho} u' v'}\frac{\partial \tilde{u}}{\partial y} - 2\tilde{\tau_{\mathrm{xy}}}\frac{\partial \tilde{u}}{\partial y}. \tag{5.8}$$

After integration in the cross-stream direction, the conservative terms vanish and the result is substituted into (5.7) to become

$$\delta' = -\frac{2}{\rho_\infty (\Delta U)^2} \int_{-\infty}^{\infty} \widetilde{\overline{\rho} u' v'} \frac{\partial \tilde{u}}{\partial y} \, \mathrm{d}y \tag{5.9}$$

where the viscous dissipation term is neglected. The growth rate of the mixing layer is thus proportional to the integrated turbulent kinetic energy production. Appealing to the Reynolds stress transport equations, the turbulent kinetic energy production is a major source term in the $\widetilde{\overline{\rho} u' u'}$ equation. The largest sink in the $\widetilde{\overline{\rho} u' u'}$ equation is the pressure strain-rate term, which acts to redistribute energy to $\widetilde{\overline{\rho} v' v'}$ and $\widetilde{\overline{\rho} w' w'}$. The $\widetilde{\overline{\rho} v' v'}$ term appears as a source in the shear stress production as $\widetilde{\overline{\rho} v' v'} \partial \tilde{u} / \partial y$ and is proportional to growth rate. Therefore, maximizing an intermediate quantity in the process which generates shear stress and increases growth rate should also increase spreading of the mixing layer. The square of the cross-stream velocity achieves this end while at the same time retaining a simple cost functional. A velocity-based mixing enhancement cost functional is thus

$$\mathcal{J}_{\mathrm{v}}(\phi) = \int_0^{T_\phi} \int_{\mathcal{T}} -(v - \langle v(\mathbf{x}) \rangle)^2 \, \mathrm{d}\mathbf{x} \, \mathrm{d}t + c_{\mathrm{m}} \int_0^{T_\phi} \int_{\mathcal{C}} \phi^2 \, \mathrm{d}\mathbf{x} \, \mathrm{d}t, \tag{5.10}$$

where c_{m} is again a price factor. The cross-stream velocity has a small mean component in a planar shear layer, so it is removed as with the sound control. The negative $-v^2$ in (5.10) is used to make the cost functional minimization consistent with maximizing v^2. For mixing maximization, $\mathcal{T}$ is located in the mixing region downstream from the convergence of a high- and low-speed stream.

The inclusion of the penalty term in the increased spreading cost functional is critical since an arbitrary large force could incite an arbitrarily large response in the mixing layer. This would be physically unrealistic.

In addition to a velocity-based mixing enhancement approach, a cost functional which is comprised of pressure fluctuations in the turbulent region of the flow can also be formulated. This approach matches the acoustic control with slight modifications. The target region, $\mathcal{T}$, is placed in the mixing region. A pressure-based mixing enhancement cost functional is thus

$$\mathcal{J}_{\mathrm{p}}(\phi) = \int_0^{T_\phi} \int_{\mathcal{T}} -(p - \langle p(\mathbf{x}) \rangle)^2 \, \mathrm{d}\mathbf{x} \, \mathrm{d}t + c_{\mathrm{m}} \int_0^{T_\phi} \int_{\mathcal{C}} \phi^2 \, \mathrm{d}\mathbf{x} \, \mathrm{d}t, \tag{5.11}$$

where the negative sign acts to maximize the pressure in the target region. The transport equation for the Reynolds stresses reveals that the pressure–strain-rate term $\widetilde{p' \frac{\partial u'}{\partial x}}$ retains a pivotal role in shear stress production and therefore mixing layer growth. It is well known that as the convective Mach number increases, a strong reduction in growth rate due to compressibility effects is observed.[23] Simulations of planar[49] and annular[50] temporally-developing mixing layers have shown that the reduction in growth rate is due to a reduction in the pressure-strain rate term. This term acts as a sink of $\widetilde{\overline{\rho} u'u'}$ and redistributes this energy to the other normal stresses, which as mentioned before are a dominant source of shear stress and therefore increase growth rate. Increasing the pressure fluctuations in the mixing layer is therefore also expected to result in enhanced spreading of the layer streams.

5.2.3 Sensitivity to Control Perturbations

Once the cost functional is defined, we must determine the sensitivity of the cost functional $\mathcal{J}$ to small modifications of the control ϕ. This step will provide a representation of a gradient, which will be used in the optimization. We consider a linearized perturbation $\mathcal{J}'$ that results from an arbitrary perturbation ϕ' to the control ϕ. This perturbation $\mathcal{J}'$ is defined via the Fréchet differential[129] as a differential of the cost functional $\mathcal{J}$ with respect to ϕ in the direction ϕ':

$$\mathcal{J}' \equiv \lim_{\varepsilon \to 0} \frac{\mathcal{J}(\phi + \varepsilon \phi') - \mathcal{J}(\phi)}{\varepsilon} = \int_0^{T_\phi} \int_{\mathcal{C}} \frac{\mathcal{D}\mathcal{J}(\phi)}{\mathcal{D}\phi} \phi' \, \mathrm{d}\mathbf{x} \, \mathrm{d}t, \tag{5.12}$$

where $\mathcal{D}\mathcal{J}(\phi)/\mathcal{D}\phi$ is identified as the gradient and the integration is over $\mathcal{C}$ since ϕ and ϕ' only have support there. When implemented, the optimal control problem is discretized in space and time, and the gradient is the Jacobian of the scalar $\mathcal{J}(\phi)$ with respect to the discretized vector ϕ, whose components correspond to the space–time points in $\mathcal{C}$. This approach is considered the "optimize then discretize" approach to adjoint-based optimization. Discretization in space and time occurs after the control problem is derived completely in differential form. The linearized cost functional perturbation will be expressed as the control perturbation convolved with the adjoint field (defined in (5.4)) with the same form as the right of (5.12), thereby relating to the solution of the adjoint problem.

For the three cost functionals presented in §5.2.2, the linearized perturbations are

$$\mathcal{J}'_{\text{sound}}(\phi;\, \phi') = \int_0^{T_\phi} \int_{\mathcal{T}} 2(p - \langle p(\mathbf{x})\rangle)p' \,\mathrm{d}\mathbf{x}\,\mathrm{d}t + 2c_{\text{p}} \int_0^{T_\phi} \int_{\mathcal{C}} \phi\,\phi' \,\mathrm{d}\mathbf{x}\,\mathrm{d}t, \tag{5.13}$$

corresponding to (5.6),

$$\mathcal{J}'_{\text{v}}(\phi;\, \phi') = \int_0^{T_\phi} \int_{\mathcal{T}} -2(v - \langle v(\mathbf{x})\rangle)\, v' \,\mathrm{d}\mathbf{x}\,\mathrm{d}t + 2c_{\text{m}} \int_0^{T_\phi} \int_{\mathcal{C}} \phi\,\phi' \,\mathrm{d}\mathbf{x}\,\mathrm{d}t, \tag{5.14}$$

corresponding to (5.10), and

$$\mathcal{J}'_{\text{p}}(\phi;\, \phi') = \int_0^{T_\phi} \int_{\mathcal{T}} -2(p - \langle p(\mathbf{x})\rangle)\, p' \,\mathrm{d}\mathbf{x}\,\mathrm{d}t + 2c_{\text{m}} \int_0^{T_\phi} \int_{\mathcal{C}} \phi\,\phi' \,\mathrm{d}\mathbf{x}\,\mathrm{d}t, \tag{5.15}$$

corresponding to (5.11).

As with the cost functional, the same procedure of Fréchet differentiation can be applied to all flow variables resulting in the linearized perturbation $\mathbf{q}'$ defined in (5.3). We take $\mathbf{q}'$ to be the perturbation to the solution due to the perturbation ϕ' to the control ϕ. This is not to be confused with the common linearization about an averaged flow state. Here it is a perturbation to the space- and time-dependent flow solution. Equations governing $\mathbf{q}'$ can be derived by taking the Fréchet differential of (5.1). The operation is shown here

$$\mathcal{N}(\mathbf{q} + \mathbf{q}') = \mathbf{F}(\mathbf{q} + \mathbf{q}')(\phi + \phi'), \tag{5.16}$$

where the right-hand side indicates that $\mathbf{F}$ depends functionally on $\mathbf{q} + \mathbf{q}'$ while multiplying the last term. Linearizing (5.16) results in the linearized Navier–Stokes operator

$$\mathcal{N}'(\mathbf{q})\mathbf{q}' = \mathbf{F}'\phi + \mathbf{F}\phi'. \tag{5.17}$$

The operation $\mathcal{N}'(\mathbf{q})\mathbf{q}'$ is linear while $\mathcal{N}'(\mathbf{q})$ retains a nonlinear dependence on $\mathbf{q}$.

Here we are interested in implementing control which can be represented as an internal energy source term. When adding a general source term into the energy equation, the vector $\mathbf{F}$ in (5.5) can be expressed as

$$\mathbf{F} = \begin{bmatrix} 0 & 0 & 0 & 0 & 1 \end{bmatrix}^T \tag{5.18}$$

and when linearized by the above procedure results in $\mathbf{F}' = \mathbf{0}$. Thus, for an internal energy control, (5.17) reduces to

$$\mathcal{N}'(\mathbf{q})\mathbf{q}' = \phi'. \tag{5.19}$$

5.2.4 Adjoint Problem Formulation

The final piece needed to obtain a useful gradient that can be incorporated into an optimization strategy is to introduce the adjoint of the linearized, perturbed operator in (5.17). The adjoint field provides the gradient of the cost functional to the control perturbations. We first define an inner product over the control time horizon and the flow domain

$$\langle \mathbf{q}', \mathbf{q}^\dagger \rangle \equiv \int_0^{T_\phi} \int_{\mathbb{R}^3} \mathbf{q}' \cdot \mathbf{q}^\dagger \, \mathrm{d}\mathbf{x} \, \mathrm{d}t. \tag{5.20}$$

To derive the adjoint, we employ integration by parts

$$\langle \mathcal{N}'(\mathbf{q})\mathbf{q}', \mathbf{q}^\dagger \rangle = -\langle \mathbf{q}', \mathcal{N}^\dagger(\mathbf{q})\mathbf{q}^\dagger \rangle + b. \tag{5.21}$$

The result of this operation yields the adjoint ($\mathcal{N}^\dagger(\mathbf{q})\mathbf{q}^\dagger$) of the linearized, perturbed, unsteady, compressible Navier–Stokes equations ($\mathcal{N}'(\mathbf{q})\mathbf{q}'$) in three dimensions. These are reported in full in Appendix B. The boundary terms b introduced by integration by parts can be eliminated by

choosing appropriate initial and boundary conditions for the adjoint system.[28] The terms evaluated on the domain boundaries (arising from the spatial domain integration) can be eliminated by causality, but since the boundary is necessarily finite in numerical computations, a radiation condition applied at these finite-distance boundaries is functionally equivalent. The initial time "boundary term" is also eliminated by causality at $t = 0$ since there can be no perturbation to the flow due to a perturbation to the control before the control has been applied. At the end of the control horizon, $t = T_\phi$, the terminal time boundary term can be eliminated by starting with $\mathbf{q}^\dagger = \mathbf{0}$ and solving the adjoint system backwards in time.

We are now prepared to select the adjoint source term $\mathbf{F}^\dagger$ that will allow us to express the gradient of a given cost functional in terms of the solution of the adjoint system. This forcing term is introduced in a similar manner as (5.5),

$$\mathcal{N}^\dagger(\mathbf{q})\mathbf{q}^\dagger = \mathbf{F}^\dagger, \tag{5.22}$$

where $\mathbf{F}^\dagger$ is selected based on the cost functional. Following Wei & Freund,[28] the source terms in (5.19) and (5.22) are substituted into (5.21) for the linearized flow and adjoint operators, respectively, to give

$$\langle \phi', \mathbf{q}^\dagger \rangle = -\langle \mathbf{q}', \mathbf{F}^\dagger \rangle. \tag{5.23}$$

The left hand side of this relation can be further reduced to

$$\langle \phi', \mathbf{q}^\dagger \rangle = \int_0^{T_\phi} \int_{\mathcal{C}} \phi' p^\dagger \, \mathrm{d}\mathbf{x} \, \mathrm{d}t, \tag{5.24}$$

since ϕ' only has support in $\mathcal{C}$.

5.2.5 Gradients of Cost Functionals

The right-hand side of (5.23) is selected to correspond to particular cost functionals. We now derive the gradient for each case of the $\mathcal{J}$ discussed in §5.2.2.

Gradient of Sound Reduction Cost Functional

Equation (5.23) can be identically satisfied by a judicious choice of $\mathbf{F}^{\dagger}{}_{\text{sound}}$. We would like to obtain

$$-\langle \mathbf{q}', \mathbf{F}^{\dagger}_{\text{sound}} \rangle = \int_0^{T_\phi} \int_{\mathcal{T}} 2(p - \langle p \rangle) p' \, \mathrm{d}\mathbf{x} \, \mathrm{d}t + 2c_{\text{p}} \int_0^{T_\phi} \int_{\mathcal{C}} \phi \, \phi' \, \mathrm{d}\mathbf{x} \, \mathrm{d}t \tag{5.25}$$

so that

$$\langle \phi', \mathbf{q}^{\dagger} \rangle = \int_0^{T_\phi} \int_{\mathcal{C}} \frac{\mathcal{D}\mathcal{J}_{\text{sound}}(\phi)}{\mathcal{D}\phi} \phi' \, \mathrm{d}\mathbf{x} \, \mathrm{d}t, \tag{5.26}$$

which is the desired form as in (5.12). Comparing the right-hand side of (5.23) with (5.13), the forcing term in the adjoint system must be

$$\mathbf{F}^{\dagger}_{\text{sound}} = \begin{bmatrix} 0 & 0 & 0 & 0 & -2(p - \langle p \rangle) \end{bmatrix}^T \quad \text{in } \mathcal{T}, \tag{5.27}$$

and using (5.12) gives

$$\mathcal{J}'_{\text{sound}}(\phi;\, \phi') = \int_0^{T_\phi} \int_{\mathcal{C}} \frac{\mathcal{D}\mathcal{J}_{\text{sound}}(\phi)}{\mathcal{D}\phi} \phi' \, \mathrm{d}\mathbf{x} \, \mathrm{d}t = \int_0^{T_\phi} \int_{\mathcal{C}} (p^{\dagger} + 2c_{\text{p}}\phi) \phi' \, \mathrm{d}\mathbf{x} \, \mathrm{d}t. \tag{5.28}$$

Since this is true for any perturbation ϕ' to the control ϕ, the desired gradient is thus the solution of the adjoint problem with corresponding forcing of $\mathbf{F}^{\dagger}_{\text{sound}}$ such that

$$g_{\text{sound}}(\phi) \equiv \frac{\mathcal{D}\mathcal{J}_{\text{sound}}(\phi)}{\mathcal{D}\phi} = p^{\dagger} + 2c_{\text{p}}\phi. \tag{5.29}$$

Gradient of Increased Spreading Cost Functional – Velocity

For $\mathbf{F}^{\dagger}_{\text{v}}$, we would like to obtain

$$-\langle \mathbf{q}', \mathbf{F}^{\dagger}_{\text{v}} \rangle = \int_0^{T_\phi} \int_{\mathcal{T}} -2(v - \langle v(\mathbf{x}) \rangle) v' \, \mathrm{d}\mathbf{x} \, \mathrm{d}t + 2c_{\text{m}} \int_0^{T_\phi} \int_{\mathcal{C}} \phi \, \phi' \, \mathrm{d}\mathbf{x} \, \mathrm{d}t, \tag{5.30}$$

so that

$$\langle \phi', \mathbf{q}^{\dagger} \rangle = \int_0^{T_\phi} \int_{\mathcal{C}} \frac{\mathcal{D}\mathcal{J}_{\text{v}}(\phi)}{\mathcal{D}\phi} \phi' \, \mathrm{d}\mathbf{x} \, \mathrm{d}t, \tag{5.31}$$

which is the desired form as in (5.12). Comparing the right-hand side of (5.23) with (5.14), the adjoint forcing must be

$$\mathbf{F}_{\mathrm{v}}^{\dagger} = \begin{bmatrix} 0 & 0 & 2(v - \langle v(\mathbf{x}) \rangle) & 0 & 0 \end{bmatrix}^T \quad \text{in } \mathcal{T}, \tag{5.32}$$

which gives

$$\mathcal{J}_{\mathrm{v}}'(\phi;\, \phi') = \int_0^{T_\phi} \int_{\mathcal{C}} \frac{\mathcal{D}\mathcal{J}_{\mathrm{v}}(\phi)}{\mathcal{D}\phi} \phi' \, \mathrm{d}\mathbf{x} \, \mathrm{d}t = \int_0^{T_\phi} \int_{\mathcal{C}} (-v^\dagger + 2c_{\mathrm{m}}\phi)\phi' \, \mathrm{d}\mathbf{x} \, \mathrm{d}t. \tag{5.33}$$

The desired gradient is thus the solution of the adjoint problem with corresponding forcing of $\mathbf{F}_{\mathrm{v}}^{\dagger}$ such that

$$g_{\mathrm{v}}(\phi) \equiv \frac{\mathcal{D}\mathcal{J}_{\mathrm{v}}(\phi)}{\mathcal{D}\phi} = -v^\dagger + 2c_{\mathrm{m}}\phi. \tag{5.34}$$

Gradient of Increased Spreading Cost Functional – Pressure

For $\mathbf{F}^{\dagger}{}_{\mathrm{p}}$, we would like to obtain

$$-\langle \mathbf{q}', \mathbf{F}_{\mathrm{p}}^{\dagger} \rangle = \int_0^{T_\phi} \int_{\mathcal{T}} -2(p - \langle p(\mathbf{x}) \rangle) p' \, \mathrm{d}\mathbf{x} \, \mathrm{d}t + 2c_{\mathrm{m}} \int_0^{T_\phi} \int_{\mathcal{C}} \phi \, \phi' \, \mathrm{d}\mathbf{x} \, \mathrm{d}t, \tag{5.35}$$

so that

$$\langle \phi', \mathbf{q}^{\dagger} \rangle = \int_0^{T_\phi} \int_{\mathcal{C}} \frac{\mathcal{D}\mathcal{J}_{\mathrm{p}}(\phi)}{\mathcal{D}\phi} \phi' \, \mathrm{d}\mathbf{x} \, \mathrm{d}t, \tag{5.36}$$

which is the desired form as in (5.12). Comparing the right-hand side of (5.23) with (5.15), the adjoint forcing must be

$$\mathbf{F}_{\mathrm{p}}^{\dagger} = \begin{bmatrix} 0 & 0 & 0 & 0 & 2(p - \langle p(\mathbf{x}) \rangle) \end{bmatrix}^T \quad \text{in } \mathcal{T}, \tag{5.37}$$

which gives

$$\mathcal{J}_{\mathrm{p}}'(\phi;\, \phi') = \int_0^{T_\phi} \int_{\mathcal{C}} \frac{\mathcal{D}\mathcal{J}_{\mathrm{p}}(\phi)}{\mathcal{D}\phi} \phi' \, \mathrm{d}\mathbf{x} \, \mathrm{d}t = \int_0^{T_\phi} \int_{\mathcal{C}} (-p^\dagger + 2c_{\mathrm{m}}\phi)\phi' \, \mathrm{d}\mathbf{x} \, \mathrm{d}t. \tag{5.38}$$

Now, the desired gradient is thus the solution of the adjoint problem with corresponding forcing of $\mathbf{F}_{\mathrm{p}}^{\dagger}$ such that

$$g_{\mathrm{p}}(\phi) \equiv \frac{\mathcal{D}\mathcal{J}_{\mathrm{p}}(\phi)}{\mathcal{D}\phi} = -p^{\dagger} + 2c_{\mathrm{m}}\phi. \tag{5.39}$$

5.2.6 Optimization Procedure

With the gradient information from the adjoint solution shown in §5.2.5, the optimization procedure is straightforward. The control is updated iteratively by

$$\phi^{i+1} = \phi^{i} - r^{i} g^{i}(\phi^{i}) \tag{5.40}$$

where g^i is the current gradient based on the current ϕ_i and r^i is a generalized distance in ϕ-coordinates, which governs how large of an update is made to minimize $\mathcal{J}(\phi^i)$ in the g^i direction. Brent's algorithm[130] for line searches, which uses both the function and its derivative,[†] iteratively determined the r^i that minimizes $\mathcal{J}(\phi^i)$. The initial control, ϕ^0 is taken to be zero.

Once a value of r_i that minimizes $\mathcal{J}(\phi^i)$ in the g^i direction has been found, an efficient conjugate gradient algorithm updates the control. The Polak-Ribiere[130] variant of the conjugate gradient algorithm was chosen for the optimizations in this work. This method was shown to be effective in nonquadratic optimization problems and a review of it and the possibility of using other control update methods has been explored elsewhere.[123]

5.3 Numerical Implementation

The adjoint field is discretized and solved with the same methods as the flow equations as outlined in §5.3. However, as formulated, $\mathbf{F}^{\dagger}$ and ϕ could be discontinuous in $\mathbb{R}^3$ because of their compact support, which is incompatible with our numerical discretization. To counter this, the term $\mathbf{F}^{\dagger}$ is

[†]The subroutines to use the function value and its derivative are denoted as `dlinmin` and `dbrent` in the documentation.[130]

modified via a "smoothing" distribution function

$$\mathcal{N}^{\dagger}(\mathbf{q})\mathbf{q}^{\dagger} = \mathbf{F}^{\dagger}\left[\left(\frac{\mathcal{T}_{\mathrm{l}} - 2x + \mathcal{T}_{\mathrm{r}}}{\mathcal{T}_{\mathrm{r}} - \mathcal{T}_{\mathrm{l}}}\right)^{2n} + 1\right] * \left[\left(\frac{\mathcal{T}_{\mathrm{b}} - 2y + \mathcal{T}_{\mathrm{t}}}{\mathcal{T}_{\mathrm{t}} - \mathcal{T}_{\mathrm{b}}}\right)^{2n} + 1\right], \tag{5.41}$$

where the subscripts l, r, t, and b refer to the left, right, top, and bottom locations of the target region, respectively. The control forcing is implemented with the same form of distribution function

$$\mathcal{N}(\mathbf{q}) = \mathbf{F}_{\mathrm{ie}}\,\phi\left[\left(\frac{\mathcal{C}_{\mathrm{l}} - 2x + \mathcal{C}_{\mathrm{r}}}{\mathcal{C}_{\mathrm{r}} - \mathcal{C}_{\mathrm{l}}}\right)^{2n} + 1\right] * \left[\left(\frac{\mathcal{C}_{\mathrm{b}} - 2y + \mathcal{C}_{\mathrm{t}}}{\mathcal{C}_{\mathrm{t}} - \mathcal{C}_{\mathrm{b}}}\right)^{2n} + 1\right], \tag{5.42}$$

where the subscripts hold the same distinction for $\mathcal{C}$ as with $\mathcal{T}$. The exponent was sufficient to smooth the control and target regions with $n = 3$, so that sixth-order polynomials in x and y smoothed the forcing over the regions. Both the target and control regions were ramped in time to avoid discontinuous behavior. The ramping function varied linearly from zero to one during the first 5% of the control time horizon for the control forcing and from one to zero during the last 5% of the horizon for the target region forcing of the adjoint system.

The adjoint operator depends on the full flow solution $\mathbf{q}$, as is evident in the coefficient matrices constituting the adjoint system shown in Appendix B. The flow field solution is thus needed in order to solve the adjoint equations. Storing an entire three-dimensional, time-resolved flow field is not practical due to memory constraints. Therefore, the flow field solutions were saved to the hard disk for the simulations in this work. Only a subset of mesh points in each the streamwise and cross-stream directions time steps were saved. The number of points chosen to keep was based on the ability to retain the features of the flow solution, yet have manageable dataset sizes. The choice was flow dependent and varied slightly based on the availability of disk space on the systems used for simulation and the features of the flow. When a spanwise direction was present, the periodic boundary conditions allowed for the fields to be Fourier transformed and only the first $2N_{\mathrm{z}}/3$ coefficients were stored. The reduced flow fields were interpolated during the solution of the adjoint system using third-order Lagrange polynomials and inverse Fourier transformed. Interpolation between subsequent fields in time was linear. Previous optimizations based on this adjoint formulation indicate that this method of reducing and re-inflating the flow field showed no significant difference in test cases where the full field was used.[28,123] Due to the large size of

the domains and long control time horizons in the present work, such a test was not feasible.

5.4 Anti-Sound Internal Energy Source Results

To test the adjoint-based optimization framework derived in §5.2, optimizations of several flow configurations were run to demonstrate the procedure's ability to minimize the cost functionals in §5.2.2. The following sections report the results of optimizations with no external flow in anti-sound configurations, where acoustic cancellation is the expected mechanism by which the control will reduce the pressure fluctuations in a target region. This is done with and without price term consideration. Mixing layer simulations in two and three dimensions with mixing layer spreading enhancement and sound control cost functionals are reported in §5.5 and §5.6, respectively.

5.4.1 Control with No Price Term Considered

The simplest control simulations tested involved a reducing the noise from a time-harmonic, Gaussian-shaped internal energy source placed in an otherwise quiescent field. An internal energy control region was placed between the source and a smaller target region as shown schematically in Fig. 5.2 along with a pressure field at the end of the simulation's control time horizon. A sound control cost functional $\mathcal{J}_{\text{sound}}(\phi)$ as (5.6), with the price term coefficient $c_{\text{p}} = 0$. A configuration such as this will cause the control to produce an anti-sound type of control, which effectively cancels the pressure waves in $\mathcal{T}$. The control region ($\mathcal{C}$) was $25\delta_{\text{w}}$ wide and $10\delta_{\text{w}}$ tall and the target region ($\mathcal{T}$) was $10\delta_{\text{w}}$ wide and $10\delta_{\text{w}}$ tall, where δ_{w} is the thickness of an isothermal solid wall, which extended out to $x = 16\delta_{\text{w}}$. The wall was placed in the domain to test stability of the solid wall characteristic boundary conditions for the adjoint system derived in Appendix C. The internal energy source

$$S_{\text{ie}}(x, y, t) = 0.4 \exp\left[-\sigma\left((x-25)^2 + (y-25)^2\right)\right] \sin\left(\frac{2\pi t}{3}\right) \tag{5.43}$$

was added to the energy equation.

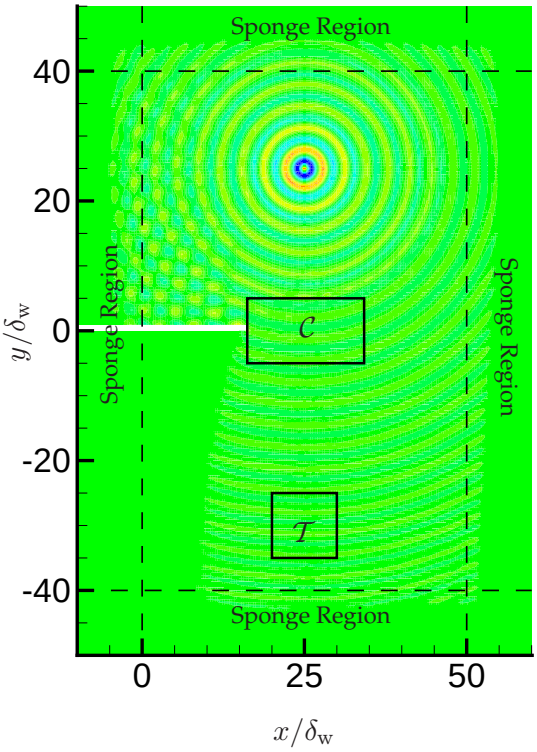

Figure 5.2: Schematic showing the internal energy control test case for a sound reduction cost functional as in (5.6). This configuration creates an "anti-sound" type of control. The dotted lines mark the border between the sponge regions and the physical domain. An internal energy source is located at $(x,\, y) = (25,\, 25)\delta_w$.

These simulations had a time horizon of $T_\phi = 250\,\delta_w/c_\infty$ and the Reynolds number based on the ambient acoustic sound speed and wall thickness was

$$\mathrm{Re} = \frac{\rho_\infty c_\infty \delta_w}{\mu_\infty} = 500. \tag{5.44}$$

The simulation mesh was $N_x \times N_y = 192 \times 221$ and the solution was advanced in time with $\Delta t = 0.05$ for 5000 time steps. The sponge regions shown in Fig. 5.2 all had a width of $10\,\delta_w$ and a strength of $\sigma = 0.2$ (see §2.2.5).

The pressure perturbations $(p - p_\infty)$ for the baseline simulation are shown in Fig. 5.3(a) for this simple case at $t = 225\,\delta_w/c_\infty$, which is slightly before the end of the control time horizon. The

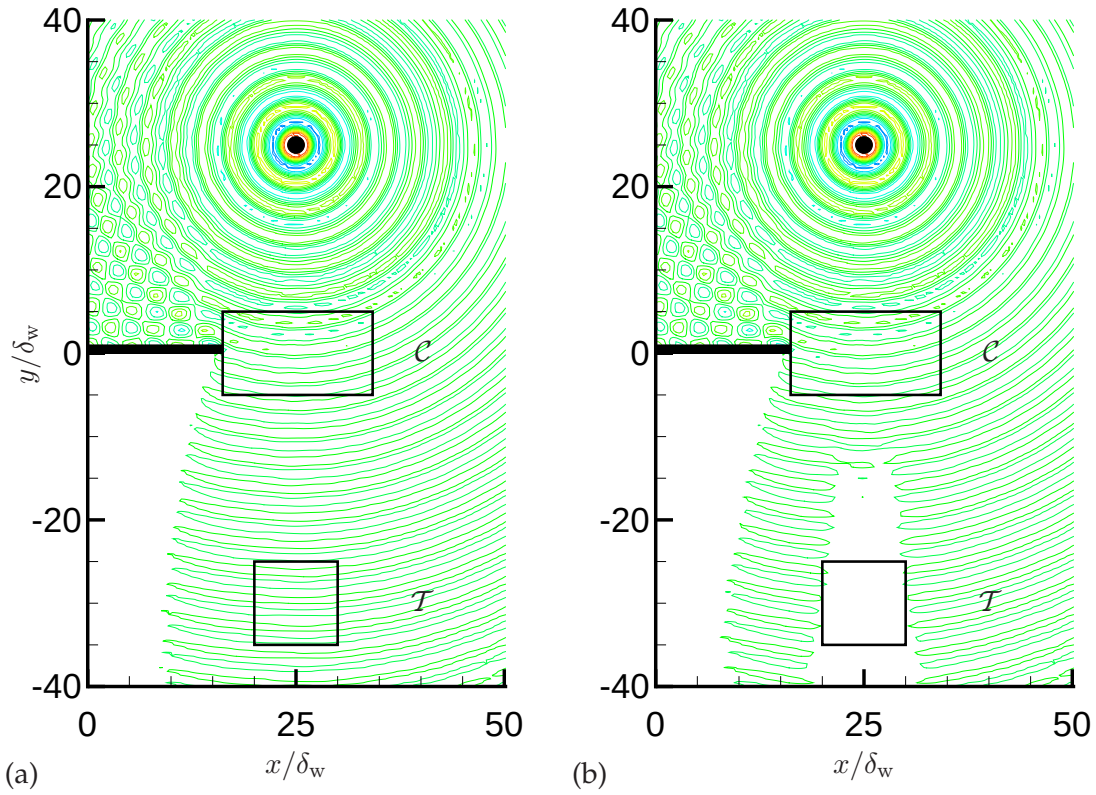

Figure 5.3: Evolution of the (a) baseline and (b) optimized pressure fields for the anti-sound control with no price term considered at times $t = 225\delta_w/c_\infty$. Fourteen evenly-spaced contours between -0.016 and 0.016 are shown. The internal energy source is shown with a black dot located at $(x,\, y) = (25,\, 25)\delta_w$.

control region $\mathcal{C}$ and target region $\mathcal{T}$ are shown in the figure along with a dot representing the center of the implanted source. A visualization of the corresponding pressure perturbation field of the controlled case is shown in Fig. 5.3(b).

This is a relatively simple linear configuration, so it is not surprising that after one iteration of the optimization procedure, the value of $\mathcal{J}_{\text{sound}}(\phi)$ was reduced by 83%. Subsequent iterations did not produce any further noise reduction. The are two possible reasons that can explain why this is the case. First, the functional space of $\mathcal{J}_{\text{sound}}$ is very large even for this problem ($\sim 7.5 \times 10^6$) due to every space-time point in $\mathcal{C}$ being an optimizable control parameter. Since this is large space, it is possible that the conjugate gradient found only a local minimum in the parameter space. That

behavior in an artifact of the minimization. However, this is speculation since knowledge of the entire parameter space would be needed to make this assessment, which is obviously not the case. Second, due to the time ramping of ϕ in the flow field and the adjoint forcing term described in §5.2.6, there are portions of the time horizon where the control is not able to sufficiently reduce the cost functional. The ramping and smoothing functions ((5.41) and (5.42)) effectively damp the gradient that is used to create the control (at the beginning of the adjoint solve) as well as damp the control at the beginning of the control time horizon. While it is not expected that the initial time ramping of ϕ is an issue in this configuration since the sound generated by the internal energy source does not reach $\mathcal{C}$ until after the ramping up is complete.

This is shown in Fig. 5.4, which shows the instantaneous cost defined as

$$\mathcal{I}_{\text{sound}}(\phi, t) = \int_{\mathcal{T}} (p - p_\infty)^2 d\mathbf{x} \tag{5.45}$$

such that

$$\mathcal{J}_{\text{sound}}(\phi) = \int_{T_\phi} \mathcal{I}_{\text{sound}}\, dt. \tag{5.46}$$

When the sound arrives at $\mathcal{T}$ near $t = 50\delta_{\text{w}}/c_\infty$, the control is able to reduce the sound. However, it is clear that around $t = 230\delta_{\text{w}}/c_\infty$, the control's effectiveness is weakened, and it is not able to cancel the sound at the end of the time series. This occurs since the control does not take into account the further development of the flow after the end of the control time horizon.[123] After $T_\phi - \Delta T$, where ΔT is the time it takes for the control's effects to propagate to $\mathcal{T}$, changes in the control have no effect in the target region. Consequently, there exists no gradient information given by the adjoint solution that are useful to the control to cancel the sound in the target region..

Evolution of the adjoint pressure is shown in Fig. 5.5 for three times in the simulation. This quantity is used in (5.29) to provide the gradient information for g_{sound}, which is then used to update the control. The compressible flow equations are self-adjoint in the acoustic limit, so the adjoint pressure propagates as a sound wave emanating from $\mathcal{T}$ according to the forcing defined in (5.27). The waves eventually reach $\mathcal{C}$ where they determine the gradient (5.29). Since the adjoint system is solved numerically backwards in time, the visualizations in Fig. 5.5 are presented from later to earlier times from left to right, respectively.

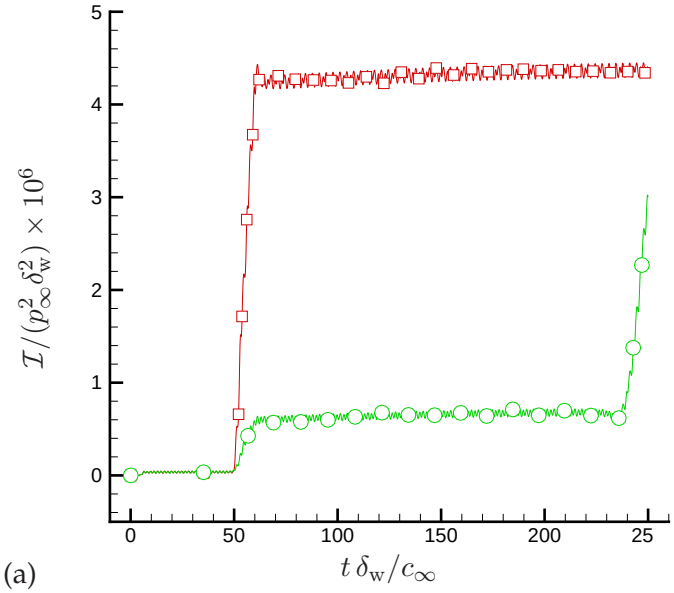

Figure 5.4: Instantaneous cost of baseline and optimized flow fields for the anti-sound control with with $c_\mathrm{p} = 0$. Curves indicate: original instantaneous cost functional (5.45) -□- and the instantaneous cost functional after optimization -○-.

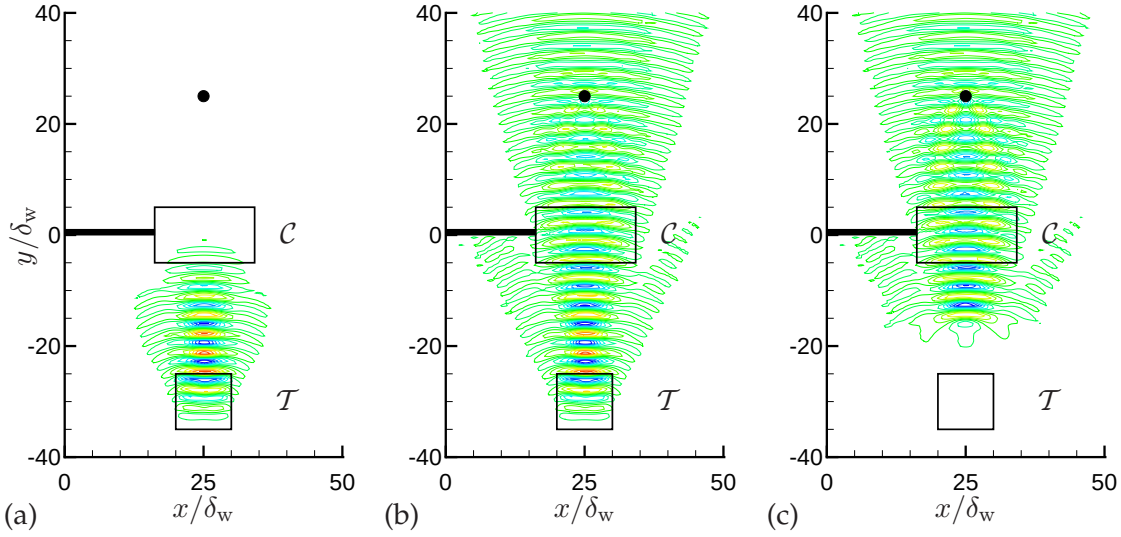

Figure 5.5: Evolution of adjoint pressure, $p^\dagger$ for the anti-sound control. The adjoint field is solved backwards in time and shown at times (a) $t = 220\delta_\mathrm{w}/c_\infty$, (b) $t = 120\delta_\mathrm{w}/c_\infty$, and (c) $t = 40\delta_\mathrm{w}/c_\infty$. Fourteen evenly-spaced contours between -0.016 and 0.016 are shown. The internal energy source is shown with a black dot located at $(x,\, y) = (25,\, 25)\delta_\mathrm{w}$.

5.4.2 Control with Finite Price Considered

The anti-sound internal energy control simulation presented in §5.4.1 did not incorporate the effects of penalizing the control. In this section, the price of the control is considered and the full cost function and gradients derived in (5.29) are used. An added price related to the control itself is important for use of such controls in eventual practical applications. The choice of c_{p} is important since setting c_{p} too low will result in similar controls as cases with no price and essentially no penalty for the cost of the control itself. On the other hand, a value that is too high will restrict the effectiveness of the control and the goal of the cost functional will not be easily reached. For this simple flow, price is only considered as a means to test and verify the method. Two additional simulations with $c_{\mathrm{p}} = 0.05$ and $c_{\mathrm{p}} = 0.5$ are presented, which sufficiently demonstrate the effects of penalizing the control to varying degrees.

The instantaneous cost for the baseline, no price control (from §5.4.1), and these simulations is shown in Fig. 5.6. The $c_{\mathrm{p}} = 0.05$ simulation shows almost no difference compared to the instantaneous cost of optimized case with no price term and likewise reduces the cost functional by 83% over the control time horizon. This suggests that the control for this simulation is not very costly, which is expected since the control is simply anti-sound. The $c_{\mathrm{p}} = 0.5$ case follows the same trends during the majority of the time horizon and is able to reduce $\mathcal{J}_{\mathrm{sound}}$ by 71%. However, due to the price term, $\mathcal{J}_{\mathrm{sound}}$ is roughly double that for the case with no price term during the bulk of the simulation. A small cost is incurred between $20 < tc_{\infty}/\delta_{\mathrm{w}} < 50$ which is not seen in the other simulations regardless of c_{p}. The controls begin to implement changes as the first sound waves reach $\mathcal{C}$ at about $t = 20\delta_{\mathrm{w}}/c_{\infty}$ and this action in penalized to a greater degree. The instantaneous cost then jumps at $t = 50\delta_{\mathrm{w}}/c_{\infty}$ as the sound reaches $\mathcal{T}$. Again, due to travel time effects, the cost jumps at the end of the control time horizon as expected. We see here that increasing the price term indeed reduces the controls ability to minimize the cost functional, $\mathcal{J}_{\mathrm{sound}}$.

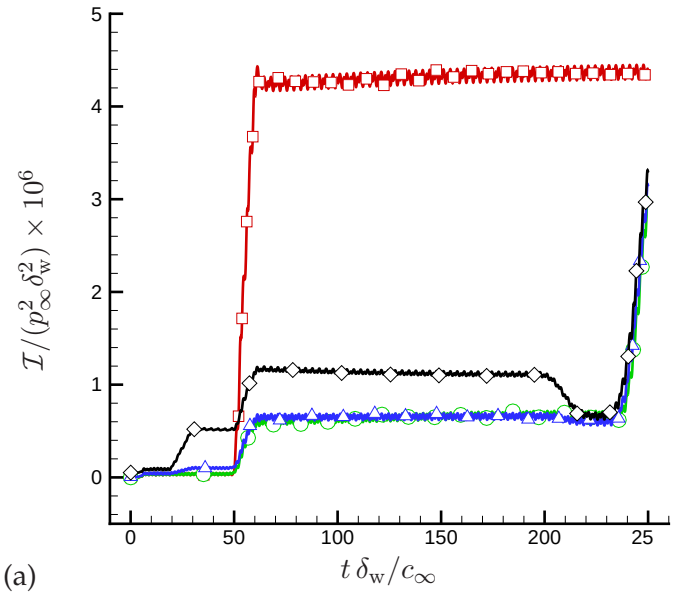

Figure 5.6: Instantaneous cost of baseline and optimized flow fields for the anti-sound control with and without price term consideration. Curves indicate: original instantaneous cost functional -▫-, optimized with $c_p = 0$ -○-, optimized with $c_p = 0.05$ -△-, and optimized with $c_p = 0.5$ -◇-.

5.5 Near-wall Two-dimensional Internal Energy Control

In this section we present the results of two adjoint-based optimizations of two-dimensional spatially-developing mixing layers. The simulations incorporate a solid wall boundary which is used in a geometry designed to model the near-nozzle region of a jet, where the thin shear layers begin the process of large-scale structure formation and roll up. Naturally, these simulations will provide the previously formulated control methodology a much more challenging problem than the idealized anti-sound optimizations presented in §5.4.1 and 5.4.2.

The simulations here demonstrate the use of cost functionals formulated specifically for increasing spreading with specific objectives formulated to increase the layer growth rate. Both cost functionals focused on maximizing an intermediate term in the process of Reynolds stress production, which is related to growth rate as shown in (5.7). The first, $\mathcal{J}_v(\phi)$, is a velocity-based cost functional meant to promote an increase in $\overline{\rho}\widetilde{v'v'}$ and $\overline{\rho}\widetilde{u'v'}$. The second, $\mathcal{J}_p(\phi)$, is a pressure-based functional to increase the pressure-strain rate term $\widetilde{p'\frac{\partial u'}{\partial x}}$ and therefore and $\overline{\rho}\widetilde{u'v'}$ as well.

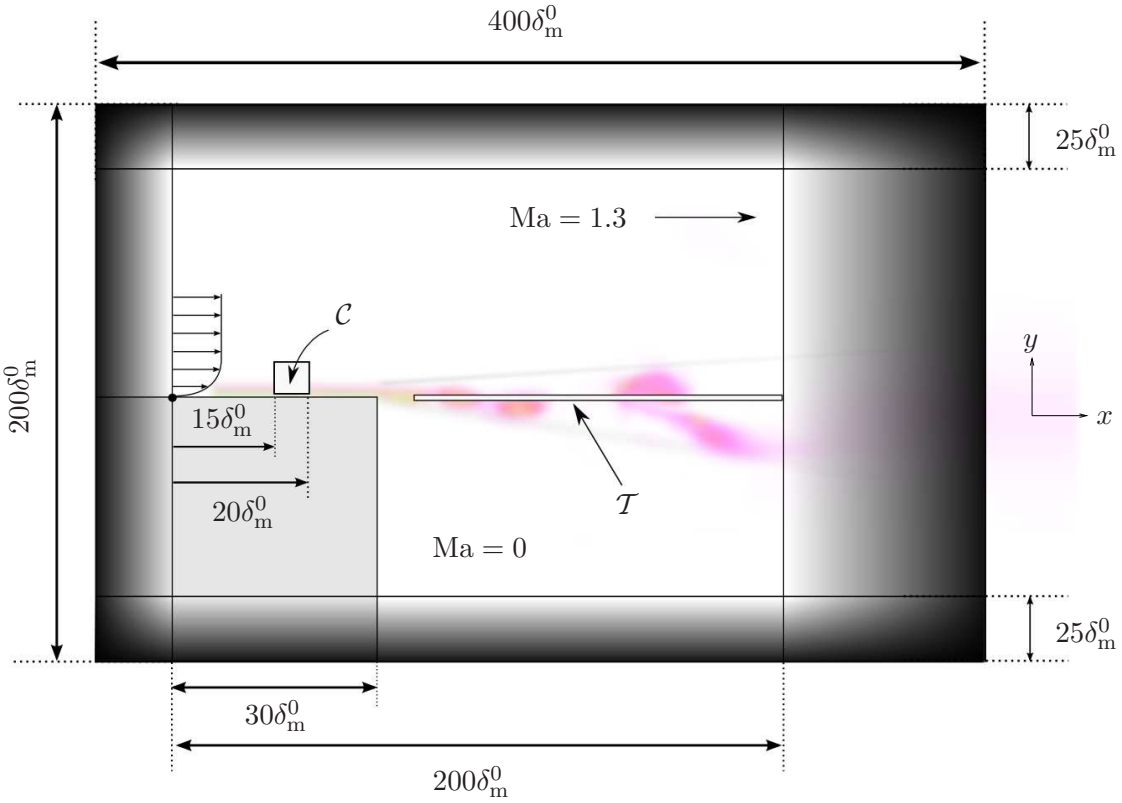

Figure 5.7: Schematic of the computational domain of the adjoint simulations. Dimensions are presented in terms of the momentum thickness at the nozzle exit, δ^0_{m}. The light grey area denotes computational space treated as a solid, isothermal wall. The shaded area on all four sides of the domain denotes the computational boundary (buffer) zones. The solid black dot denotes the $(x,\, y) = (0,\, 0)$ origin. Dimensions are not to scale in the schematic.

The pressure-strain rate term has been shown to decrease with increasing convective Mach number and is also a part of shear stress production. The cost functionals are based on attempting to increase the magnitude of the cross-stream velocity and pressure fluctuations, respectively. The results presented here will demonstrate the control effectiveness by showing the effects of the two spreading enhancement objectives concurrently and in comparison to the baseline, uncontrolled mixing layer.

5.5.1 Simulation Parameters

Figure 5.7 shows a schematic of the full computational domain of the two-dimensional mixing layer simulations. The geometry is meant to provide a simple model geometry of the near-nozzle

region of the exhaust region on a jet, i.e. the nozzle lip. The physical domain of the simulation extends to $x = 200\,\delta_{\mathrm{m}}^0$ in the streamwise direction and to $y = \pm 75\,\delta_{\mathrm{m}}^0$ in the cross-stream direction. There is no imposed mean flow below $y = 0$ downstream of the nozzle exit, which is located at $x = 30\,\delta_{\mathrm{m}}^0$. The base flow is a Mach 1.3 compressible boundary layer above a solid, no-slip wall located at $y = 0$ with a fixed wall temperature T_∞. The laminar inflow boundary layer was specified above the wall using the method outlined by Lui[93] and scaled such that the momentum thickness is $\delta_{\mathrm{m}}^0 = 1$ as the shear layer separates from the wall. Using $L^* = \delta_{\mathrm{m}}^0$ for nondimensionalization (see §2.1), the Reynolds number was $\mathrm{Re} = 3330$.

The flow and adjoint solutions were solved using the methods outlined in §5.3 and §2.2. Both the flow and adjoint solutions were filtered every five time steps in the entire physical domain of the simulation using the high-wavenumber filter described in §2.2.7. The filtered field was used as the flow solution and not a combination of the filtered and unfiltered flow fields. This means that in the flow domain, the filtering coefficient $\varrho(y) = 1$ in (2.42) and (2.43). The numerical time step was $\Delta t c_\infty / \delta_{\mathrm{m}}^0 = 0.015$ and the control horizon was 52000 time steps. This allowed for a change in the flow induced by the control to travel through the physical flow domains three times, assuming that change traveled at the average speed of the upper and lower streams. The mesh size of the simulations was $N_{\mathrm{x}} \times N_{\mathrm{y}} = 1760 \times 575$. The control region as shown in Fig. 5.7 was a square with sides $5\delta_{\mathrm{m}}^0$ in length with its bottom left corner at $(x, y) = (15,\, 0.5)$, placing it just above the wall. The mesh in $\mathcal{C}$ had 44×35 points. The target region extended from $x = 50\,\delta_{\mathrm{m}}^0$ to $x = 200\,\delta_{\mathrm{m}}^0$ between $y = \pm 4\,\delta_{\mathrm{m}}^0$ with a mesh of 1174×55. The price coefficient was chosen to be $c_{\mathrm{m}} = 0.005$. A price coefficient had to be imposed in the cost functionals for these flows to ensure stability of the simulation. If no penalty was enforced on ϕ, the optimization could seek an arbitrarily large ϕ to create an arbitrarily large increase in the cost functional. This action would ultimately result in the numerics of the code failing.

5.5.2 Optimization Results

The optimizations for the two cost functionals $\mathcal{J}_{\mathrm{v}}$ and $\mathcal{J}_{\mathrm{p}}$ were computed for two iterations of the algorithm. About fifteen line searches were completed for each iteration. At the end of these

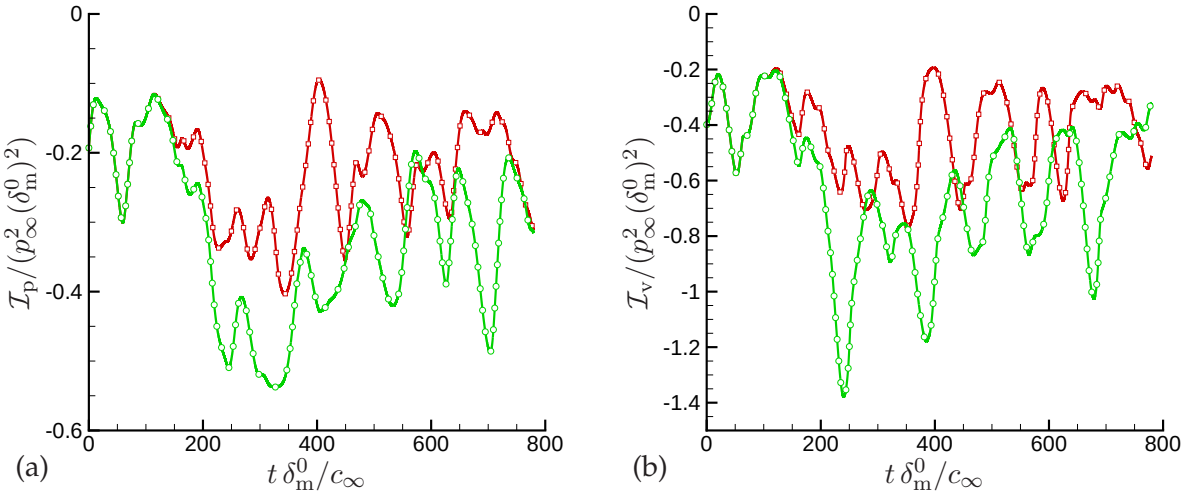

Figure 5.8: Instantaneous cost of the two-dimensional mixing layers simulation over the entire simulation time horizon. (a) Cost for the pressure-based spreading enhancement cost functional $\mathcal{J}_p$ (--○--) compared to the baseline mixing layer (--□--). (b) Cost for the velocity-based spreading enhancement cost functional $\mathcal{J}_v$ (--○--) compared to the baseline mixing layer (--□--).

two iterations, $\mathcal{J}_p$ was increased by 43% and $\mathcal{J}_v$ was increased by over 48% compared to the baseline. The instantaneous cost (similar to (5.46)) for each of the cost functionals is shown in Fig. 5.8. The curves for the optimized simulation show that the effect of the control is not seen until $t = 125c_\infty/\delta_m^0$ due to the travel time of the effect of the control. Removing the time period where the control could not affect change in the control region, the pressure-based cost functional was increased by 50% and the velocity-based cost functional was increased by 55%. The cost functional is "decreased" (minimized in the sense that it is more negative) for almost the entire remaining portion of the time horizon for $\mathcal{J}_p$. There are several points in time where this is not true for $\mathcal{J}_v$, but the difference in instantaneous cost during these times is minimal. The largest increases in the cost functional occur in the earlier portions of the control time horizon between 200 and $400c_\infty/\delta_m^0$.

The controls formulated for spreading enhancement were directly attempting to increase the magnitude of the cross-stream velocity and pressure fluctuations on the mixing layer centerline according to (5.10) and (5.11). Figure 5.9 shows the root-mean-square (rms) of the pressure and velocity fluctuations along $y = 0$ (the center of $\mathcal{T}$) for the two optimizations versus the baseline

flow. While both controls increase both quantities above the baseline over the entire domain, the velocity-based control shows higher RMS levels over the majority of the flow domain. The velocity control induces higher magnitude pressure fluctuations than the pressure control over the first three-quarters of the domain including over the wall itself ($x < 30\delta_{\mathrm{m}}^0$). The pressure control does not produce p_{rms} levels of the same magnitude until $x = 150\delta_{\mathrm{m}}^0$ and at this point the baseline mixing layer is beginning to catch up to the controlled flows. Despite targeting the maximization of cross-stream velocity on the layer centerline, the velocity-based control also increases pressure fluctuations more than the pressure-based control.

The greatest increase above baseline values for v_{rms} in Fig. 5.9(b) occurs in the flow domain just after the end of the wall. A dramatic jump in v_{rms} is seen in both controls while the curve slowly increases away from the wall edge for the baseline case. This is also true of p_{rms} in Fig. 5.9(a) to a similar degree. We expect that the velocity-based control does better than the other control here since it increased its cost functional by a higher percentage. As with the rms pressure, the pressure-based control and baseline flow catch up to the velocity-based control by the end of the flow domain. With the largest disparity in the rms quantities happening closer to the nozzle and showing little increase near the end of the flow domain. This suggests that the changes imparted by the control are most strongly realized in the region directly downstream of the wall.

To further investigate the control's effect on the mixing layer, especially in the near-wall-edge region, consider the visualization of large-scale structure pairing presented in Fig. 5.10. Pairing is represented by showing the pressure fluctuations above and below p_∞ in white and black shades. When two black structures merge in the figure, we say a pairing of large-scale vorticies occurs in the mixing layer. Coinciding with the observations of greater effects due to the control closer to the wall edge from the curves of v_{rms} and p_{rms}, the pairing in Fig. 5.10 is shown to occur more upstream in the controlled cases than the baseline case. Fig. 5.10(a) reveals that the baseline case does not show a significant vortex pairing until around $x = 120\,\delta_{\mathrm{m}}^0$ over the entire simulation time. Most of the pairings in the baseline simulation occur near $x = 150\,\delta_{\mathrm{m}}^0$.

For the pressure-based control, the first pairing occurs at $x = 100\,\delta_{\mathrm{m}}^0$ and this is even closer to the wall edge at $x = 50\,\delta_{\mathrm{m}}^0$ for the velocity-based control in Fig. 5.10(c). The pairings in the

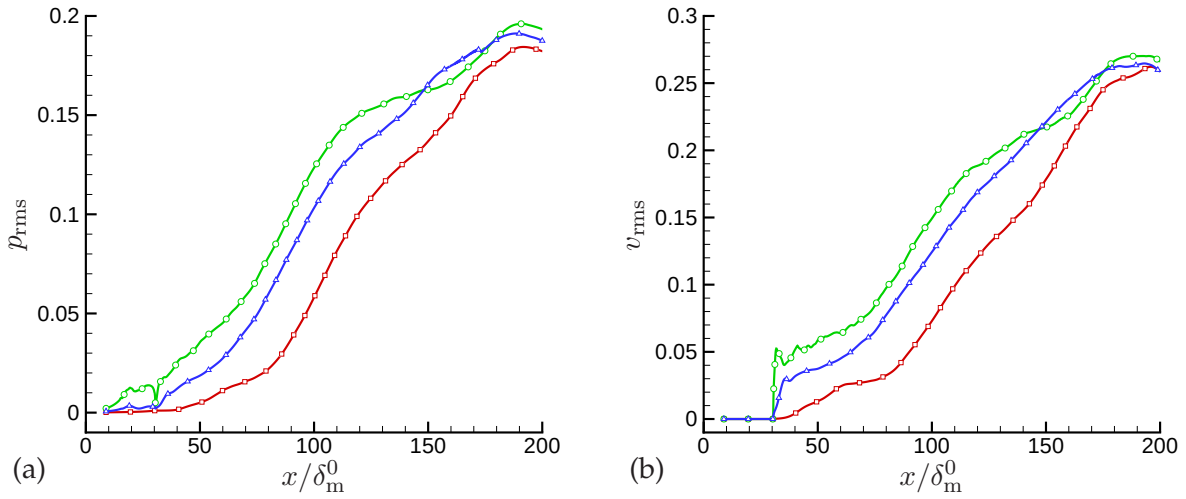

Figure 5.9: RMS fluctuations of (a) pressure and (b) cross-stream velocity (v) along the layer centerline ($y = 0$). Velocity-based spreading enhancement (– – ○ – –), pressure-based spreading enhancement (– – △ – –) and the baseline mixing layer (– – □ – –).

controlled cases begin much closer to the wall although steadily happen further downstream as time progresses. Corresponding to the higher levels of $p_{\rm rms}$ in Fig. 5.9(a) for the velocity-based control, the pressure fluctuations induced by the control are seen more readily in the control region above the wall in Fig. 5.10(c). The times where the pressure fluctuations due to ϕ are the strongest (between $t = 50\,c_\infty/\delta^0_{\rm m}$ and $t = 300\,c_\infty/\delta^0_{\rm m}$) appear to be the direct cause of the pairings which occur very close to the nozzle. It is clear from Fig. 5.10 that the controls fundamentally alter the dynamics of the structures of the mixing layer and cause vortex pairing (and subsequent roll up) farther upstream than the uncontrolled mixing layer.

The control's effect is also shown via the frequency content in the mixing layer. The pressure frequency spectra plotted as a function of the streamwise coordinate for the three mixing layers is shown in Fig. 5.11. The baseline spectrum shown in Fig. 5.11(a) reveals the natural frequency content of the mixing layer since no external forcing of the mixing layer was attempted in the simulation. The Strouhal number of the most amplified frequency is $\mathrm{St} = f\delta^0_{\rm m}/c_\infty = 0.013$ based on inviscid parallel-flow linear stability theory[118] and this Strouhal number corresponds to the peak of energy for the baseline simulation at the end of the flow domain. A weaker harmonic at twice this most amplified frequency occurs slightly upstream of this position.

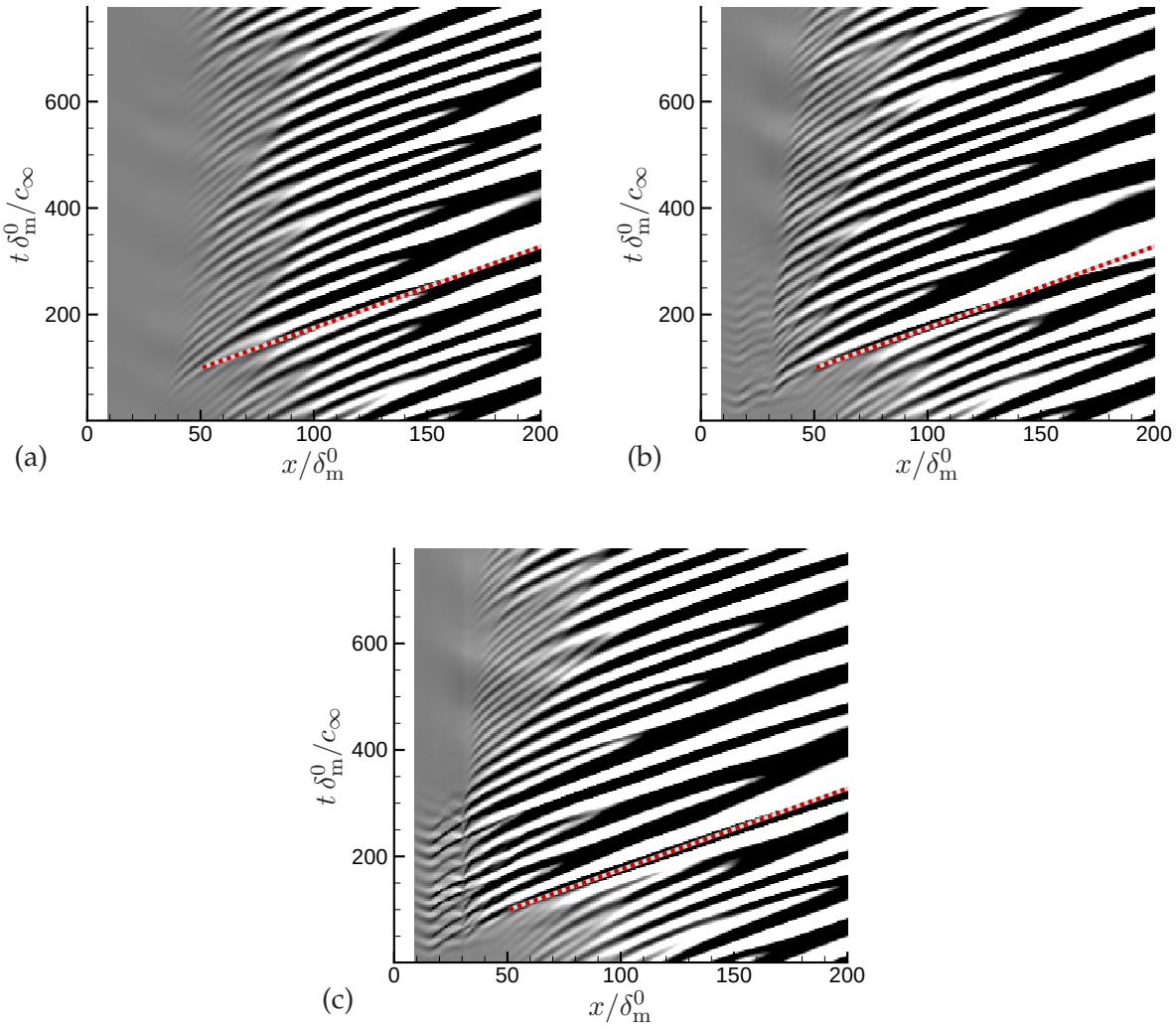

Figure 5.10: Space-time pressure evolution at $y = 0$ for the (a) baseline, (b) pressure-based control, and (c) velocity-based control. Black denotes $(p - p_\infty)/(\rho_\infty c_\infty^2) < 0$ and white $(p - p_\infty)/(\rho_\infty c_\infty^2) > 0$. The dashed line denotes the convection velocity of the mixing layers based on the free stream streamwise velocity.

Both the pressure-based and velocity-based controls rearrange the spectral energy in the mixing layer such that it occurs more upstream than the baseline. The pressure-based control in Fig. 5.11(b) shifts the majority of the energy slightly upstream to about $f\delta^0_{\rm m}/c_\infty = 0.01$. The energy in frequencies above this point are noticeably diminished compared to the baseline. The more successful velocity-based control in Fig. 5.11(c) shifts the spectral energy to a very strong $f\delta^0_{\rm m}/c_\infty = 0.014$ peak which occurs farther upstream than any other significant area of energy.

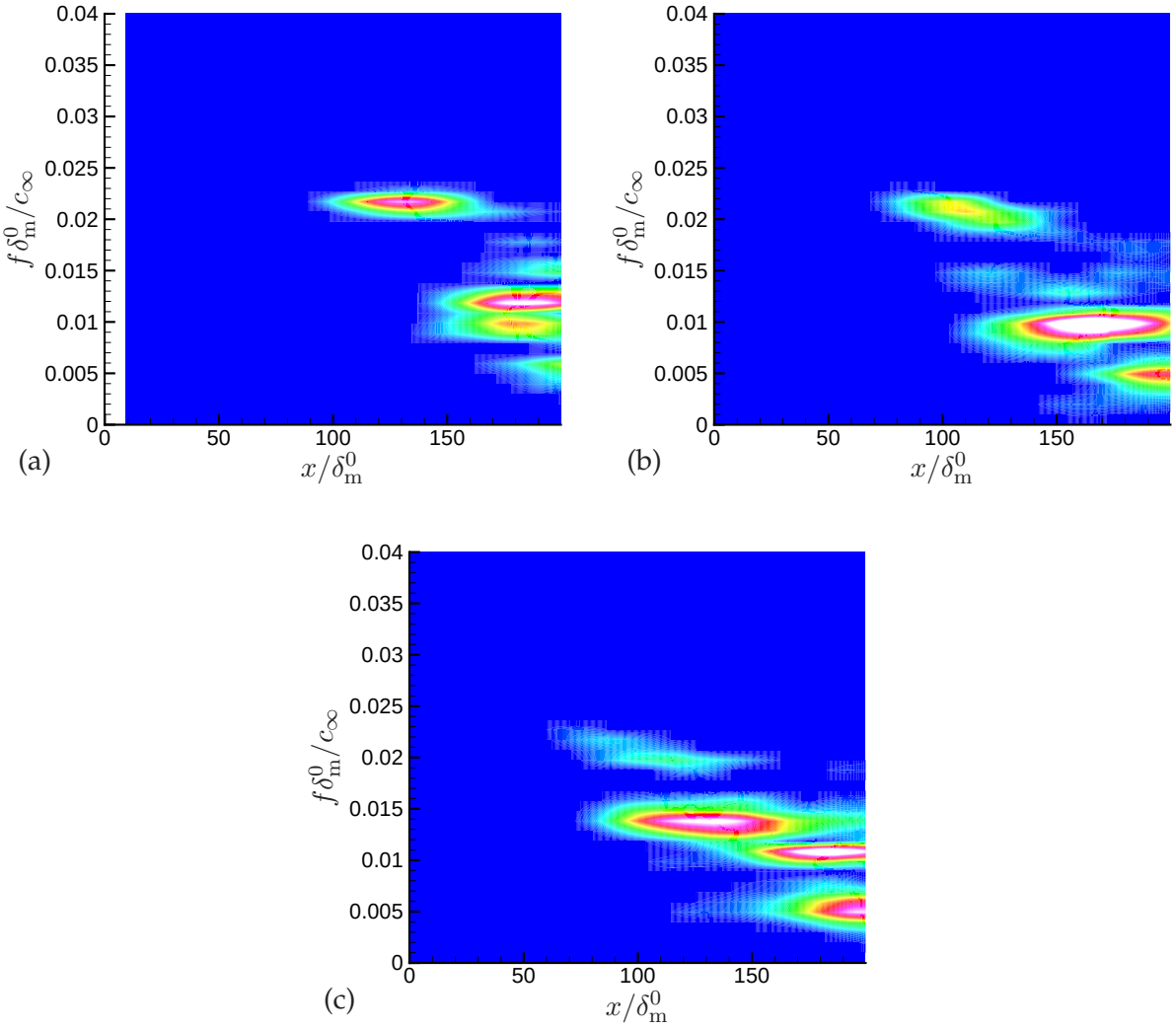

Figure 5.11: Pressure frequency spectrum plotted along the streamwise coordinate x for the (a) baseline, (b) pressure-based control, and (c) velocity-based control. The white regions correspond to the peaks of spectral energy. An identical scaling is used for all three spectra.

Energy found in the harmonic in the baseline case is converted to very energetic frequencies below $f\delta_{\mathrm{m}}^0/c_\infty = 0.014$ which occur closer to the wall edge than in the pressure-based control or the baseline simulation. The most successful control has shifted its frequency spectra to have more energy in lower frequencies, closer to the wall edge.

The cost functionals formulated in (5.10) and (5.11) were designed to provide a means of enhancing mixing between the low- and high-speed streams of the layer. The quantities to be max-

imized (v' and p') were chosen for their simplicity in the adjoint derivation but also such that an increase in them would produce $\overline{\rho}\widetilde{u'v'}$. The Reynolds shear stress is proportional to the growth rate of the layers, which should enhance spreading.

Figure 5.12 shows contour plots of the calculated $\overline{\rho}\widetilde{u'u'}$, $\overline{\rho}\widetilde{u'v'}$, and $\overline{\rho}\widetilde{v'v'}$ for the baseline and controlled simulations. As is the trend with the other results for this optimization, the velocity-based control see higher levels of all three stress quantities further upstream than the pressure-based control and the baseline. Its control is more successful at generating these stresses for the majority of the target region stretching from $x = 50\delta_{\mathrm{m}}^0$ to $x = 200\delta_{\mathrm{m}}^0$. Interestingly, the maximum values of $\overline{\rho}\widetilde{u'u'}$ and $\overline{\rho}\widetilde{u'v'}$ over the entire simulation domain are obtained by the pressure-based control and baseline simulation, respectively. However, the velocity-based control clearly reaches greater magnitudes of all three stresses closer to the wall edge (in comparison) especially for $\overline{\rho}\widetilde{v'v'}$, as seen in Fig. 5.12(i). The cross-stream width of the stresses is also increased by both controls despite the target region only being $8\delta_{\mathrm{m}}^0$ wide and centered around $y = 0$. The control is effective at increasing the magnitude and width of the stress profiles over the majority of the streamwise extent of the target region. It is not until the very end of the simulation domain where the baseline flow begins to achieve similar stress width profiles and magnitudes.

As a result of the additional production and corresponding increase in the Reynolds stress in the target region, a subsequent increase in the momentum thickness of the controlled mixing layers is realized. This was the stated goal of the optimizations in this portion of the adjoint study. Figure 5.13 show the percentage increase of the controlled mixing layers' momentum thickness compared to the baseline case beginning at the wall edge. At the edge, the controls have already increased the thickness of the boundary layer and the mixing layers have an approximately 10% larger layer thickness than the baseline by $x = 100\delta_{\mathrm{m}}^0$. Despite the velocity-based control showing higher p_{rms} and v_{rms} over the domain as shown in Fig. 5.9 and having higher magnitude stresses upstream, the pressure-based control causes the mixing layer to grow more. The pressure-based control increases the thickness by a maximum of over 15%, while the velocity is slightly over 10%. Since the layer growth rate is proportional to $\overline{\rho}\widetilde{u'v'}$ by (5.9), the pressure-based control causes higher growth downstream of $x = 150\delta_{\mathrm{m}}^0$ since its Reynolds stress is higher there (see Fig. 5.12(e)). Also, the growth diminishes at the end of the streamwise domain as the baseline simulation has

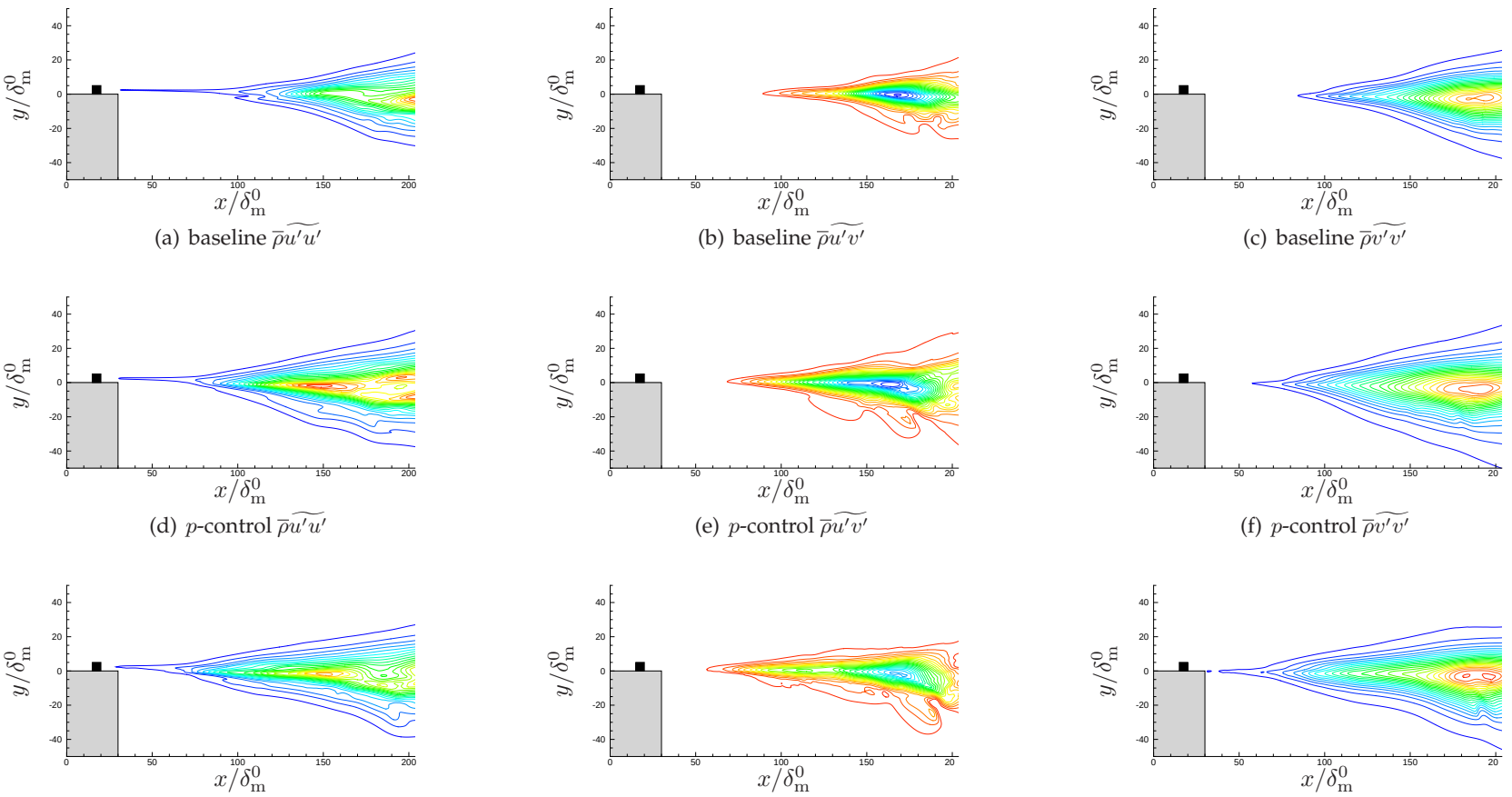

(a) baseline $\overline{\rho}\widetilde{u'u'}$ (b) baseline $\overline{\rho}\widetilde{u'v'}$ (c) baseline $\overline{\rho}\widetilde{v'v'}$

(d) p-control $\overline{\rho}\widetilde{u'u'}$ (e) p-control $\overline{\rho}\widetilde{u'v'}$ (f) p-control $\overline{\rho}\widetilde{v'v'}$

(g) v-control $\overline{\rho}\widetilde{u'u'}$ (h) v-control $\overline{\rho}\widetilde{u'v'}$ (i) v-control $\overline{\rho}\widetilde{v'v'}$

Figure 5.12: Normal and Reynolds stresses of the baseline, pressure-based control, and velocity-based control simulations. The grey shaded area designates the solid wall in the simulation and the black box is the control region, $\mathcal{C}$. The stresses shown are normalized by $\rho_\infty c_\infty^2$. For $\overline{\rho}\widetilde{u'u'}$, 20 evenly-spaced contours between 0.005 and 0.1 are shown. For $\overline{\rho}\widetilde{u'v'}$, 15 evenly-spaced contours between -0.03 and -0.001 are shown. For $\overline{\rho}\widetilde{v'v'}$, 23 evenly-spaced contours between 0.002 and 0.68 are shown.

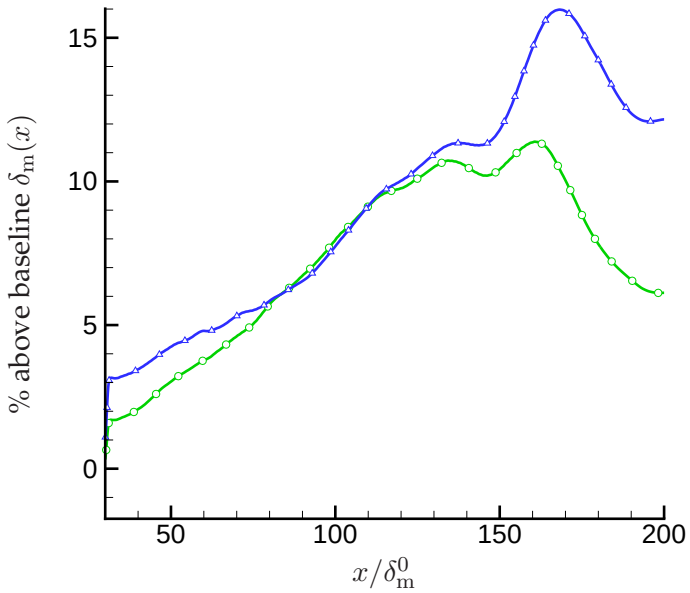

Figure 5.13: Percent increase of momentum thickness along the streamwise direction for the velocity-based (--○--) and pressure-based (--△--) controls.

the highest magnitude $\widetilde{\overline{\rho}u''v''}$.

5.6 Three-dimensional Mixing Layer Control

We now report the results of implementing the adjoint-based optimization procedure for a three-dimensional spatially-developing mixing layer.

5.6.1 Flow and Simulation Parameters

The three-dimensional mixing layer simulated is shown in Fig. 5.14. The Mach numbers of the upper and lower streams are $\mathrm{Ma} = 0.9$ and $\mathrm{Ma} = 0$, respectively. The flow was nondimensionalized by c_∞, ρ_∞, and the inflow vorticity thickness

$$\delta_\omega = \frac{\Delta U}{|dU/dy|_{\max}}, \tag{5.47}$$

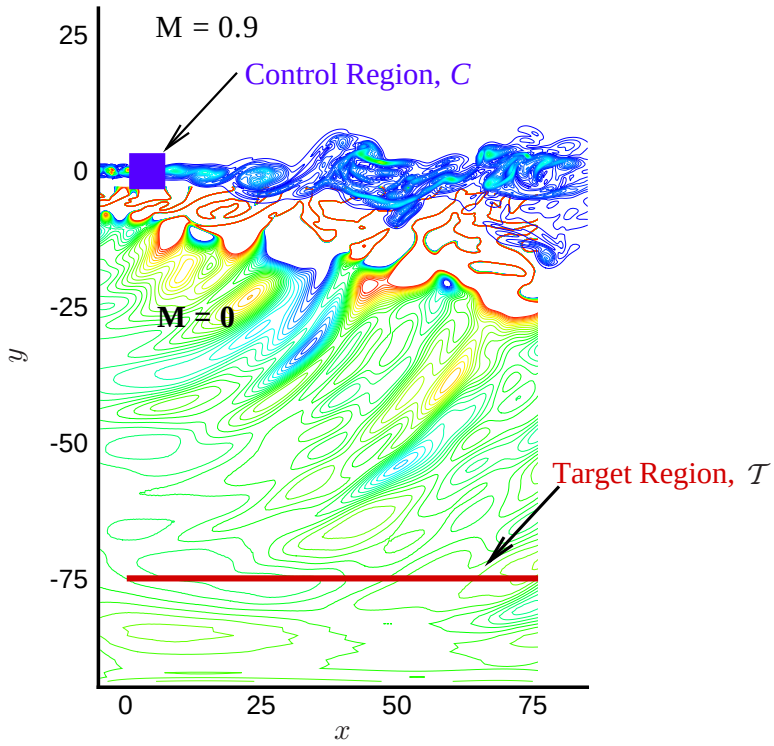

Figure 5.14: Schematic of the control setup of the three-dimensional spatial mixing layer. A x-y plane of the flow field is shown. The target region was initially located at $y = -75\delta_\omega$ for the first portion of the optimization and later moved to $y = -40\delta_\omega$.

where ΔU is the velocity difference across the mixing layer. The density, temperature, and viscosity were the same in both streams and zero bulk viscosity was assumed. The Reynolds number was 200 based on this nondimensionalization and the Prandtl number was 0.7. The flow equations were solved without modeling assumptions on a mesh of $N_x \times N_y \times N_z = 512 \times 400 \times 48$ points. The physical domain of the simulations extended to $75\,\delta_\omega$ in the streamwise direction, to $12.8\,\delta_\omega$ in the spanwise direction, and from $-80\,\delta_\omega$ to $12\,\delta_\omega$ in the cross-stream direction. The control region $\mathcal{C}$ covered $x = \{0, 7\}\,\delta_\omega$, $y = \{-4, 4\}\,\delta_\omega$, and the entire spanwise domain. The control region mesh had $39 \times 53 \times 48$ in the x, y, and z coordinate directions, respectively. The target region $\mathcal{T}$ (an x–z plane) was located at $y = -40\,\delta_\omega$ covering the full streamwise extent of the physical domain. The target region mesh contained 442×48 points in the streamwise and cross-stream directions,

respectively.

5.6.2 Simulation Methodology

The flow was started with an initial mean streamwise velocity profile of

$$U(x,y) = \frac{\mathrm{Ma}}{2}\left[\tanh\left(20.5\frac{y}{x}\right)+1\right] \tag{5.48}$$

and no cross-stream or spanwise velocities. To properly challenge the controller and provide more realistic turbulent inflow conditions, a means to "feed" developed turbulence from an auxiliary simulation of a streamwise periodic mixing layer into the mixing layer simulation was developed. Subsequent y–z planes from the "frozen" auxiliary simulation of a temporally-developing mixing layer were used as the target state of a buffer zone at the inflow of the spatial mixing layer simulation. The entire physical simulation domain was surrounded by an absorbing buffer zone as outlined in §2.2.5 to mimic an infinite domain. In this zone the solution was damped toward a quiescent state by adding a dissipative term to the flow (and adjoint) equations. Similarly, for the inflow zone, the $\mathbf{q}_{\mathrm{bc}}$ vector in (2.38) comes from the auxiliary computation, and was fed in at the estimated convection speed $U_c = 0.45$ of the current spatial mixing layer. Thus, the flow is effectively forced towards the inflow's turbulent flow field. A schematic of the inflow forcing is shown in Fig. 5.15. The inflow forcing occurred between $x = -20\,\delta_\omega$ and $x = -5\,\delta_\omega$. the inflow data was interpolated on to the current simulation's mesh. The period of this inflow data was long enough to allow multiple flow through times without repeating, which is longer than the time required to properly evaluate the controls.

With this inflow turbulence from the auxiliary simulation, the flow was simulated from its initial state for 3700 time steps ($449\,c_\infty/\delta_\omega$). This allowed for obvious visual transients in the physical domain to diminish before accumulating statistics or applying the control. The control time horizon was 5000 time steps, or $T_\phi = 625\,c_\infty/\delta_\omega$. This allowed for the following sequence of (hypothetical) events to occur five times during T_ϕ: the effect of the control advects from the region $\mathcal{C}$ at speed $U_c = 0.45$ to the downstream midpoint in the shear layer ($x = 37.5\,\delta_\omega$), the controlled flow generates a sound event, the sound wave then travels at the ambient sound speed

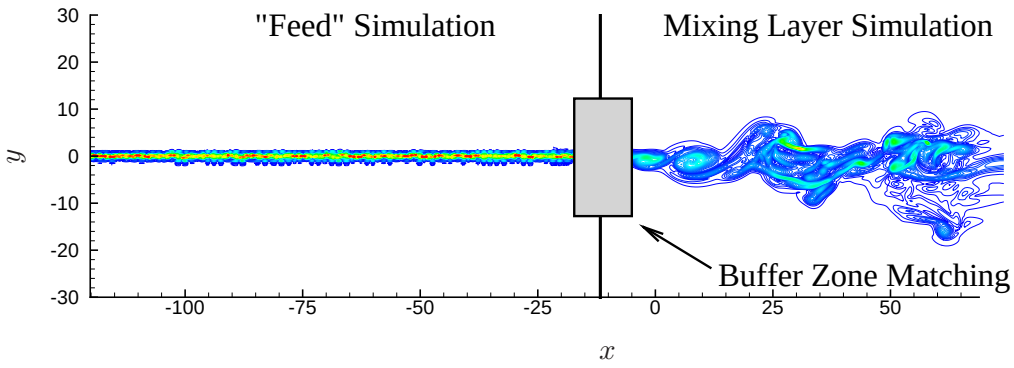

Figure 5.15: Schematic of the inflow turbulence feeding process. High-resolution temporal mixing layer data (at left) is steadily fed into the inflow "buffer zone" which overlaps with the spatial mixing layer simulation (at right). Magnitude of vorticity is shown to visualize each mixing layer.

c_∞ to the target plane $\mathcal{T}$. This length of time horizon ensures that the control not only reaches the target plane, but has ample opportunity to reduce noise there. The number of discrete parameters representing ϕ in $\mathcal{C}$ for this time horizon is approximately 500 million.

The calculations presented in this section used the time and spatial differencing schemes outlined in §2.2.1 and §2.2.4. Nonreflecting boundary conditions are also as outlined in §2.2.5, but no high-order, high-wavenumber filtering was applied to the flow fields.

5.6.3 Flow and Adjoint Field Visualization

Figure 5.16 shows the three-dimensional structure of the flow and its fundamental differences from the two-dimensional simulation. The vortex stretching mechanism clearly creates a much more chaotic flow even at the low Reynolds number of the flow. Figure 5.16(a) shows a visualization as an x–y slice taken through the mid-plane of the spanwise direction of the simulation of the mixing layer. Contours of the magnitude of vorticity in the shear layer and contours of the dilatation are shown. Figure 5.16(b) shows isosurfaces of vorticity magnitude and slices at various streamwise locations of the three-dimensional structure of the flow.

A slice at the midpoint in the spanwise direction of the adjoint pressure field is shown in Fig. 5.17. The adjoint pressure begins as a sound wave (the equations are, of course, self-adjoint in

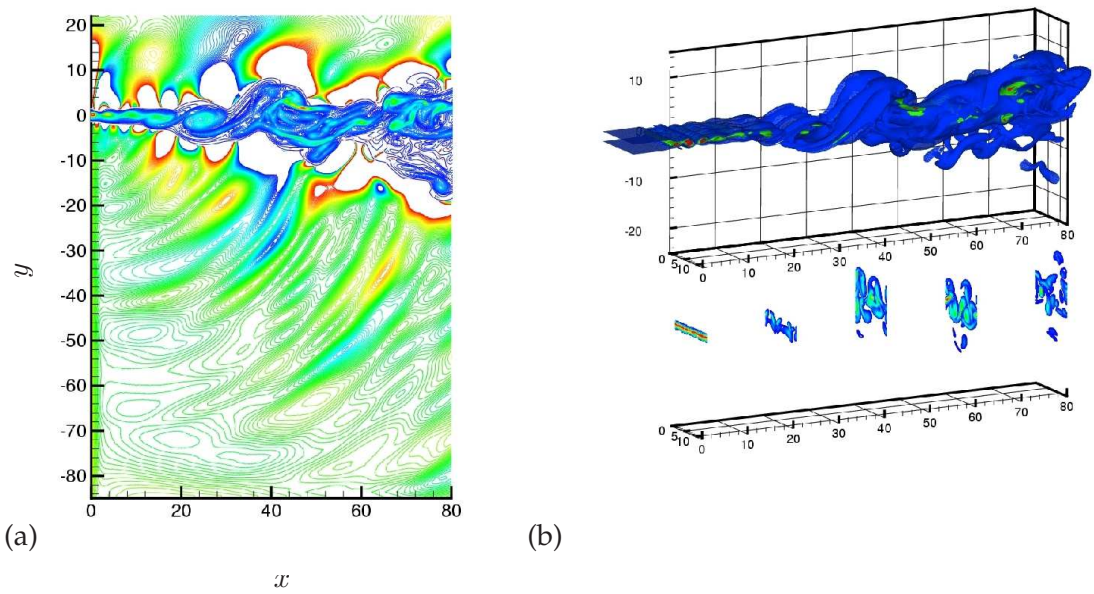

Figure 5.16: Visualization of the three-dimensional mixing layer flow field. (a) vorticity and dilatation fields and (b) isosurfaces of vorticity (top) and vorticity slices corresponding to several streamwise locations (bottom).

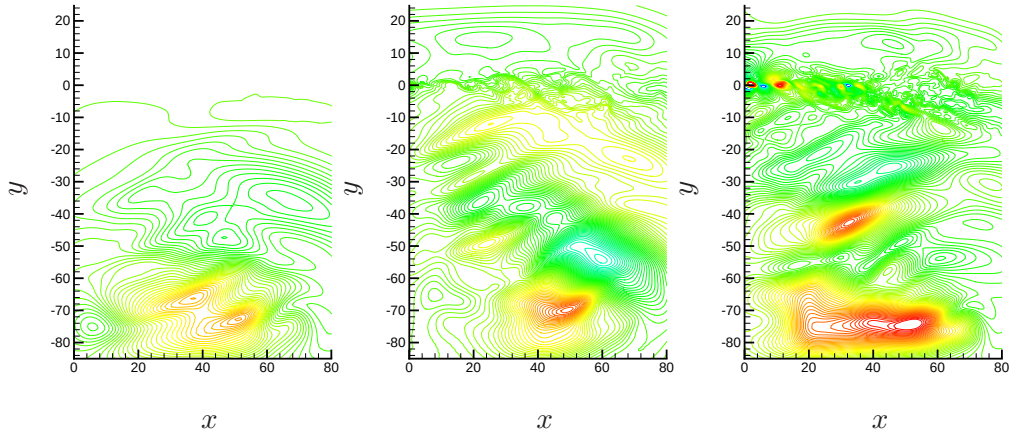

Figure 5.17: Snapshots of x–y plane of the adjoint pressure field at $z = 6.4\,\delta_\omega$ being forced in the target region $\mathcal{T}$ corresponding to the x–z plane at $y = -75\,\delta_\omega$. Time is progressing backwards from left to right.

the acoustic limit) forced by the flow data on the $\mathcal{T}$-plane. Once the disturbances of $p^\dagger$ encounter the shear layer, the instabilities are excited in the adjoint field which travel upstream towards the control region. The adjoint pressure field in $\mathcal{C}$, for a sound control as specified in (5.6), is used as gradient information to update the control ϕ.

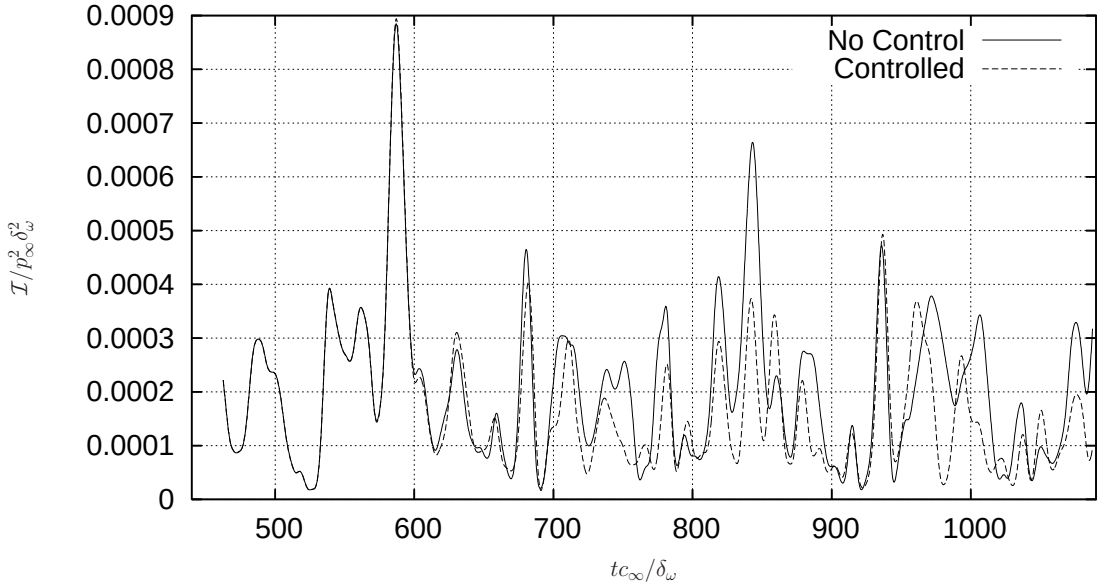

Figure 5.18: Instantaneous cost for a sound control in the three-dimensional mixing layer. Cost is shown for the baseline (no control) flow: —— , and the controlled flow after five iterations: - - - - .

5.6.4 Sound Control Results

Using the adjoint-based optimization methodology outlined in §5.2 for a far-field sound reduction control objective, the total overall noise in $\mathcal{T}$ was reduced plane by over 28% from the baseline flow. Figure 5.18 shows the control taking effect and reducing the pressure fluctuations in $\mathcal{T}$ by plotting the instantaneous cost, which is defined in (5.45). The optimization has made this reduction after five conjugate gradient iterations. The first three iterations were done with the $\mathcal{T}$ on the x–z plane at $y = -75\,\delta_\omega$. The control was only able to reduce $\mathcal{J}_{\text{sound}}$ by 18% in this configuration. The simulation then commenced on the fourth iteration, but the target region plane was moved to $y = -40\,\delta_\omega$ where the full 28% reduction in cost functional was achieved.

It is evident that there is no distinguishable difference between the values of the baseline and controlled $\mathcal{I}(\phi)$ until $tc_\infty/\delta_\omega \approx 600$. Even at this point, it is unlikely that the control is fully able to reduce noise on the target plane due to its spanwise width and the fact that changes due to the control must be advected by structures traveling at U_c and then emitted to $\mathcal{T}$, a process which takes longer to occur than simple noise radiation directly from $\mathcal{C}$. Still, the control appears to have the ability to reduce some peaks of pressure fluctuation later in the time horizon, where others are

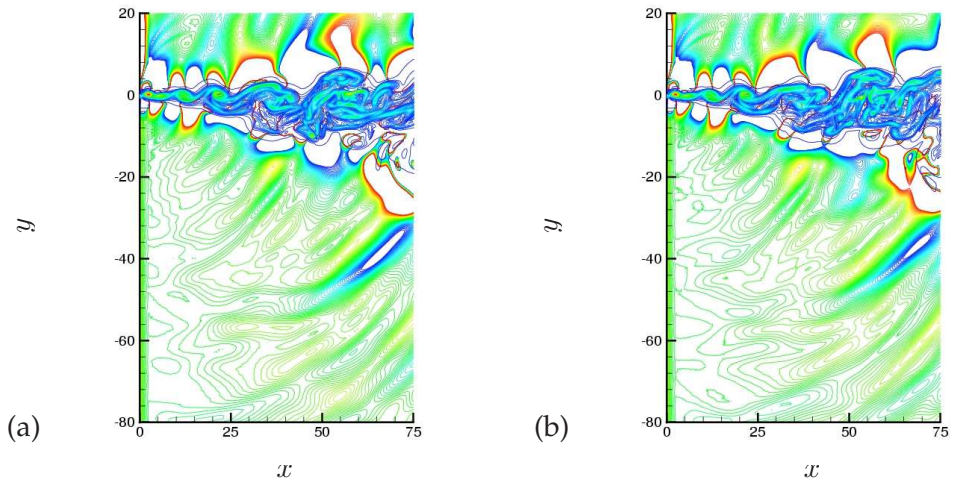

Figure 5.19: Comparison of the baseline dilatation and vorticity magnitude field (a) and the controlled field after the fifth control iteration (b). Contours of both quantities are the same for each plot.

either relatively unchanged, or slightly increased such as is the case near $tc_\infty/\delta_\omega \approx 930$.

Figure 5.19 compares x–y slices of the dilatation fields of the mixing layer at $tc_\infty/\delta_\omega = 831$ with no control and with the control corresponding to the current reduction. Considering this qualitative view with the instantaneous cost function in Fig. 5.18, it appears that the control is less successful at reducing noise on $\mathcal{T}$ closer to $\mathcal{C}$ — the sideline noise. Many of the loud sound events seen in $\mathcal{I}$ correspond to sound waves near the edges of the domain that may not be as controllable as those more directly underneath where the control is applied. The comparison of the two views of the shear layer also appears to agree with the previous two-dimensional simulation results of Wei and Freund.[28] The turbulent structures appear to be changed, but not significantly. Noticeable differences exist in the near field, but the sound field is changed in a more significant way visually. Although the noise has only been reduced 28% over the whole horizon, the higher amplitude events in the dilatation field are diminished.

5.7 Conclusions

In this chapter we have presented an adjoint control methodology which was applied to problems of interest in aeroacoustics and shear flow control. Given the historic difficulties associated

with jet noise reduction and complex flow control, we have created a optimization framework designed to circumvent flow complexity and investigate control directly. The adjoint of the linearized, perturbed compressible flow equations was derived and solved with a high-fidelity numerical scheme incorporating solid wall boundaries in simple geometries. The adjoint solution was used as a means to give the sensitivity to changes in the flow made by a control. Cost functionals defined as metrics of sound reduction and mixing layer growth enhancement due to the control were minimized (or maximized when appropriate) via a conjugate gradient optimization algorithm.

The adjoint approach was applied to three model problems of varying degrees of complexity in this study. The method proved to show considerable promise as a means to control complex flows. First, the cost functional from a time-harmonic internal energy sound source was reduced using this technique by 83%. Optimizing a cost functional which included a price term which penalized the strength of the control using the same sound source in the same geometrical configuration was able to reduce the cost by 71%.

Second, a two-dimensional simulation with a boundary layer above a solid wall edge and a corresponding downstream Mach 1.3 mixing layer were optimized for enhanced mixing and layer growth in the downstream region. A control region was placed just above the wall near the end of the "splitter plate" and an internal energy type control was implemented. Two cost functionals were formulated to attempt to promote rapid growth in the mixing region compared to a baseline mixing layer. The first control focused on maximizing the pressure fluctuations on the layer centerline downstream of the plate and increased its cost functional metric by 50% over the baseline pressure fluctuations. A second control attempted to maximize the cross-stream (vertical) velocity fluctuations in the same region and did so by 55%. Both controls increased the average magnitude of the pressure and velocity fluctuations compared to the baseline and incited earlier large-structure pairing and vortex merging in the mixing layer. Both controls also increased the production of the Reynolds stresses, which resulted in 10%-15% increases in the mixing layer thickness over the extent of the streamwise domain. The pressure-based and velocity-based controls were successful at increasing the mixing layer growth in their respective target regions. However, the increases were more modest near the target region edges and in the vicinity of the trailing edge of

the wall, which was not included in the target region.

Third, a three-dimensional, turbulent mixing layer was simulated and optimized to reduce noise. The cost functional was reduced by over 28% on a sideline target plane parallel to the mean flow stationed below. The adjoint approach controlled this flow to a lesser degree than the other studies due to the additional complexities associated with its turbulent nature.

Given the results presented here, adjoint-based optimization has been shown to be a successful tool for use in simple flow control problems with a promising future. Because of its high computational cost, this method is not practical for flow control in engineering applications although this limitation is becoming less of a burden as computational bandwidth is improved. Beyond the computational burden is the disparity between the space-time profile of ϕ generated via the optimization and the abilities of flow control hardware to implement such a forcing. This entails constraining the form of the control as it is implemented as forcing to physically-realizable actions, which are of course dependent on hardware. Control constraint was done in the study by Wei[28] and showed the constraint was responsible for significant reduction in the control's ability to reduce it's cost functional. The behavior is likely to vary on a case-by-case basis, however. Adjoint-based optimization may also be a useful tool in the future to drive the design of actuators themselves. This is opposite of the strategy just described where the control ϕ is limited by the abilities of a proposed actuator technology. Given an optimization result which successfully controlled a flow of interest, determining the characteristics of the control and how it achieved its goal would be a highly useful starting point on which to begin actuator design.

Appendix A

Decay of Non-planar Waves in Doubly-periodic Domains

Lele & Ho[53] analyze a two-dimensional streamwise periodic domain via a model wave equation, which we generalize here to include a spanwise coordinate direction, z. A disturbance ϕ due to an arbitrary sound source distribution Q is governed by

$$\left(\frac{\partial}{\partial t}+U\frac{\partial}{\partial x}\right)^2\phi-c_\infty^2\nabla^2\phi=Q(x,y,z,t), \tag{A.1}$$

where U is assumed to be the mean velocity of the flow.

A Fourier transform in x and z yields an advected Klein-Gordon equation

$$\left(\frac{\partial}{\partial t}+ik_{\mathrm{x}}U\frac{\partial}{\partial x}\right)^2\hat{\phi}-c_\infty^2\left(\frac{\partial^2}{\partial y^2}-(k_{\mathrm{x}}^2+k_{\mathrm{z}}^2)\right)\hat{\phi}=\hat{Q}(k_{\mathrm{x}},y,k_{\mathrm{z}},t). \tag{A.2}$$

Note that the same equation as above results regardless of whether the domain is periodic with corresponding transform

$$\hat{\phi}(k_{\mathrm{x}}^n,y,k_{\mathrm{z}}^m,t)=\frac{1}{L_{\mathrm{x}}L_{\mathrm{z}}}\int_0^{L_{\mathrm{x}}}\int_0^{L_{\mathrm{z}}}\phi(x,y,z,t)e^{ik_{\mathrm{x}}^nx+ik_{\mathrm{z}}^mz}\,\mathrm{d}x\mathrm{d}z, \tag{A.3}$$

which give discrete wavenumbers

$$k_{\mathrm{x}}^n=\frac{2\pi n}{L_{\mathrm{x}}}\qquad n=-\infty,\ldots-1,0,1,\ldots\infty \tag{A.4}$$

$$k_{\mathrm{z}}^m=\frac{2\pi m}{L_{\mathrm{z}}}\qquad m=-\infty,\ldots-1,0,1,\ldots\infty, \tag{A.5}$$

or if the domain is infinite with transform

$$\hat{\phi}(k_\mathrm{x}, y, k_\mathrm{z}, t) = \frac{1}{(2\pi)^2} \int_{-\infty}^{\infty} \int_{-\infty}^{\infty} \phi(x, y, z, t) e^{ik_\mathrm{x}x + ik_\mathrm{z}z} \, \mathrm{d}x \mathrm{d}z, \tag{A.6}$$

which has a continuous wavenumber spectrum.

Equation (A.2) has the free space Green's function

$$G(y, t;\, y', t') = \frac{1}{2} e^{-ik_\mathrm{x}U(t-t')} H\left[t - t' - \frac{|y - y'|}{c_\infty}\right] J_0\left[kc_\infty \sqrt{(t-t')^2 - \frac{(y-y')^2}{c_\infty}}\right], \tag{A.7}$$

where $k = \sqrt{k_\mathrm{x}^2 + k_\mathrm{z}^2}$, H is the Heaviside function, and J_0 is the zeroth-order Bessel function. The solution of Eq. (A.2) is

$$\hat{\phi}(k_\mathrm{x}, y, k_\mathrm{z}, t) = \int_{-\infty}^{\infty} \int_{-\infty}^{\infty} \hat{Q}(k_\mathrm{x}, y, k_\mathrm{z}, t) G(y, t;\, y', t') \, \mathrm{d}y' \mathrm{d}t'. \tag{A.8}$$

Since for any k the sound-field behavior is independent of whether or not the domain is periodic—whether or not the spectrum is discrete or continuous—any effects of the periodicity is not due to the periodic images *per se*. When the discrete spectrum is a good model for the infinite-domain continuous spectrum (that is, it retains adequate wavenumber resolution), we do not expect any direct effects of the periodicity. This amounts to having a sufficiently large periodic domain size.

The $k = 0$ dominance in the sound field immediately adjacent to the mixing layer seen clearly in the Lele & Ho simulations results from a strong correlation on the scale of the computational box, which is equivalent to coarse resolution of the low wavenumbers. Radiation with $k = 0$ is the only possibility when the sound wavelength is comparable to the periodic box size. The specific criterion comes most easily by also Fourier transforming Eq. (A.2) in time,

$$\frac{\partial^2}{\partial y^2} \hat{\phi}(k_\mathrm{x}, y, k_\mathrm{z}, \omega) + \left(\frac{\omega^2}{c_\infty^2} - k^2\right) \tilde{\phi}(k_\mathrm{x}, y, k_\mathrm{z}, \omega) = 0. \tag{A.9}$$

The mean velocity U and Q are set equal to zero for convenience, but doing so does not affect the

outcome of the analysis. Equation (A.9) only has wave solutions for $|\omega| > |k|c_\infty$. As an example, for $k_\mathrm{z} = 0$ and discrete wavenumber $k_\mathrm{x} = 2\pi n/L_\mathrm{x}$ in x, this yields $n\lambda < L_\mathrm{x}$, where λ is the wavelength of the sound. At lower frequencies when the sound wavelength is comparable to the periodic box size, only $k = 0$ radiation is possible since this is the only discrete wavenumber that satisfies the $|\omega| > |k|c_\infty$ condition for radiation. At higher frequencies, or larger L_x, a large number of n can propagate.

Appendix B

The Adjoint of the Three-dimensional Compressible Navier-Stokes Equations

The adjoint of the three-dimensional compressible Navier-Stokes equations expanded from its operator form in §5.2.4 is

$$\mathcal{N}^\dagger(\mathbf{q})\mathbf{q}^\dagger = \left(\mathbf{A}^\dagger\frac{\partial}{\partial t} + \mathbf{B}^\dagger\frac{\partial}{\partial x} + \mathbf{C}^\dagger\frac{\partial}{\partial y} + \mathbf{D}^\dagger\frac{\partial}{\partial z} + \mathbf{E}^\dagger\right)\mathbf{q}^\dagger \tag{B.1}$$

where the vector of adjoint variables $\mathbf{q}^\dagger$ is defined in (5.4) and the derivative coefficient matrices are

$$\mathbf{A}^\dagger = \begin{bmatrix} 1 & u & v & w & \frac{1}{2}\left(u^2+v^2+w^2\right) \\ 0 & \rho & 0 & 0 & \rho u \\ 0 & 0 & \rho & 0 & \rho v \\ 0 & 0 & 0 & \rho & \rho w \\ 0 & 0 & 0 & 0 & \frac{1}{\gamma-1} \end{bmatrix} \tag{B.2}$$

$$\mathbf{B}^\dagger = \begin{bmatrix} u & u^2 & uv & uw & \frac{1}{2}u\left(u^2+v^2+w^2\right) \\ \rho & 2\rho u & \rho v & \rho w & \frac{\gamma p}{(\gamma-1)} + \frac{\rho}{2}\left(3u^2+v^2+w^2\right) + \frac{5}{3\mathrm{Re}}\left(\frac{\partial v}{\partial y}+\frac{\partial w}{\partial z}\right) \\ 0 & 0 & \rho u & 0 & \rho uv - \frac{5}{3\mathrm{Re}}\frac{\partial u}{\partial y} \\ 0 & 0 & 0 & \rho u & \rho uw - \frac{5}{3\mathrm{Re}}\frac{\partial u}{\partial z} \\ 0 & 1 & 0 & 0 & \frac{\gamma u}{\gamma-1} \end{bmatrix} \tag{B.3}$$

$$\mathbf{C}^{\dagger} = \begin{bmatrix} v & uv & v^2 & vw & \frac{1}{2}v\left(u^2+v^2+w^2\right) \\ 0 & \rho v & 0 & 0 & \rho uv - \frac{5}{3\mathrm{Re}}\frac{\partial v}{\partial x} \\ \rho & \rho u & 2\rho v & \rho w & \frac{\gamma p}{(\gamma-1)} + \frac{\rho}{2}\left(u^2+3v^2+w^2\right) + \frac{5}{3\mathrm{Re}}\left(\frac{\partial u}{\partial x}+\frac{\partial w}{\partial z}\right) \\ 0 & 0 & 0 & \rho v & \rho vw - \frac{5}{3\mathrm{Re}}\frac{\partial v}{\partial z} \\ 0 & 0 & 1 & 0 & \frac{\gamma v}{\gamma-1} \end{bmatrix} \tag{B.4}$$

$$\mathbf{D}^{\dagger} = \begin{bmatrix} w & uw & vw & w^2 & \frac{1}{2}w\left(u^2+v^2+w^2\right) \\ 0 & \rho w & 0 & 0 & \rho uw - \frac{5}{3\mathrm{Re}}\frac{\partial w}{\partial x} \\ 0 & 0 & \rho w & 0 & \rho vw - \frac{5}{3\mathrm{Re}}\frac{\partial w}{\partial y} \\ \rho & \rho u & \rho v & 2\rho w & \frac{\gamma p}{(\gamma-1)} + \frac{\rho}{2}\left(u^2+v^2+3w^2\right) + \frac{5}{3\mathrm{Re}}\left(\frac{\partial u}{\partial x}+\frac{\partial v}{\partial y}\right) \\ 0 & 0 & 0 & 1 & \frac{\gamma w}{\gamma-1} \end{bmatrix} \tag{B.5}$$

and the matrix of viscous terms is

$$\mathbf{E}^{\dagger} = \frac{1}{\mathrm{Re}} \begin{bmatrix} 0 & 0 & 0 & 0 & -\frac{\gamma p}{\mathrm{Pr}(\gamma-1)\rho^2}\left(\frac{\partial^2}{\partial x^2}+\frac{\partial^2}{\partial y^2}+\frac{\partial^2}{\partial z^2}\right) \\ 0 & \frac{4}{3}\frac{\partial^2}{\partial x^2}+\frac{\partial^2}{\partial y^2}+\frac{\partial^2}{\partial z^2} & \frac{1}{3}\frac{\partial^2}{\partial x \partial y} & \frac{1}{3}\frac{\partial^2}{\partial x \partial z} & \frac{4u}{3}\frac{\partial^2}{\partial x^2}+u\left(\frac{\partial^2}{\partial y^2}+\frac{\partial^2}{\partial z^2}\right)+\frac{v}{3}\frac{\partial^2}{\partial x \partial y}+\frac{w}{3}\frac{\partial^2}{\partial x \partial z} \\ 0 & \frac{1}{3}\frac{\partial^2}{\partial x \partial y} & \frac{\partial^2}{\partial x^2}+\frac{4}{3}\frac{\partial^2}{\partial y^2}+\frac{\partial^2}{\partial z^2} & \frac{1}{3}\frac{\partial^2}{\partial y \partial z} & \frac{4v}{3}\frac{\partial^2}{\partial y^2}+v\left(\frac{\partial^2}{\partial x^2}+\frac{\partial^2}{\partial z^2}\right)+\frac{u}{3}\frac{\partial^2}{\partial x \partial y}+\frac{w}{3}\frac{\partial^2}{\partial y \partial z} \\ 0 & \frac{1}{3}\frac{\partial^2}{\partial x \partial z} & \frac{1}{3}\frac{\partial^2}{\partial y \partial z} & \frac{\partial^2}{\partial x^2}+\frac{\partial^2}{\partial y^2}+\frac{4}{3}\frac{\partial^2}{\partial z^2} & \frac{4w}{3}\frac{\partial^2}{\partial z^2}+w\left(\frac{\partial^2}{\partial x^2}+\frac{\partial^2}{\partial y^2}\right)+\frac{u}{3}\frac{\partial^2}{\partial x \partial z}+\frac{v}{3}\frac{\partial^2}{\partial y \partial z} \\ 0 & 0 & 0 & 0 & \frac{\gamma}{\mathrm{Pr}(\gamma-1)\rho}\left(\frac{\partial^2}{\partial x^2}+\frac{\partial^2}{\partial y^2}+\frac{\partial^2}{\partial z^2}\right) \end{bmatrix}. \tag{B.6}$$

Appendix C

Adjoint Characteristic Boundary Conditions

To reduce numerical artifacts introduced by the limits of a computational domain or solids walls in a computation, boundary conditions need to be specified. As with the flow equations, these conditions are necessary to reduce unphysical, reflected waves introduced by the domain edges. This ensures that the flow calculation is independent of the placement of the boundaries.

C.1 Derivation

Using the same process as outlined in earlier work by Wei,[128] we derive the boundary conditions for the adjoint system using a one-dimensional characteristic analysis. At the domain boundaries, viscous effects are assumed to be negligible and no forcing is applied. Therefore, (B.6) is assumed to be zero. Rearranging, the adjoint equations on the boundaries are

$$\frac{\partial \mathbf{q}^\dagger}{\partial t} + (\mathbf{A}^\dagger)^{-1}\mathbf{B}^\dagger \frac{\partial \mathbf{q}^\dagger}{\partial x} + (\mathbf{A}^\dagger)^{-1}\mathbf{C}^\dagger \frac{\partial \mathbf{q}^\dagger}{\partial y} + (\mathbf{A}^\dagger)^{-1}\mathbf{D}^\dagger \frac{\partial \mathbf{q}^\dagger}{\partial z} = 0. \tag{C.1}$$

Decomposing the coefficient matrices on the spatial derivative terms in (C.1) above gives for the x direction:

$$(\mathbf{A}^\dagger)^{-1}\mathbf{B}^\dagger = (\mathbf{S}_\mathrm{x}^\dagger)^{-1}\mathbf{\Lambda}_\mathrm{x}^\dagger \mathbf{S}_\mathrm{x}^\dagger \tag{C.2}$$

where

$$(\mathbf{S}_{\mathrm{x}}^{\dagger})^{-1} = \frac{1-\gamma}{c^2}\begin{bmatrix} 1 & u & v & w & \frac{1}{2}(u^2+v^2+w^2) \\ -w & -uw & -vw & -w^2+\frac{c^2}{1-\gamma} & -\frac{1}{2}w(u^2+v^2+w^2)+w\frac{c^2}{1-\gamma} \\ -v & -uv & -v^2+\frac{c^2}{1-\gamma} & -vw & -\frac{1}{2}v(u^2+v^2+w^2)+v\frac{c^2}{1-\gamma} \\ -\frac{1}{2} & -\frac{u-c}{2} & -\frac{v}{2} & -\frac{w}{2} & -\frac{u^2+v^2+w^2}{4}-\frac{uc}{2}-\frac{c^2}{2(\gamma-1)} \\ -\frac{1}{2} & -\frac{u+c}{2} & -\frac{v}{2} & -\frac{w}{2} & -\frac{u^2+v^2+w^2}{4}+\frac{uc}{2}-\frac{c^2}{2(\gamma-1)} \end{bmatrix}, \tag{C.3}$$

$$\mathbf{S}_{\mathrm{x}}^{\dagger} = \begin{bmatrix} \frac{1}{2}(u^2-v^2-w^2)+\frac{c^2}{1-\gamma} & -w & -v & \frac{1}{2}(u^2+v^2+w^2)+\frac{uc}{\gamma-1} & \frac{1}{2}(u^2+v^2+w^2)-\frac{uc}{\gamma-1} \\ -u & 0 & 0 & -u-\frac{c}{\gamma-1} & -u+\frac{c}{\gamma-1} \\ 0 & 0 & 1 & -v & -v \\ 0 & 1 & 0 & -w & -w \\ 1 & 0 & 0 & 1 & 1 \end{bmatrix}, \tag{C.4}$$

and

$$\mathbf{\Lambda}_{\mathrm{x}}^{\dagger} = \begin{bmatrix} u & 0 & 0 & 0 & 0 \\ 0 & u & 0 & 0 & 0 \\ 0 & 0 & u & 0 & 0 \\ 0 & 0 & 0 & u-c & 0 \\ 0 & 0 & 0 & 0 & u+c \end{bmatrix}. \tag{C.5}$$

The matrix, $\mathbf{\Lambda}_{\mathrm{x}}^{\dagger}$, contains on its diagonal the expected characteristic speeds of the corresponding entropy, (two) vorticity, and (two) acoustic waves derived in a similar decomposition of the flow field equations.[131] These characteristics are interpreted in a similar fashion for the adjoint field.

Likewise, in the y direction, we have

$$(\mathbf{A}^{\dagger})^{-1}\mathbf{C}^{\dagger} = (\mathbf{S}_{\mathrm{y}}^{\dagger})^{-1}\mathbf{\Lambda}_{\mathrm{y}}^{\dagger}\mathbf{S}_{\mathrm{y}}^{\dagger} \tag{C.6}$$

where

$$(\mathbf{S}_{\mathrm{y}}^{\dagger})^{-1} = \frac{1-\gamma}{c^2}\begin{bmatrix} 1 & u & v & w & \frac{1}{2}(u^2+v^2+w^2) \\ -w & -uw & -vw & -w^2+\frac{c^2}{1-\gamma} & -\frac{1}{2}w(u^2+v^2+w^2)+w\frac{c^2}{1-\gamma} \\ -u & -u^2+\frac{c^2}{1-\gamma} & -uv & -uw & -\frac{1}{2}u(u^2+v^2+w^2)+u\frac{c^2}{1-\gamma} \\ -\frac{1}{2} & -\frac{u}{2} & -\frac{v-c}{2} & -\frac{w}{2} & -\frac{u^2+v^2+w^2}{4}-\frac{vc}{2}-\frac{c^2}{2(\gamma-1)} \\ -\frac{1}{2} & -\frac{u}{2} & -\frac{v+c}{2} & -\frac{w}{2} & -\frac{u^2+v^2+w^2}{4}+\frac{vc}{2}-\frac{c^2}{2(\gamma-1)} \end{bmatrix}, \tag{C.7}$$

$$\mathbf{S}_{\mathrm{y}}^{\dagger} = \begin{bmatrix} \frac{1}{2}(u^2-v^2-w^2)+\frac{c^2}{1-\gamma} & -w & -u & \frac{1}{2}(u^2+v^2+w^2)+\frac{vc}{\gamma-1} & \frac{1}{2}(u^2+v^2+w^2)-\frac{vc}{\gamma-1} \\ 0 & 0 & 1 & -u & -u \\ -v & 0 & 0 & -v-\frac{c}{\gamma-1} & -v+\frac{c}{\gamma-1} \\ 0 & 1 & 0 & -w & -w \\ 1 & 0 & 0 & 1 & 1 \end{bmatrix}, \tag{C.8}$$

and

$$\mathbf{\Lambda}_{\mathrm{y}}^{\dagger} = \begin{bmatrix} v & 0 & 0 & 0 & 0 \\ 0 & v & 0 & 0 & 0 \\ 0 & 0 & v & 0 & 0 \\ 0 & 0 & 0 & v-c & 0 \\ 0 & 0 & 0 & 0 & v+c \end{bmatrix}. \tag{C.9}$$

Since all simulations presented in this work were either in two dimensions or applied a periodic boundary condition in the spanwise direction, the above decompositions supply all of the needed information to apply the characteristic boundary condition. There is no need to derive a decomposition for $(\mathbf{A}^{\dagger})^{-1}\mathbf{D}^{\dagger}$. The matrices $\mathbf{\Lambda}_{\mathrm{x}}^{\dagger}$ and $\mathbf{\Lambda}_{\mathrm{y}}^{\dagger}$ determine the direction of propagation at the left/right and top/bottom boundaries, respectively. Modes entering the domain are to be suppressed, taking care to account for the fact that the flow is solved backward in time.

C.2 Implementation

C.2.1 Adjoint Characteristic Variables

To implement the boundary condition on the domain boundaries or the solid wall edge, the one-dimensional equation

$$\frac{\partial \mathbf{q}^\dagger}{\partial t} + (\mathbf{A}^\dagger)^{-1}\mathbf{B}^\dagger \frac{\partial \mathbf{q}^\dagger}{\partial x} = 0 \tag{C.10}$$

is considered. Substituting (C.2) and left-multiplying by $(\mathbf{S}_\mathrm{y}^\dagger)^{-1}$ gives

$$\frac{\partial \mathbf{c}_\mathrm{x}^\dagger}{\partial t} + \mathbf{\Lambda}_\mathrm{x}^\dagger \frac{\partial \mathbf{c}_\mathrm{x}^\dagger}{\partial x} = 0 \tag{C.11}$$

where $\mathbf{c}_\mathrm{x}^\dagger = (\mathbf{S}_\mathrm{x}^\dagger)^{-1}\mathbf{q}^\dagger$ is defined as the vector of x-direction characteristics and denoted as

$$\mathbf{c}_\mathrm{x}^\dagger = \begin{bmatrix} c_{1\mathrm{x}}^\dagger \\ c_{2\mathrm{x}}^\dagger \\ c_{3\mathrm{x}}^\dagger \\ c_{4\mathrm{x}}^\dagger \\ c_{5\mathrm{x}}^\dagger \end{bmatrix} = \begin{bmatrix} -\frac{\gamma-1}{2c^2}\left[p^\dagger(u^2+v^2+w^2) + 2(uu^\dagger + vv^\dagger + ww^\dagger + \rho^\dagger)\right] \\ (p^\dagger w + w^\dagger) - wc_{1\mathrm{x}}^\dagger \\ (p^\dagger v + v^\dagger) - vc_{1\mathrm{x}}^\dagger \\ \frac{p^\dagger}{2} - \frac{(p^\dagger u + u^\dagger)(\gamma-1)}{2c} - \frac{c_{1\mathrm{x}}^\dagger}{2} \\ \frac{p^\dagger}{2} + \frac{(p^\dagger u + u^\dagger)(\gamma-1)}{2c} + \frac{c_{1\mathrm{x}}^\dagger}{2} \end{bmatrix}. \tag{C.12}$$

For completeness, $\mathbf{c}_\mathrm{x}^\dagger$ can be converted back to adjoint variables via

$$\mathbf{q}^\dagger = \begin{bmatrix} \frac{-c_1^\dagger c^2}{(\gamma-1)} + \frac{(c_4^\dagger - c_5^\dagger)uc}{(\gamma-1)} - (c_3^\dagger v + c_2 w) + \frac{c_1^\dagger}{2}(u^2 - v^2 - w^2) + \frac{(c_4^\dagger + c_5^\dagger)}{2}(u^2+v^2+w^2) \\ -(c_1^\dagger + c_4^\dagger + c_5^\dagger)u + \frac{c}{(\gamma-1)}(c_5^\dagger - c_4^\dagger) \\ c_3^\dagger - v(c_4^\dagger - c_5^\dagger) \\ c_2^\dagger - w(c_4^\dagger - c_5^\dagger) \\ c_1^\dagger + c_4^\dagger + c_5^\dagger \end{bmatrix}. \tag{C.13}$$

Likewise, the y-direction characteristics derived in a similar fashion as in (C.10) and (C.11) for

use on the top/bottom boundaries are

$$\mathbf{c}_{\mathrm{y}}^{\dagger} = \begin{bmatrix} c_{1\mathrm{y}}^{\dagger} \\ c_{2\mathrm{y}}^{\dagger} \\ c_{3\mathrm{y}}^{\dagger} \\ c_{4\mathrm{y}}^{\dagger} \\ c_{5\mathrm{y}}^{\dagger} \end{bmatrix} = \begin{bmatrix} -\frac{\gamma-1}{2c^2}\left[p^{\dagger}(u^2+v^2+w^2) + 2(uu^{\dagger}+vv^{\dagger}+ww^{\dagger}+\rho^{\dagger})\right] \\ (p^{\dagger}w + w^{\dagger}) - wc_{1\mathrm{y}}^{\dagger} \\ (p^{\dagger}u + u^{\dagger}) - uc_{1\mathrm{y}}^{\dagger} \\ \frac{p^{\dagger}}{2} - \frac{(p^{\dagger}v+v^{\dagger})(\gamma-1)}{2c} - \frac{c_{1\mathrm{y}}^{\dagger}}{2} \\ \frac{p^{\dagger}}{2} + \frac{(p^{\dagger}v+v^{\dagger})(\gamma-1)}{2c} + \frac{c_{1\mathrm{y}}^{\dagger}}{2} \end{bmatrix} \tag{C.14}$$

and can be converted back to adjoint variables using

$$\mathbf{q}^{\dagger} = \begin{bmatrix} \frac{-c_{1\mathrm{y}}^{\dagger}c^2}{(\gamma-1)} + \frac{(c_{4\mathrm{y}}^{\dagger}-c_{5\mathrm{y}}^{\dagger})vc}{(\gamma-1)} - (c_{3\mathrm{y}}^{\dagger}u + c_{2\mathrm{y}}w) + \frac{c_{1\mathrm{y}}^{\dagger}}{2}(-u^2+v^2-w^2) + \frac{(c_{4\mathrm{y}}^{\dagger}+c_{5\mathrm{y}}^{\dagger})}{2}(u^2+v^2+w^2) \\ c_{3\mathrm{y}}^{\dagger} - u(c_{4\mathrm{y}}^{\dagger} - c_{5\mathrm{y}}^{\dagger}) \\ -(c_{1\mathrm{y}}^{\dagger} + c_{4\mathrm{y}}^{\dagger} + c_{5\mathrm{y}}^{\dagger})v + \frac{c}{(\gamma-1)}(c_{5\mathrm{y}}^{\dagger} - c_{4\mathrm{y}}^{\dagger}) \\ c_{2\mathrm{y}}^{\dagger} - w(c_{4\mathrm{y}}^{\dagger} - c_{5\mathrm{y}}^{\dagger}) \\ c_{1\mathrm{y}}^{\dagger} + c_{4\mathrm{y}}^{\dagger} + c_{5\mathrm{y}}^{\dagger} \end{bmatrix}. \tag{C.15}$$

C.2.2 Nonreflecting Boundary Conditions

In the cases where nonreflecting conditions are needed on the left/right and top/bottom portions of the domain, incoming modes are set to zero. This implies setting the following conditions:

$$\begin{aligned} \text{Left:} \quad & c_{4\mathrm{x}}^{\dagger} = 0 \\ \text{Right:} \quad & c_{5\mathrm{x}}^{\dagger} = 0 \\ \text{Top:} \quad & c_{5\mathrm{y}}^{\dagger} = 0 \\ \text{Bottom:} \quad & c_{4\mathrm{y}}^{\dagger} = 0. \end{aligned} \tag{C.16}$$

C.2.3 Solid Wall Boundary Conditions

In the computations with a solid wall, the adjoint characteristic equations are simplified due to the no-slip condition imposed in our simulations. However, on this surface the appropriate treatment

is reflecting conditions implemented by setting the incoming characteristic equal to the outgoing. This implies setting the following conditions (recalling the time-reversed solution of the adjoint):

$$\begin{aligned} \text{Right edge:} \quad & c^\dagger_{4\mathrm{x}} = c^\dagger_{5\mathrm{x}} \\ \text{Top:} \quad & c^\dagger_{4\mathrm{y}} = c^\dagger_{5\mathrm{y}} \\ \text{Bottom:} \quad & c^\dagger_{5\mathrm{y}} = c^\dagger_{4\mathrm{y}}. \end{aligned} \tag{C.17}$$

The wall extends all the way to the left edge of the computational domain for the simulations in chapter 5, so no boundary condition needs to be applied in that region.

List of References

[1] M. Conner, *Hans von Ohain: Elegance in Flight* (American Institute of Aeronautics and Astronautics, Inc., Reston, Virginia) (2001).

[2] T. Colonius and S. K. Lele, "Computational aeroacoustics: Progress on nonlinear problems of sound generation," Progress in Aerospace Sciences **40**, 345 (2004).

[3] Rand Corporation, "First-generation jet engine development," Appendix B of "An Overview of Military Jet Engine History", http://www.rand.org/publications, accessed March 17, 2009.

[4] European Patent Office Online Featured Topics, "The story behind: Quieter jet engines," http://www.epo.org, accessed March 17, 2009.

[5] T. Kelly and J. Allan, *Environmental Pollution*, chapter The Ecology of Transportation: Managing Mobility for the Environment, pages 5–24 (Springer Netherlands) (2006).

[6] Boeing, Inc., http://www.boeing.com/commercial/noise/restrictions.pdf, accessed May 19, 2008.

[7] M. J. Lighthill, "On sound generated aerodynamically: I. General theory." Proceedings of the Royal Society of London. Series A. **211**, 564 (1952).

[8] T. Colonius, S. K. Lele and P. Moin, "Sound generation in a mixing layer," J. Fluid Mech. **330**, 375 (1997).

[9] J. B. Freund, "Noise sources in a low-Reynolds-number turbulent jet at Mach 0.9," J. Fluid Mech. **438**, 277 (2001).

[10] G. M. Lilley, "On the noise from air jets," Aeronautical Research Council Reports and Memoranda (1958), No. 20, 376.

[11] G. M. Lilley, "On the noise from jets," AGARD Tech. Rep. CP-131 (1974).

[12] M. E. Goldstein, "A generalized acoustic analogy," J. Fluid Mech. **488**, 315 (2003).

[13] J. Laufer, R. H. Schlinker and R. E. Kaplan, "Experiments on supersonic jet noise," AIAA J. **40**, 489 (1976).

[14] C. K. W. Tam and L. Auriault, "Jet mixing noise from fine-scale turbulence," AIAA J. **37**, 145 (1999).

[15] A. T. Fedorchenko, "On some fundamental flaws in present aeroacoustic theory," J. Sound Vib. **232**, 719 (2000).

[16] D. G. Crighton, "Basic principles of aerodynamic noise generation," Progress in Aerospace Sciences **16**, 31 (1975).

[17] K. Hünecke, *Jet Engines: Fundamentals of Theory, Design, and Operation* (Motorbooks International Publishers, Osceola, WI) (1997).

[18] NASA Glenn Research Center, "Making future commercial aircraft quieter," http://www.nasa.gov/centers/glenn/about/fs03grc.html (November 2004), accessed March 26, 2009.

[19] M. F. Reeder and M. Samimy, "The evolution of a jet with vortex generating tabs: Real-time visualization and quantitative measurements," J. Fluid Mech. **311**, 73 (1996).

[20] K. B. M. Q. Zaman, "Spreading characteristics of compressible jets from nozzles of various geometries," J. Fluid Mech. **383**, 197 (March 1999).

[21] C. K. W. Tam and K. B. M. Q. Zaman, "Subsonic jet noise from non-axisymmetric and tabbed nozzles," AIAA Paper 2000-0086 (2000).

[22] C. K. W. Tam, "Influence of nozzle geometry on the noise of high-speed jets," AIAA J. **36**, 1396 (1998).

[23] G. L. Brown and A. Roshko, "On density effects and large structure in turbulent mixing layers," J. Fluid Mech. **64**, 775 (1974).

[24] S. Crow and F. Champagne, "Orderly structure in jet turbulence," J. Fluid Mech. **48**, 547 (1971).

[25] C.-M. Ho and P. Heurre, "Perturbed free shear layers," Annu. Rev. Fluid Mech. **16**, 365 (1984).

[26] S. Narayanan, T. Barber and D. R. Polak, "High subsonic jet experiments: Turbulence and noise generation studies," AIAA J. **40**, 430 (2002).

[27] M. Samimy, J. H. Kim, J. Kastner, I. Adamovich and Y. Utkin, "Active control of high-speed and high-reynolds-number jets using plasma actuators," J. Fluid Mech. **578**, 305 (2007).

[28] M. J. Wei and J. B. Freund, "A noise-controlled free shear flow," J. Fluid Mech. **546**, 123 (2006).

[29] R. R. Kleinman and J. B. Freund, "Adjoint-based control of the noise from a turbulent mixing layer," 12th AIAA/CEAS Aeroacoustics Conference, Cambridge, MA. (May 2006), AIAA Paper No. 2006-2501.

[30] S. Lele, "Compact finite-difference schemes with spectral-like resolution," J. Comp. Phys. **103**, 16 (1992).

[31] C. Tam and J. Webb, "Dispersion-relation-preserving finite-difference schemes for computational acoustics," J. Comp. Phys. **107**, 262 (1993).

[32] R. Hixon, V. Allampali, M. Nallasamy and S. Sawyer, "High-accuracy large-step explicit Runge-Kutta (HALE-RK) schemes for computational aeroacoustics," 44th AIAA Aerospace Sciences Meeting and Exhibit, Reno, Nevada. (January 2006), AIAA Paper No. 2006-797.

[33] J. B. Freund, "Proposed inflow/outflow boundary condition for direct computation of aerodynamic sound," AIAA J. **35**, 740 (1997).

[34] T. Colonius, S. K. Lele and P. Moin, "Boundary-conditions for direct computation of aerodynamic sound generation," AIAA J. **31**, 1574 (1993).

[35] M. Rai and P. Moin, "Direct numerical-simulation of transition and turbulence in a spatially evolving boundary-layer," Journal of Computational Physics **109**, 169 (1993).

[36] T. J. Poinsot and S. K. Lele, "Boundary-conditions for direct simulations of compressible viscous flows," J. Comp. Phys. **101**, 104 (1992).

[37] M. Visbal and D. Gaitonde, "On the use of higher-order finite-difference schemes on curvilinear and deforming meshes," J. Comp. Phys. **181**, 155 (2002).

[38] D. J. Bodony and S. K. Lele, "On using large-eddy simulation for the prediction of noise from cold and heated turbulent jets," Phys. Fluids **17**, 85 (2005).

[39] C. K. W. Tam, M. Golebiowski and J. M. Seiner, "On the two components of turbulent mixing noise from supersonic jets," 2nd AIAA/CEAS Aeroacoustics Conference, State College, PA. (May 1996), AIAA Paper No. 1996-1716.

[40] K. Viswanathan, "Analysis of the two similarity components of turbulent mixing noise," AIAA J. **40**, 1735 (2002).

[41] M. Goldstein and S. J. Leib, "The role of instability waves in predicting jet noise," J. Fluid Mech. **525**, 37 (2005).

[42] M. Goldstein, "Ninety-degree acoustic spectrum of a high speed air jet," AIAA J. **43**, 96 (2005).

[43] S. R. Venkatesh, D. R. Polak and S. Narayanan, "Beamforming algorithm for distributed source localization and its application to jet noise," AIAA J. **41**, 1238 (2003).

[44] M. Harper-Bourne, "Radial distribution of jet noise sources using far-field microphones," 4th AIAA/CEAS Aeroacoustics Conference, Toulouse, France (June 1998), AIAA Paper No. 1998-2357.

[45] D. J. Bodony and S. K. Lele, "Current status of jet noise predictions using large-eddy simulation," AIAA J. **46**, 364 (2008).

[46] C. Bogey and C. Bailly, "Investigation of downstream and sideline subsonic jet noise using large eddy simulation," Theor. Comput. Fluid Dyn. **20**, 23 (2006).

[47] N. D. Sandham and W. C. Reynolds, "Three-dimensional simulations of large eddies in the compressible mixing layer," J. Fluid Mech. **224**, 133 (1991).

[48] M. Rogers and R. Moser, "Direct simulation of a self-similar turbulent mixing layer," Phys. Fluids **6**, 903 (1994).

[49] A. W. Vreman, N. D. Sandham and K. H. Luo, "Compressible mixing layer growth rate and turbulence characteristics," J. Fluid Mech. **320**, 235 (1996).

[50] J. B. Freund, S. K. Lele and P. Moin, "Compressibility effects in a turbulent annular mixing layer. Part 1. Turbulence and growth rate," J. Fluid Mech. **421**, 229 (2000).

[51] C. Pantano and S. Sarkar, "A study of compressibility effects in the high-speed turbulent shear layer using direct numerical simulation," J. Fluid Mech. **451**, 329 (2002).

[52] E. J. Avital, N. D. Sandham and K. H. Luo, "Mach wave radiation by mixing layers. Part I: Analysis of the sound field," Theoret. Comput. Fluid Dyn. **12**, 73 (1998).

[53] S. K. Lele and C. M. Ho, Personal Communication (1993).

[54] V. Fortuné, E. Lamballais and Y. Gervais, "Noise radiated by a non-isothermal, temporal mixing layer. Part I: Direct computation and prediction using compressible DNS," Theoret. Comput. Fluid Dyn. **18**, 61 (2004).

[55] D. Bodony, *Aeroacoustic Prediction of Turbulent Free Shear Flows*, Ph.D. thesis, Stanford University, Department of Aeronautics and Astronautics (2004).

[56] J. H. Bell and R. D. Mehta, "Development of a two-stream mixing layer from tripped and untripped mixing layers," AIAA J. **28**, 2034 (1990).

[57] S. Goebel and J. C. Dutton, "Experimental study of compressible turbulent mixing layers," AIAA J. **29**, 538 (1991).

[58] M. Samimy and G. S. Elliot, "Effects of compressibility on the characteristics of free shear layers," AIAA J. **28**, 439 (1990).

[59] G. K. Batchelor, "Pressure fluctuations in isotropic turbulence," Proc. Camb. Phil. Soc. **47**, 359 (1951).

[60] W. K. George, P. D. Beuther and R. E. Arndt, "Pressure spectra in turbulent free shear flows," J. Fluid Mech. **148**, 155 (1984).

[61] J. E. Ffowcs Williams, "The noise from turbulence convected at high speed," Philosophical Transactions of the Royal Society of London A **255**, 469 (1963).

[62] D. G. Crighton, "Excess noise field of subsonic jets," J. Fluid Mech. **56**, 683 (1972).

[63] M. E. Goldstein, W. Braun and J. J. Adamczyk, "Unsteady-flow in a supersonic cascade with strong in-passage shocks," J. Fluid Mech. **83**, 569 (1977).

[64] M. J. Lighthill, *Waves in Fluids* (Cambridge University Press, Cambridge, U.K.) (1978).

[65] A. D. Pierce, *Acoustics – An Introduction to Its Physical Principles and Applications* (Acoustical Society of America, Woodbury, New York) (1989).

[66] J. Bridges and F. Hussain, "Direct evaluation of aeroacoustic theory in a jet," J. Fluid Mech. **240**, 469 (1992).

[67] J. Laufer and T. Yen, "Noise generation by a low-mach-number jet," J. Fluid Mech. **134**, 1 (1983).

[68] J. E. Ffowcs Williams and A. J. Kempton, "Noise from large-scale structure of a jet," J. Fluid Mech. **84**, 673 (1978).

[69] M. J. Lighthill, "An estimate of the covariance of T_{xx} without using statistical assumptions," Appendix 1 of "On the Noise Radiated from a Turbulent High Speed Jet", by G. M. Lilley in *Computational Aeroacoustics* edited by J. C. Hardin and M. K. Hussaini, New York: Springer-Verlag. (1992).

[70] M. E. Goldstein and B. M. Rosenbaum, "Effect of anisotropic turbulence on aerodynamic noise," J. of Acoust. Soc. Am. **54**, 630 (1973).

[71] A. Khavaran, "Role of anisotropy in turbulent mixing noise," AIAA J. **37**, 832 (1999).

[72] D. G. Crighton and P. Huerre, "Shear-layer pressure-fluctuations and superdirective acoustic sources," J. Fluid Mech. **220**, 355 (1990).

[73] C. K. W. Tam, K. Viswanathan, K. Ahuja and J. Panda, "The sources of jet noise: Experimental evidence," 13th AIAA/CEAS Aeroacoustics Conference, Rome, Italy. (May 2007), AIAA Paper No. 2007-3641.

[74] T. Maeder, N. A. Adams and L. Kleiser, "Direct simulation of supersonic boundary layers by an extended temporal approach," J. Fluid Mech. **429**, 187 (2001).

[75] T. S. Lund, X. Wu and K. D. Squires, "Generation of turbulent inflow data for spatially-developing boundary layer simulations," J. Comp. Phys. **140**, 233 (1998).

[76] A. Jirasek, "A vortex generator model and its application to flow control," (2004), AIAA Paper 2004-4965.

[77] M. Samimy, K. B. M. Q. Zaman and M. Reeder, "Effect of tabs on the flow and noise field of an axisymmetric jet," AIAA J. **31**, 609 (1993).

[78] B. Callender, E. Gutmark and S. Martens, "Far-field acoustic investigation into chevron nozzle mechanisms and trends," AIAA J. **43**, 87 (2005).

[79] A. Glezer and M. Amitay, "Synthetic jets," Annu. Rev. Fluid Mech. **34**, 503 (2002).

[80] B. Cybyk, K. Grossman and D. V. Wie, "Computational assessment of the sparkjet flow control actuator," 33rd AIAA Fluid Dynamics Conference and Exhibit, Orlando, Florida. (June 2003), AIAA Paper No. 2003-3711.

[81] T. Corke and M. Post, "Overview of plasma actuators: Concepts, optimization, and applications," (January 2005), AIAA Paper 2005-0563.

[82] R. L. Kimmel, J. R. Hayes, J. A. Menart and J. Shang, "Effect of surface plasma discharges on boundary layers at mach 5," (January 2004), AIAA Paper 2004-0509.

[83] S. Merriman, E. Ploenjes, P. Palm and I. Adamovich, "Shock wave control by nonequilibrium plasmas in cold supersonic gas flows," AIAA J. **39**, 1547 (2001).

[84] M. Samimy, I. Adamovich, B. Webb, J. Kastner, J. Hileman, S. Keshav and P. Palm, "Development and characterization of plasma actuators for high speed and reynolds number jet control," Exp. Fluids **37**, 577 (2004).

[85] Y. G. Utkin, S. Keshav, J. Kim, J. Kastner, I. V. Adamovich and M. Samimy, "Development and use of localized arc filament plasma actuators for high-speed flow control," J. Phys. D: Appl. Phys. **40**, 685 (2007).

[86] T. C. Corke, M. L. Post and D. M. Orlov, "SDBD plasma enhanced aerodynamics: concepts, optimization and applications," Prog. Aero. Sci. **43**, 193 (2007).

[87] S. O. Macheret, M. N. Schneider and R. B. Miles, "Magnetohydrodynamic and electrohydrodynamic control of hypersonic flows of weakly ionized plasmas," AIAA J. **42**, 1378 (2004).

[88] S. Leonov, V. Bityurin, D. Yarantsev and A. Youriev, "The effect of plasma induced separation," (2003), AIAA Paper 2003-3853.

[89] M. Samimy, J.-H. Kim, I. Adamovich, Y. Utkin and J. Kastner, "Towards noise mitigation in high speed and high Reynolds number jets using plasma actuators," AIAA Paper 2006-2703 (May 2006).

[90] J. H. Kim, I. Adamovich and M. Samimy, "Active noise control in a mach 1.3 ideally-expanded jet with plasma actuators," 46th AIAA Aerospace Sciences Meeting and Exhibit, Reno, Nevada (January 2008), AIAA Paper No. 2008-0038.

[91] J. S. Shang, S. T. Surzhikov, R. Kimmel, D. Gaitonde, J. Menart and J. Hayes, "Mechanisms of plasma actuators for hypersonic flow control," Progress in Aerospace Sciences **41**, 642 (2005).

[92] M. Samimy, "Preliminary results on characterization of LAFPAs," Gas Dynamics and Turbulence Laboratory, The Ohio State University. Internal Document.

[93] C. Lui, *A Numerical Investigation of Shock-Associated Noise*, Ph.D. thesis, Stanford University (2003).

[94] J. Kastner, J. Hileman and M. Samimy, "Exploring high-speed axisymmetric jet noise control using Hartmann tube fluidic actuators," AIAA Paper 2004-0186 (January 2004).

[95] K. Viswanathan and L. T. Clark, "Effect of nozzle contour on jet aeroacoustics," 42nd AIAA Aerospace Sciences Meeting and Exhibit, Reno, Nevada. (January 2004), AIAA Paper No. 2004-0008.

[96] C. S. Yoo and H. G. Im, "Characteristic boundary conditions for simulations of compressible reacting flows with multi-dimensional, viscous and reaction effects," Combustion Theory and Modelling **11**, 259 (2007).

[97] M. Samimy, J. Kastner, J.-H. Kim, Y. Utkin, I. Adamovich and C. Brown, "Flow and noise control in high speed and high reynolds number jets using plasma actuators," AIAA Paper 2006-2846 (June 2006).

[98] J. M. Seiner, S. M. Dash and D. C. Kenzakowski, "Historical survey on enhanced mixing in scramjet engines," J. Propul. Power **17**, 1273 (2001).

[99] R. E. Dix and R. C. Bauer, "Engineering model predictions of aeroacoustic amplitudes in a weapons cavity," AIAA Paper No. 1993-0858 (1993).

[100] M. Gharib and A. Roshko, "The effect of flow oscillations on cavity drag," J. Fluid Mech. **177**, 501 (1987).

[101] C. W. Rowley, T. Colonius and A. J. Basu, "On self-sustained oscillation in two-dimensional compressible flow over rectangular cavities," J. Fluid Mech. **455**, 315 (2002).

[102] L. F. East, "Aerodynamically induced resonance in rectangular cavities," J. Sound Vib. **3**, 277 (1966).

[103] C. K. W. Tam and P. J. W. Block, "On the tones and pressure oscillations induced by flow over rectangular cavities," J. Fluid Mech. **89**, 373 (1978).

[104] L. Larcheveque, P. Sagaut, I. Mary, O. Labbe and P. Comte, "Large-eddy simulation of a compressible flow past a deep cavity," Phys. Fluids **15**, 193 (2003).

[105] N. Forestier, L. Jacquiny and P. Geffroy, "The mixing layer over a deep cavity at high-subsonic speed," J. Fluid Mech. **475**, 101 (2003).

[106] J. E. Rossiter, "Wind-tunnel experiments on the flow over rectangular cavities at subsonic and transonic speeds," NASA Ames Research Center, R&M 3438 (October 1964).

[107] C. W. Rowley and D. R. Williams, "Dynamics and control of high-reynolds-number flow over open cavities," Annu. Rev. Fluid Mech. **38**, 251 (2006).

[108] H. H. Heller and D. B. Bliss, "The physical mechanisms of flow-induced pressure fluctuations in cavities and concepts for their suppression," (March 1975), AIAA Paper 1975-491.

[109] O. Unalmis, N. Clemens and D. Dolling, "Cavity oscillation mechanisms in high-speed flows," AIAA J. **42**, 2035 (2004).

[110] J. Malone, M. Debiasi, J. Little and M. Samimy, "Analysis of the spectral relationships of cavity tones in subsonic resonant cavity flows," Phys. Fluids **21** (2009).

[111] D. Rockwell and E. Naudascher, "Review: Self-sustaining oscillations of flow past cavities," J. Fluids Eng. **100**, 152 (1978).

[112] C. Knisley and D. Rockwell, "Self-sustained low-frequency components in an impinging shear layer," J. Fluid Mech. **116**, 157 (1982).

[113] N. Delprat, "Rossiter's formula: A simple spectral model for complex amplitude modulation process?" Phys. Fluids **18** (2006).

[114] W. R. Miksad, "Experiments on nonlinear-interactions in transition of a free shear layer," J. Fluid Mech. **59**, 1 (1973).

[115] M. A. Kegerise, E. F. Spina, S. Garg and L. N. Cattafesta, "Mode-switching and nonlinear effects in compressible flow over a cavity," Phys. Fluids **16**, 678 (2004).

[116] L. Larcheveque, P. Sagaut, T.-H. Le and P. Comte, "Large-eddy simulation of a compressible flow in a three-dimensional open cavity at high reynolds number," J. Fluid Mech. **516**, 265 (2004).

[117] R. Mittal, P. Rampunggoon and H. S. Udaykumar, "Interaction of a synthetic jet with a flat-plate boundary layer," 31st AIAA Fluid Dynamics Conference and Exhibit, Anaheim, CA. (June 2001), AIAA Paper No. 2001-2773.

[118] A. Michalke, "On spatially growing disturbances in an inviscid shear layer," J. Fluid Mech. **23**, 521 (1965).

[119] A. C. Marta, J. Alonso and L. Tang, "Automatic magnetohydrodynamic control of hypersonic flow using a discrete adjoint formulation," AIAA Paper 2006-0370 (2006).

[120] M. G. Larson and T. J. Barth, "A posteriori error estimation for discontinuous Galerkin approximations of hyperbolic systems," 1^{st} International Symposium on Discontinuous Galerkin Methods, Newport, R.I., May 1999 (1999).

[121] M. B. Giles and N. A. Pierce, "Improved lift and drag estimates using adjoint euler equations," AIAA Paper 1999-3293 (1999).

[122] K. Palaniappan, P. Sahu, J. Alonso and A. Jameson, "Active flutter control using an adjoint method," AIAA Paper 2006-0370 (2006).

[123] T. R. Bewley, P. Moin and R. Temam, "DNS-based predictive control of turbulence: an optimal benchmark target for feedback algorithms," J. Fluid Mech. **447**, 179 (2001).

[124] C. K. W. Tam and L. Auriault, "Mean flow refraction effects on sound radiated from localized sources in a jet," J. Fluid Mech. **370**, 149 (1998).

[125] S. S. Collis, K. Ghayour, M. Heinkenschloss, M. Ulbrich and S. Ulbrich, "Numerical solution of optimal control problems governed by the compressible Navier-Stokes equations," Proceedings of the International Conference on Optimal Control of Complex Structures, G. Leugering, J. Sprekels, and F. Troltzsch (Eds.), Birkhauser Verlag (2000).

[126] S. S. Collis, K. Ghayour, M. Heinkenschloss, M. Ulbrich and S. Ulbrich, "Towards adjoint-based methods for aeroacoustic control," AIAA Paper 2001-0821 (2001).

[127] S. S. Collis, K. Ghayour, M. Heinkenschloss, M. Ulbrich and S. Ulbrich, "Optimal control of unsteady compressible viscous flows," Intl. J. Num. Meth. Fluids **40**, 1401 (2002).

[128] M. J. Wei, *Jet Noise Control by Adjoint-Based Optimization*, Ph.D. thesis, University of Illinois at Urbana-Champaign (2004).

[129] M. M. Vainberg, *Variational Methods for the Study of Nonlinear Operators* (Holden-Day, San Francisco, CA.) (1964).

[130] W. Press, B. Flannery, S. Teukolsky and W. Vetterling, *Numerical Recipes* (Cambridge University Press) (1986).

[131] K. Thompson, "Time-dependent boundary-conditions for hyperbolic systems," J. Comp. Phys. **68**, 1 (1987).

Author Biography

Randall Kleinman was born in Golden Valley, Minnesota on July 28, 1981. He attended Bethel College (now Bethel University) and earned a Bachelor of Science degree in May 2003 majoring in Physics and in Applied Physics and minoring in Mathematics and German. He then entered the Department of Theoretical and Applied Mechanics (now Mechanical Science and Engineering) at the University of Illinois at Urbana-Champaign under the guidance of Professor Jonathan B. Freund. Randall earned a Master of Science degree in Theoretical and Applied Mechanics in December 2004. His research topics while at the University of Illinois were high-fidelity numerical simulation of free shear flows, noise generation by turbulence, simulation methodologies for optimal control in aeroacoustics, and numerical modeling of active controls in compressible mixing layers.

In April 2009, Randall began working for Boston Scientific Cardiac Rhythm Management's Research and Development division in St. Paul, Minnesota, working on the Latitude Patient Management System supporting the Cognis/Teligen series of implantable cardioverter defibrillators and cardiac resynchronization therapy devices.